MEDICAL CENTER HAMBURG-EPPENDORF

Institute of Experimental Pharmacology and Toxicology

Prof. Dr. med. Thomas Eschenhagen

Establishment of human engineered atrial heart tissue and an optogenetic arrhythmia model

Dissertation

With the aim of achieving the PhD

at the Medical Faculty of the University of Hamburg

by

Marta Lemme

Rho (Milano)

Hamburg 2019

Accepted by the

Medical Faculty of the University of Hamburg on: 24.05.2019

Published with permission of

Medical Faculty of the University of Hamburg.

Examining Board, Chair: Prof. Dr. Thomas Eschenhagen

Examination board, second reviewer: Prof. Dr. Christian Meyer

Examination board, third reviewer: Prof. Dr. Renate Schnabel

Table of Contents

1. Introduction

1.1 Atrial fibrillation

Atrial fibrillation (AF), the most common cardiac arrhythmia, is a major contributors to morbidity and mortality in the Western world. The prevalence of AF increases with the aging of the population. This cardiac arrhythmia is characterized by extremely fast, irregular electrical activity of the atria. As a result, regular P waves are absent in the ECG. AF-induced atrial contractile dysfunction is responsible for blood stasis and clot formation. AF-related thrombus is a major risk factor for ischemic stroke (Lip and Beevers 1995; Schotten et al. 2001; Marini et al. 2005). In clinical practice 20-25% of all strokes are caused by AF. Strokes in AF patients are particularly severe, but appropriate anticoagulation therapy can reduce the incidence of strokes and mortality among AF patients (Schotten et al. 2011; Nattel and Dobrev 2012).

AF promotes ventricular dysfunction which in turn causes atrial remodeling favoring the progression of AF. This mechanism represents a vicious circle. AF also induces atrial hypocontractility and remodeling, which perpetuate AF and finally results in treatment-resistant AF (the concept of "AF begets AF", Wijffels et al. 1995; Iwasaki et al. 2011). Atrial contractile dysfunction can be explained by AF-induced myolysis (loss of atrial myofilaments) and by disturbed activation of the contractile machinery. Downregulation and/or impaired function of L-type Ca^{2+} channel might be responsible for the atrial contractile dysfunction (Grand et al. 1994; Schotten et al. 2001).

Familial AF, associated with genetic variations, can be inherited and contributes to AF risk. Table 1 relevant genetic variants underlying AF are shown. Despite the limited prevalence of the familial disease, these variants could be valuable to determine the risk of future AF in asymptomatic individuals and to uncover novel molecular targets for pharmacotherapy (Mahida 2014).

Locus	Gene	Gene name
1q21	KCNN3	Potassium calcium-activated channel subfamily N member 3
4q25	PITX2	Paired-like homeodomain transcription factor 2
16q22	ZFHX3	Zinc finger homeobox protein 3
1q24	PRRX1	Paired related homeobox 1
7q31	CAV1	Caveolin 1
3p22	SCN5A	Sodium voltage-gated channel alpha subunit 5

	SCN10A	Sodium voltage-gated channel alpha subunit 10
5q35	NKX2.5	Homeobox protein Nkx-2.5
12p12	SOX5	SRY (sex determining region Y)-box 5
12q24	TBX5	T-box 5
15q24	HCN4	Hyperpolarization activated cyclic nucleotide gated potassium channel 4
14q23	SYNE2	Spectrin repeat containing nuclear envelope protein 2
10q22	SYNOP2	Synaptopodin 2
9q22	C9orf3	Chromosome 9 open reading frame 3
10q24	NEURL	Neuralized E3 ubiquitin protein ligase
5q31	WNT8A	Wnt family member 8A
3q25	CAND2	Cullin associated and neddylation dissociated 2
6q22	GJA1	Gap junction protein alpha 1
12q24	CUX2	Cut like homeobox 2
1p32	DMRTA2, CDKN2C	Doublesex- and mab-3-related transcription factor A2 Cyclin dependent kinase inhibitor 2C
2q31	TTN	Titin
1q24	METTL11B KIFAP3	Methyltransferase like 11B Kinesin associated protein 3
2p13	ANXA4 GMCL1	Annexin A4 Germ cell-less protein-like 1
2p14	CEP68	Centrosomal protein 68
5q22	KCNN2	Potassium calcium-activated channel subfamily N member 2
6q22	SCL35F1 PLN	Solute carrier family 35 member F1 Phospholamban
8p22	ASAH1, PCM1	N-acylsphingosine amidohydrolase 1 Pericentriolar material 1
10q24	SH3PXD2A	SH3 and PX domains 2A
11q24	KCNJ5	Potassium voltage-gated channel subfamily J member 5

Table 1: **List of genes associated with atrial fibrillation (AF)**. Genetic variants identified in AF by Genome-wide Association Studies (adapted from Sinner et al. 2011; Mahida 2014; Campuzano et al. 2016a; Feghaly et al. 2018; Nielsen et al. 2018).

1.1.1 AF mechanism

Three clinical types of AF can be identified: paroxysmal, persistent and permanent AF. Paroxysmal AF shows episodes of the arrhythmia terminating spontaneously within 7 days. It can evolve in persistent AF characterized by episodes that are sustained longer than 7 days and are not self-terminating. However, persistent AF can be still converted into sinus rhythm by

Introduction

pharmacological or electrical intervention. Finally AF eventually becomes permanent (or chronic) when sinus rhythm can no longer be restored (Figure 1D).

The progression from paroxysmal to persistent to chronic AF is influenced by electrical and structural remodeling of the atria promoted by AF itself or caused by underlying heart diseases. The majority of paroxysmal AF cases are driven by pulmonary vein (PV) sources which can be well isolated with ablation procedures. As AF develops into permanent, atrial substrate abnormality increases and catheter ablation becomes more complex and less efficient (Figure 1D; Iwasaki et al. 2011).
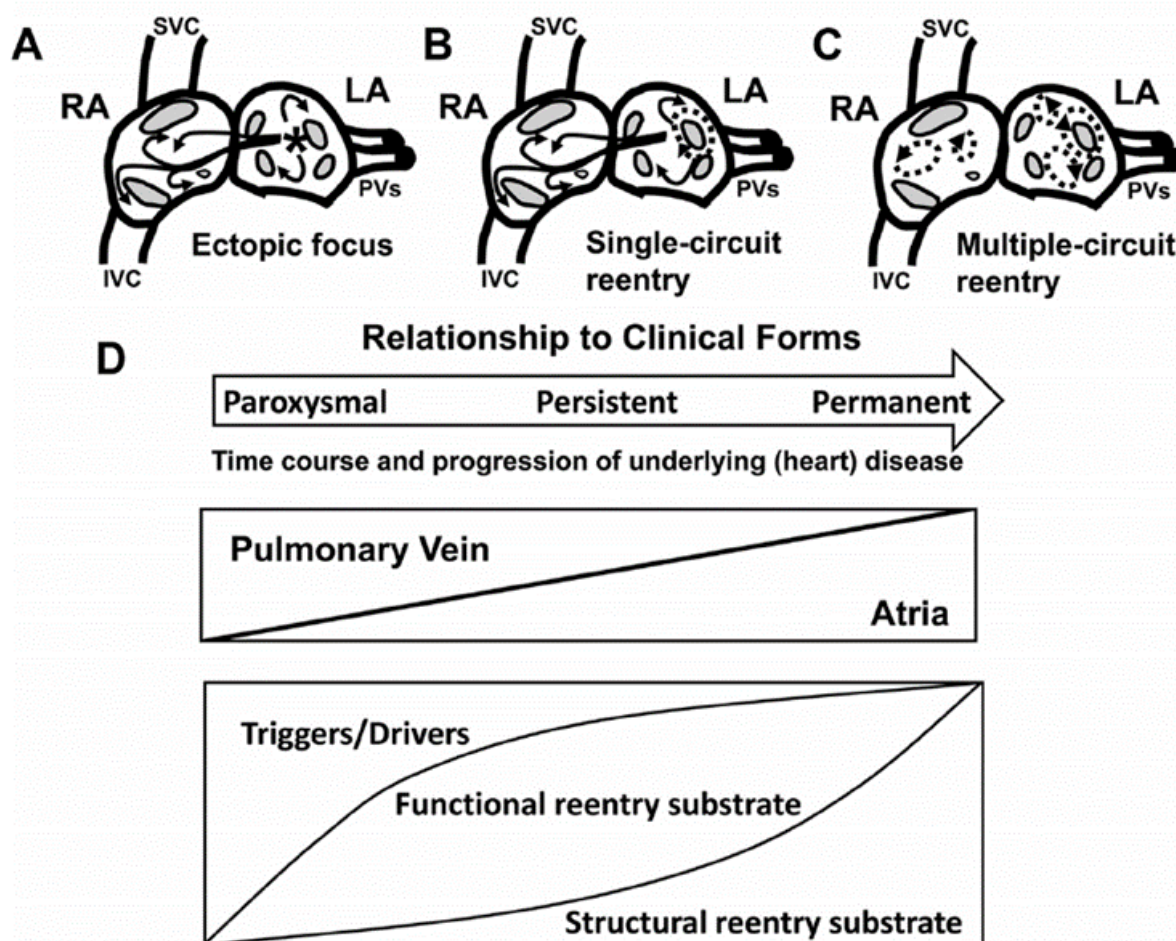
Figure 1: **Schematic overview of atrial fibrillation (AF) mechanism and evolution**. The drivers triggering AF can be distinguished in (A) local ectopic firing, (B) single-circuit reentry and (C) multiple-circuit reentry. (D) Time course and progression of different clinical types of AF. Paroxysmal AF originates predominantly from pulmonary vein. During AF evolution functional and structural reentry substrate predominate leading to persistent and permanent AF, respectively. RA indicates right atrium; LA, left atrium; SVC, superior vena cava and IVC, inferior vena cava (adapted from Iwasaki et al. 2011).

Reentry and focal ectopic firing are the drivers of AF maintenance (Figure 1A, B and C). Potential mechanism of ectopic firing can be related to enhanced automaticity, early afterdepolarizations (EADs) and delayed afterdepolarizations (DADs, Figure 2). Enhanced

Introduction

automaticity can be caused by decreased inward rectifier potassium current (I_{K1}) and/or increased depolarizing currents. EADs are spontaneous cell membrane depolarizations during the repolarization phase of an action potential (AP). The main factor causing EADs is prolongation of AP duration (APD). This prolongation can result from an increase in inward L-type Ca^{2+} current (I_{CaL}) or late Na^+ current (I_{NaL}), as well as from a decrease in outward K^+ currents. Longer plateau duration allows I_{CaL} to recover from inactivation and trigger additional Ca^{2+} release from the sarcoplasmic reticulum (SR). Thus, as I_{CaL} increases, Na^+-Ca^{2+} exchanger current (I_{NCX}) synergistically increases producing an inward depolarizing current during the AP plateau which can contribute to EAD formation (Figure 2).
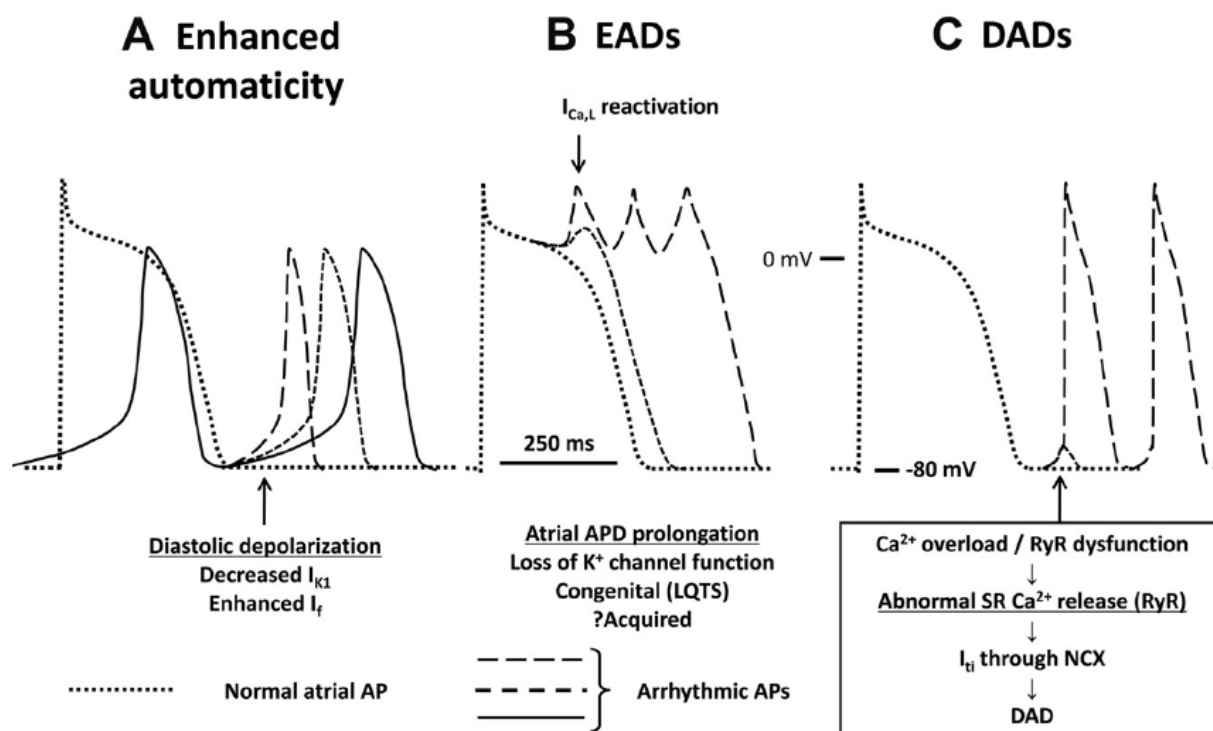
Figure 2: **Potential mechanisms of ectopic firing**. Mechanisms of atrial fibrillation (AF) generating ectopic firing can be (A) enhanced automaticity, (B) early afterdepolarizations (EADs) and (C) delayed afterdepolarizations (DADs; adapted from Iwasaki et al., 2011).

In contrast, DADs occur after completion of AP repolarization and are caused by abnormal diastolic release of Ca^{2+} from SR. Ryanodine receptor 2 (RyR2) and its accessory regulatory proteins including FKBP12.6, junctophilin, triadin, calsequestrin and junction are responsible for the Ca^{2+} release into the cytosol in response to transmembrane Ca^{2+} entry during each cardiac cycle (Figure 3).

Introduction
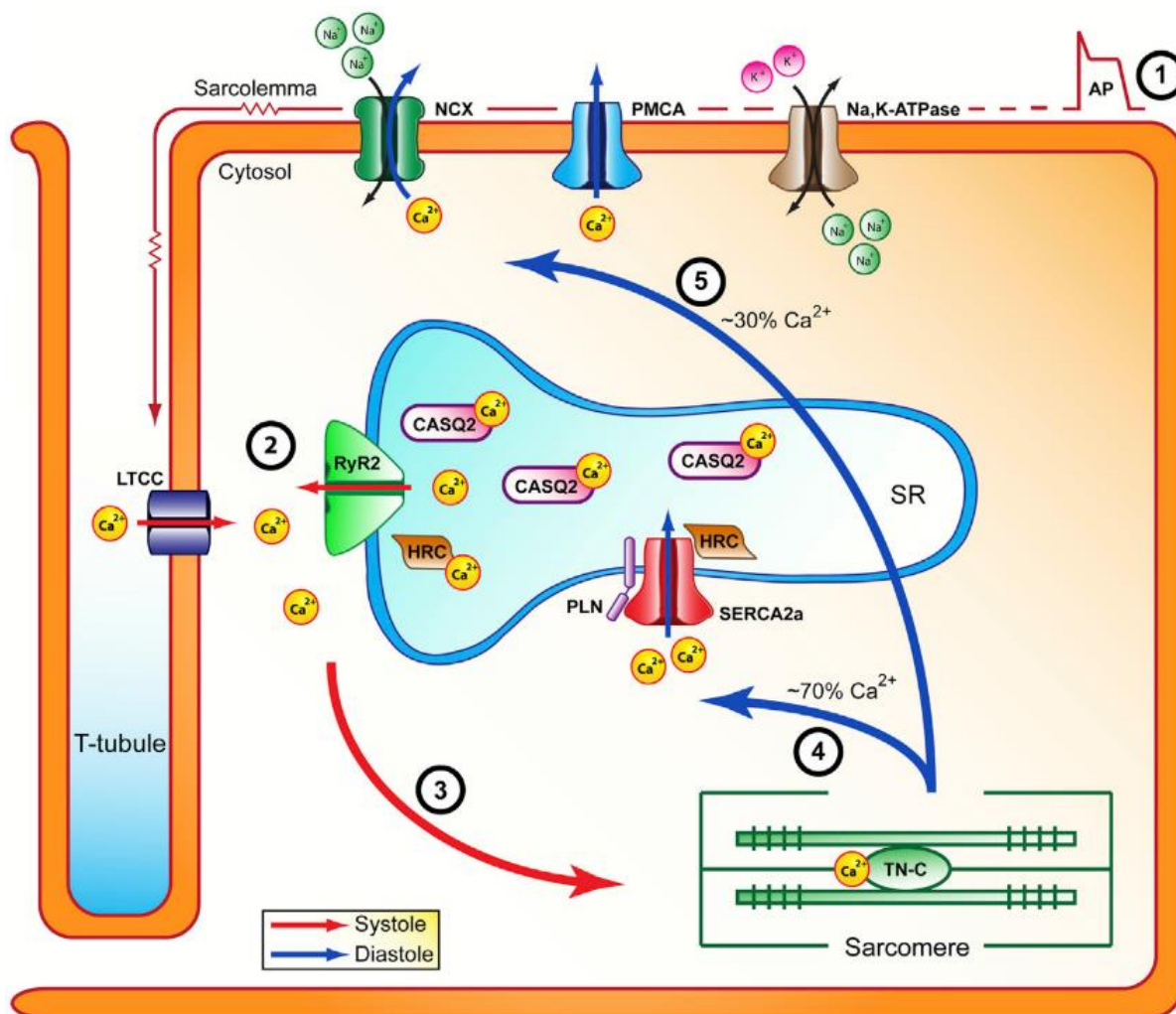
Figure 3: **Excitation-contraction coupling in cardiomyocytes**. During systole, an action potential travelling along the sarcolemma and down the T-tubules depolarizes the sarcolemma inducing the opening of LTCC. These opened channels permit calcium entry into the cytosol (step 1). In turn, this calcium influx triggers a subsequent calcium release from the sarcoplasmic reticulum (SR) through the RyR2 receptors (step 2). This cytosolic free calcium binds to troponin-C (TN-C) initiating muscle contraction (step 3). Cytosolic calcium during diastole is primarily sequestered by SERCA2a, which returns calcium to the SR (step 4). Cytosolic calcium also exits the cell through NCX and PMCA (step 5). This decrease in intracellular calcium leads to unbinding of calcium from TN-C and muscle relaxation. NCX, sodium calcium exchanger; Na,K-ATPase, sodium-potassium ATPase; PMCA, plasmamembrane calcium ATPase; LTCC, voltage-dependent L-type calcium channel; CASQ2, calsequestrin isoform 2; RyR2, ryanodine receptor isoform 2; SERCA2a, sarco(endo)plasmic reticulum calcium ATPase; PLN, phospholamban; HRC, histidine-rich calcium-binding protein; TN-C, troponin-C (adapted from Gorski et al. 2015).

RyR2 is normally closed during diastole, but it can open if it is functionally defective or the SR is Ca^{2+} overloaded (Figure 2). When RyR2 opens during diastole, the increase in cytoplasmic Ca^{2+} concentration activates the Na^+-Ca^{2+} exchanger (NCX). It transports one Ca^{2+} ion out of the cell in exchange with three extracellular Na^+ ions, causing a net depolarizing inward current that triggers DADs (Glitsch et al. 1970; Iwasaki et al. 2011; Nattel and Dobrev 2012). Therefore, altered RyR2 function and NCX overexpression are the major determinants of

Introduction

spontaneous SR Ca^{2+} release events in AF patients (Hove-Madsen et al. 2004; Dobrev et al. 2011; Nattel and Dobrev 2012).

Reentry requires a vulnerable atrial substrate and its maintenance depends on the refractoriness and conduction velocity (CV) of the tissue. Functional reentry in AF can be described by the leading circle model or by the spiral wave (Figure 4). In the leading-circle model, the wavelength (WL) of reentry circuits represents the distance the impulse travels in one refractory period (RP) and it can be calculated with the following equation: WL=RP*CV. Short WL allows formation of multiple reentry circuits in the atria. Simultaneous termination of reentry circuits is unlikely increasing the probability of sustained AF (Figure 4). In other words, shortened RP and reduced CV facilitate reentry and increase AF duration (Iwasaki et al. 2011; Nattel and Dobrev 2012). On the other hand, long WL reduces the number of simultaneous reentry circuits forming in the atria. Therefore, reentry is unstable and AF self-terminates.

Figure 4: **Conceptual models of functional reentry in atrial fibrillation (AF)**. (A) Leading circle. (B) Spiral-wave. (C) Normal wavelength (WL) gives rise to small number of reentry circuits and AF can easily self-terminate. (D) Decrease of refractory period (RP) or conduction velocity (CV) determines WL reduction. Atria can contain higher amount of reentry circuits. AF does not easily self-terminate. (E) Drugs increasing WL can reduce the number of reentry circuits, favoring AF termination (adapted from Iwasaki et al., 2011).

Introduction

Reentry mechanism in AF can also be described with a spiral wave model. The wavefront and the wavetail meet at the focal point called phase singularity (PS, Figure 5). At the PS, the wavefront curvature is so high and CV so slow that the core of the rotor becomes unexcitable. The wavefront velocity of the spiral wave is not constant and it is able to move through space, while a reentry circuit in the leading circle model shows a constant velocity and it is fixed in space (Waks and Josephson 2014).
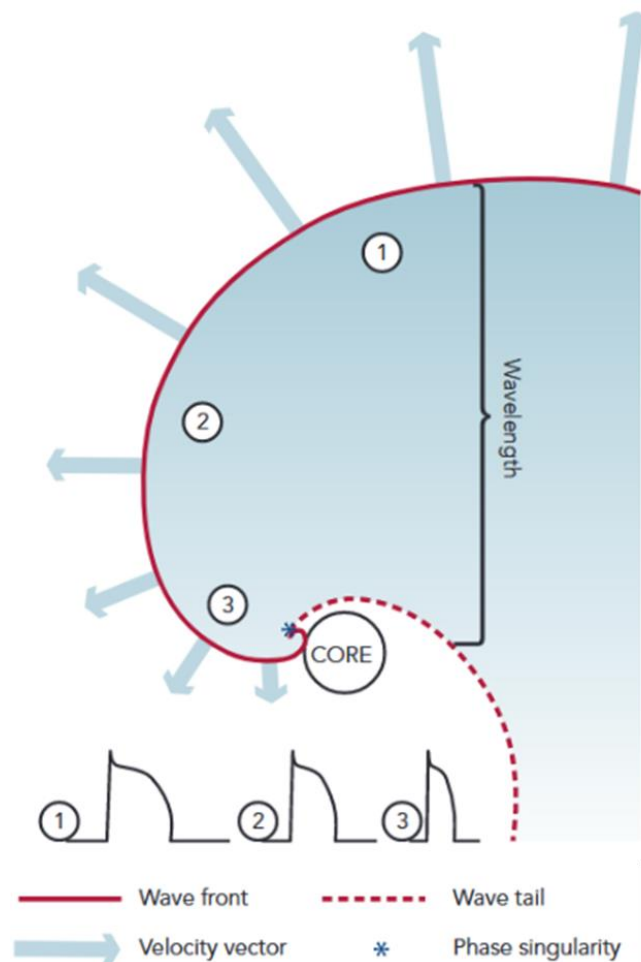
Figure 5: **Spiral wave of functional reentry in atrial fibrillation**. Phase singularity represents the meeting point of the wavefront and the wavetail of the rotor. The core of the rotor is extremely difficult to penetrate and excite (adapted from Waks and Josephson 2014).

1.1.2 Electrical remodeling

Electrical remodeling includes alteration in ion channel expression and/or function in a way that promotes AF (Figure 6). Shortening of APD and the loss of rate adaptation are detectable in atrial tissue and single myocytes from patients with chronic AF (Figure 6B). Rapid atrial rate in AF induces increased Ca^{2+} loading and activation of autoprotective mechanisms aiming to reduce Ca^{2+} entry. Ca^{2+} entry can be reduced directly by downregulation/inactivation of I_{CaL} or

indirectly by enhancement of inward rectifier potassium currents (I_{k1} and constitutively active acetylcholine-activated current [I_{KAChC}]), which reduces Ca^{2+} entry by shortening APD. However, shorter APD promotes functional reentry stability favoring AF vulnerability. Furthermore, enhancement of inward potassium currents determines hyperpolarization of resting membrane potential (RMP) in atrial cardiomyocytes (CMs), leading to higher sodium channel availability and faster CV.

However, sodium channel conductivity is about 20% lower in AF and the net effect on upstroke velocity as a surrogate for Na-channel activity is rather small (Wettwer et al. 2013; Sánchez et al. 2014). In addition, altered Ca^{2+} handling may be responsible for Ca^{2+} release from SR during diastole and ectopic firing (Dobrev and Ravens 2003; Iwasaki et al. 2011).
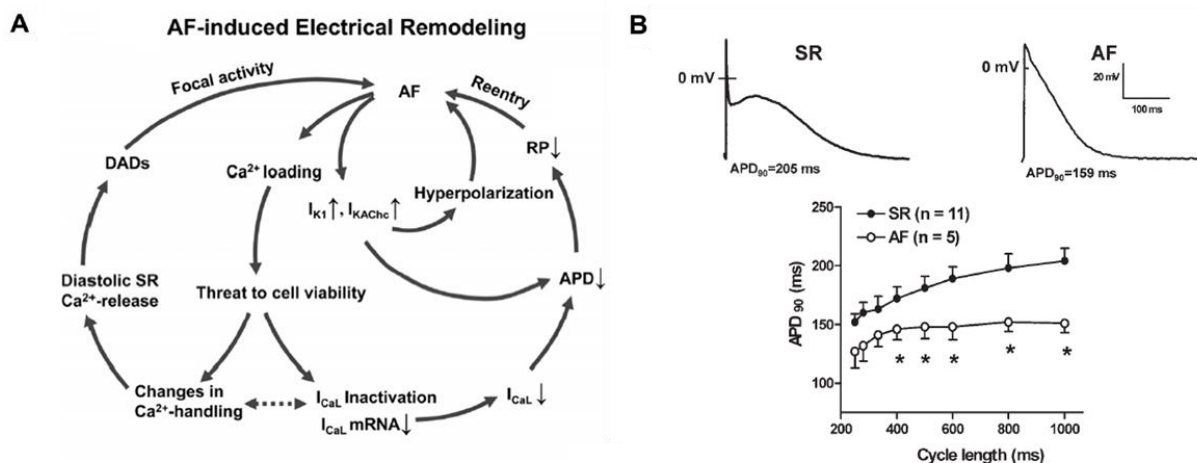
Figure 6: **Electrical remodeling in atrial fibrillation (AF)**. (A) Mechanisms promoting electrical remodeling during AF. Decrease of Ca^{2+} current and enhancement of inward K^+ currents determine AP duration shortening (adapted from Iwasaki et al. 2011). (B) Top, Representative AP traces recorded in human right atrial trabeculae from patients in sinus rhythm (left) and in AF (right). Bottom, APD_{90} adaptation to rate changes in sinus rhythm and AF (adapted from Dobrev & Ravens, 2003).

1.1.3 Structural remodeling

Apart from the tachyarrhythmia itself, several factors such as inflammation, atrial stretching, interstitial fibrosis, oxidative stress and apoptotic cell death are involved in the self-perpetuating positive feedback mechanism of AF. Structural remodeling includes changes in tissue and myocyte morphology. Fibrosis, a key factor of AF structural remodeling, impairs both mechanical and electrical function of the heart (Ebert et al. 2012). Reparative fibrosis replaces dead CMs with fibroblasts. These fibroblasts proliferate and differentiate into myofibroblasts, which are responsible for collagen secretion. Myofibroblast can couple to CMs and affect their electrical properties thus contributing to AF (Nattel and Dobrev 2012). Moreover, excessive

secretion of extracellular matrix (ECM) proteins by myofibroblasts cause atrial fibrosis, which can interfere with muscle bundle continuity and impair local conduction, thereby promoting reentry and/or ectopic activity (Figure 7).

In addition, CM hypertrophy, loss of sarcomeres (myolysis), glycogen accumulation and chromatin and connexin redistribution were the major histological findings in atria of patients with chronic AF. Structural remodeling contributes to stabilization of AF and to reduced efficacy of pharmacological cardioversion in AF (Dobrev and Ravens 2003; Nattel and Dobrev 2012).
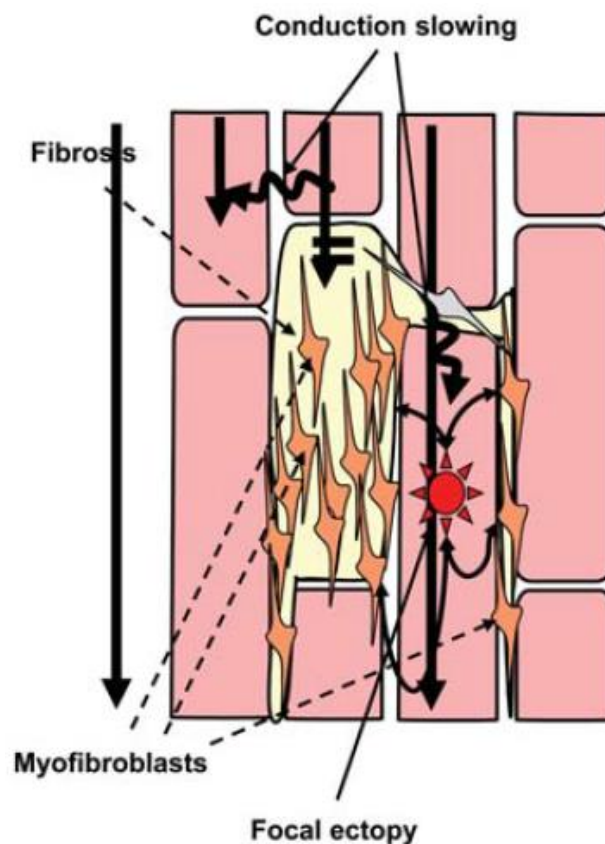
Figure 7: **Role of fibrosis in atrial fibrillation**. Schematic representation of a cardiac muscle bundle. Myofibroblasts (orange) secret collagen (yellow) causing fibrosis. Fibrosis impairs atrial tissue conduction (black arrow). Interaction between cardiomyocytes (pink) and myofibroblasts results in slow conduction and it can trigger focal ectopy (adapted from Nattel and Dobrev 2012).

1.1.4 AF treatment

The first step in managing AF is typically to treat it with medications to prevent stroke. Pharmacological therapies for AF include anticoagulants as well as rate and rhythm control medications.

Introduction

Blood thinners are administered to AF patients for their efficacy in preventing blood clot formation. Vitamin K–dependent oral anticoagulants such as warfarin efficiently prevent AF-related thromboembolism. Newer non vitamin K-dependent anticoagulants targeting factor Xa or thrombin exhibit a reduced risk of bleeding and a better benefit/risk ratio and will therefore increasingly replace warfarin (Iwasaki et al. 2011; Patel et al. 2011).

Rate control medications aim at restoring a normal ventricular rate by slowing down atrioventricular (AV)-node conduction. Digitalis glycosides have long been the standard for slowing down AV-node conduction and consequently the ventricular rate. However, they have a well-known low therapeutic index, and a recent study showed that the administration of digoxin, the most common cardiac glycoside, in AF patients is associated with higher incidence of mortality (Frayne et al. 2014). Today, β-adrenergic receptor blockers (bisoprolol, metoprolol, carvedilol) and L-type Ca^{2+}-channel blockers (dilitiazem, verapamil) are the most commonly used drugs for rate control.

The rhythm control strategy aims at restoring ("pharmacological cardioversion") or maintaining sinus rhythm. It is based on antiarrhythmic drugs of the Vaughan & Williams classes I and III, i.e. Na^+ and K^+ channel blockers, respectively (Goodman and Gilman 1966). Current rhythm control pharmacotherapy is limited by low efficacy and high risk for adverse cardiac side effects. The major concern is the risk of life-threatening ventricular arrhythmia. The most popular Na^+ channel blockers are propafenone and flecainide (Class Ic agents) and, historically, quinidine (Class Ia). Quinidine blocks also α-adrenoceptors and muscarinic receptors. Blockade of α-adrenoceptors causes a drop in blood pressure and a consequent release of catecholamines, which together with the blockade of muscarinic receptors increase speed of AV-conduction and ventricular rate. Thus, quinidine, if prescribed at all, should always be combined with an AV-conduction slowing drug (see above). Most importantly, quinidine has the potential to cause life-threatening ventricular arrhythmias, namely torsade des pointes (Bauman et al. 1984). The reason is that quinidine also blocks the major repolarizing K^+ current I_{Kr}, which explains its AP-prolonging effect and makes it the prototypical Class Ia agent. Due to its side effects quinidine is only rarely used in humans today. Flecainide, a potent Na^+ channel inhibitor, can restore sinus rhythm in AF patients by reducing conduction velocity, raising the excitation threshold and prolonging APD and RP (Andrikopoulos et al. 2015). However, by the same mechanism (particularly conduction slowing) flecainide can also provoke severe proarrhythmia in patients with structural heart disease (Echt et al. 1991). Flecainide is therefore contraindicated in patients with heart failure (HF) and other forms of structural heart disease.

Introduction

Potassium channel blockers (Class III drugs) are antiarrhythmic drugs that affect refractoriness via APD prolongation. Sotalol, dofetilide and amiodarone block potassium currents (rapid delayed rectifier potassium current (I_{Kr}), conducted via human ether a-go-go-related gene (hERG) K^+ channels) that are active during the plateau phase. Thus, they prolong atrial and ventricular effective refractory periods (ERP). However, since hERG-channel blockade is considered the major cause for drug-induced proarrhythmias, the use of class III drugs in clinical practice is very limited (Christ et al. 2015). Sotalol and amiodarone were similarly effective in cardioversion of AF, but sotalol caused a significant positive inotropy, consistent with APD prolongation and prolonged influx of Ca^{2+} (Kaumann and Olson 1999). Amiodarone also prolongs APD, but the concomitant block of Na^+ as well as Ca^{2+} channels balances this effect. The biggest advantage of amiodarone is its low incidence for ventricular proarrhythmia. Amiodarone suppresses not only ventricular arrhythmias but also prevents the recurrence of AF. However, the drug shows remarkable extracardiac toxicity such as thyreotoxicity and lung fibrosis.

Although enhancement of I_{CaL} could theoretically prolong atrial APD and RP, it would also increase the risk for ventricular EADs and for prolongation of the QT interval, thus representing a pathophysiological substrate for long-QT syndrome (Nattel and Dobrev 2012).

Atrium-selective drug targets promise to mediate suppression of AF without risk for ventricular proarrhythmia. Atrium-selective agents should selectively affect atria but not ventricles by targeting ion channels predominantly expressed in the atria. Atrial-specific ion channels include those which conduct the ultra-rapidly activating delayed rectifier K^+ current (I_{Kur}), I_{KACh} and the small conductance Ca^{2+}-activated K^+ (SK) current. However, atrial-selective approaches for the management of AF are still in an early stage of development and their actual utility remains unclear. I_{Kur} blockade showed a positive inotropic effect in atrial tissue which could revert the contractile atrial dysfunction in AF. On the other hand, since expression of Kv1.5 channel underlying I_{Kur} is downregulated in chronic AF and rapid rates of AF increase I_{Kur} inactivation, the value of a selective I_{Kur} inhibitor as a drug target to terminate AF is uncertain (Shunmugam et al. 2018). Vernakalant is an I_{Kur} blocker but it lacks selectivity as it also blocks sodium channel, hERG channel and $I_{K,ACh}$. As a result of AF electrical remodeling, an increase of inward rectifier currents (I_{k1} and $I_{K,ACh}$) was described. Atrial-selective inhibition of $I_{K,ACh}$ is particularly interesting, because $I_{K,ACh}$ is predominantly expressed in the atria and not in the ventricles and it becomes constitutively active in AF. However, expression of ion channels conducting $I_{K,ACh}$ are also expressed in the sinoatrial and AV nodes, therefore general inhibition

Introduction

of $I_{K,ACh}$ may have unwanted side effects. Moreover, first clinical trials showed disappointing results (Anfinsen et al. 2015).

Novel strategies to prevent Ca^{2+}-related focal ectopy are being explored. These approaches include to stabilize RyR2 and to prevent diastolic Ca^{2+} leak. RyR2 stabilization can be achieved by prolonging closed state or reducing open state of RyR2 channels. The local anesthetic drug tetracaine can stabilize the closed state of RyR2, while flecainide can reduce the mean-open time of RyR2, thereby suppressing spontaneous Ca^{2+} release from SR. It was demonstrated that tetracaine is effective in completely suppressing Ca^{2+} sparks in atrial myocytes from chronic AF patients (Liang et al. 2008). Alternatively, 1,4-benzothiazepine derivative JTV519 inhibits SR Ca^{2+} leak by stabilizing RyR2 channel complex. This compound reduced AF inducibility in a canine model of AF (Ebert et al. 2012). Blockade of NCX forward-mode represents another approach to reduce incidence of RyR2-mediated SR Ca^{2+} release resulting in DADs, but with a risk of Ca^{2+} overload. In addition, prevention of Ca^{2+}/calmodulin-dependent protein kinase type-II (CaMKII) phosphorylation suppresses SR Ca^{2+} leak and DADs triggering AF (Christ et al. 2015). Pharmacological inhibition of CaMKII could attenuate AF inducibility in mice with mutant RyR2 channels (Chelu et al. 2009). On the other hand, other studies showed "calcium silencing" and disappearance of arrhythmias. The latter finding was associated with a reduction of CaMKII contribution of I_{ca} regulation and CaMKII dependent phosphorylation in tissues from patients with chronic AF. These findings question the use of CaMKII inhibitors in AF (Christ et al. 2014; Greiser et al. 2014).

Finally, a challenging potential therapeutic approach is preventing atrial structural remodeling. Upstream therapy acts on the structural changes in the atria induced by AF remodeling. Atrial inflammation, apoptosis, hypertrophy, fibrosis and oxidative stress represent the key targets of upstream therapy. These agents acting on the atrial substrate could prevent recurrence of AF (Sanders et al. 2017). Potential agents for upstream therapy comprise statins, steroids, n-3 polyunsaturated fatty acids, angiotensin-converting enzyme inhibitors and angiotensin receptor blockers (Savelieva et al. 2011).

Alternatively to medications, treatment options for AF also include non-surgical and surgical approaches. Non-surgical procedures for AF include electrical cardioversion and catheter ablation. Electrical cardioversion is a procedure in which a patient receives an electrical shock to restore sinus rhythm. Patients with paroxysmal AF can undergo catheter ablation to isolate PV, which plays a key role in the pathogenesis of AF. Isolation of PV is the most effective therapy currently available for focal atrial ectopic activity. Efficacy rate of catheter ablation in

Introduction

AF patients is 61-89% (Kearney et al. 2014). The success rate decreases in patient with long-standing persistent AF. These patients often undergo multiple ablation procedures due to complications and AF recurrence (Behram et al. 2017). Surgical approaches for persistent AF include maze operation. This technique involves creating a multitude of surgical lesions throughout the left atrium to prevent fibrillatory conduction. Open chest procedures may be performed in association with planned coronary bypass or cardiac valve replacement. However, ablation of persistent AF remains less effective, mainly limited by the difficulty to identify the sources sustaining AF (Cheniti et al. 2018).

1.2 Human induced pluripotent stem cells (hiPSC)

Human atrial appendages were first used to study changes in cellular electrophysiology of dilated atria (Grand et al. 1994). Human atrial tissue could be used to investigate AF-associated remodeling, but low availability and difficult culture conditions of single CMs isolated from patients limit their use in disease modeling (Yang et al. 2015). Therefore, several animal models of rapid atrial pacing were developed to study AF (Morillo et al. 1995; Wijffels et al. 1995; Fareh et al. 1998; Yue et al. 1999; Verheule et al. 2004). However, animal models do not accurately represent the physiology of human CMs. Extrapolation of those findings to humans may be inappropriate because of species differences and undue simplifications (Denayer et al. 2014). Fundamental differences exist between CMs from animal models and adult human CMs. These differences include spontaneous beating rate, energy metabolism, calcium handling, myofilament protein isoforms, contractility, expression of ion channels and electrophysiology (Karakikes et al. 2015). Furthermore, human tissue is usually available from diseased hearts only, where age, underlying heart disease, or concomitant medication may have an additional influence so that pathophysiological mechanisms accompanying human AF may differ from corresponding animal models (Dobrev and Ravens 2003). Therefore, human induced pluripotent stem cells (hiPSCs) could represent a useful tool to model AF. The increasingly refined capacity to differentiate hiPSC into disease-relevant cell types such as CMs (hiPSC-CMs) provides an unprecedented opportunity for the generation of human patient-specific cells. The hiPSC technology has a great potential in disease modeling, personalized drug screening and regenerative approaches towards precision medicine (Karakikes et al. 2015).

In 2006, Takahashi and Yamanaka discovered that mouse embryonic and adult fibroblasts could be reprogrammed into iPSCs by retroviral transduction of four transcription factors: Oct4, Sox2, c-Myc, and Klf4 (Takahashi and Yamanaka 2006). These murine-derived iPSCs exhibited the

Introduction

same morphology and marker gene expression as embryonic stem cells (ESCs). One year later the same group established the first human induced pluripotent stem cells (hiPSC) by reprogramming human dermal fibroblasts (Takahashi et al. 2007). Methodological improvements have shown that iPSCs can be generated from other cell types, such as urine cells, keratinocytes or peripherally circulating T cells. However, the retroviral delivery of the four factors into somatic cells carries the risk of random integration of the virus into the host genome, causing unwanted genomic alterations. To avoid retrovirus-mediated changes in iPSCs, integration-free delivery methods such as Sendai viruses, episomal vectors and synthetic modified messenger ribonucleic acid (mRNA) have been established. All these methods are based on a transient expression of the reprogramming factors, which suffices to induce an endogenous pluripotency program (Schlaeger et al. 2015).

The great advantages of hiPSC can be summarized in three points. First, the procedure to generate iPSC is simple and ethically uncritical and, thanks to their infinite self-renewal and multipotency, hiPSC can theoretically provide an unlimited source of differentiated cells such as human CMs. Second, iPSC-CMs can be functionally characterized *in vitro* to model the complex cellular physiology of CMs. Third, iPSC-CMs include the genome of a subject, allowing for the evaluation of genotype–phenotype associations (Karakikes et al. 2015).

The possibility to differentiate iPSCs into disease-relevant cell types such as CMs represents an exceptional opportunity for disease modeling. Different protocols have been established to differentiate iPSCs into CMs. The aim of these protocols is to recapitulate the stepwise stages of embryological development leading to differentiation of CMs from embryonic mesoderm. It is possible to direct iPSCs into one of the three primary germ layers: ectoderm, mesoderm, and endoderm (Palpant et al. 2016; Breckwoldt et al. 2017). Once cells are differentiated into a specific germ layer, they can be programmed to become a specific cell type like a hepatocyte, a CM or a neuron (Okabe et al. 1996; Hescheler et al. 1997; Hamazaki et al. 2001). Current cardiac differentiation protocols are based on suspension culture of embryoid bodies (EBs) or monolayer (ML) culture on ECM proteins. Both approaches rely on stage-specific application of key growth factors (GFs) in defined media to induce mesodermal commitment, followed by cardiac specification (Mummery et al. 2012). In Figure 8 the cardiac differentiation process is described. Mesodermal differentiation is usually induced by activation of TGFβ nodal signaling (bone-morphogenetic protein), activin A and/or Wnt signaling activators (CHIR99021, Gsk3 inhibitor). The inhibition of Wnt signaling pathway allows cardiac lineage specification (Burridge et al. 2012; Yang et al. 2015).

Introduction
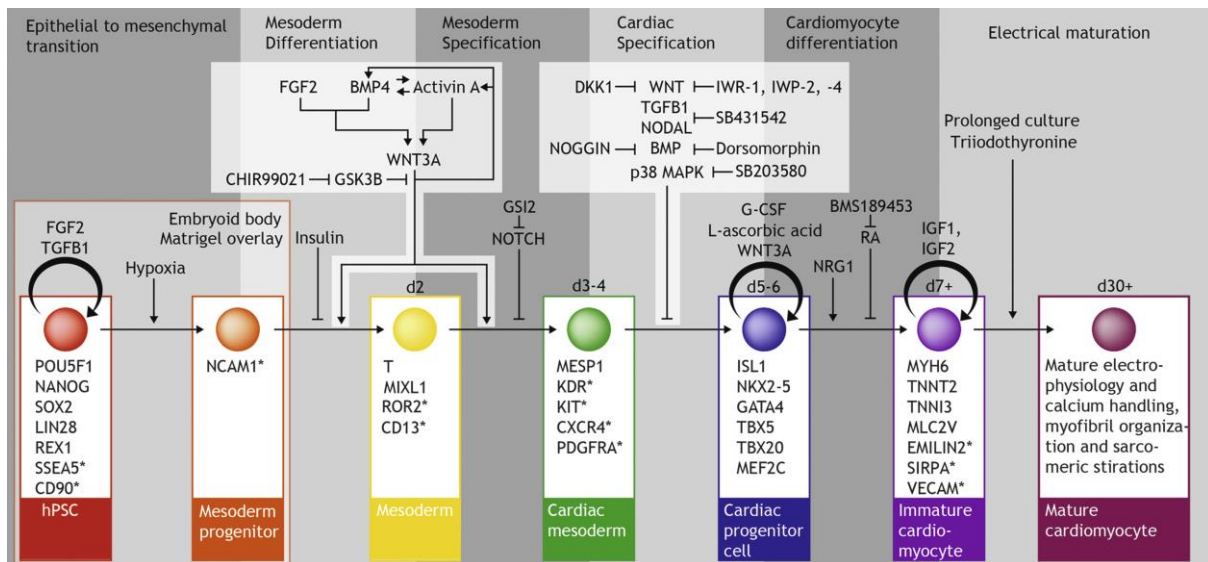
Figure 8: **Schematic overview of the differentiation process from hiPSCs to cardiomyocytes**. For each developmental stage specific cell type markers are identified (adapted from Burridge et al. 2012).

Since there are several different methods to differentiate iPSC into CMs, efforts to further enhance their stability, efficiency and reproducibility are underway (Tanaka et al. 2015).

1.2.1 Comparison between hiPSC-CMs and human adult CMs

Before considering using hiPSC-CMs to study disease mechanism and to test new potential drugs, it is necessary to question how similar they are compared to adult human CMs.

Structural level

Compared to adult CMs, hiPSC-CMs are smaller with a round or polygonal shape (Hwang Seok et al. 2015; Uzun et al. 2016) and they lack a regular ultrastructure and T-tubule network. They display ultrastructure features of early and immature phenotype comparable to fetal CMs (Kane et al. 2015). Electron microscopy studies showed lower abundance and structural maturity of mitochondria than normally observed in adult CMs (Savelieva et al. 2011).

Several methods have been implemented to promote hiPSC-CM maturation. Prolonged culture, electrical stimulation, mechanical stretch and coculture with other cell types could improve structural maturity of hiPSC-CMs, inducing sarcomere alignment (showing clear I bands, A bands, H zones and Z disks), high density of mitochondria and T-tubules formation (Tu et al. 2018). However, mature expression of some protein components of the sarcomere, such as the adult isoform of cardiac troponin I is not yet achievable with hiPSC by any current CM differentiation protocol (Yang et al. 2015; Ye et al. 2018).

Introduction

Calcium handling

HiPSC-CMs show the same Ca^{2+}-induced Ca^{2+}release mechanism underlying excitation-contraction coupling of human adult CMs (Bers 2002). Upon cell depolarization, calcium enters into the cell through L-type Ca^{2+} channel, inducing Ca^{2+} release from SR through RyR2. However, the calcium kinetics in hiPSC-CMs are slower than in human adult CMs. In fact, the calcium transients in hiPSC-CMs are characterized by a U-shape waveform across the width of the cell. The U-shape Ca^{2+} waveform, measured by transverse line-scan, demonstrates a marked Ca^{2+} delay between the periphery and the center of the cell. This delay suggests a spatial distance between L-type Ca^{2+} channel and RyR2 receptor, probably due to the lack or poor organization of T-tubules. Therefore, the U-shaped Ca^{2+} waves and a poorly developed SR suggest that hiPSC-CMs have an immature Ca^{2+}-induced Ca^{2+}-release mechanism (Tanaka et al. 2015). In fact, hiPSC-CMs respond to adrenergic/cholinergic stimulation but the response is much smaller than normal and they generally show a negative force-frequency relationship (FFR) compared to a positive relationship for adult ex vivo CMs (Karakikes et al. 2015; Yang et al. 2015). Furthermore, contractile force is an indicator of CM maturity. Contractile force depends on the developmental state of the sarcomeres and myofibrils. HiPSC-CMs cultured in 3D tissues (Mannhardt et al. 2016) develop much smaller contractile force than intact human heart muscle preparations (Hasenfuss et al. 1991).

Electrophysiology properties

A recent study demonstrated that the ion currents measured in mature human CMs are also present in hiPSC-CMs leading to characteristic cardiac APs (Zhao et al. 2018). Several ion currents have been measured in single hiPSC-CMs, including the sodium (I_{Na}), the L- and T-type calcium ($I_{Ca,L}$ and $I_{Ca,T}$), the pacemaker (I_f), the transient outward potassium (I_{to}), I_{K1}, I_{Kr} and the slow delayed rectifier potassium (I_{Ks}) currents (Zhao et al. 2018). The presence of I_f, resulting in spontaneous beating, remains a peculiarity of hiPSC-CMs since human ventricular myocytes do not exhibit spontaneous automaticity. Several groups working with hiPSC-CMs showed APs characterized by less negative RMP and lower upstroke velocity. Immaturity of I_{Na} and I_{K1} was considered to be responsible for these electrophysiological differences. However, methodological issues may be responsible for these differences, since APs in engineered heart tissue (EHT) showed RMP and upstroke velocity comparable with human cardiac tissue (Lemoine et al. 2017; Lemme et al. 2018). Moreover, it was shown recently that I_{K1} current density in hiPSC-CMs can be as high as in human adult CMs (Horváth et al. 2018).

Introduction

1.2.2 HiPSC-CMs for disease modeling and drug testing

The research field of disease modeling can benefit from hiPSCs generated from patients with genetic disorders, named patient-specific hiPSCs (PS-hiPSCs). Differentiation of PS-hiPSCs into disease-relevant cell types can generate a stable and unlimited source of target cells for disease modeling. These systems have the potential to improve our understanding of disease mechanisms, leading to new therapeutic strategies (Tanaka et al. 2015). Before choosing to model a disease with hiPSCs, some considerations regarding the type of human disease and the biological characteristics of hiPSCs should be done. For example, the time of onset and the progression through time of the disease should be taken into consideration. Since hiPSC-derived cells have immature phenotypes, they are more suitable for modeling early-age onset diseases than adult-onset diseases. PS-hiPSCs are valuable for disease modeling when a genetic mutation is a causative or contributing factor to the disease. For example, PS-hiPSCs derived CMs may reflect dysfunctional characteristics comparable to those of the CMs *in vivo*, thus allowing the correlation of the genetic mutations with the disease phenotypes.

Furthermore, diseases manifesting their phenotype only at the whole organ level and not at the cellular level may be difficult to model using PS-hiPSCs. For instance, if the dysfunction present in the diseased CMs contributes to the development of fibrotic tissue, the disease may be difficult to model using CMs alone (Tanaka et al. 2015; Yang et al. 2015). Disease modeling can be useful to uncover novel insights into disease mechanisms and to evaluate new potential drug candidate. In the clinics, it is not possible to predict the patient response to a specific drug, because its side effects and efficacy differ on an individual basis. PS-hiPSCs have the advantage to retain patients' genetic background and genetic mutations, which is crucial to develop personalized safety pharmacology (Ebert et al. 2012; Tanaka et al. 2015).

HiPSC technology can also be used for drug screening to evaluate cardiac safety of new drugs. In fact, off-target drug effects and cardiac toxicities need to be tested for all new drug entities according to guidelines from the Federal Drug Administration in the US and European Medicines Agency (Figure 9). In the process of drug discovery, drug-induced arrhythmias are one of the most common causes for early termination of drug development and post-approval pharmaceutical withdrawal. Proarrhythmic risks of drugs are often associated with inhibition of hERG channels that are mediating I_{kr} and largely responsible for AP repolarization. HERG assays are used to identify drugs able to block hERG in pharmaceutical drug development. However, the effect of I_{kr} inhibition on APD and the propensity to develop arrhythmias can be

modulated by multiple ion channels. Therefore, hERG assays cannot fully evaluate the safety of drugs. In this context, hiPSC-CMs, integrating the entirety of cardiac ion channels, represent a unique tool for drug development and arrhythmia risk assessment. Thus, hiPSC-CMs could be helpful in preclinical drug development to predict drug-induced arrhythmias and to test whether the drug has a positive or negative inotropic effect.

To conclude, hiPSC-CMs show several advantages for their application in disease modeling and drug testing. These cells overcome the interspecies differences, they do not raise ethical concerns and they reduce costs compared with animal experiments. However, experiments in cultured cells are more difficult to interpret than animal experiments, due to cellular heterogeneity, variable culture conditions, batch-to-batch variations and, particularly for hPSC, the risk of karyotype abnormalities (Weinberger et al. 2017).
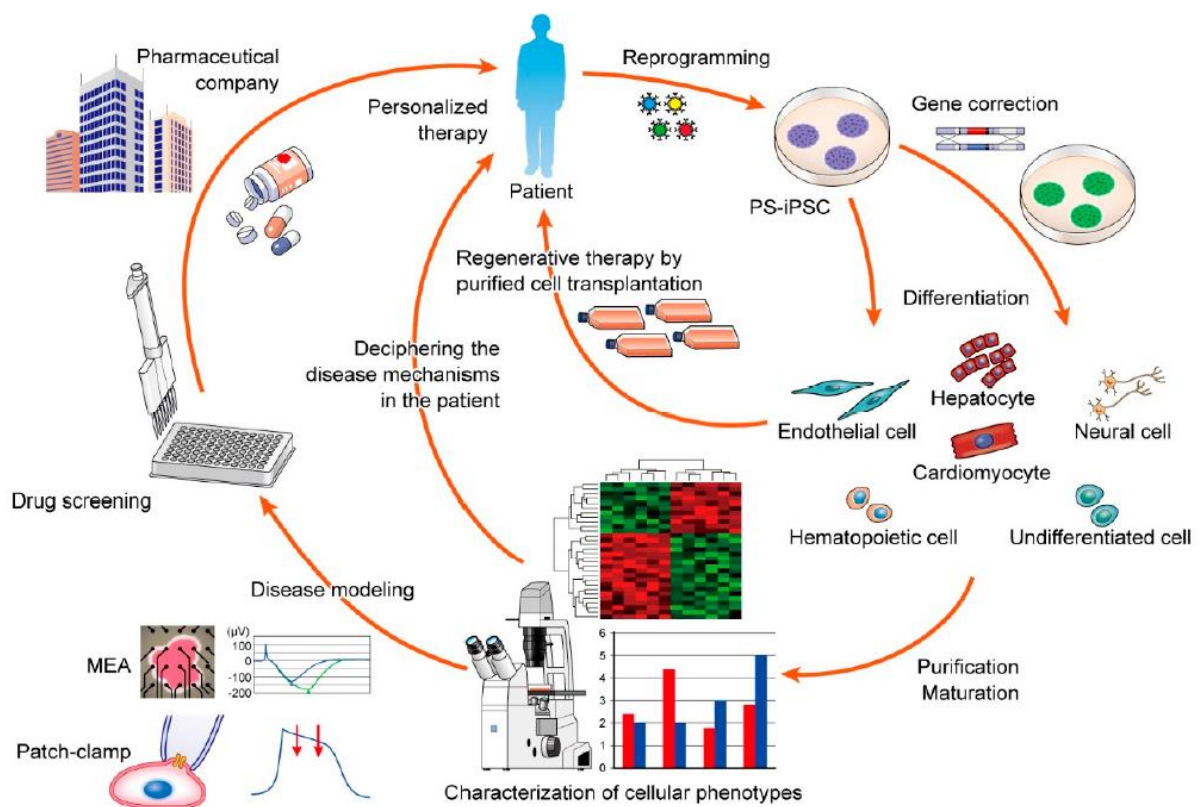
Figure 9: **Overview of potential applications of patient-specific induced pluripotent stem cell (PS-iPSC)**. Somatic cells obtained from patients are reprogrammed in iPSCs. PS-iPSCs can be differentiated in the target cell type. After differentiation these cells can be transplanted inside the patient for regenerative therapies. Alternatively, PS-iPSCs can be used in disease modeling and drug screening (adapted from Tanaka et al., 2015).

1.2.3 3D model

3D models of hiPSC-CMs are important in disease modeling and in new drug validation. The principal advantage of a 3D format lies in a more physiological cellular environment promoting

Introduction

hiPSC-CM maturation. The imposed direction of contraction and the definite afterload applied to this culture format are essential for CM alignment and sarcomere maturation.

Several cardiac tissue engineering approaches have been developed to obtain engineered heart constructs. These approaches include the use of prefabricated casting molds to generate 3D tissues using hydrogels such as collagen I, gelatin, alginate, hyaluronic acid, fibronectin, matrigel and fibrin (Hansen et al. 2010; Hirt et al. 2014b).

The higher level of cell maturation obtained in hiPSC-CM constructs cultured in 3D compared to 2D allows to generate disease models better representing the *in vivo* disease. 3D tissues proved to be particularly helpful in modeling diseases that manifest in a contractile deficit, which could not be detected in 2D models (Hinson et al. 2015). Moreover, the higher degree of cell maturation in 3D cultures offers a more reliable prediction of *in vivo* response to a potential drug. In 3D cultures the cells form tight junctions which affect the diffusion of drugs. The major advantage is that 3D tissues integrate the contractile and electrophysiological properties of thousands of cells, thus significantly reducing the variability between single cells (Weinberger et al. 2017).

1.2.4 Atrial-like myocytes

Various animal models have been used to study the pathophysiology of AF. These animal studies contributed to our understanding of molecular and electrophysiological mechanisms involved in AF initiation and maintenance. However, cardiac ion channels are highly species specific and may not precisely reproduce the human AF phenotype.

The majority of hPSC cardiac differentiation protocols produce a mixture of CM subtypes (Ma et al. 2011; Blazeski et al. 2012; Van den Berg et al. 2016; Marczenke et al. 2017). However, electrophysiological studies of these cells showed a predominance of ventricular-like myocytes (Lemoine et al. 2017; Horváth et al. 2018; Lemme et al. 2018). The different CM subtypes possess distinct molecular and functional properties. Therefore, to study a chamber-specific disease it is necessary to be able to produce a specific CM subtype. In this respect, recent studies described how to direct cardiac differentiation of hiPSCs towards an atrial-like or ventricular-like phenotype by modulating the mesodermal induction and the retinoic acid (RA). Modulation of activin A and BMP4 during mesodermal induction showed the potential to generate RA-non-responsive, ventricular-like CMs and RA-responsive, atrial-like CMs, respectively (Lee et al. 2017). Retinoids are involved in heart morphogenesis and contribute to cardiac reprograming. RA treatment can alter the specification of cardiac progenitors (Zaffran et al. 2014; Lemme et

al. 2018). Previous studies have shown that treatment of hESC and hiPSC differentiation cultures with RA is sufficient to generate cells displaying molecular and functional properties comparable to early atrial-like myocytes' characteristics (Zhang et al. 2011; Josowitz et al. 2014; Devalla et al. 2015; Chen et al. 2017; Lee et al. 2017). Additionally, enrichment of atrial- and nodal-like CMs could be achieved with timed supplementation of the chemical compound 1-ethyl-2-benzimidazolinone (Jara-Avaca et al. 2017).

Therefore, the establishment of a differentiation protocol to generate atrial-like myocytes could represent a new approach to study AF *in vitro*. In fact, the generation of a 3D model constituted of hiPSC derived atrial-like myocytes could be helpful to better understand the initiation and progression of AF and to provide a preclinical model for the validation of novel atrial-specific therapeutic targets.

1.3   Chronic rapid pacing

Chronic tachypacing is commonly used in animals to model human cardiac diseases. Ventricular tachypacing, e.g. pacing of the right ventricle with 240 beats/min for three weeks, can be used to induce HF with alterations of APD (Kääb et al. 1996; Moe and Amstrong 1999; Han et al. 2001). Atrial pacing at 400 beats per min for 6 weeks in dogs and goats induced sustained AF and atrial remodeling characterized by shortened APD, shortened ERP and reduced Ca^{2+} current density (Morillo et al. 1995; Wijffels et al. 1995; Jayachandran et al. 2000). Long-term rapid atrial pacing produces electrophysiological and structural changes similar to those caused by AF and it can induce sustained AF in animal models (Wijffels et al. 1995; Fareh et al. 1998; Yue et al. 1999).

Until now, electrical stimulation of hiPSC-CMs or hiPSC-EHTs was used as an approach to improve the maturity of hiPSC-CMs (Radisic et al. 2004; Tandon et al. 2009; Nunes et al. 2013; Hirt et al. 2014a; Ruan et al. 2016; Ronaldson-Bouchard et al. 2018). Ronaldson-Bouchard et al. showed that increasing intensity of the electrical stimulation allows hiPSC-CM maturation with a positive FFR and robust T-tubules, however FFR up to 6 Hz is unphysiological and no quantification of T-tubules formation was shown. On the contrary, chronic electrical pacing can also induce structural and electrophysiological dysfunction in hiPSC-CMs (Cui et al. 2017). Rapid electrical pacing of hiPSC-CMs disturbed Ca^{2+} homeostasis and activated the mitochondrial apoptotic pathway. The mitochondrial stress promoted CM apoptosis and induced electrophysiological remodeling (Geng et al. 2018). The mechanisms of these adverse consequences of electrical pacing are not clear and may also have technical reasons. While

electrical stimulation in intact animals can be done without temporal limitations, chronic pacing under *in vitro* conditions is complicated by irreversible Faradaic reactions. Negative effects of Faradaic reactions are the oxidation of electrodes, generation of chlorine and hydroxyl radicals and formation of hypochlorous acid and chlorate (Zhang et al. 2018). Electrode charging in culture medium also raises the probability for water hydrolysis causing pH alterations (Humayun et al.). These electrochemical reactions limit the efficacy and time span of application of electrical stimuli (Boyle et al. 2015). In this regard, light sensitive ion channels represent an alternative to overcome this constraint.

1.4 Optogenetics

Channelrhodopsin-2 (ChR2) is a genetically targeted, light-activated nonselective cation channel used in optogenetics to modulate cell excitability (Figure 10). Once activated by blue light (470 nm), ChR2 allows the influx of cationic ions, mainly Na^+, consequentially depolarizing the membrane potential and generating APs (Merrill et al. 2005; Bruegmann et al. 2010).
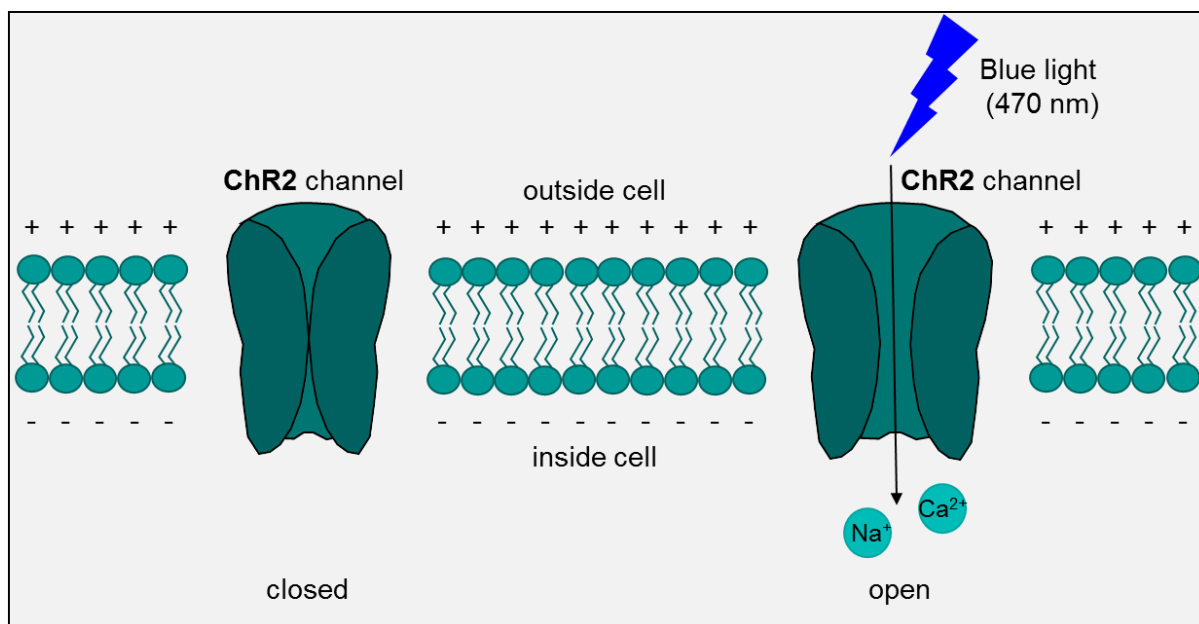
Figure 10: **Basic principle of optogenetic**. ChR2, a light sensitive membrane channel, allows the influx of cations upon blue light illumination. The cation entry depolarizes the cell and triggers an action potential.

Previous studies have demonstrated the feasibility to use ChR2 for light pacing in hearts of transgenic mice (Bruegmann et al. 2010), rats (Nussinovitch and Gepstein 2015) and zebrafish (Arrenberg et al. 2010) *in vivo*. Moreover, ChR2 can be expressed in CMs generated from hPSC by viral vectors (Abilez et al. 2011). MLs of ChR2 transduced hiPSC-CMs were successfully

used for drug screening to test drug effects on cardiac electrophysiology (Lapp et al. 2017; Rehnelt et al. 2017). Pacing via optogenetics can be used to transiently induce arrhythmias. Zaglia et al. were able to induce sustained arrhythmias in ischemic ventricles of mice through rapid optical pacing (10-20 Hz). Burton et al. induced sustained spiral waves by applying spiral wave-shaped illumination patterns in MLs of rat CMs. ChR2 can be also applied to stop arrhythmias. The works of Bruegmann et al. and Nyns et al. have demonstrated optogenetic termination of ventricular tachycardias in mice and rats, respectively (Bruegmann et al. 2016; Nyns et al. 2017). Prolonged optogenetic stimulation of spatially constrained areas can render these regions temporarily nonexcitable (Karathanos et al. 2016). Constant illumination of ChR2-expressing CMs *in vitro* electrically silences the illuminated areas by prolonging depolarization and refractoriness (Sasse 2011; Bingen et al. 2014). Illuminated regions behave as temporary "ablation lesions" since propagation of the electrical signal through these areas was impossible.

Interest in cardiac optogenetics is growing due to the simplicity of opsin expression, minimal interference with endogenous CM function, selective opsin expression in specific cell types, exceptional spatial and temporal resolution, versatility of opsin function (excitatory or inhibitory response) and low energy required for opsin activation (Boyle et al. 2018). Optogenetic technology might represent a novel alternative to the traditional electrical pacemakers and defibrillators. Although pacemakers and defibrillators are safe and reliable and represent the gold standard in the management of cardiac arrhythmias, they have limited battery life and they use painful high-energy shock to terminate tachyarrhythmias. The ability of optogenetics to target specific cell type could help to perform selective His bundle pacing that is superior to conventional right ventricular pacing (Sharma et al. 2015). An optogenetic defibrillator could achieve pain-free termination of tachyarrhythmias using significantly less energy and targeting specific cardiac cells, thus avoiding unwanted excitation of the muscles surrounding the heart. The growing field of optogenetics may provide the opportunity for restoring sinus rhythm painlessly, thus increasing the quality of patients' life.

Although remarkable advances in cardiac optogenetics have been achieved, further progress is required before optical approaches can be applied *in vivo* to the beating human heart. Since one of the possible long-term clinical application of optogenetics is the optical pacemaker, experiments to test how chronic optical pacing affects electrophysiology and function of human CMs need to be performed.

1.5 Aim of the work

AF is the most common cardiac arrhythmia, but there is still no atrial-selective drug for its treatment. This work therefore aimed at generating an *in vitro* model of AF to study the mechanism of this disease and to test new potential drugs. The first step was to establish a protocol to differentiate hiPSC into atrial-like CMs, using RA-treatment. These atrial-like myocytes were used for EHT generation. An extensive molecular and functional characterization of atrial-like EHTs was performed to investigate their similarity to the human atrial tissue. After generation of a model of human atrium, induction of AF remodeling in atrial-like EHTs was attempted. Since chronic electrical tachypacing produces changes similar to those caused by AF in the atria of animal models, chronic tachypacing was tested to induce AF in atrial-like EHTs. However, to overcome the technical limitations of chronic electrical pacing *in vitro*, tachypacing based on optogenetics was implemented. Structural and electrical remodeling was investigated after chronic optical tachypacing.

The entire project was divided into three main steps that are illustrated in Figure 11 and will be presented in the following chapters:

1. Generation and characterization of atrial-like vs. ventricular-like EHTs (RA-EHTs vs. Ctrl-EHTs)

2. Effect of chronic optical tachypacing on Ctrl-EHTs

3. Effect of chronic optical tachypacing on RA-EHTs

Introduction
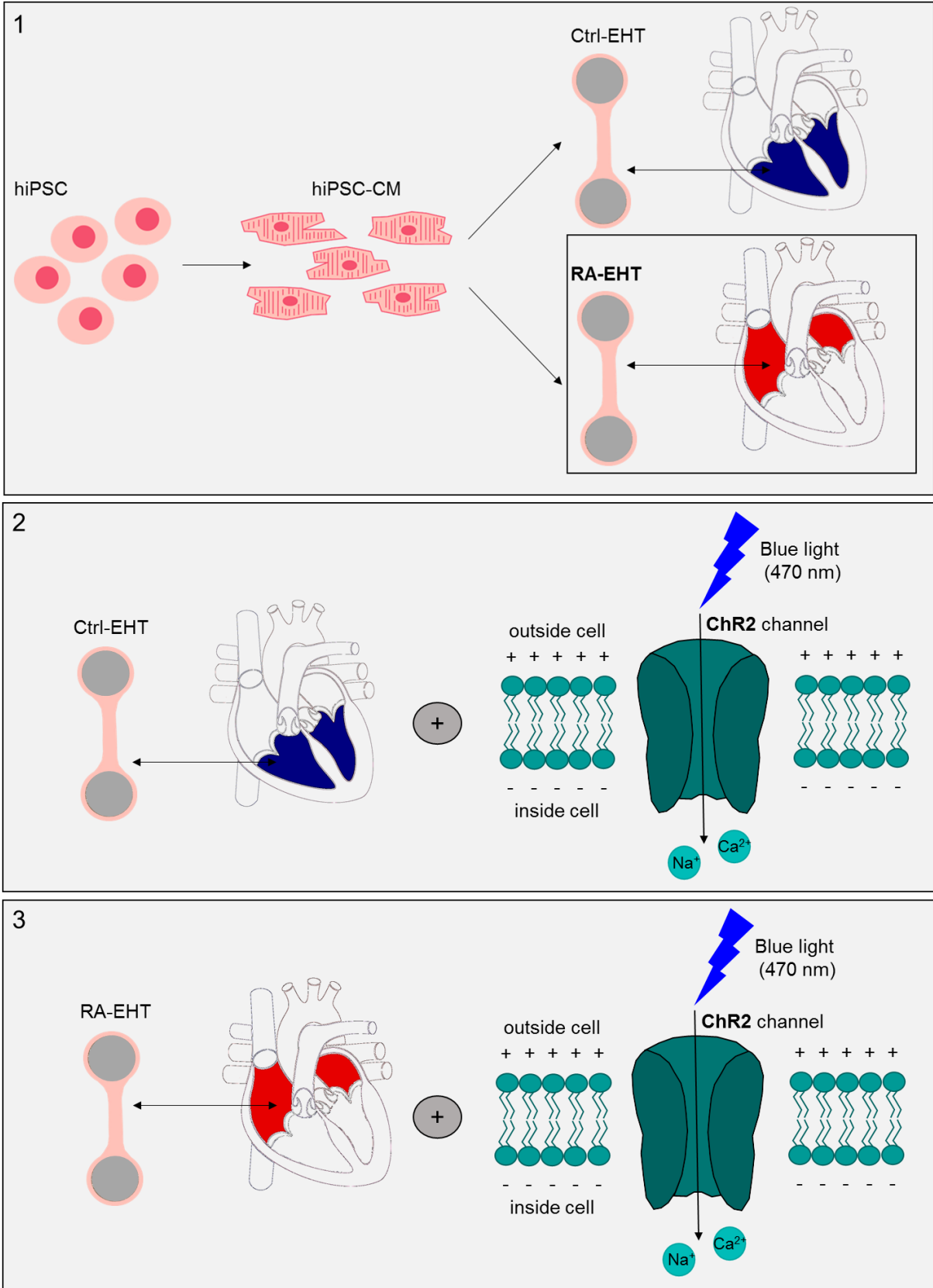
Figure 11: **Schematic view illustrating the aim of the project**. Illustration of the three main steps of the project: 1) generation and characterization of ventricular-like and atrial-like EHTs, 2) analysis of electrical and structural remodeling in ventricular-like EHTs (Ctrl-EHTs) upon chronic optical tachypacing and 3) analysis of electrical and structural remodeling in atrial-like EHTs (RA-EHTs) after chronic optical tachypacing.

2. Material and methods

A detailed overview of media, materials, chemicals, reagents and devices used in this project can be found in the supplement (chapter 7.2).

2.1 HiPSC culture

Expansion of hiPSC was performed as previously described (Breckwoldt et al. 2017) by Thomas Schulze and Birgit Klampe (Institute of Experimental Pharmacology and Toxicology, UKE, Hamburg). Undifferentiated in-house control hiPSC lines (C25, ERC1 and ERC18) were obtained from skin biopsies of healthy donors by reprograming the fibroblasts using the Sendai virus-based CytoTune kit (Life Technologies). HiPSCs were expanded in FTDA under hypoxic conditions on Geltrex (1:200 in DMEM, 1 ml/10 cm^2) coated 6-well-dishes and T80-flasks. Standard hiPSC passaging was performed with Accutase (Sigma-Aldrich). This research conforms to the ethical guidelines outlined by the Declaration of Helsinki and the Medical Association of Hamburg. All the donors gave informed consent. All methodologies used to generate and analyze in-house control hiPSC lines were approved by the local ethics committee of Hamburg (Az PV4798, 28.10.2014).

2.2 Differentiation of hiPSC-CMs

Cardiac differentiation of three undifferentiated hiPSC control cell lines (C25, ERC18 and ERC1) was performed with the EB-based differentiation protocol previously established by our research group (Breckwoldt et al. 2017). A schematic overview of the three-stage protocol is illustrated in Figure 12.

Material and methods
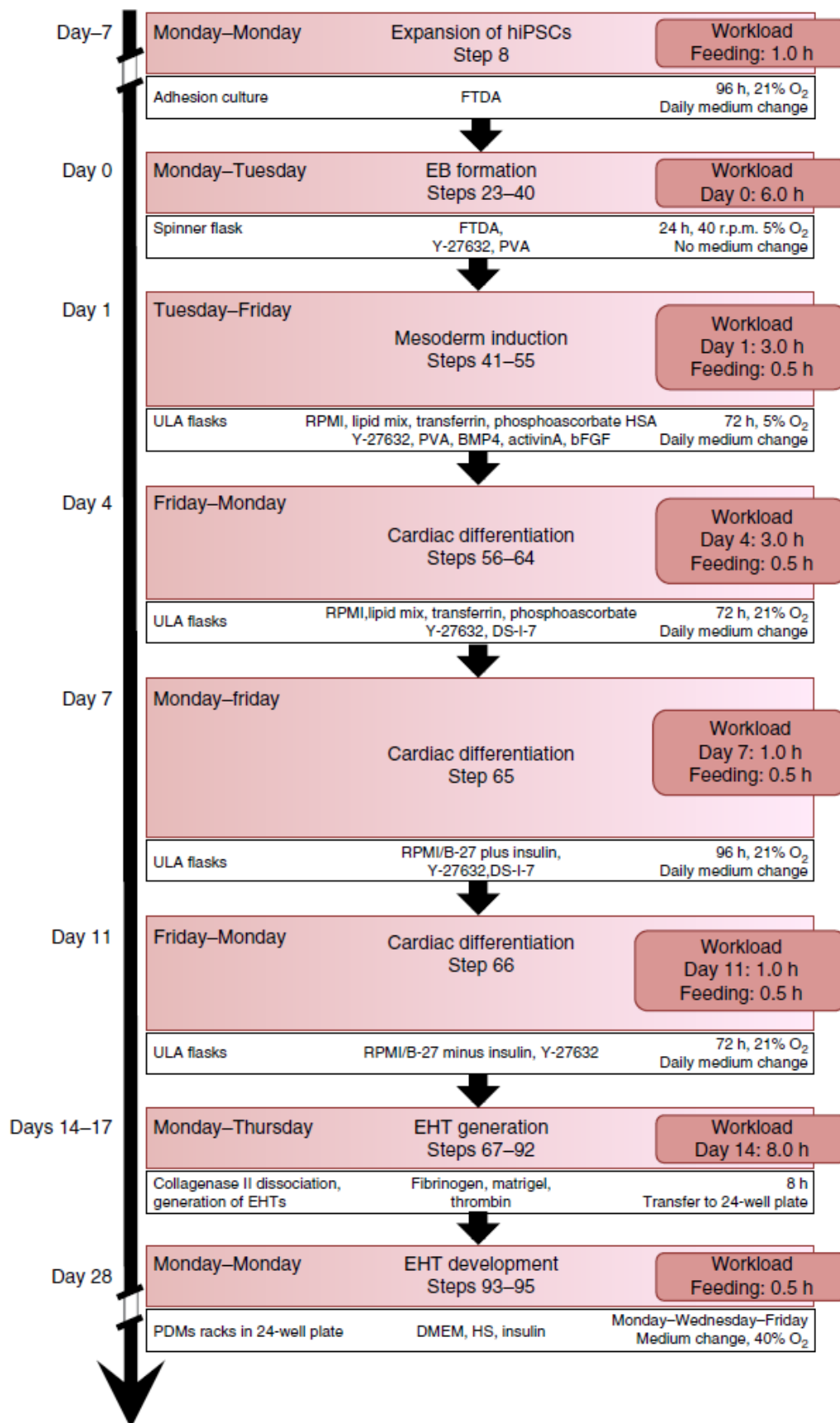
Figure 12: **Schematic overview of the cardiac differentiation protocol**. For each stage time points, culture conditions and medium composition are described (adapted from Breckwoldt et al., 2017).

Material and methods

Undifferentiated hiPSC cultured in a ML in Geltrex-coated T80 cell culture flasks were incubated with Rho kinase inhibitor Y-27632 for one hour (h). Afterwards, they were detached with EDTA and incubated into 500 mL spinner flasks (30 Mio cells per 100 mL) in EB formation medium. To allow EB formation, single cells underwent a constant stirring on a magnetic plate overnight. On the next day, the EBs were washed and total EB volume was estimated. Mesodermal differentiation was induced in suspension culture using T175 Pluronic F-127-coated suspension flasks. 200-250 µL EBs were cultured in mesoderm induction medium under hypoxic conditions (5% O_2) for three days with daily medium change of 50% of the volume. Mesodermal induction could be achieved using BMP-4 (10 ng/ml), activin A (3 ng/ml) and bFGF (5 ng/ml) in the absence of insulin in RPMI medium (Breckwoldt et al. 2017). For cardiac differentiation EBs were harvested, washed and their volume was estimated. 200-250 µL of EBs were transferred to cardiac induction medium I for three days with daily medium change of 50% of the volume.

After the first three days of cardiac differentiation, the medium was exchanged completely for cardiac induction medium II containing insulin and the WNT-signaling inhibitor XAV-939. After 4 days of culture in this medium with daily medium change of 50% of the volume, the WNT-inhibitor was no longer added to the medium and the cells were cultured in cardiac induction medium III for 5 more days. Spontaneous beating of EBs usually occurred around day 9-11 of cardiac differentiation.

At day 17, differentiated EBs were enzymatically dissociated into single cell suspension with collagenase II (200 U/ml, Worthington, LS004176 in HBSS minus Ca^{2+}/Mg^{2+}, Gibco, 14175-053) for 3.5 h at 37 °C and then transferred into cryovials in freezing solution (fetal calf serum [FCS] containing 10% DMSO, Breckwoldt et al. 2017). The cryopreservation equipment Asymptote EF600M (Grant Instruments) was used to precisely control the cooling down to -80 °C of the cells in 60 min, before the differentiated cells could be transferred to -150 °C for long-term storage. The cardiac differentiation efficiency was determined by flow cytometry after hiPSC-CMs were fluorescently labeled by anti-cardiac troponin T (cTnT) antibody. This differentiation protocol resulted in a population of primarily ventricular CMs.

According to previous reports (Zhang et al. 2011; Devalla et al. 2015; Jee Hoon Lee et al. 2017; Cyganek et al. 2018) RA-treatment during the first three days of Wnt signaling inhibition was sufficient to generate atrial-like CMs from hPSC. Therefore, cardiac induction medium I was supplemented with RA (1 µmol/L) to generate primarily atrial CMs. RA (Sigma Aldrich) was

diluted in DMSO to prepare a solution of 50 mmol/L and further diluted in distilled water to have a stock solution of 0.1 mmol/L (Devalla et al. 2015).

2.3 ML and EHT generation

CMs were thawed in a water bath and transferred into a centrifuge tube where RPMI 1640 medium supplemented with 1% penicillin/streptomycin was added dropwise to avoid the osmotic stress on the hiPSC-CMs.

These cells were then cultured in 2D MLs or in 3D EHTs. With regard to the 2D culture, hiPSC-CMs were plated onto black-sided 96-well plates (NUNC; 10,000 cells per well) pre-coated with Geltrex (Gibco, A1413302; 1:100 in DMEM, 37 °C, 1 h) to form a uniform cell ML. For the 3D culture, hiPSC-CMs were used to generate fibrin-based human EHTs according to the procedure previously described (Hansen et al. 2010; Schaaf et al. 2011). HiPSC-CMs cultured in EHT form a synchronously beating syncytium, which generates auxotonic contractile force by deflecting two elastic silicone posts (Hansen et al. 2010; Mannhardt et al. 2016; Breckwoldt et al. 2017).

Molds for EHT casting were generated by placing polyetrafluorethylene (PTFE) spacers into a 24-well plate previously filled with 2% agarose/PBS solution. After solidification of the agarose solution at room temperature (RT), the spacers were gently removed from the 24-well plate and the silicone EHT racks were placed inside the molds. Afterwards, the EHT master mix containing the hiPSC-CMs suspended in EHT casting medium, 2x DMEM, Matrigel, Y-27632, and fibrinogen (Table 2) was prepared. 100 µL of the master mix were mixed wth 3 µL of thrombin (100 U/mL, Sigma Aldrich T7513) and then rapidly pipetted into the molds between the silicon posts of the EHT racks.

To generate EHT suitable for the optogenetic technology, ChR2 lentivirus was added to the master mix for EHT casting. The exact lentivirus volume to add to the master mix was calculated from the transducing units per ml of the specific lentivirus preparation in order to have a multiplicity of infection (MOI) equal to 0.2. The calculated lentivirus volume was subtracted from the volume of the EHT casting medium in the master mix (Table 2).

Material and methods

Component	Volume
hiPSC-derived cardiomyocytes	1.1×10^6
EHT casting medium	86.9 μL – V
2x DMEM	6.2 μL
10% Matrigel	11 μL
0.1% Y-27632	0.11 μL
Fibrinogen	2.8 μL
ChR2-lentivus	$V = \left(\dfrac{\text{MOI} * \text{cell number}}{\frac{\text{TU}}{\text{ml}}} \right) * 1000$

Table 2: **Master mix composition per single engineered heart tissue**. Master mix components and their respective volumes are summarized in the table. The ChR2 lentivirus is included in the master mix only for experiments based on the optogenetic technology. The volume of ChR2 lentivirus in the master mix is subtracted from the EHT casting medium. The volumes include 10% excess for pipetting errors. MOI=multiplicity of infection, TU=transducing units.

After EHT polymerization at 37 °C for 1.5 h, EHTs were moistened with 200 μL of pre-warmed medium for 30 min to help their detachment from the molds. After complete fibrin polymerization, the silicone racks with attached the fibrin gels were transferred to a new 24-well plate and cultured with EHT culture medium. EHTs were cultured at 37 °C, 7% CO_2, 40% O_2 and 98% humidity with medium changes three times per week until EHT analysis were performed (Breckwoldt et al. 2017). After 7-8 days of culture, human EHTs exhibited spontaneous regular beating by deflection of the silicone posts, allowing video-optical contraction analysis.

2.4 Molecular analyses

2.4.1 ChR2 lentivirus

Lentivirus was prepared to transduce hiPSC-CM with the gene encoding ChR2. To express ChR2 under control of the EF-1α promoter together with a puromycin resistance under control of the SV40 promoter, a polymerase chain reaction (PCR) was performed using Phusion polymerase and the Addgene plasmid pcDNA3.1/hChR2(H134R)-EYFP #20940 as a template (Figure 13). The following primer pair was employed (5´-gggggacaagtttgtacaaaaaagcaggcttaaccatggactatggcggc and 5´-gggggaccactttgtacaagaaagctgggtttttacttgtacagctcgtccatgcc) to amplify hChR2(H134R)-EYFP and to introduce an attB1 and an attB2 site, respectively. The resulting PCR product was then

Material and methods

inserted into a donor vector pDONR/Zeo (Life Technologies) by Gateway recombination using BP Clonase II (Life Technologies) according to the recommendations of the manufacturer. Resulting Entry clones were evaluated by restriction digest and PCR and finally verified by sequencing. Subsequently, a selected Entry clone was incubated with the destination vector pLEX_307 (Addgene plasmid #41392) in the presence of LR Clonase II (Life Technologies) according to the recommendations of the manufacturer. Resulting expression clones were assessed by restriction digest and PCR and finally verified by sequencing.

A stock of VSV-G pseudotyped viral particles was produced at the Vector Facility of the University Medical Center Eppendorf using lentiviral packaging plasmids psPAX2 (Addgene plasmid #12260) and pMD2.G (Addgene plasmid #12259). After concentration by ultracentrifugation for 2 h at 4°C (25,000 rpm, SW32Ti rotor) on a 20% sucrose cushion, the pellet was resuspended in EHT casting medium. The functional titer was determined by transduction of HEK293T and quantification by flow cytometry (FACS CantoII, BD Biosciences; FITC Channel) and further used for transduction of CMs. The efficiency of transduction was evaluated by live cell fluorescence microscopy. ChR2 lentivirus was produced by Ingke Braren (Institute of Experimental Pharmacology and Toxicology, UKE, Hamburg).

Figure 13: **Channelrhodopsin 2 lentivirus**. Mammalian expression vector of humanized ChR2 with H134R mutation fused to EYFP.

Material and methods

2.4.2 Gene expression analysis

Gene expression analysis was performed by quantitative real-time PCR (RT-qPCR) and the nCounter SPRINT Profiler (NanoString). Total RNA was extracted from hiPSC-CMs cultured in ML/EHT format and from human atrial and ventricular muscle preparations. Total RNA was extracted with RNeasy Mini Kit (Qiagen) according to manufacturer's instructions. For EHTs, proteinase K (Thermo Scientific) digestion was performed before RNA extraction. For RNA isolation, 350 μL of RLT Plus buffer with β-mercaptoethanol were added to the snap frozen tissues and cultured cells in a 2 mL Eppendorf tube. In case of tissue samples, a stainless steel bead was added into the Eppendorf tube and the tissue was homogenized using a TissueLyser system (QIAGEN) for 2 min at 30 Hz.

For assessing gene expression by real-time qPCR, isolated RNA (200 ng) was reverse transcribed into complementary DNA (cDNA) using high capacity cDNA reverse transcription kit (Applied Biosystems, Table 3 and Table 4). QPCR was performed with Maxima SYBR Green/ROX (Thermo Scientific) on an ABI PRISM 7900HT Sequence Detection System (Applied Biosystems). Each reaction was performed in triplicates and a minus-RT and no-template control reactions were used as negative controls. PCR cycling parameters were 50 °C for two min followed by 95 °C for 10 min, 15 seconds at 95 °C and one min at 60 °C for 40 cycles. Cycle threshold (Ct) values of each gene were normalized with Ct values of human GUSB (β-glucuronidase, housekeeping gene) and with their respective controls. Relative gene expression was calculated with ΔΔCt method for relative quantification. Primer sequences are enclosed in the Table S4. These primers were selected for their ability to distinguish between atrial and ventricular phenotype (Wobus et al. 1995; Ellinghaus et al. 2005; Gaborit et al. 2007).

Component	Per reaction
10x RT buffer	2.5 μL
10x RT random primer	2.5 μL
25x dNTPs [100 mmol/L]	1 μL
MultiScribe RT [50 U/μL]	1 μL
RNA	Up to 2000 ng
Aqua dest.	Ad 25 μL

Table 3: **Reaction mix High-Capacity cDNA Reverse Transcription Kit**. All the components and their respective volumes are listed above.

Material and methods

Temperature	Time
25 °C	10 minutes
37 °C	120 minutes
85 °C	5 minutes
4 °C	hold

Table 4: **Reverse transcription cycler program**. Temperature and time of each step involved in the reverse transcription of RNA into cDNA.

For expression analysis with the nanoString nCounter Elements technology, a total amount of 50 ng RNA was hybridized with a customized nanoString Gene Expression CodeSet and analyzed using the nCounter Sprint Profiler (Prondzynski et al. 2017). Transcript levels were normalized to a set of 6 housekeeping genes and expressed as fold change compared to their respective controls. The CodeSets used are shown in Table S5. Expression analysis with nanoString nCounter were performed by Lisa Krämer and Dr. Maks Prondzynski (Institute of Experimental Pharmacology and Toxicology, UKE, Hamburg).

2.4.3 Protein analysis by Western Blot

For analysis of protein levels, cell pellets or homogenized tissues were dissolved in 100 µL T-PER Tissue Protein Extraction Reagent (ThermoScientific, 78510) with cOmplete Mini EDTA-free protease inhibitor cocktail (Roche Diagnostics, 04693159001). 1xlaemmli buffer was added to the sample lysate. Subsequently, the samples were heated for 5 min at 95 °C and then loaded on a SDS-PAGE gel. Proteins were separated by 12% acrylamide/bisacrylamide (29:1, BioRad, 1610156) electrophoresis gels and thereafter transferred onto nitrocellulose (NC) or polyvinylidene fluoride (PVDF) membranes (0.45 µm). Membranes were washed with TBS-Tween 0.1% and blocked in 5% skim milk powder. Primary antibodies (Table S2) were incubated overnight at 4°C in TBS-Tween 0.1%, secondary antibodies (Table S3) for 1 h at RT in 5% skim milk powder/TBS-Tween 0.1% with gentle shaking. Visualization was performed with the Clarity Western ECL Substrate (BioRad) on the ChemiDoc imaging system (BioRad). Finally, the band analysis tool of ImageLab (Bio-Rad Laboratories) was used to quantify protein bands of the blots. Each protein band was normalized to the housekeeping protein α-actinin 2. Protein analysis was performed with the help of Antonia Zech and Anna Steenpass (Institute of Experimental Pharmacology and Toxicology, UKE, Hamburg).

Material and methods

2.4.4 Flow cytometry

To determine cardiac differentiation efficiency, 2×10^5 cells were subjected to flow cytometry analysis. Cells were fixed with ice-cold methanol (-20 °C) for 20 min at 4 °C (Breckwoldt et al. 2017) and the cell membrane permeabilized in FACS buffer containing 5% fetal bovine serum, 0.5% saponin (Sigma) and 0.05% sodium azide. For intracellular protein staining, cells were stained with directly labeled antibody anti-cTnT-FITC, 1:10 dilution (Miltenyi Biotec) in FACS buffer for 30 min at 4 °C. As negative control appropriate isotype antibody was used. For determination of ChR2 transduction efficiency, one week after EHT casting, ChR2 transduced EHTs and non-transduced EHTs were dissociated using collagenase II (200 U/ml, Worthington, LS004176 in HBSS minus Ca^{2+}/Mg^{2+}, Gibco, 14175-053) for 4 h at 37 °C. Freshly dissociated live cells were subjected to flow cytometry analysis to determine the percentage of YFP positive cells in the ChR2 transduced EHTs compared to non-transduced EHTs. For flow cytometry analysis the cells were re-suspended in 200 μL 1x PBS and analyzed with the Flow Cytometer FACSCanto II (BD) and the FACSDiva software 6.0 (BD). Gating strategy was adjusted according to the isotype control to distinguish between negative and positive cells.

2.4.5 Cell size measurement

Cell area

Cell area was measured by confocal microscopy Zeiss LSM 800 with Airyscan technology (Prondzynski et al. 2017). HiPSC-CMs were fixed with Histofix for 20 min at 4 °C and stained for α-actinin 2 (1:800, Sigma) in 96-well plates (μClear/Greiner). More than >100 images of single cells were acquired with the confocal microscope (40x oil objective). Cell area from confocal images was measured with Fiji software (ImageJ). Only areas of hiPSC-CMs showing well-formed sarcomeres were measured.

Cell volume

Volumetric flow cytometry was performed to estimate the cell volume (Mosqueira et al. 2018). Beads of known dimensions (2-14.3μm diameter, Spherotech #PPS-6K) were analyzed with BD FACSCanto II Flow Cytometer in order to draw a calibration curve relating forward light scattered and cell size. Only cTnT positive hiPSC-CMs were considered for cell volume measurement. Therefore, the size of hiPSC-CMs was estimated as the volume of a perfect sphere ($V= (\pi/6)*d^3$) using the calibration curve. Volumetric flow cytometry analysis was

Material and methods

performed with the help of Dr. Bärbel Ulmer (Institute of Experimental Pharmacology and Toxicology, UKE, Hamburg).

2.4.6 Immunohistochemistry and immunofluorescence

EHTs were fixed in formaldehyde (Roti-Histofix 4%, Carl Roth, P087.3) overnight at 4 °C. For cross-sections the EHT was gently removed from the silicon posts and embedded in 2% (w/v) agarose in a 24-well plate. The block of solidified agarose containing the EHT was cut out and transferred into a 2 mL Eppendorf tube filled with TBS azide. For longitudinal sections the EHTs were carefully removed from the silicon posts and directly transferred to an Eppendorf tube containing TBS azide. After embedding the EHTs in paraffin, 4 μm thick histological sections were processed for immunohistochemical staining (Table S2, Table S3). All microscopic images were acquired with Axioskop 2 microscope (Zeiss). Histological sections were prepared by Kristin Hartmann and Susanne Krasemann (Institute of Neuropathology, UKE, Hamburg).

For whole mount immunofluorescence staining, EHTs were fixed in formaldehyde followed by permeabilization in blocking solution (6 h in TBS 0.05 mol/L pH 7.4, 10% FCS, 1% BSA, 0.5% Triton X-100). Subsequently EHTs were incubated in antibody solution (TBS 0.05 mol/L pH 7.4, 1% BSA, 0.5% Triton X-100) with primary antibodies overnight (Table S2). After three wash steps in PBS, primary antibodies were detected with secondary antibodies conjugated to fluorophores (Table S3) and nuclei were stained with DAPI (Sigma Aldrich D9564 1:1000) for two h at RT. Finally, stained EHTs were rinsed 2-3 times in PBS and embedded in Fluoromount-G (SouthernBiotech, 0100-01) in concave microscope slides (Carl Roth, H884.1). The same staining procedure was used for cell MLs with the exception of a shorter fixation period of 20 min and a different permeabilization buffer (1x PBS, milk powder 3% (w/v), Triton X-100). All immunofluorescence images were captured using the laser scanning microscope Zeiss LSM 800.

2.4.7 Periodic Acid-Schiff (PSA) staining

Glycogen storage was evaluated using the Periodic Acid (Carl Roth, 3257.1) and the Schiff's reagent (Carl Roth X900.2), according to manufacturer's instructions. Briefly, EHTs were fixed in 4 % formaldehyde for 10 min, washed with PBS, stained for 5 min with 1 % periodic acid, and washed with distilled water prior to incubation with Schiff's reagent for 15 min. After washing three times with water, EHTs were counterstained for 2 min with hematoxylin solution

and washed again three times with water prior to microscopic examination and imaging. All these steps were performed at RT. PAS staining was performed by Kristin Hartmann (Institute of Neuropathology, UKE, Hamburg).

2.4.8 Transmission electron microscopy

For transmission electron microscopy, EHTs were washed twice in PBS, incubated in 2-butandionemonoxime (Sigma, B0753; 30 mmol/L in PBS, 10 min, 37 °C) to relax sarcomeres and fixed for 1 h in 4% glutaraldehyde (0.36%, pH 7.5, 4 °C). Fixed EHTs were removed from silicone racks and osmicated in osmium tetroxide solution (1%, 2 h; Science Services, 19110), dehydrated and embedded in epoxy resin. Ultra-thin sections (60 nm) were cut using UltraCut-E microtome (Leica Reichert Jung), stained with 0.5% uranyl acetate and analyzed on a transmission electron microscope Zeiss LEO 912AB. Transmission electron microscopy was performed by Kristin Hartmann (Institute of Neuropathology, UKE, Hamburg).

2.5 Functional analysis

2.5.1 Contractility measurements

ML

ML contractility was measured using an established technology (CellOPTIQ, Clyde Biosciences, UK). HiPSC-CMs were plated on 96-well glass bottom plates (MatTek, p96G-1.5-5-F) pre-coated with fibronectin (1:100 in DPBS, Sigma, F1141) at 37°C for three h. HiPSC-CMs were seeded at a final density of 65,000 cells/cm^2 in 200 µL. At day 14 videos of spontaneous beating MLs were acquired at a sampling rate of 100 frames/second for 10 s with Hamamatsu camera (ORCA-flash4.0 V2 digital CMOS camera C13440–20CU). The 96 well plate was placed in an on-stage incubator (O_2-CO_2 [95:5], 37 °C) during video recording. The incubator was located on an inverted microscope: Olympus IX73; Objective: Olympus, 40x air, NA 0.60. Contraction peaks of spontaneous beating MLs were calculated with the algorithm of MUSCLEMOTION software (Sala et al. 2018). For every hiPSC-CM preparation, average contraction peaks were calculated from 6 distinct MLs. Finally, these average peaks were normalized to the smallest and largest value in the data set and described as mean±SEM. Contractility measurements with CellOPTIQ were performed with the help of Miriam Rol García (Clyde Bioscience, Glasgow).

Material and methods

EHT

Contractions of EHTs were measured with a video-optical analysis set-up (Hansen et al. 2010; Schaaf et al. 2011) commercially available from EHT Technologies GmbH, Hamburg. EHT contractility measurements were performed in modified Tyrode's solution (in mmol/L: NaCl 120, KCl 5.4, $MgCl_2$ 1, $CaCl_2$ 1.8, NaH_2PO_4 0.4, $NaHCO_3$ 22.6, glucose 5, Na2EDTA 0.05, and HEPES 25) pre-equilibrated overnight (37 °C, 7% CO_2, 40% O_2). The EHTs were placed into a glass-roof incubator (37 °C, 7% CO_2, 72% N_2 and 21% O_2). A video camera mounted onto a motorized xyz-axis can be moved above the glass roof in order to record a video of each EHT contractions (Figure 14). These videos are analyzed with a custom-designed software (Consulting Team Machine Vision; CTMV) based on an automated figure-recognition. This software is able to track the deflection of the silicon posts caused by the EHT contractions. Contraction analysis calculates the beating rate, force, kinetics and beating regularity (interdecile range of beat-to-beat interval length; RR scatter). More in details, contraction kinetics are described with time to peak (TTP) and relaxation time (RT). TTP$_{-80\%}$ and TTP$_{-50\%}$ refer to the 20% and 50% of contraction time to the peak, respectively. While RT$_{50\%}$ and RT$_{80\%}$ are equivalent to the time from the peak to 50% and 80% relaxation, respectively. Average contraction peaks were obtained from 6 contraction peaks of distinct EHTs, subsequently normalized to the smallest and largest value in the data set and displayed as mean±SEM.
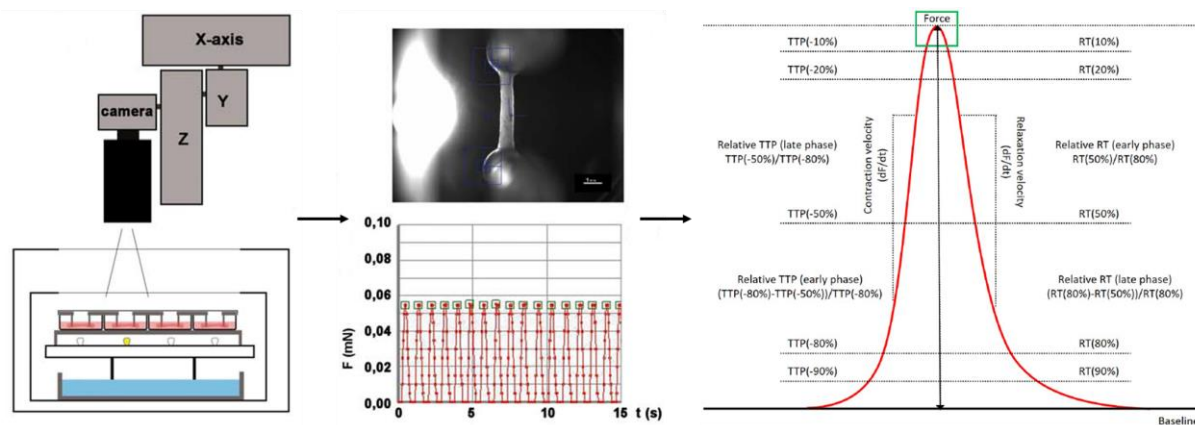
Figure 14: **Video-optical analysis of EHTcontractility** (adapted from Schaaf et al. 2011). (Left) Schematic view of the video-optical system to record EHT contractility. The 24-well plate is placed in the glass-roof incubator and the video camera moves above the glass roof along X, Y, and Z-axis to record EHT contractions. (Middle) Force over time calculated by CTMV software by tracking the deflection of the silicon posts caused by EHT contraction. (C) EHT contraction peak and all contractility parameters calculated by CTMV software.

Material and methods

2.5.2 Force-frequency relationship

FFR of EHTs was assessed in Gibco DMEM, High Glucose (LS11965092) supplemented with 25 mmol/L HEPES, 1.8 mmol/L $CaCl_2$ pre-equilibrated overnight (37 °C, 7% CO_2, 40% O_2). Ivabradine (300 nmol/L) was used to reduce the spontaneous beating rate of EHTs. After the equilibration period of 30 min in the new medium, FFR was measured. To measure FFR, EHTs were electrically stimulated stepwise from 0.5 to 5.7 Hz with 0.2 Hz increments after each measurement. EHT contractions were recorded for 15 sec at each stimulation frequency.

2.5.3 Calcium transients

EHTs were first washed in 1.8 mM calcium Tyrode's solution for 15 min and then transferred to 1.8 mM calcium Tyrode's solution containing Fluo-4 (30 µmol/L, Sigma-Aldrich F14201) and 0.02% Pluronic (Sigma-Aldrich P2443). After 30 min incubation fluorescence signals of spontaneous beating EHTs were recorded with a Nikon A1 confocal microscope equipped with a 10x air objective and resonant scanner (256×512 pixel frame). Excitation of Fluo-4 was maximal at 488 nm and emission occurred at 500-550 nm. The experiment was carried out at ~34 °C. Image analysis was performed using NIS Elements Advanced Research software (Nikon). The recorded fluorescence signal was analyzed with ImageJ. Pixel intensity variation of selected areas of the EHT was calculated and then normalized to the smallest and highest value of the dataset.

2.5.4 AP recordings

ML

APs in ML were measured using CellOPTIQ technology previously described for ML contractility measurements (section 2.5.1). After 14 days of culture hiPSC-CMs were loaded with Di-4-ANEPPS (6 µmol/L, Biotium, Hayward California) in serum-free medium (DMEM, Gibco 11 966, supplemented with galactose 10 mmol/L and sodium pyruvate 1 mmol/L) for one min at RT. Subsequently, hiPSC-CMs were washed in serum- and indicator-free medium and placed in an incubator (O_2-CO_2 [95:5], 37 °C) mounted on an inverted microscope. The emitted light was collected by two photomultipliers (Cairn Research Ltd, Kent UK) at 510–560 nm and 590–650 nm (Hortigon-Vinagre et al. 2016; Figure 15). The ratio of fluorescence (short WL/long WL) allowed to obtain ratiometric measurements of membrane voltage of hiPSC-CMs. Di-4-ANEPPS signals were recorded at 10 KHz for 15 s in each well and analyzed off-

line using proprietary software (Clyde Biosciences). AP recordings with CellOPTIQ were performed with the help of Miriam Rol García (Clyde Bioscience, Glasgow).
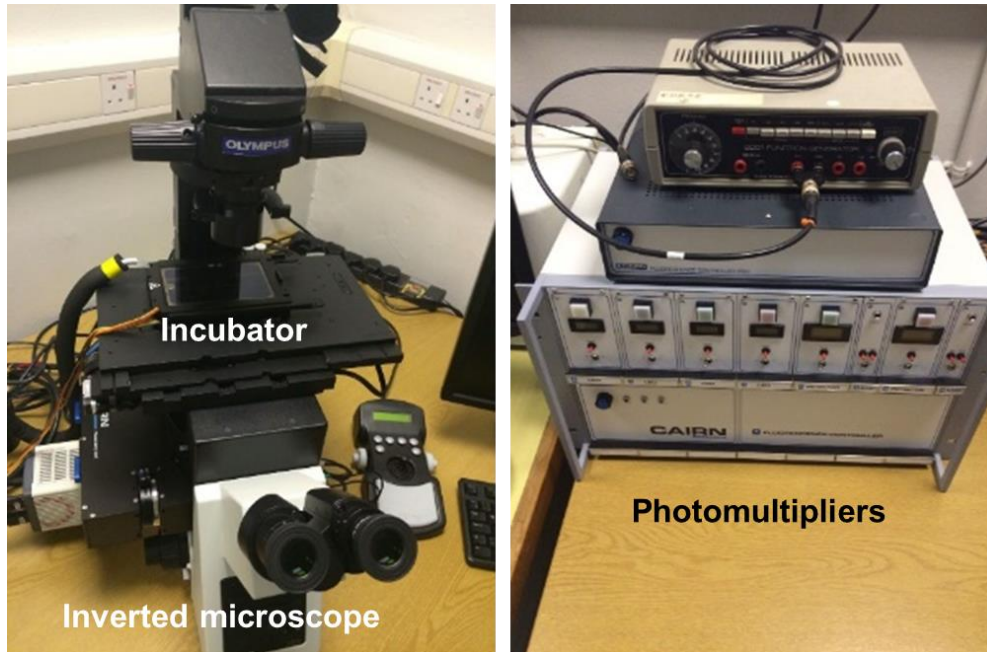
Figure 15: **CellOPTIQ system for contractility and action potential measurements in cell monolayers**. The incubator (fitted for 96-well plates) is mounted on an inverted microscope. The photomultipliers collect the fluorescence signal emitted by the cells upon 470 nm wavelength excitation and a proprietary software allows ratiometric measurements of the membrane voltage.

EHTs and human atrial/ventricular tissues

APs were recorded in intact EHTs and adult human cardiac tissues using standard sharp microelectrodes (Lemoine et al. 2017, 2018). Tissues were placed in a small recording chamber and hold in place with two needles (Figure 16). Tissues were continuously superfused with Tyrode's solution (in mmol/L: NaCl 127, KCl 5.4, $MgCl_2$ 1.05, $CaCl_2$ 1.8, Glucose 10, $NaHCO_3$ 22, $NaHPO_4$ 0.42, equilibrated with O_2-CO_2 [95:5] at 36.5±0.5 °C, pH 7.4). APs were recorded by sharp microelectrodes pulled from filamented glass (Hilgenberg, DMZ Puller) with a tip resistance ranging from 30 to 50 MΩ when filled with 3 mol/L KCl. Prior to AP measurements, tissues were superfused with Tyrode's solution at 36.5±0.5 °C for at least 30 min and then field-stimulated at a fixed rate at 50% above the stimulation threshold.

Material and methods
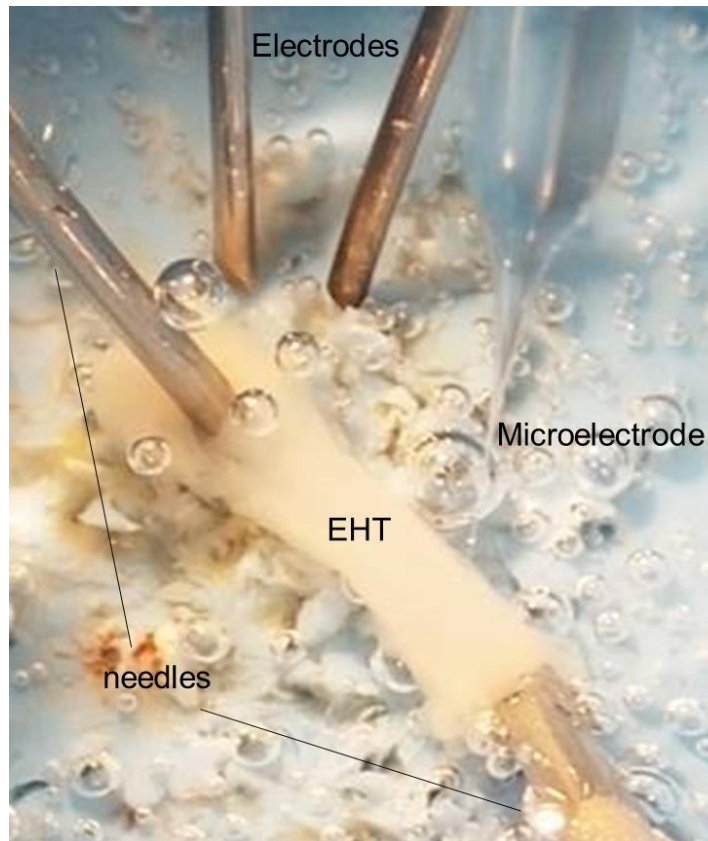
Figure 16: **Sharp microelectrode chamber**. Picture of an EHT to record AP. EHT is placed in the middle of the chamber and superfused in Tyrode's solution. Two needles hold the EHT in place while the microelectrode impales the EHT to measure APs. On top the electrodes for the electrical pacing of the EHT.

APs were analyzed with Lab-Chart software (ADInstruments, Spechbach, Germany) and the following parameters were measured: action potential amplitude (APA), APD, maximum upstroke velocity (dV/dt$_{max}$), take-off potential (TOP), RMP, ERP and CV. APD was corrected for the beating rate using Bazett formula (Bazett 1997). ERP was assessed at 500 ms CL using S1-S2 stimulation protocol (Figure 17). Tissues were paced with a train of nine basic (S1) stimuli followed by a premature (S2) stimulus with the coupling S1-S2 interval decreasing by 5 ms increments until capture no longer occurred. The ERP was identified as the longest S1-S2 interval failing to produce an extra S2-mediated AP.

Material and methods
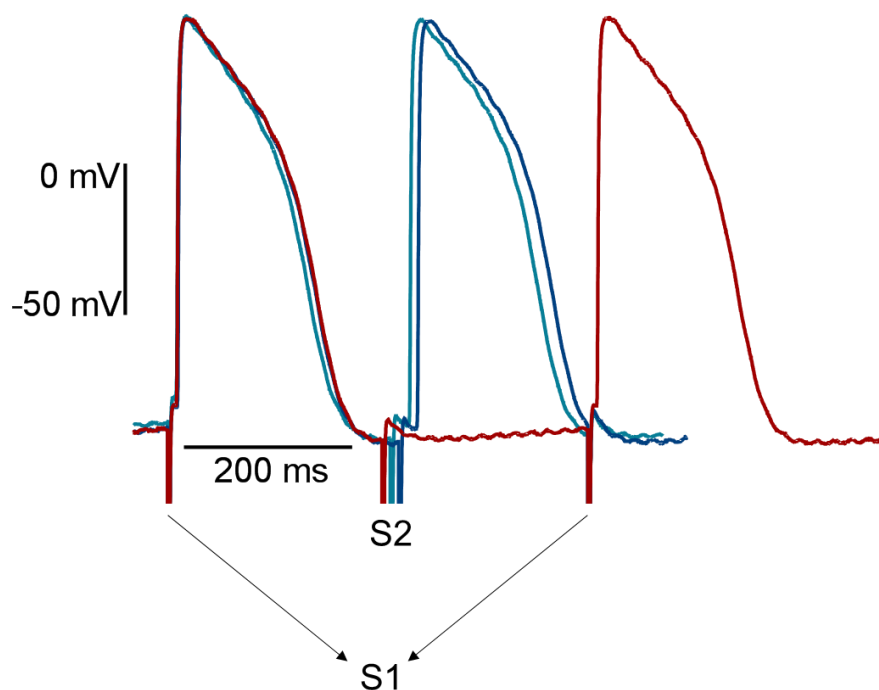
Figure 17: **Example of effective refractory period (ERP) measurement**. Train of basic stimuli (S1) followed by a premature stimulus (S2) with the coupling interval decreased in 5 ms steps. ERP is calculated as S1-S2 interval, where S2 is the first premature stimulus that fails to generate an action potential (red S2 stimulus).

CV was measured by positioning the pacing electrodes in the close proximity of one pillar and measuring the AP at both pillars of the EHT (without changing the pacing electrode position). The delay (ms) from the electrical pacing artifact and the actual start of the AP upstroke was measured. CV was calculated with the following equation:

$$CV = \frac{\text{EHT length}}{delay_{pillar1} - delay_{pillar2}}$$

During AP measurements, a maximum of 20 attempts of burst pacing (CL 50 ms, pacing duration 300-500 ms) was used to check whether tachycardia could be induced. Termination of tachycardia was attempted with: burst pacing (CL 50 ms, pacing duration 100-200 ms), illumination with blue light for 500 ms (at 0.07 mW/mm^2) and drug exposure.

Human tissue samples were transferred in Ca^{2+}-free transport solution at 20–25 °C for maximum 30 min, composition in mmol/L: 100 NaCl, 10 KCl, 1.2 KH$_2$PO$_4$, 5 MgSO$_4$, 50 taurin, 5 MOPS, 30 butanedione monoxime (BDM), pH 7.0. Right atrial appendages (RAA) were obtained from patients suffering from coronary artery disease or valve disease undergoing valve replacement or bypass. Left ventricular (LV) free wall samples derived from patients suffering from cardiomyopathy or valve disease (details are given in Table 5). All patients gave informed consent. The study conforms to the principles outlined by the Declaration of Helsinki.

	RAA	LV
N	38	30
Gender [m/f]	20 / 18	12 / 18
Age [years]	70.2±2.3	59.4±3.1
BMI [kg/m^2]	26.3±0.8	25.3±0.7
Sinus rhythm	38	30
Hypertension, n	38	16
Diabetes mellitus, n	5	5
Hyperlipidaemia, n	12	7
Coronary artery disease, n	21	3
Valve disease, n	17	20
Hypertrophic obstructive	0	5
LVEF [%]	59.3±3.3	52.4±3.4
Cardiovascular medication (n)		
Digitalis	2	1
ACE-Inhibitors	9	16
AT$_1$-blockers	2	5
β-blockers	12	17
Ca^{2+}-channel-blockers	6	1
Diuretics	8	12
Nitrates, n	0	1
Lipid-lowering drugs	11	8

Table 5: **Clinical information of patients**. Personal data and medical history of right atrial appendages (RAA) and left ventricular (LV) tissue donors (adapted from Lemme et al. 2018).

2.5.5 Poincaré plot

The Poincaré plot is a scattergram in which each measurement is plotted as a function of a previous one (Mirescu and Harden 2012). To quantify rate variability of EHTs, Poincaré plots were constructed by plotting each AP cycle length against the previous one (Figure 18). The Poincaré plots were analyzed quantitatively by fitting an ellipse to the plotted shape and calculating short term (SD1) and long term (SD2) variability. SD1 and SD2 are the standard descriptors of Poincaré plot. SD1 identifies the minor axis of the ellipse and represents the standard deviation of the signal perpendicular to the line-of-identity. SD2 identifies the major axis of the ellipse and represents the standard deviation of the signal along the line-of-identity (Figure 18).

Material and methods
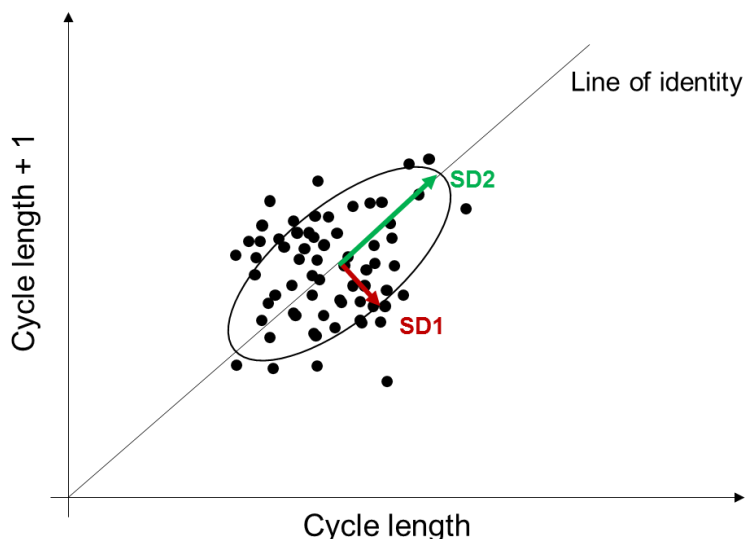
Figure 18: **Example of Poincaré plot**. Short term (SD1) and long term (SD2) standard deviation are used to quantify cycle length variability.

Poincaré indexes (Golińska 2013) were calculated with the following equations:

$$SD1 = \frac{\sqrt{2}}{2} * SD_{CL-CL_{+1}}$$

$$SD2 = \sqrt{2 * (SD_{CL})^2 - \frac{1}{2} * (SD_{CL-CL_{+1}})^2}$$

2.5.6 Voltage clamp recordings

Tip resistances of heat-polished pipettes were 2.5–5 MΩ. The cells were placed in a small perfusion chamber located on the stage of an inverted microscope. The experiments were performed with the following bath solution (in mmol/L): NaCl 145, KCl 2.5, HEPES 10, CaCl$_2$ 2, MgCl$_2$ 1 and glucose 12.5 (pH 7.4, adjusted with NaOH and 308 Osm). Contaminating Na$^+$ currents were suppressed with tetrodotoxin (1 µmol/L). The intracellular solution included (in mmol/L): K gluconate 135, EGTA 0.2, MgCl$_2$ 4, HEPES 10, Na$_2$-ATP 4, Na-GTP 0.4, Na$_2$-phosphocreatine 10, ascorbate 3, pH 7.2 adjusted with KOH. Inward current amplitudes were determined as currents at -70 mV. Voltage clamp recordings were performed by Dr. Christine Gee (Center for Molecular Neurobiology, UKE, Hamburg).

2.5.7 Drugs

The pharmacological agents used in the electrophysiological studies included atrial/ventricular selective drugs and antiarrhythmic medications.

Material and methods

Carbachol (CCh) and 4-aminopyridine (4-AP) were tested to discriminate between atrial and ventricular phenotype. CCh and 4-AP (Sigma-Aldrich, St. Louis, MO, USA) were used at a final concentration of 10 and 50 µmol/L, respectively. CCh was dissolved in DMSO to have a stock solution of 10 mmol/L and then stored at -20 ºC. 4-AP was prepared as a 1 mmol/L stock solution in Tyrode's solution and stored at 4 ºC, after its pH was adjusted to 7.4.

Different drugs with potential antiarrhythmic action were applied to terminate a stable tachycardia episode: ivabradine (1 µmol/L), flecainide (1 µmol/L), and JTV-519 (1 µmol/L). Ivabradine, flecainide and JTV-519 were obtained from Sigma-Aldrich (St. Louis, MO, USA). Ivabradine was prepared as a 10 mmol/L stock solution in water and stored at 4 ºC. Flecainide was prepared as a 1 mmol/L stock solution in DMSO and stored at -20 ºC. JTV-519 was prepared as a 1 mmol/L stock solution in DMSO and stored at 4 ºC. Incubation time of each drug was > 15 min. All stock solutions were diluted appropriately before use.

2.6 Statistics

Statistical analyses of the results were conducted with GraphPad Prism software 6.0. Bar graphs and scatterplots were used for data representation. Differences between groups were expressed as mean±SEM and analyzed by unpaired and paired t-test when appropriate. The incidence of tachycardia in two distinct groups was evaluated using Fisher's exact probability test. A p-value lower than 0.05 was considered to be statistically significant. Replicates were expressed as n=EHT number/batch number. All experiments consist of three independent batches.

3. Results

The data presented in the first part of the project were recently published in the journal Stem Cell Reports in December 2018. Title: "Atrial-like Engineered Heart Tissue: An in vitro Model of the Human Atrium". List of authors: Marta Lemme, Bärbel M. Ulmer, Marc D. Lemoine, Antonia T.L. Zech, Frederik Flenner, Ursula Ravens, Hermann Reichenspurner, Miriam Rol-Garcia, Godfrey Smith, Arne Hansen, Torsten Christ and Thomas Eschenhagen.

3.1 Generation and characterization of atrial-like vs. ventricular-like EHTs (RA-EHTs vs. Ctrl-EHTs)

The first step of the project consisted in the establishment of a protocol to differentiate hiPSC into atrial-like myocytes. This differentiation phase was then followed by the generation and characterization of atrial-like EHTs vs. ventricular-like EHTs (RA-EHTs vs. Ctrl-EHTs). The ultimate goal was the development of an RA-EHT that could be used as an *in vitro* model of human atrium.

3.1.1 RA-treatment after mesodermal induction during cardiac differentiation

RA treatment was included in the established three step EB-based protocol (Breckwoldt et al., 2017, Figure 12). Different RA concentration (0.1, 0.5, 1 and 10 µmol/L) and exposure times were tested to identify the optimal differentiation protocol to generate atrial-like CMs. Low concentrations of RA (0.1 and 0.5 µmol/L) improved hiPSC differentiation towards a cardiac lineage, but they did not increase expression of atrial specific markers. On the other hand, high concentration of RA (10 µmol/L) dramatically decreases CM differentiation. HiPSC treated with 1 µmol/L RA from day 4 to day 7 after mesodermal induction showed differentiation towards the atrial phenotype (Figure 19 and Figure S5). Both Ctrl and RA-treated cells formed stable EBs, which did not differ in morphology (Figure 21). Moreover, RA-treatment did not impair cardiac differentiation efficiency (Lemme et al. 2018). In fact, the total percentage of cTnT positive cells was not altered after RA-treatment (Figure 20).

Results
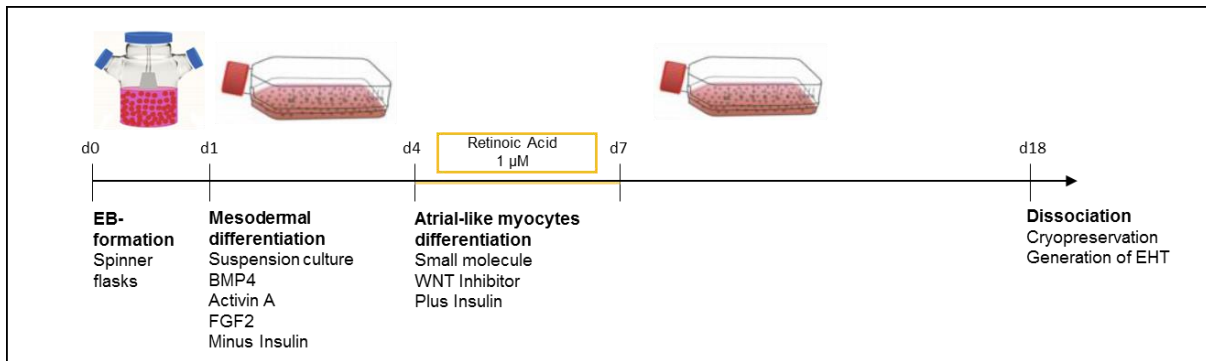
Figure 19: **Embryoid-based cardiac differentiation protocol**. Retinoic acid (RA, 1 µmol/L) was added from day 4 to day 7 to induce differentiation of hiPSC towards atrial-like myocytes (adapted from Lemme et al. 2018).
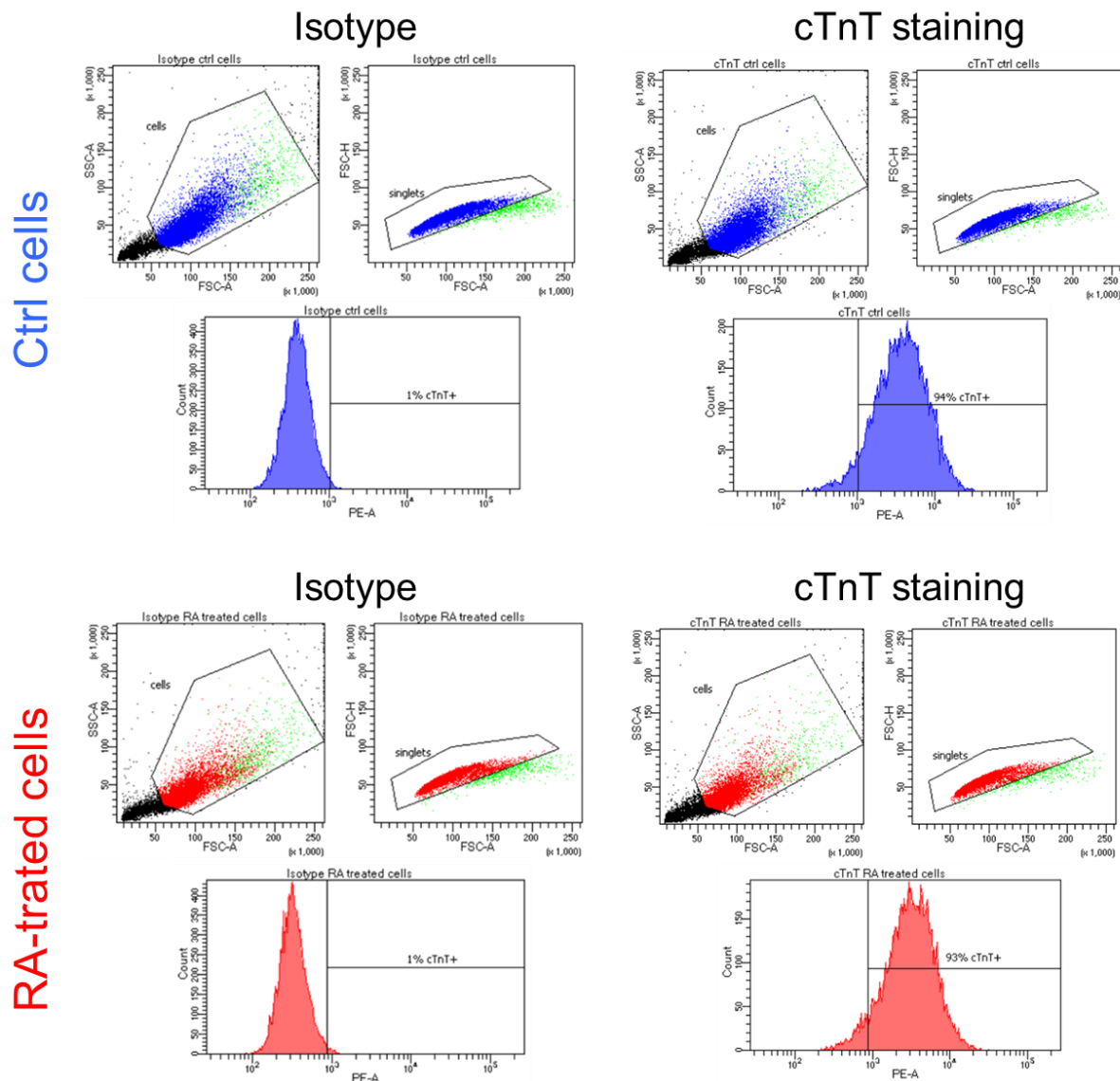
Figure 20: **Flow cytometry analysis of cardiac troponin T after retinoic acid treatment**. Flow cytometry analysis of control (blue) and retinoic acid-treated cells (red). After exclusion of debris and doublets, the gating was set according to the negative controls with appropriate isotype antibodies (graphs on the left) and the proportion of cardiac troponin T-positive cells was calculated (graphs on the right; adapted from Lemme et al. 2018).

Results

<div align="center">

Ctrl cells   RA-treated cells

</div>
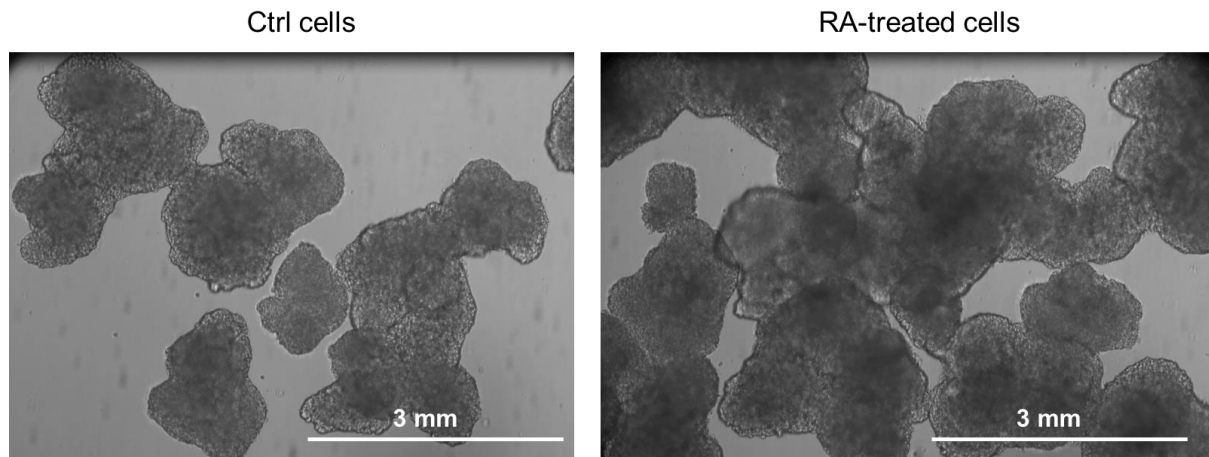
Figure 21: **Embryoid bodies (EBs) at day 18 of cardiac differentiation protocol**. EB morphology of Ctrl and RA-treated cells on the day before EB dissociation.

3.1.2 RA-treatment reduces cell size

Cell size can be estimated as cell area or cell volume. Image analysis of α-actinin 2 staining showed that RA-treated hiPSC-CMs exhibited smaller cell areas than Ctrl hiPSC-CMs (Figure 22A). Although a substantial overlap between the two groups was noted, the mean values of the area were significantly smaller after RA treatment ($1736\pm64\ \mu m^2$ vs. $2469\pm192\ \mu m^2$, n=209 and 88; $p<0.05$, unpaired t-test). However, cell area could be affected by the propensity of a cell to spread. Therefore, cell volume, a better indicator of cell size, was calculated. Cell volume estimated as the volume of a perfect sphere was measured using flow volumetric analysis (Mosqueira et al. 2018). Directly after cardiac differentiation, RA-treated cells showed smaller volume compared to Ctrl-cells ($560\pm1.3\ \mu m^3$ vs. $588\pm1.6\ \mu m^3$, n=26,508 and 21,577; $p<0.05$, unpaired t-test; Figure 22B; Lemme et al. 2018). In addition, this difference in volume increased after 14 days of EHT culture, due to an increase in size of Ctrl-cells in 3D culture ($569\pm3\ \mu m^3$ vs. $854\pm2.8\ \mu m^3$, n=15,474 and 20,931; $p<0.05$, unpaired t-test; Figure 22B; Lemme et al. 2018). The resulting thickness of a single hiPSC-CM estimated from its area and volume was ~ 0.3 µm. This thickness is too small for 2D cultured cells, but this discrepancy cannot be explained at present. Although hiPSC-CMs are in general smaller than adult human CMs, the same difference in size between native atrial and ventricular CMs was observed (Bensley et al. 2016).
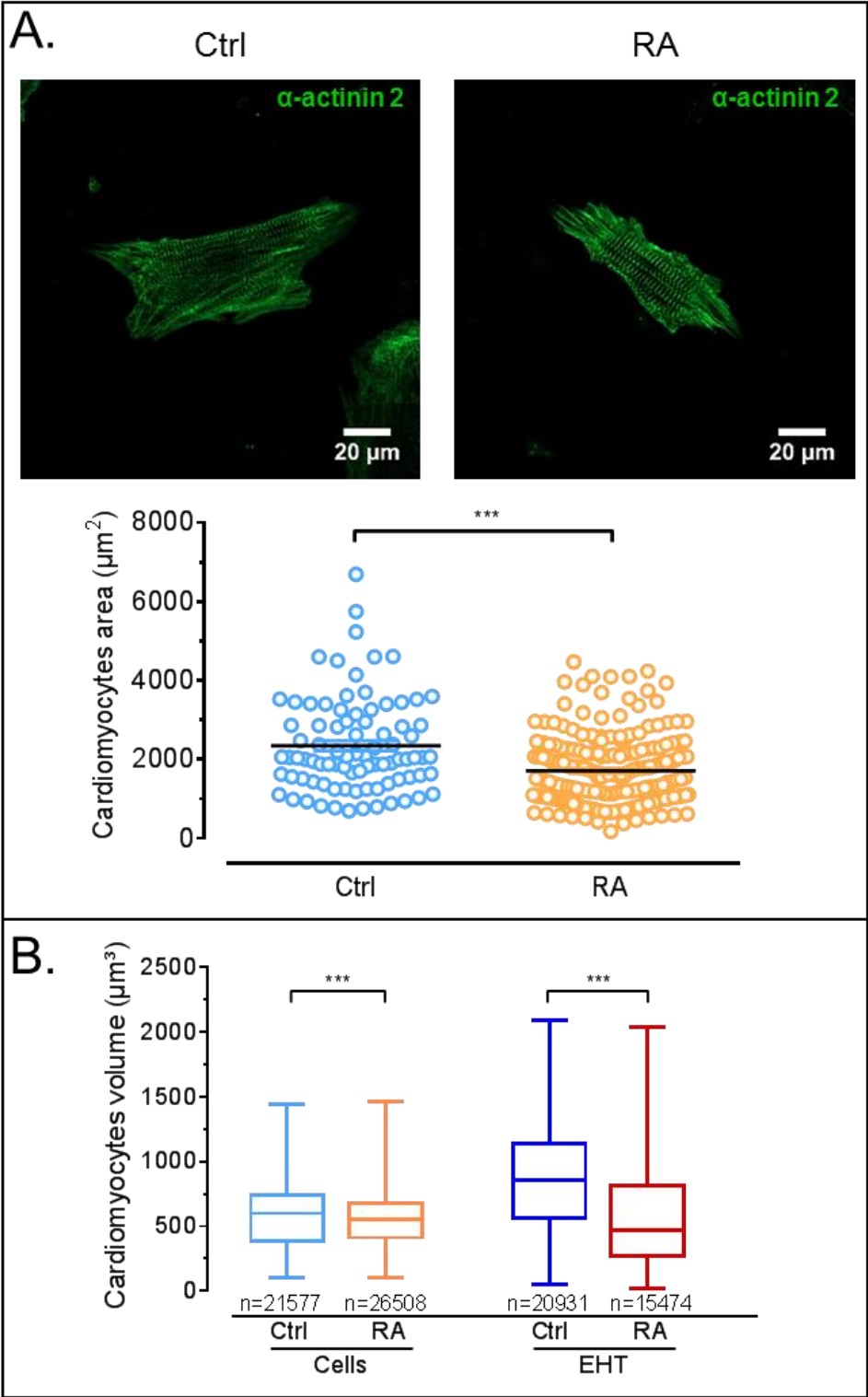
Figure 22: **Cell size evaluation after retinoic acid (RA)-treatment**. (A) Cell area was analyzed using α-actinin 2 staining. RA-treated cells exhibit smaller area than Ctrl-cells (1,736.2±64.4 µm², n=209 and 88 from 3 batches each; p<0.05, unpaired t-test). (B) Box plots showing median, first and third quartile of the volume of Ctrl vs. RA-treated cells. (Left) Volume of RA-treated cells at the end of cardiac differentiation protocol was smaller than Ctrl-cells (560±1.3 µm³ vs. 588±1.6 µm³, n=26,508 and 21,577 from 3 batches each; p<0.05, unpaired t-test). (Right) Volume of cells cultured for 14 days in RA-EHTs was smaller than in Ctrl-EHTs (569±3 µm³ vs. 854±2.8 µm³, n=15,474 and 20,931 from 4 EHTs each; p<0.05, unpaired t-test). Error bars show mean±SEM. (adapted from Lemme et al. 2018).

Results

3.1.3 RA-treatment upregulates expression of atrial specific genes

Native atrial and ventricular CMs are characterized by a specific gene expression profile (Wobus et al. 1995; Ellinghaus et al. 2005; Gaborit et al. 2007; Table S4, Figure S2 and S3). To test whether RA-treatment indeed direct hiPSC differentiation towards an atrial-like phenotype, expression of chamber specific genes was analyzed by RT-qPCR (Figure 23).
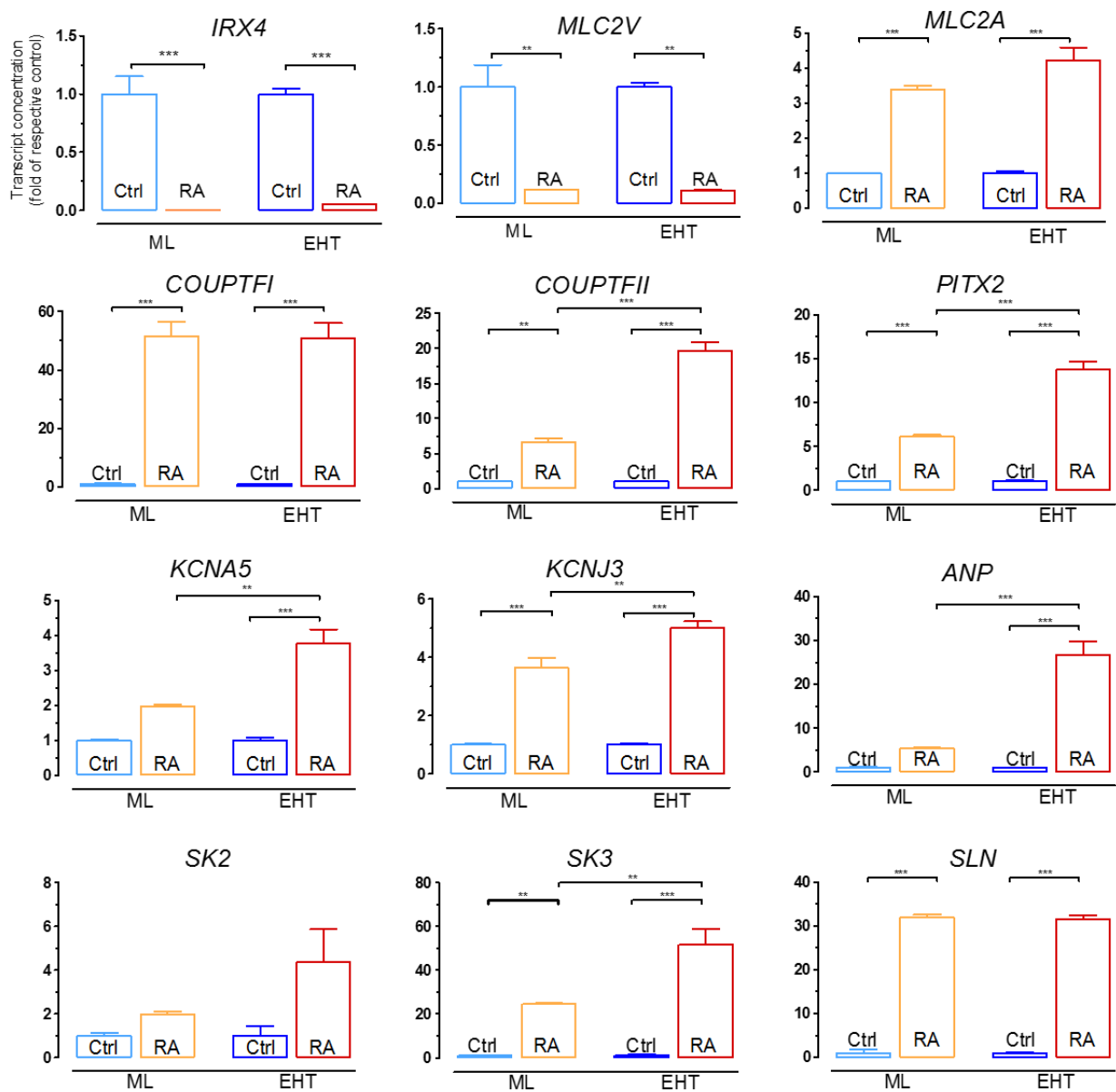
Figure 23: **Effect of retinoic acid (RA)-treatment on gene expression**. Gene expression of RA-treated cells compared to Ctrl-cells after 14 days of culture in ML and EHT format. RA-treated cells show downregulation of ventricular markers and upregulation of atrial markers. The upregulation of atrial specific genes is more prominent in EHT compared to ML (n=9 ML/EHT from three batches). Ct values of each gene were normalized to Ct values of the housekeeping gene GUSB and to their respective control (adapted from Lemme et al. 2018).

Expression levels of the housekeeping genes cTnT and GUSB did not differ between Ctrl-ML and Ctrl-EHT. RA-treated CMs expressed significantly higher levels of genes associated with

atrial phenotype, including typical atrial markers (*MLC2A*, *ANP*, *SLN*), transcription factors (*COUPTFII*, *COUPTFI*, *PITX2*) and ion channels (*KCNJ3*, *KCNA5*, *SK2* and *SK3*; Figure 23). Moreover, RA-treated CMs exhibited a downregulation of ventricular markers *IRX4* and *MLC2V* (Figure 23, for full gene names see Table S4. The atrial specification after RA-treatment was further accentuated in 3D model of auxotonically beating EHT compared to ML (Lemme et al. 2018). In fact, six out of ten atrial specific genes showed increased expression levels after 14 days of culture in EHT compared to ML (Figure 23).

3.1.4 RA-treatment increases protein level of atrial specific markers

Antibody specificity was determined by western blotting of human adult cardiac tissue RAA and LV (Figure S1). Western blot analysis revealed the same differential expression of atrial markers between Ctrl- and RA-MLs previously observed with RT-qPCR (Lemme et al. 2018). Higher levels of atrial specific proteins in RA-ML compared to Ctrl-ML were detected by WB analysis (Figure 24). Quantification of protein bands was performed by normalization to the housekeeping gene α-actinin 2 and to their respective control. These results suggest that RA-treatment promotes atrial specification in hiPSC-CM.
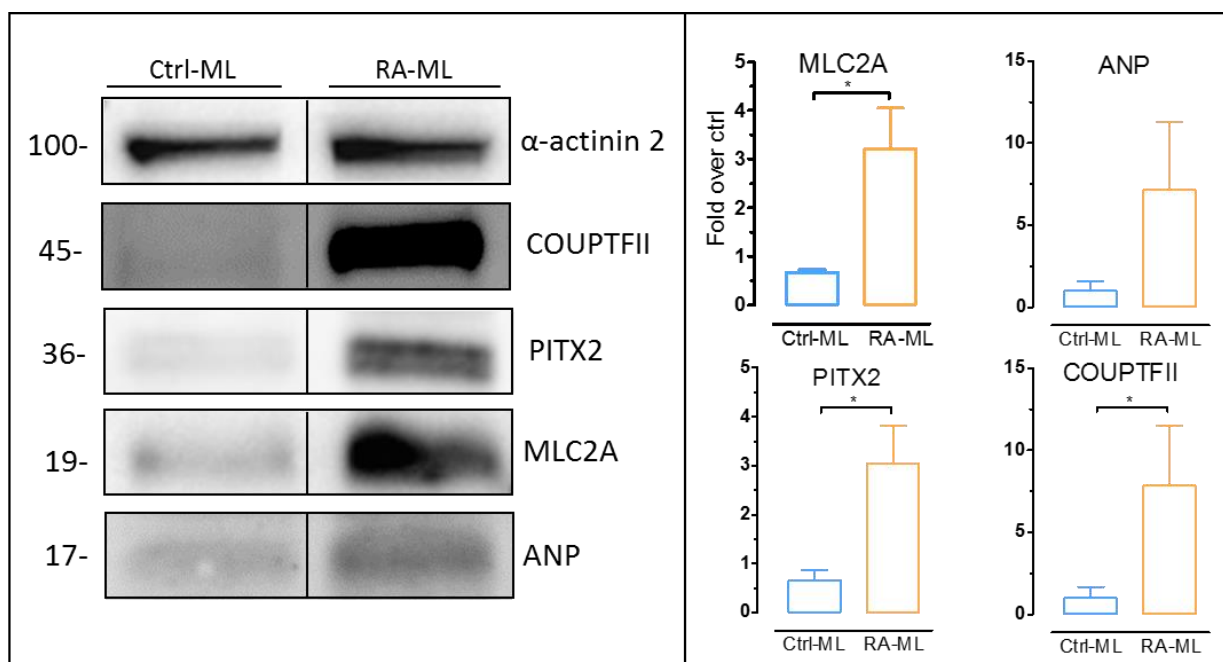
Figure 24: **Effect of retinoic acid (RA)-treatment on atrial specific protein levels**. (Left) Western blot analysis for α-actinin 2, COUPTFII, PITX2, MLC2A and ANP in 14 day-old MLs. (Right) Quantification of protein bands normalized to the housekeeping gene α-actinin 2 and to their relative control. Error bars show mean±SEM (n=3 batches; adapted from Lemme et al. 2018).

Results

3.1.5 RA-treatment increases the number of MLC2A$^+$ cells over MLC2V$^+$ cells

EHTs were generated from Ctrl- and RA-treated hiPSC-CMs showing a percentage of cTnT positive cells ranging from 75% and 95% (Lemme et al. 2018). These differentiated CMs were able to form functional contracting EHTs. However, RA-treatment affected the development and the resting length of the EHTs (Lemme et al. 2018). RA-EHTs displayed a slower development than Ctrl-EHTs determined by a later onset of spontaneous beating, and they showed higher resting length compared to Ctrl-EHTs (5.4±0.07 mm vs. 5.0±0.16 mm; $p<0.05$, unpaired t-test; Figure 25).
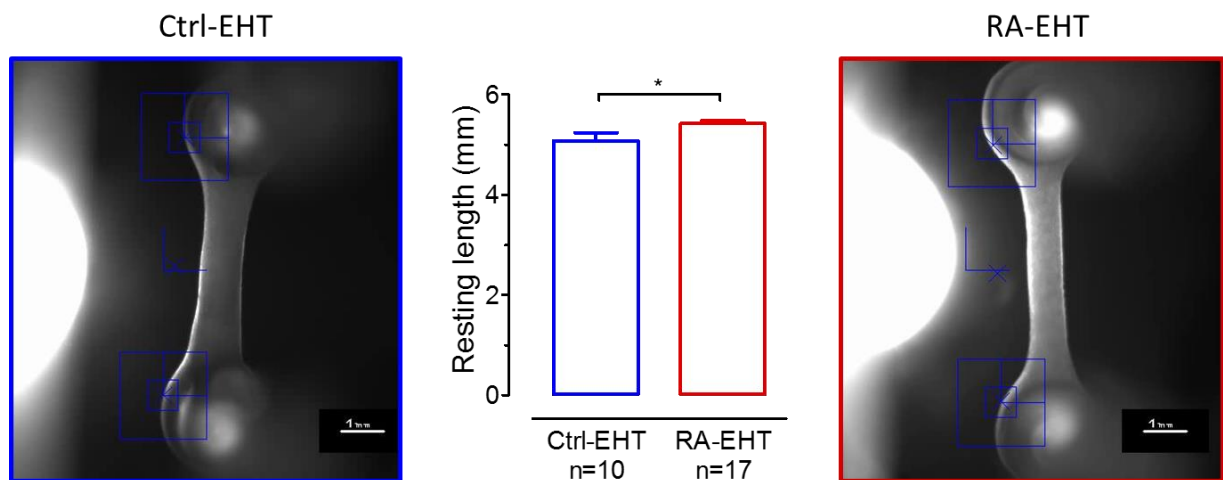
Figure 25: **Resting length of Ctrl- and RA-EHTs**. Images (scale bar 1 mm) of 20 day-old Ctrl- and RA-EHTs recorded by the contractility video-optical system. RA-EHTs exhibited significantly higher resting length than Ctrl-EHTs (5.4±0.07 mm vs 5±0.16 mm, n=17/10 EHTs from 3 batches; $p<0.05$, unpaired t-test). Error bars show mean±SEM (adapted from Lemme et al. 2018).

Both Ctrl- and RA-EHTs showed macroscopically distinguishable muscle bundles. The α-actinin positive CMs exhibited advanced sarcomeric structures with high degree of CM alignment and orientation in the direction of the force lines (Figure 26A and B; Lemme et al. 2018). Cross sections of EHTs were stained with dystrophin, membrane skeleton protein, to visualize the CM distribution within the EHT (Figure 26C; Lemme et al. 2018). CMs were predominantly located at the outer surface of the EHTs, where the oxygen and nutrient supply is higher and the force lines are stronger (Vollert et al. 2013; Hirt et al. 2014a).

Results
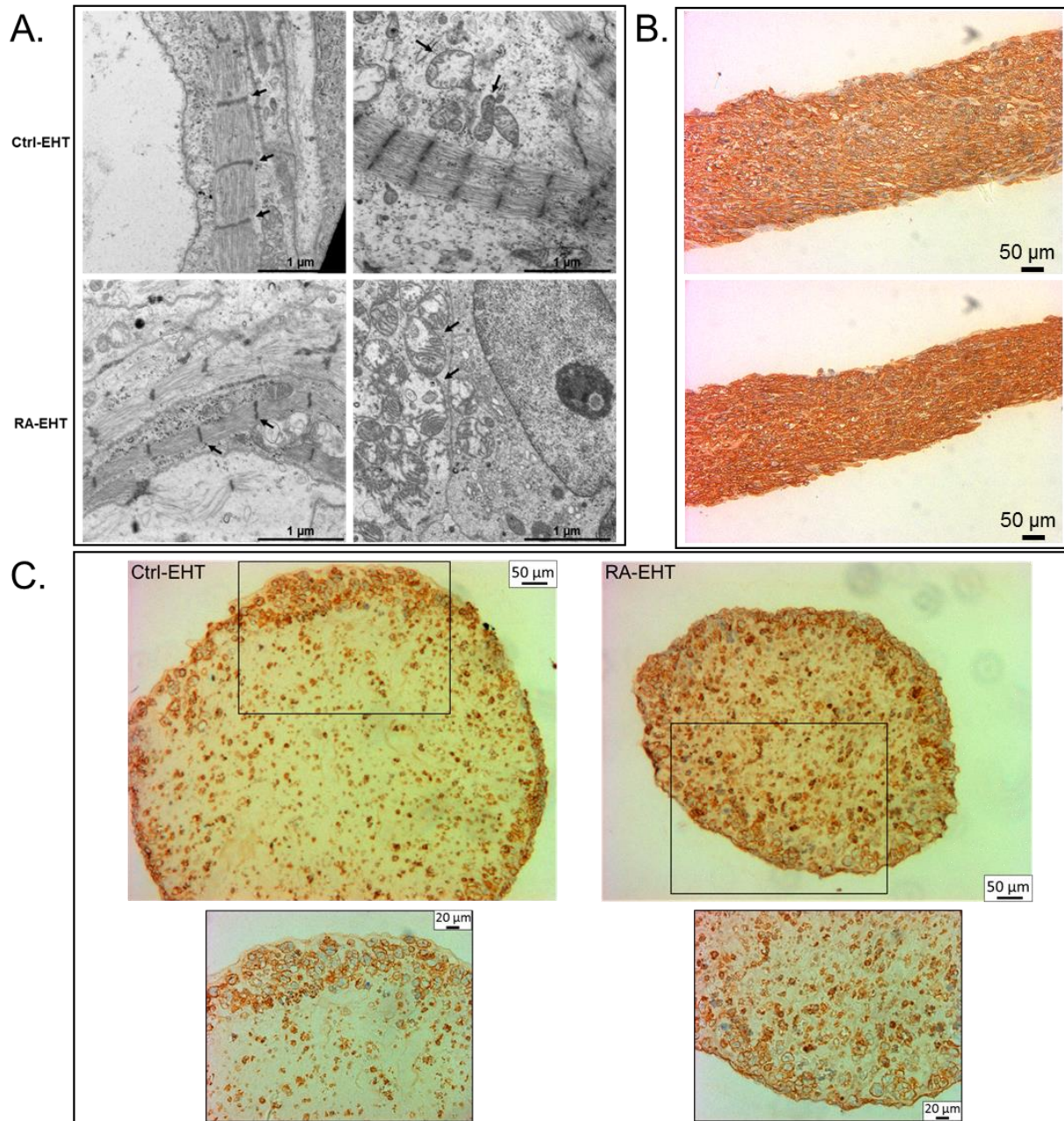
Figure 26: **Structural organization of EHTs**. (A) Well-developed sarcomeres were observed in 20 day-old Ctrl- and RA-EHTs by transmission electron microscopy. Qualitatively, Ctrl-EHTs exhibited an higher level of sarcomere organization than RA-EHTs, in line with previous results showing less organized contractile machinery in fetal human atrial myocytes than in ventricular (Claycomb et al. 1989). Black arrows in the figure point to Z-discs and mitochondria. (B) α-actinin expression analyzed by immunohistochemistry of paraffin sections of Ctrl- and RA-EHTs. (C) Dystrophin staining of Ctrl- and RA-EHT cross sections (adapted from Lemme et al. 2018).

Immunohistochemistry and immunofluorescence analysis confirmed the differential expression of myosin light chain between hiPSC-CMs treated with or without RA. RA-ML/EHT displayed a higher fraction of MLC2A$^+$ CMs compared to Ctrl-ML/EHT (Figure 27 and Figure 28). HiPSC-CMs treated with RA during their cardiac differentiation displayed robust expression of MLC2A and low levels of MLC2V (Figure 27 and Figure 28) while hiPSC-CMs generated

Results

under the control condition showed the opposite distribution (Figure 27 and Figure 28). The expression pattern of MLC2A and MLC2V in hiPSC-CMs treated with or without RA reflected myosin light chain distribution observed in human cardiac tissues. RAA revealed high expression of MLC2A and no expression of MLC2V (Figure 28) whereas, LV tissues showed almost exclusively MLC2V$^+$ CMs (Figure 28). These data support the conclusion that RA signaling effectively induces the development of atrial-like myocytes at the expense of the ventricular phenotype (Lemme et al. 2018).
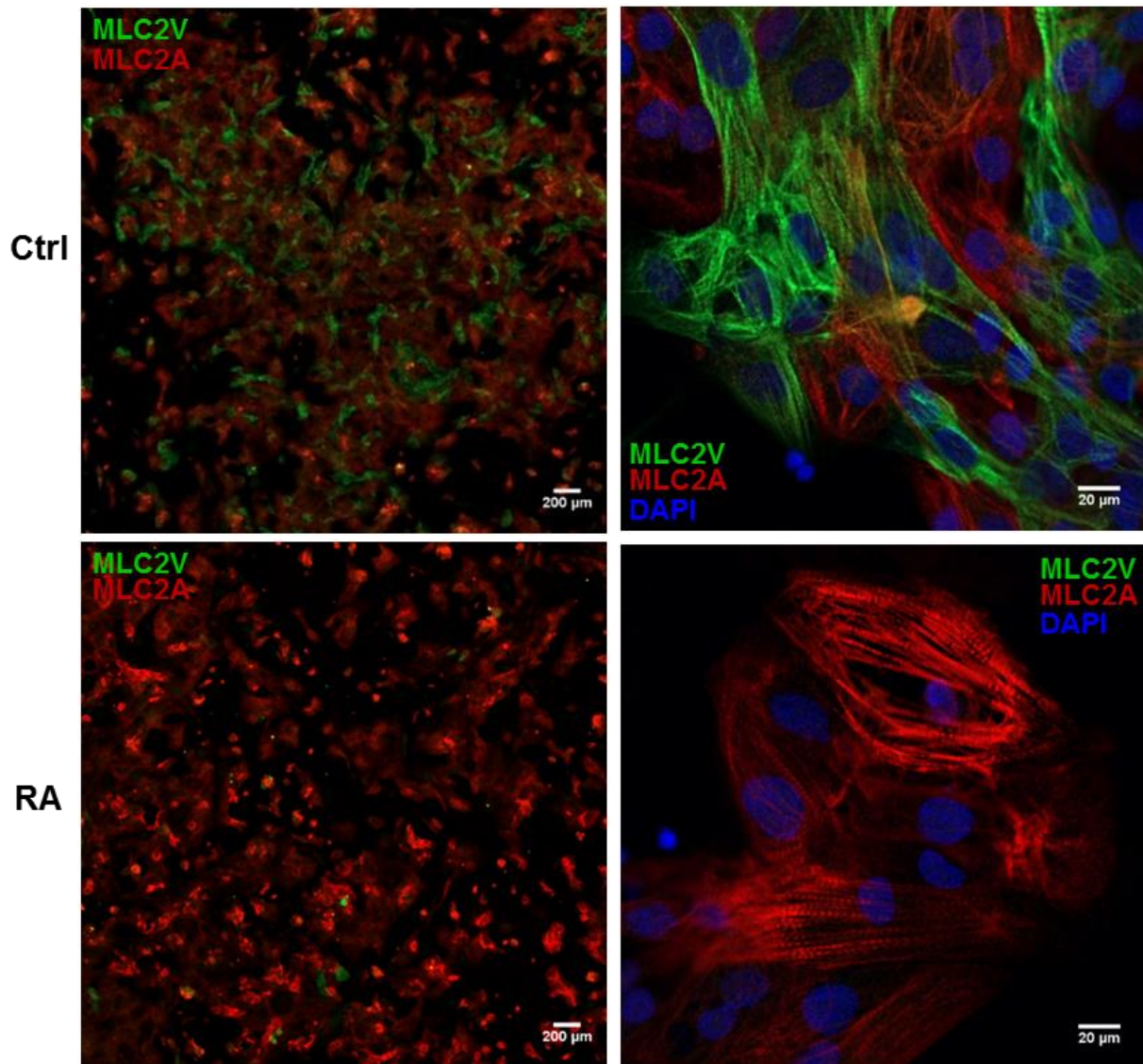
Figure 27: **Immunofluorescence of myosin light chain in Ctrl- and RA-ML**. Immunofluorescence staining of MLC2V (green), MLC2A (red) and DAPI (blue) in 14 days-old Ctrl- and RA-ML. Images were acquired with confocal microscope (Zeiss LSM 800) using 2.5x (left) and 40x (right) magnification (adapted from Lemme et al. 2018).

Results

Scale bar 100 µm
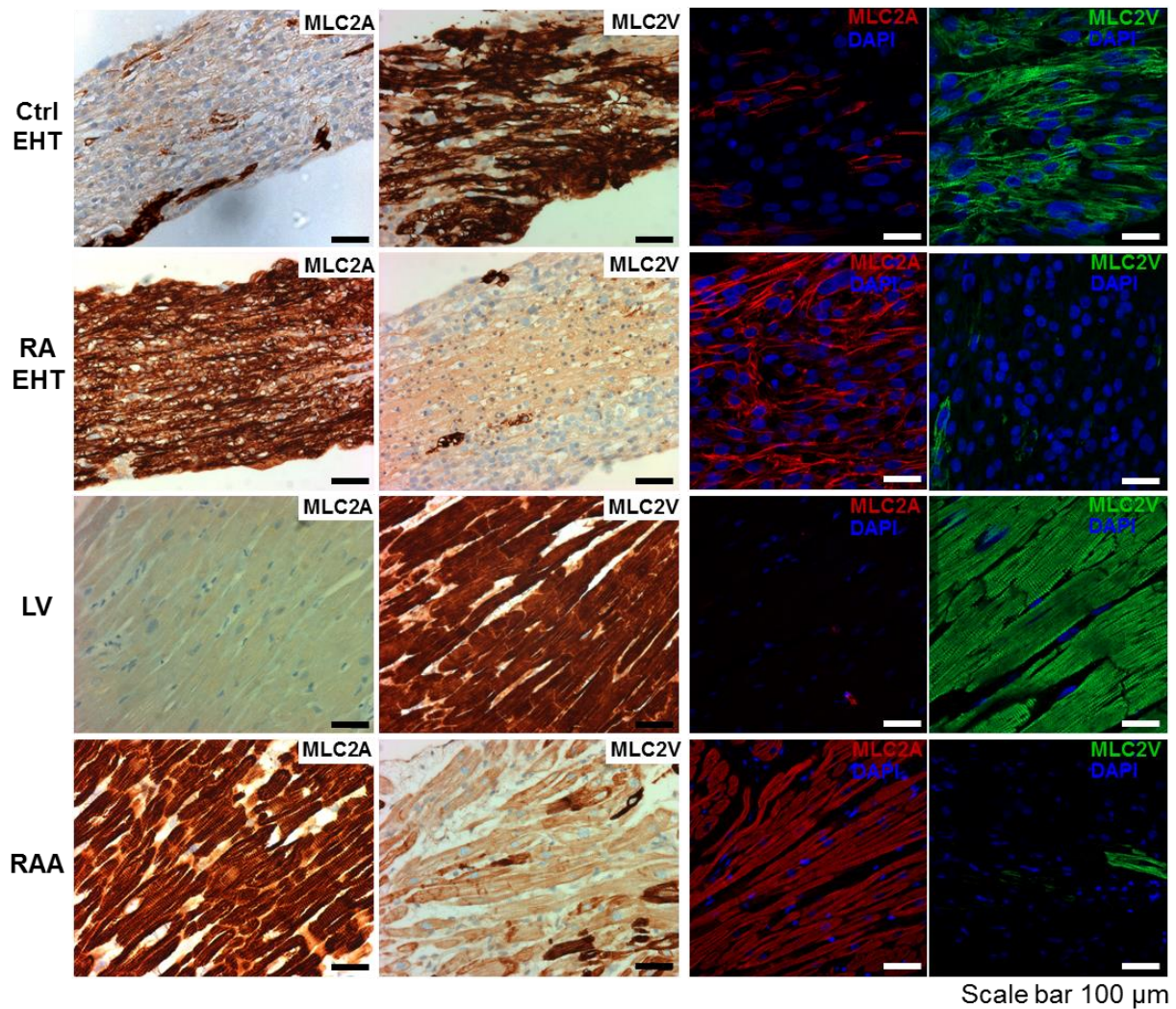
Figure 28: **Immunofluorescence and immunohistochemistry of myosin light chain in Ctrl/RA-EHTs and human cardiac tissues**. Immunohistochemistry (first two columns) and immunofluorescence (last two columns) of MLC2V and MLC2A in Ctrl/RA-EHTs, left ventricular tissue and right atrial appendage (adapted from Lemme et al. 2018). Immunofluorescence staining: MLC2V (green), MLC2A (red) and DAPI (blue); scale bar: 100 µm. These images show EHTs where CMs are evenly distributed throughout the EHT diameter, whereas generally the CMs were mainly located at the outer layer of the EHT as shown previously (Figure 26C; Vollert et al. 2013; Hirt et al. 2014a).

3.1.6 RA-treatment accelerates beating rate and contraction kinetics in ML and EHT

EHTs showed faster spontaneous beating rate than MLs whether hiPSC-CMs were treated with RA or not. CMs that were differentiated in the presence of RA showed significantly faster spontaneous beating rate compared to CMs differentiated under control condition (Figure 30). This difference in beating frequency was accentuated in EHT culture format compared to ML (increase by 61±4% vs. 28±2%; $p<0.05$, unpaired t-test; Figure 30; Lemme et al. 2018). RA-EHTs developed lower forces than Ctrl-EHTs (Figure 30B). The same conclusion cannot be drawn from ML contraction analysis, because the software MUSCLE MOTION (Sala et al. 2018), used to analyze ML contractions, could not calculate absolute force values, but only

Results

contraction amplitudes in arbitrary units. FFR, an important intrinsic regulatory mechanism of cardiac contractility, was measured in Ctrl- and RA-EHTs. FFR of RA- and Ctrl-EHTs showed the same behavior (Figure 29). They displayed positive FFR up to 1.8 Hz and negative FFR from 1.8 Hz to 5.7 Hz (Figure 29; Lemme et al. 2018).
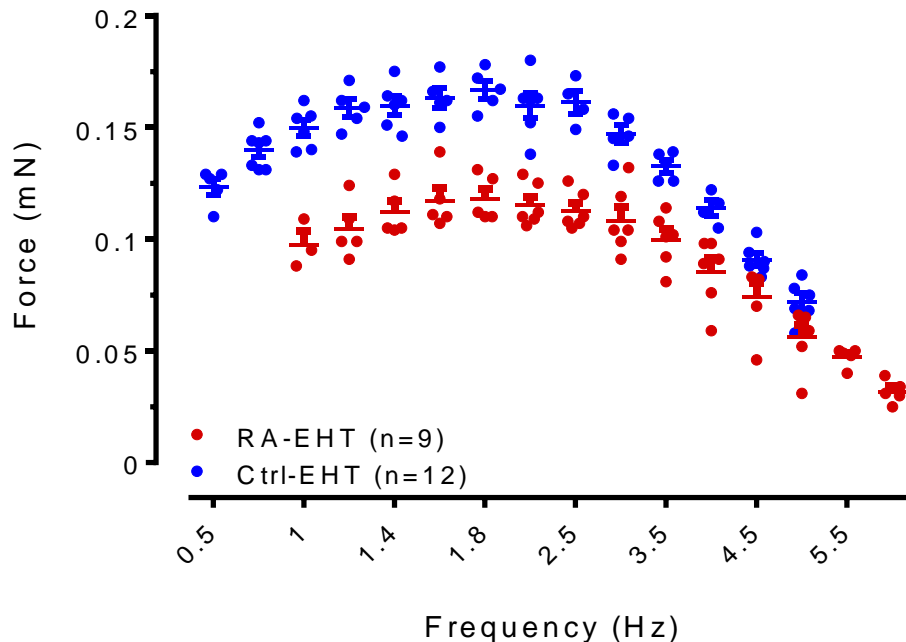
Figure 29: **Force-frequency relationship (FFR) in Ctrl- and RA-EHTs**. FFR of RA-EHTs (n=9 from 2 batches) and Ctrl-EHTs (n=12 from 2 batches) was measured by electrically stimulating EHTs from 0.5 to 5.7 Hz with 0.2 Hz steps. Both EHTs showed a positive FFR until 1.8 Hz and a negative FFR from 1.8 to 5.7 Hz.

Based on previous observations showing that RAA contract faster than LV (Molenaar et al. 2013; Berk et al. 2016), the effect of RA-treatment on contraction kinetics was investigated, both in ML and EHT (Figure 30; Lemme et al. 2018). RA-treatment induced faster TTP and RT both in ML and EHT (Figure 30A and B). To exclude the possibility that the difference in contraction kinetics induced by RA-treatment was the consequence of different spontaneous beating frequencies, contraction kinetics of Ctrl- and RA-EHTs were measured under electrical pacing. Even under field stimulation at 3 Hz, TTP and RT were faster in RA-EHTs (n=6) than in Ctrl-EHTs (n=5). TTP was 80±0.65 ms in RA-EHTs and 110±1.3 ms in Ctrl-EHTs, while RT was 117±1.8 ms in RA-EHTs and 123±2.5 ms in Ctrl-EHTs.

As contractions are initiated by a transient rise in calcium (Figure 31), cytosolic calcium transients were measured in Ctrl- and RA-EHTs by fluorescence imaging. The faster contraction kinetics were confirmed by faster calcium transients in RA-EHTs compared to Ctrl-EHTs (Figure 31). These functional data suggest that RA-treatment can successfully induce an atrial-like contractility pattern (Lemme et al. 2018).
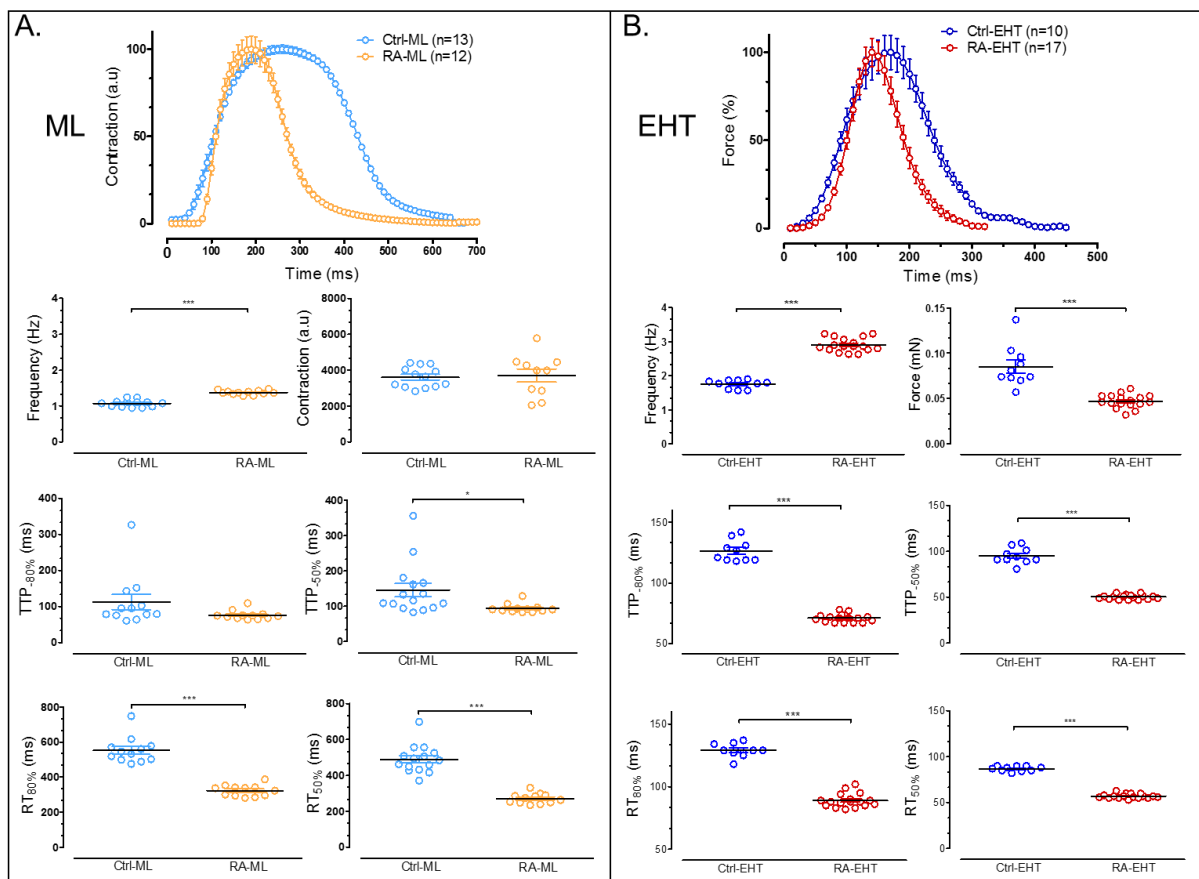
Figure 30: **Effect of retinoic acid (RA)-treatment on contractility in ML and EHT**. Contraction analysis in (A) ML and in (B) EHT. Average contraction peaks were calculated from 6 single wells or EHTs and normalized to the smallest and largest values of the data set. (A) RA-MLs (n=12 wells from 2 batches) showed faster spontaneous beating rate and contraction kinetics (TTP and RT) compared to Ctrl-MLs (n=13 wells from 2 batches). (B) RA-EHTs (n=17 from 3 batches) developed faster spontaneous beating rate, faster contraction kinetics and smaller force compared to Ctrl-EHTs (n=10 from 3 batches). Data are expressed as mean±SEM (p<0.05, unpaired t-test). To better visualize the effect of RA-treatment, y-axes in ML and EHT graphs do not match (adapted from Lemme et al. 2018).
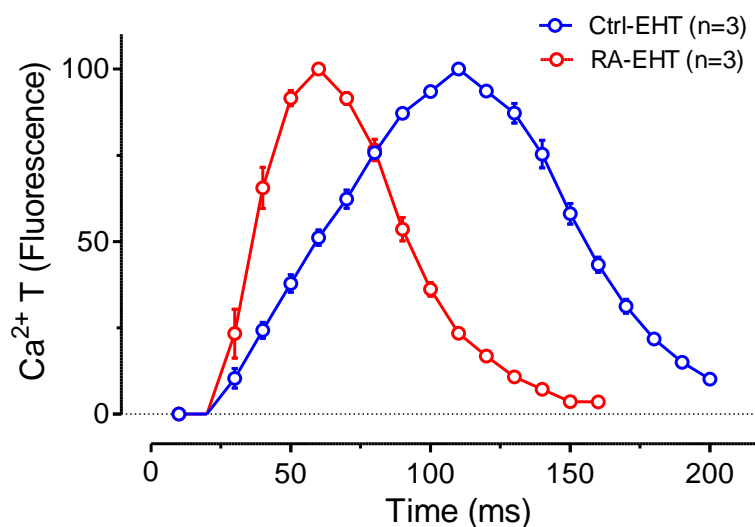
Figure 31: **Recordings of calcium transients**. Fluorescence intensity of calcium transients during spontaneous beating of Ctrl- and RA-EHTs.

Results

3.1.7 RA-treatment shortens APD$_{90}$ and increases repolarization fraction

Cellular electrophysiology in MLs and EHTs was studied in order to investigate whether the molecular changes upon RA-treatment were associated with an atrial-like AP shape (Figure 32 and Figure S6).
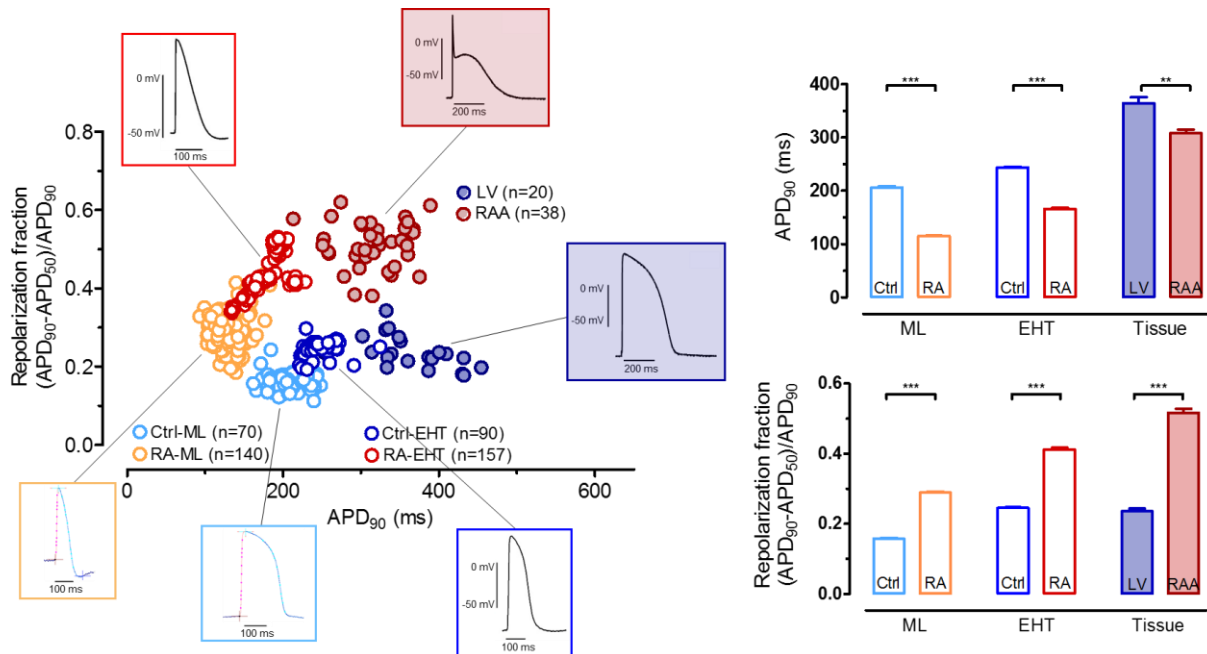
Figure 32: **Effect of retinoic acid (RA)-treatment on electrophysiology in ML and EHT**. (Left) Scatter plot of APD$_{90}$ vs. repolarization fraction (APD$_{90}$-APD$_{50}$)/APD$_{90}$. The plot includes APs from Ctrl-MLs (n=70 wells from 2 batches) and RA-MLs (n=140 wells from 2 batches) measured with CellOPTIQ and from Ctrl-EHTs (n=90/6, number of impalements/EHTs, 3 batches), RA-EHTs (n=157/6, number of impalements/EHTs, 3 batches), LV (n=20 patients) and RAA (n=38 patients) obtained with sharp microelectrode. A representative AP trace is shown for every group. (Right) Bar graphs comparing APD$_{90}$ and repolarization fraction in the different groups (adapted from Lemme et al. 2018). Data are expressed as mean±SEM (p<0.05, unpaired t-test).

APD$_{90}$ and repolarization fraction (APD$_{90}$-APD$_{50}$)/APD$_{90}$ were used to distinguish between atrial and ventricular-like APs (Du et al. 2015). It was previously demonstrated that the repolarization fraction is higher in RAA than in LV (Horváth et al. 2018) and thus represents a suitable discriminator between atrial and ventricular phenotype. APs were measured by voltage sensitive dye from MLs and by standard sharp microelectrode from EHTs. In line with recent results (Lemoine et al. 2018), Ctrl-EHTs displayed shorter APD$_{90}$ compared to LV. APD$_{90}$ was shorted in RA-MLs/EHTs compared to Ctrl-MLs/EHTs (126±10 ms vs. 206±24 ms, n=70/140 in ML and 166±2 ms vs. 243±2 ms, n=90/157 in EHT; p<0.05, unpaired t-test; Figure 32). Repolarization fraction increased upon RA-treatment (Lemme et al. 2018). RA-MLs/EHTs exhibited higher repolarization fraction compared to Ctrl-MLs/EHTs (0.28±0.003 vs. 0.15±0.002, n=70/140 in ML and 0.41±0.005 vs. 0.24±0.002, n=90/157 in EHT; p<0.05, unpaired t-test; Figure 32). Although no purification process was performed after cardiac

Results

differentiation with or without RA-treatment, repolarization fraction demonstrated the presence of two distinct, non-overlapping populations (Figure 32 and Figure S4). These electrophysiology studies demonstrated that RA-treatment induces AP changes reflecting atrial phenotype.

3.1.8 RA-treatment induces shortening of APD upon muscarinic receptor activation

The acetylcholine activated potassium current $I_{K,Ach}$ is an atrial specific ion current, which contributes to AP repolarization. CCh is expected to activate $I_{K,Ach}$ and hence shorten APD_{90}. According to previous experiments in RAA (Dobrev et al. 2001), the maximum APD_{90} shortening in RAA could be detected two min after CCh exposure. CCh did not show any effect on the APD of LV, but it reduced APD_{90} in RAA from 314 ± 14 ms to 174 ± 15 ms, n=10; p<0.05, paired t-test (Figure 34B). Of note, the effect of CCh on APD_{90} shortening was affected by beating rate. At shorter CL APD_{90}-shortening induced by CCh decreased (Figure 33).
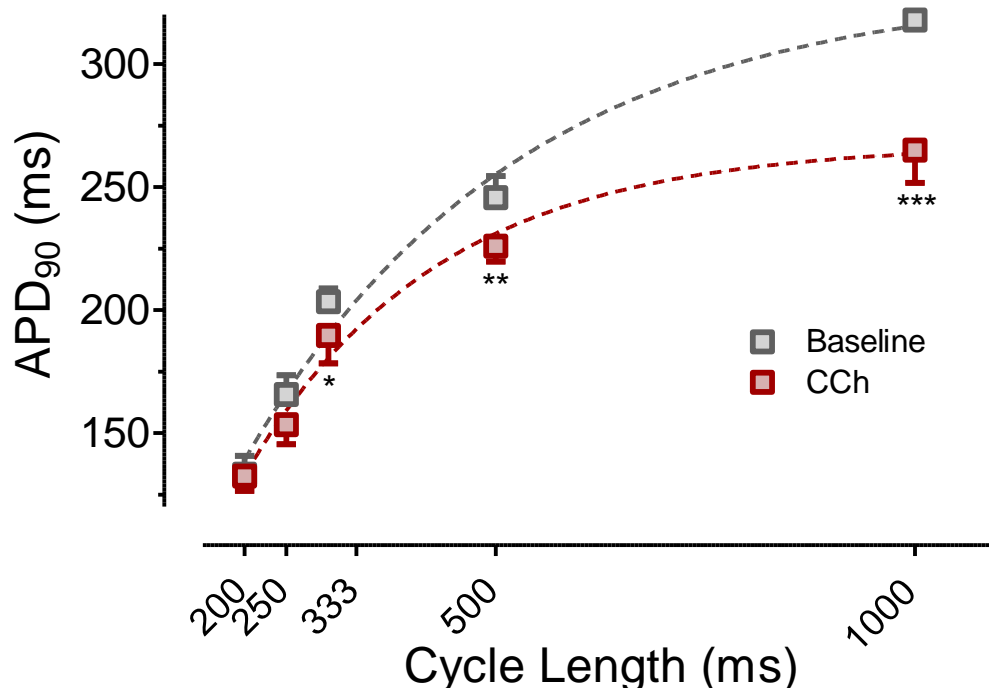
Figure 33: **Rate-dependency of carbachol (CCh)-induced AP shortening in adult human atrium**. APs were measured in right atrial appendages with sharp microelectrode (n=6 patients, p<0.05, paired t-test) and an exponential function was fitted to the data points (adapted from Lemme et al. 2018).

Effect of CCh on Ctrl- and RA-EHTs is in line with the data observed in LV and RAA. CCh shortened APD_{90} in RA-EHTs from 221 ± 2.4 to 183 ± 9.4 ms and it did not affect APD_{90} in Ctrl-EHTs (Figure 34A). The CCh-induced hyperpolarization of RMP in RAA was reflected in a

more negative TOP in RA-EHTs (from -69.3±3 to -73.7±2.8), whereas TOP in Ctrl-EHTs was not altered by CCh exposure (Figure 34A; Lemme et al. 2018).
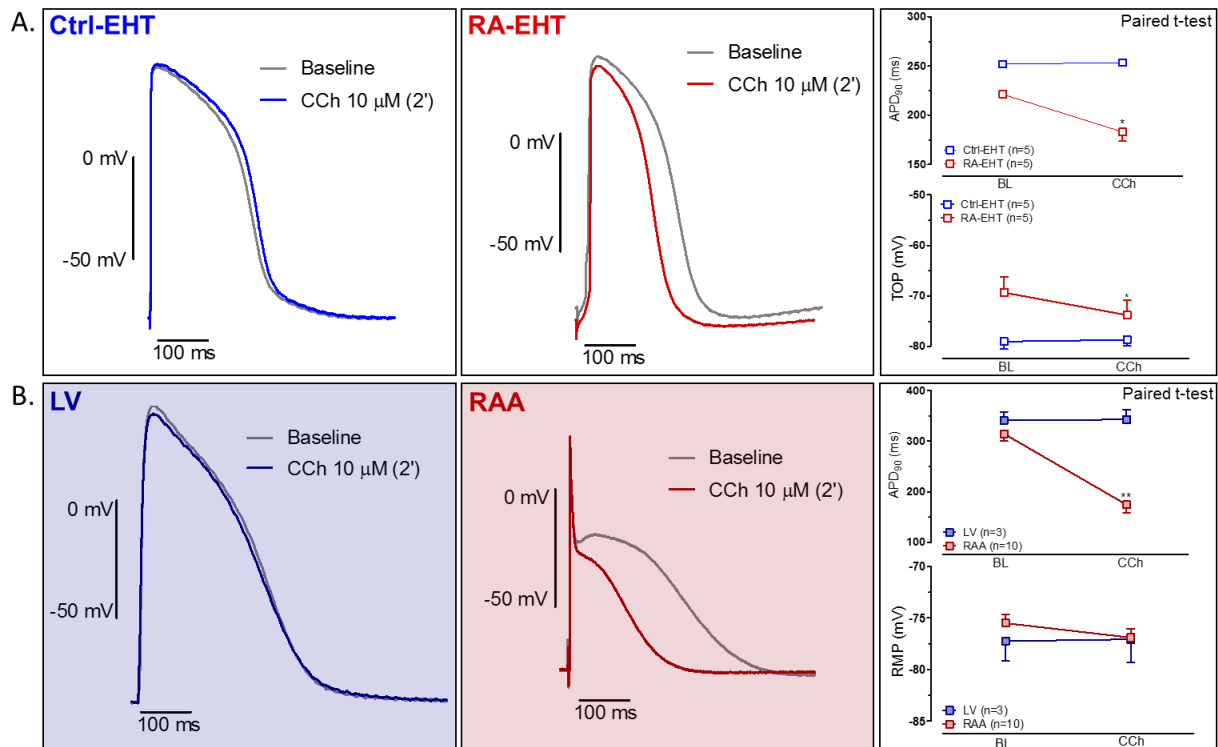
Figure 34: **Effect of retinoic acid (RA)-treatment on pharmacological activation of $I_{K,Ach}$.** Effect of 2 min CCh (10 µmol/L) exposure in (A) Ctrl- and RA-EHTs (n=5 from 3 batches) and in (B) LV (n=3 patients) and RAA (n=10 patients). Representative AP traces (left) and AP parameters (right) show APD_{90} shortening and take-off potential (TOP)/RMP hyperpolarization upon CCh exposure (adapted from Lemme et al. 2018). APs were measured at 37 °C with 2 Hz pacing for EHTs (generated with ERC18 cell line) and 1 Hz pacing for human cardiac tissues. To better visualize CCh effect, y-axes of EHTs and human cardiac tissues were not matched. Data are expressed as mean±SEM (p<0.05, unpaired t-test).

Contraction analysis showed that CCh (10 µmol/L) decreased beating frequency and force of both Ctrl- and RA-EHTs (Figure 35). Time to 50% relaxation increased in RA-EHTs and decreased in Ctrl-EHTs upon CCh exposure (Figure 35). However, CCh (1 µmol/L) decreased contraction force and time to 50% relaxation in RAA (Figure 36).
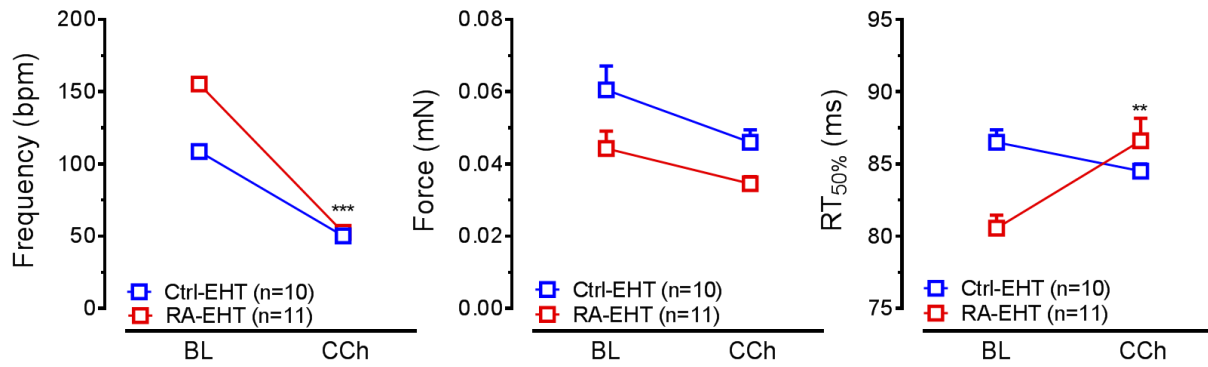
Figure 35: Effect of carbachol (CCh) on Ctrl- and RA-EHT contractility. Spontaneous beating frequency, contractile force and time to 50% relaxation of Ctrl- (n=10 from 3 batches) and RA-EHTs (n=11 from 3 batches) before (baseline, BL) and after CCh (10 µmol/L) exposure ($p < 0.05$, paired t-test; n=12; adapted from Lemme et al. 2018).
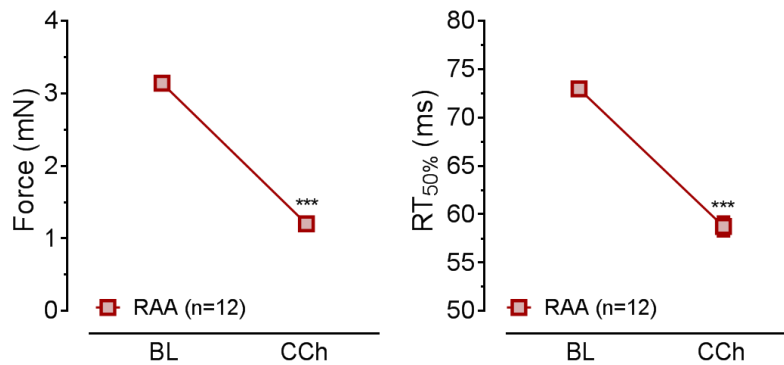
Figure 36: **Effect of carbachol (CCh) on RAA contractility**. Force and time to 50% relaxation in RAA (n=12) measured with organ bath 1 min after CCh (1 µmol/L) exposure ($p < 0.05$, paired t-test; n=12).

3.1.9 RA-treatment induces I_{Kur} responsiveness upon 4-AP exposure

I_{Kur} is another atrial selective potassium current. To test whether RA-treatment could induce functional I_{Kur} in hiPSC-CMs, block of I_{Kur} by a low concentration of 4-AP was tested on Ctrl- and RA-EHTs (Figure 38A). In RAA, 4-AP (50 µmol/L) prolonged APD_{20} (by 194%), reduced APD_{90} (by 11.2%) and increased APA (by 6%). On the other hand, 4-AP did not have any effect on AP in LV even at high concentration of 1 mmol/L (Figure 38B, Wettwer et al. 1994, 2004). RA-EHTs exposed to 4-AP (50 µmol/L) showed APD_{20} prolongation (by 43%), higher APA (by 10.5%), but, in contrast to RAA, they did not exhibit any APD_{90} shortening (Figure 37). AP of Ctrl-EHTs was not altered by 4-AP (50µmol/L) exposure (Figure 38A). These findings demonstrated the presence of I_{Kur} induced by RA-treatment in RA-EHTs (Lemme et al. 2018).

Results
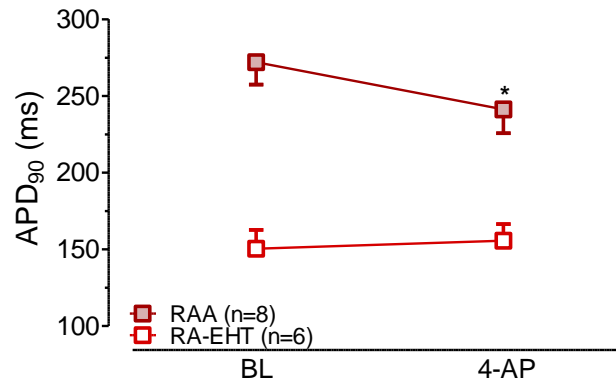
Figure 37: **Comparison of 4-aminopyridine (4-AP) effect on APD$_{90}$ between RAA and RA-EHTs**. Effect of 4-AP (50 µmol/L) on APD$_{90}$ measured with sharp microelectrode in RA-EHTs (n=6 from 3 batches) and RAA (n=8 patients; adapted from Lemme et al. 2018).
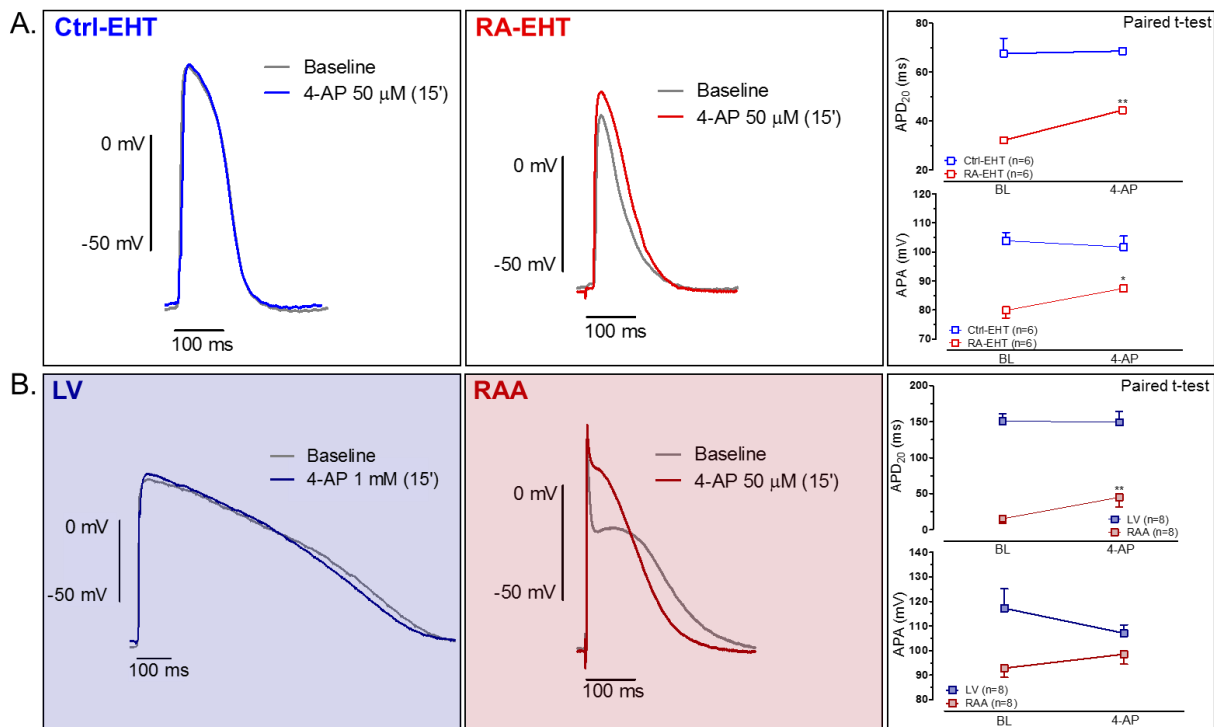
Figure 38: **Effect of retinoic acid (RA)-treatment on AP responsiveness to I$_{Kur}$ blocker 4-AP**. Effect of 15 min 4-AP (50 µmol/L) exposure in (A) Ctrl- and RA-EHTs (n=6 from 3 batches) and in (B) LV (n=8 patients) and RAA (n=8 patients). Representative AP traces (left) and AP parameters (right) show APD$_{20}$ prolongation and APA increase upon 4-AP exposure (adapted from Lemme et al. 2018). APs were measured at 37 °C with 2 Hz pacing for Ctrl-EHTs, 4 Hz pacing for RA-EHTs and 1 Hz pacing for human cardiac tissues. To better visualize the effect of 4-AP, y-axes differ between EHT and human adult cardiac tissues. Data are expressed as mean±SEM (p<0.05, unpaired t-test).

3.2 Effect of chronic optical tachypacing on Ctrl-EHTs

In the second step of the project, the main goal was the generation of a custom-made optogenetic set-up for EHT optical pacing, which could be integrated with the video-optical system for EHT contractility measurements. Moreover, feasibility of ChR2 transduction and optical pacing of

Results

Ctrl-EHTs was tested. Finally, structural and electrical remodeling of Ctrl-EHTs upon chronic optical tachypacing was investigated. The results presented in the following chapter are taken from an unpublished work that I have drafted.

3.2.1 Establishment of the model to perform optical pacing

To allow simultaneous application of blue light and contractility recording of EHTs, we refined a commercially available platform (EHT Technologies GmbH, Hamburg, Hansen et al. 2010; Schaaf et al. 2011). The standard array with 24 white light-emitting diodes (LED) was replaced by a custom-made plate that contained 24 red LEDs (NSPR510CS Nichia, λ=700 nm, Tokushima Japan) and 24 blue LEDs (NSPB510BS Nichia, λ=470 nm, Tokushima Japan). The plate with LEDs was mounted 8 mm below the bottom of the 24-well plate in a way that the red/blue LEDs were positioned left/right of the center of each well and thereby of each EHT suspended in the 24-well-plate above (Figure 39).
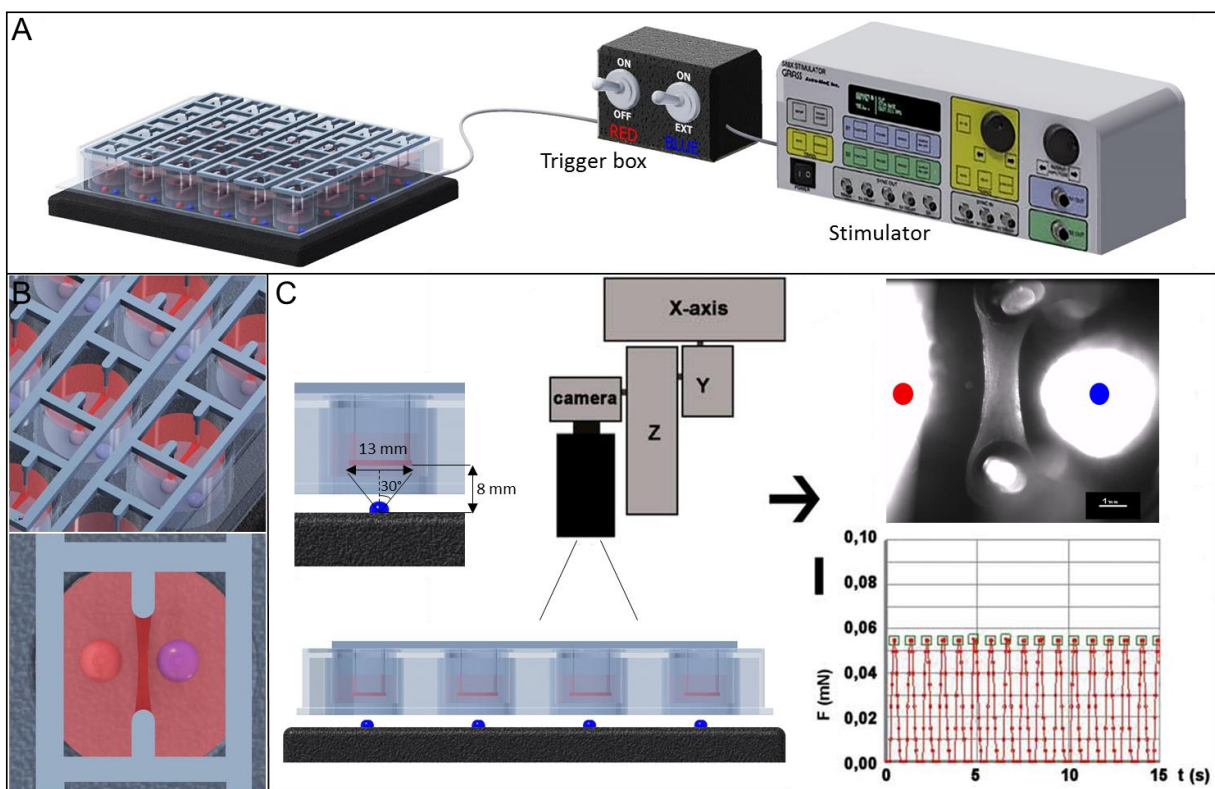
Figure 39: **Custom-made optogenetic set-up for optical pacing of EHTs**. (A) Optogenetic platform containing 24 red and blue light-emitting diodes (LEDs) for mounting a 24-well plate containing ChR2 transduced EHTs (left). This platform can be placed inside the incubator to perform chronic optical tachypacing. Red and blue LEDs were used for visualization and optical pacing of the EHTs, respectively. The platform was controlled by a trigger box, which was connected to an external stimulus generator. The trigger box enabled to switch on/off and to manipulate the intensity of LEDs, while the external stimulus generator was used to define the waveform of the blue light pacing. (B) View from the top of the 24 well plate. EHTs were positioned between the red and blue LEDs. (C) Cross section of the optogenetic platform (left) to visualize the distance between the blue LED and the EHT, as the system to perform video-optical contraction analysis of EHTs (right).

Results

Red LEDs replaced the standard white LEDs, because white light contains also the WL of blue light and therefore it affected EHT behavior (Figure S7). Red LEDs were turned on during contractility recording to allow the camera to visualize the beating EHT. Blue LEDs were used for the optical pacing of ChR2 transduced EHTs. The platform was controlled by a trigger box, which was connected to an external stimulus generator (S88X Dual Output Square Pulse Stimulator, Figure 39). The trigger box enabled to switch on/off and to manipulate the intensity of the red and blue LEDs, while the stimulus generator was used to define the waveform of the blue light pacing. The platform containing the 24-well plate with the EHTs and the bottom plate with the LEDs was placed in a standard cell culture incubator (37 °C, 40% O_2, 7% CO_2) during optical tachypacing of the ChR2 transduced EHTs. Ctrl-EHTs were casted from hiPSC-CMs with a percentage of cTnT-positive cells of 91.6±2.9% (n=3 batches). Ctrl-EHTs were characterized by a repolarization fraction (APD_{90}-APD_{50})/APD_{90} of 0.22±0.01, typical of a ventricular phenotype (n=13 EHTs). Transduction with ChR2-lentivirus of hiPSC-CMs during EHT casting did not principally interfere with Ctrl-EHT generation (>90% of Ctrl-EHTs formed functional contracting tissues, 32/33), but ChR2 transduced Ctrl-EHTs (ChR2-Ctrl-EHTs) showed a later onset of spontaneous beating (7.5±0.2 days vs. 4.8±0.2 days, n=20/2) and a higher spontaneous beating rate (2.3±0.1 Hz vs. 1.2±0.03 Hz, n=20/2) than non-transduced Ctrl-EHTs. ChR2-eYFP transduction efficiency in Ctrl-EHTs was quantified by flow cytometry analysis. At an MOI equal to 0.2, 25.7±0.6% (n=4/2) of cells within the EHT were ChR2-YFP positive (Figure 40A). The photosensitive protein was mainly localized at the sarcolemma of the hiPSC-CMs (Figure 40B). Immunofluorescence analysis showed that ChR2 was still expressed and localized at the sarcolemma at day 28 after transduction (Figure 40B).
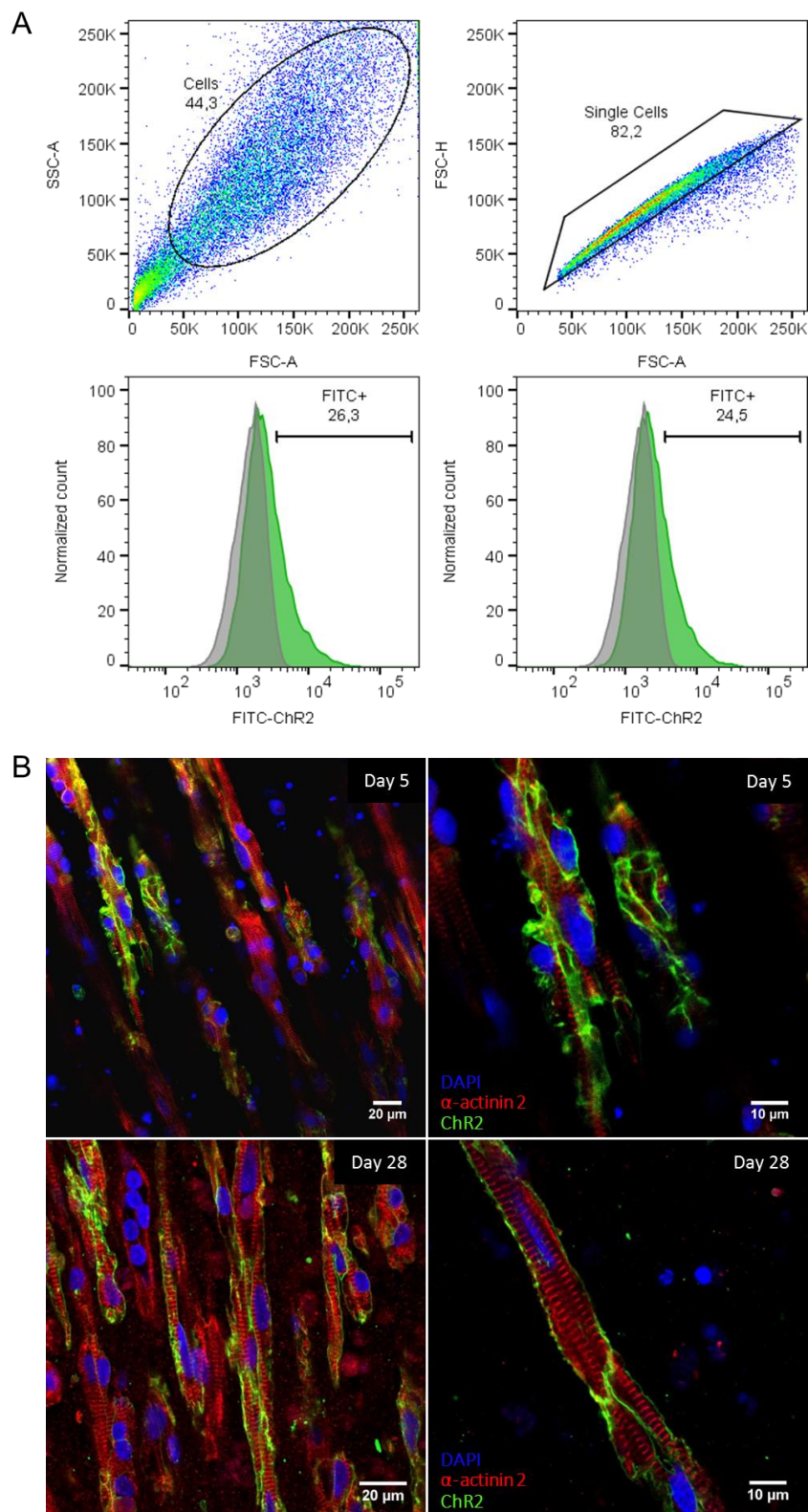
Figure 40: **Efficiency and stability of ChR2 transduction in Ctrl-EHTs**. (A) Representative FACS analyses showing ChR2 transduction efficiency with multiplicity of infection (MOI) of 0.2. ChR2 positive (FITC[+]) hiPSC-CMs were determined by the difference between the green peak (ChR2 transduced Ctrl-EHTs) and the grey peak (non-transduced Ctrl-EHTs). (B) Immunofluorescence of ChR2 (green), α-actinin 2 (red) and DAPI (blue) of ChR2-Ctrl-EHTs at 5 and 28 days after transduction.

Results

3.2.2 ChR2-Ctrl-EHTs follow optical pacing

HiPSC-CMs differentiated under control condition were transduced with ChR2 lentivirus. To test whether these cells were sensitive to blue light, inward current induced by blue light pulses (1 Hz) was measured with voltage patch-clamp. Blue light intensity and duration determined the induction of an inward photocurrent sufficient to trigger an AP (Figure 41).
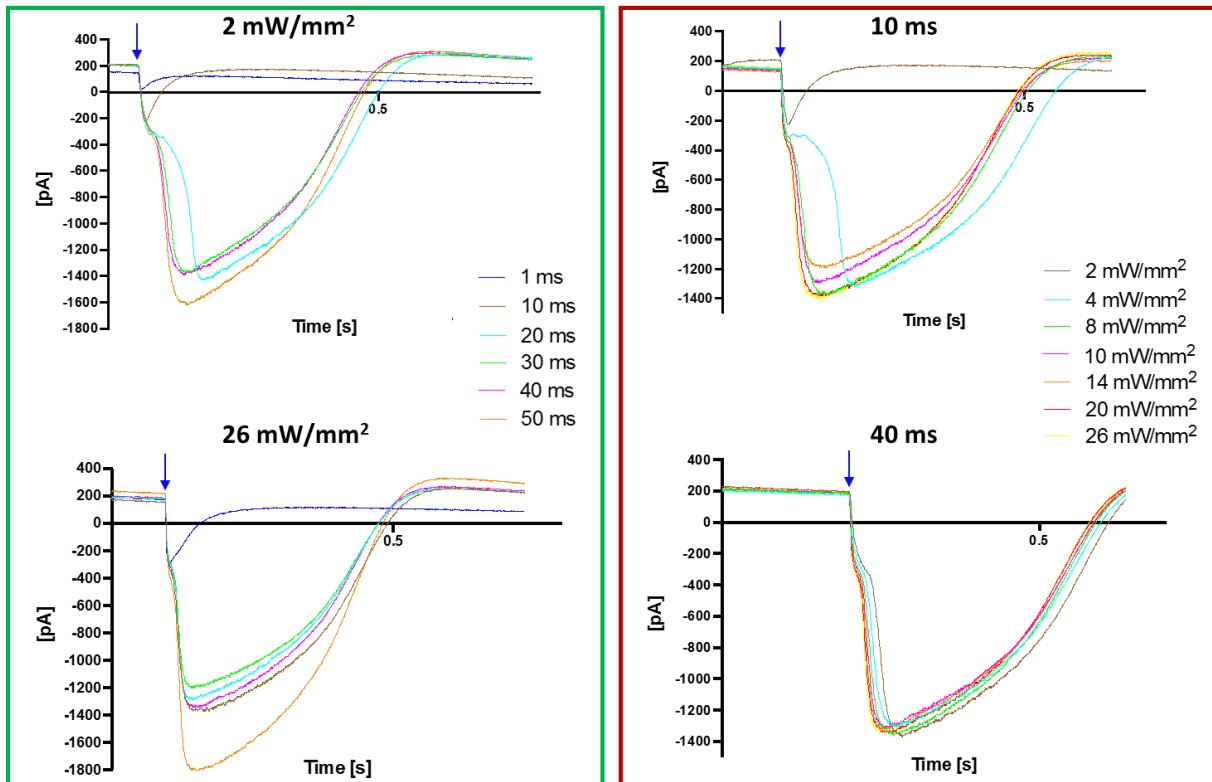
Figure 41: **Effect of blue light pulses on hiPSC-CMs transduced with ChR2**. Voltage patch-clamp of hiPSC-CMs obtained under control condition and transduced with ChR2 lentivirus. Single cells were optically paced using 10 blue light pulses in 10 seconds (blue arrow). Inward current was measured during manipulation of intensity (red box) and duration (green box) of the blue light pulses.

The spontaneous beating rate of non-transduced Ctrl-EHTs was unaffected by light pacing, while ChR2-Ctrl-EHTs followed pacing from 2 to 5 Hz with 30 ms light pulses at 0.3 mW/mm^2 (Figure 42A). ChR2-Ctrl-EHTs showed an increase in force compared to their spontaneous baseline rate (~1.9±0.05 Hz, n=15) until 2 Hz pacing. From 2 to 5 Hz ChR2-Ctrl-EHTs showed an inverse FFR. The force decreased from 0.12±0.004 mN at 2 Hz to 0.07±0.003 mN at 5 Hz (n=15, Figure 42B). As expected, the contraction kinetics accelerated at higher frequencies. TTP$_{-80\%}$ and RT$_{80\%}$ decreased from 95.5±1.4 ms at 2 Hz to 77.3±1.6 ms at 5 Hz and from 116.0±1.6 ms at 2 Hz to 83.5±2.3 ms at 5 Hz, respectively (Figure 42B).
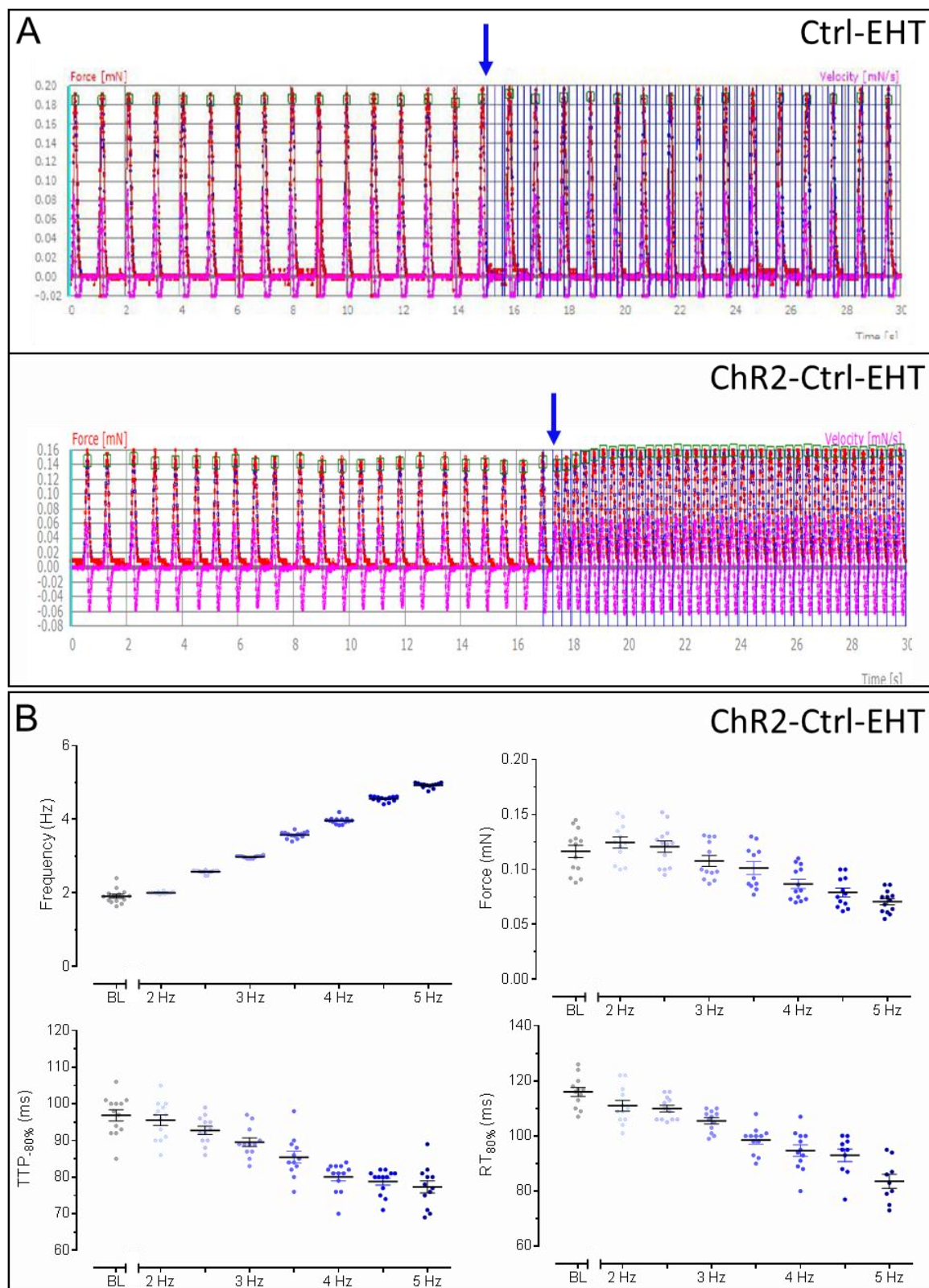
Figure 42: **Optical pacing of ChR2-Ctrl-EHTs**. (A) Original recordings of contractions over time (30 s) in non-transduced and ChR2 transduced Ctrl-EHTs; green squares indicate automatically identified contractions used for calculating total number of beats per minute, force, and times of contraction and relaxation. The graphs showed regular beating pattern under baseline condition and under optical pacing (blue arrow represent the start of optical pacing). (B) Summary of contraction parameters measured in ChR2-Ctrl-EHTs while optical pacing rate was increased acutely. Data are expressed as mean±SEM. n=15/2, with n=number of EHTs/number of batches.

Results

3.2.3 Establishment and validation of the optogenetic platform for chronic tachypacing

To characterize the custom-made optogenetic system, a strength–duration curve of optical pacing threshold was constructed by varying pulse duration (5–100 ms) and light intensity/irradiance (0.003–0.3 mW/mm^2, Figure S8). Continuous light pacing induces desensitization which reduces the consistency of depolarization (Lin 2012). In line with these observations, we found that 7 days of continuous 3 Hz optical tachypacing led to loss of capture in ChR2-Ctrl-EHTs. We therefore chose a repetitive train stimulation protocol at the maximal irradiance achievable with our setup (0.3 mW/mm^2). Light pulse duration and pulse rate were set at 30 ms (Figure S9) and 3 pulses per second respectively, while the train duration and train rate were set at 15 s and 0.03 s. This optical interval pacing characterized by 15 s bursts at 3 Hz separated by 15 s without pacing was applied to ChR2-Ctrl-EHTs for three weeks, starting 7 days after casting.

3.2.4 Chronic optical tachypacing evokes faster contraction kinetics in EHTs

Contractility measurements of optically paced and unpaced ChR2-Ctrl-EHTs were performed at day 28 (Figure 43A).
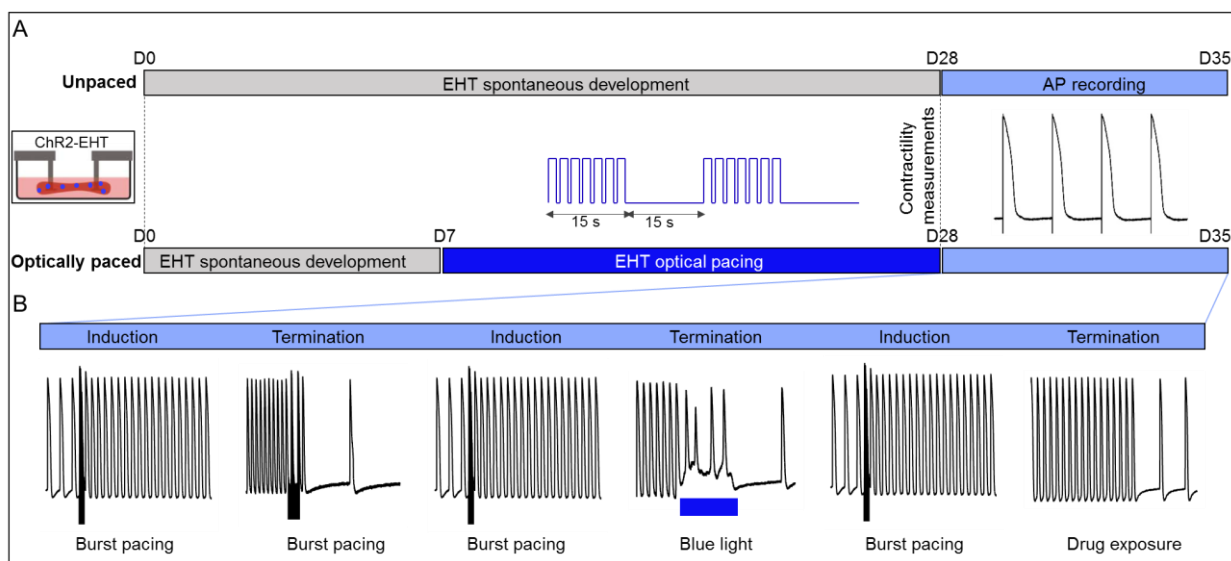
Figure 43: **Protocol to test the effect of chronic tachypacing on ChR2-Ctrl-EHTs**. (A) ChR2-Ctrl-EHTs included in the optically paced group were paced with 15 sec burst at 3 Hz followed by 15 sec without pacing for three weeks. From day 28 functional analysis (contractility and action potential) of optically paced vs. unpaced ChR2-Ctrl-EHTs were performed. (B) Protocol to induce sustained tachycardia episodes by 20 Hz burst pacing and to terminate these episodes with different interventions.

Chronic interval pacing accelerated the contraction kinetics of the EHTs (Figure 44). TTP$_{-80\%}$ decreased from 128.5±1.6 ms to 118.7±1.8 ms (p<0.001, unpaired t-test; n=16/3, Figure 44C).

Results

Chronic optical tachypacing also induced $RT_{80\%}$ shortening from 154.0 ± 5.0 ms to 132.0 ± 2.4 ms (p<0.001, unpaired t-test; n=16/3, Figure 44D). Spontaneous beating rate and force were not affected by the chronic tachypacing (Figure 44A and B).
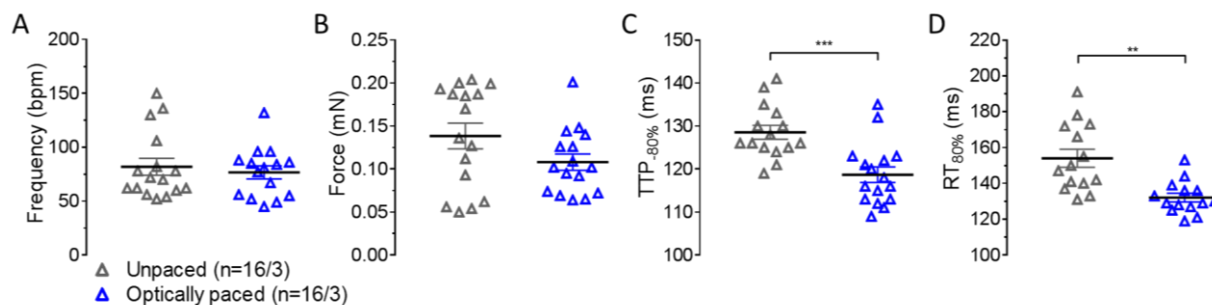
Figure 44: **Effect of chronic tachypacing on contractility of ChR2-Ctrl-EHTs**. (A) Frequency, (B) force, (C) contraction and (D) relaxation time of unpaced and optically paced ChR2-Ctrl-EHTs measured at day 28. Data are expressed as mean±SEM (p<0.05, unpaired t-test; n=16/3, with n=number of EHTs/number of batches).

3.2.5 Chronic optical tachypacing induces APD_{90} shortening

After three weeks of optical interval pacing at 3 Hz, APs of optically paced and unpaced ChR2-Ctrl-EHTs were elicited by field stimulation (2 Hz). APD_{90} of optically paced ChR2-Ctrl-EHTs was shorter than the one of unpaced ChR2-Ctrl-EHTs (176.6 ± 5.6 ms vs. 205.6 ± 6.4 ms, n=16-14/3; p=0.007, unpaired t-test, Figure 45D). In line with the changes in APD, ERP was shorter in the optically paced than in the unpaced ChR2-Ctrl-EHTs (199.6 ± 7 ms vs. 232.5 ± 6 ms, n=16-14/3; p=0.002, unpaired t-test, Figure 45E). The optically paced ChR2-Ctrl-EHTs showed less negative TOP (-66.3 ± 0.7 mV vs. -72.8 ± 1 mV, n=16-14/3; p<0.001, unpaired t-test, Figure 45A), lower upstroke velocity (dV/dt, 38.9 ± 4.2 V/s vs. 89.6 ± 17.8 V/s, n=16-14/3; p<0.001, unpaired t-test, Figure 45B) and smaller APA (89.5 ± 2.2 mV vs. 102.2 ± 3.6 mV, n=16-14/3; p=0.007, unpaired t-test, Figure 45C).
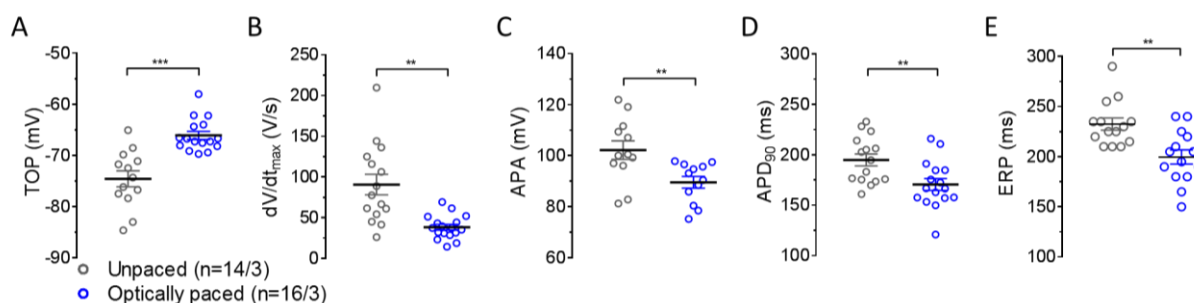
Figure 45: **Effect of chronic tachypacing on APs of ChR2-Ctrl-EHTs**. Mean values for (A) take-off potential (TOP), (B) upstroke velocity (dV/dt_{max}), (C) action potential amplitude (APA), (D) APD_{90} and (E) effective refractory period (ERP) of optically paced vs. unpaced ChR2-Ctrl-EHTs were measured from day 28 to day 35. APs were recorded at 37 °C under electrical field stimulation at 2 Hz. Data are expressed as mean±SEM (p<0.05, unpaired t-test; n=14-16/3, with n=number of EHTs/number of batches).

Results

3.2.6 Chronic optical tachypacing increases tachycardia inducibility

To evaluate whether chronic interval pacing also affected arrhythmia vulnerability, ChR2-Ctrl-EHTs were subjected to a burst pacing protocol (Figure 43B). In accordance to clinical electrophysiology (Clasen et al. 2018), electrical burst pacing (20 Hz, ~ 500 ms) induced a sustained tachycardia episode in some EHTs, during which the EHT beat spontaneously with a shorter cycle length (CL) of 220±9 ms (~4.5 Hz; n=13/3) compared to the basal rate (CL 702±100 ms, ~1.4 Hz, n=13/3, p<0.001, paired t-test). Optically paced EHTs showed burst-induced tachycardia in 64% of cases (11/17), while unpaced EHTs only in 13% (2/15; Figure 46A). Tachycardia episodes did not differ qualitatively between optically paced and unpaced ChR2-Ctrl-EHTs. They showed a mean duration of 29.8±3.4 min (Figure 46B). After induction, the tachycardia accelerated with CL decreasing from 249±3 ms to 230±4 ms (Figure 46C). APD_{90} decreased from 161±15 ms to 144±13 ms, similar to values under normal paced conditions (Figure 46C). Interestingly, after 1.5 min from tachycardia induction the upstroke velocity increased from 43±10 V/s to 58±11 V/s, paralleled by lowering of TOP (Figure 46C). Tachycardia episodes demonstrated a time-dependent decrease in CL variability calculated as the CL standard deviation of consecutive tachycardia beats (Figure 47), which was in parallel to an electrophysiological study with monomorphic tachycardia in humans (Volosin et al. 1991). Stability of tachycardia episodes was confirmed by Poincaré plots (Piskorski and Guzik 2007) of CL, showing the relationship of the RR intervals versus the next RR interval (Figure 47).
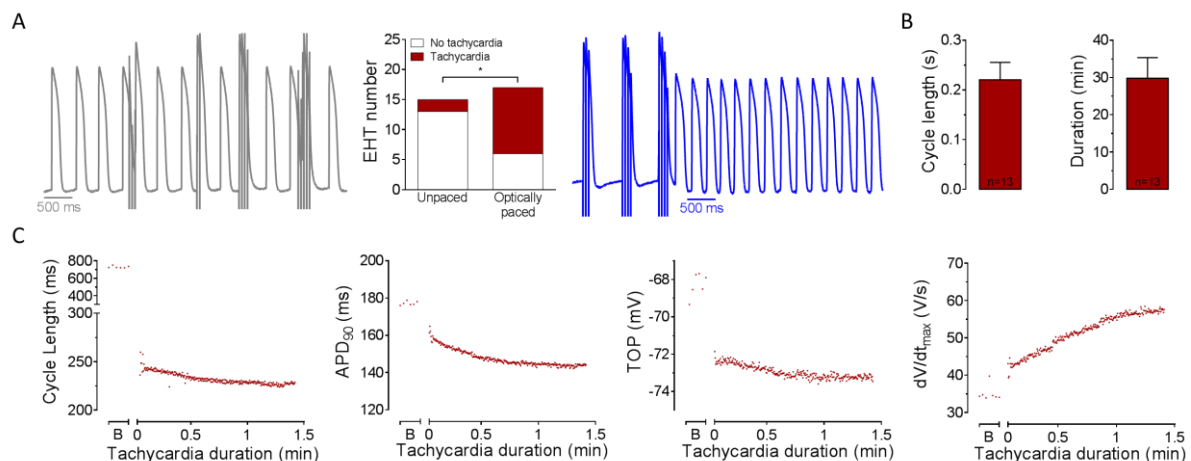
Figure 46: **Effect of chronic tachypacing on tachycardia inducibility**. (A) Fraction of EHTs in which tachycardia could be induced by 20 Hz burst pacing (red) in unpaced and optically paced EHTs (p<0.05, Fisher's exact test; n=15-17/3 EHTs). (B) Mean values of cycle length and duration of tachycardia episodes. Data are expressed as mean±SEM, n=13/3, with n=number of EHTs/number of batches. (C) Averaged cycle length, APD_{90}, upstroke velocity (dV/dt_{max}) and take-off potentials (TOP) obtained from 6 EHTs during spontaneous baseline (B) and during the first min of tachycardia episodes.

74

Results
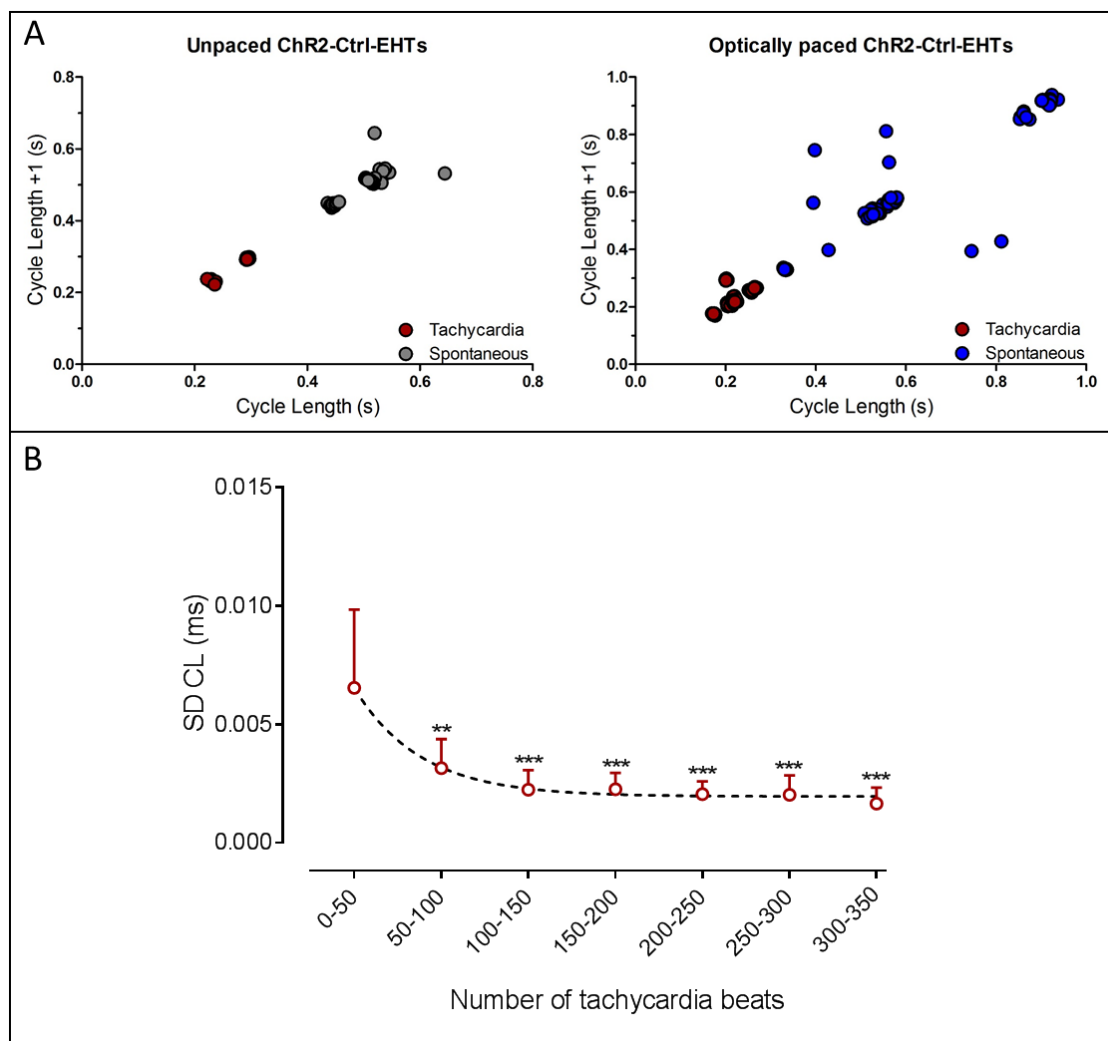
Figure 47: **Cycle length (CL) during tachycardia episodes**. (A) CL poincaré plots of unpaced and optically paced ChR2-Ctrl-EHTs during spontaneous activity and tachycardia. For each EHT, CL of 10 APs obtained from two impalements is shown in the plots. (B) Comparison of tachycardia cycle length variability (Standard Deviation CL) to the duration of tachycardia (measured in number of beats). Cycle length variability decreases significantly after the first 50 beats of tachycardia.

3.2.7 Chronic optical tachypacing induces faster diastolic depolarization

Optically paced ChR2-Ctrl-EHTs showed faster diastolic depolarization (DD), both during spontaneous beating and 2 Hz field stimulation (Figure 48A). The higher DD was weakly correlated to higher AP firing rate (Figure S10). The weakness of correlation was in accordance with unaltered spontaneous contraction rate in chronically paced EHTs (Figure 48A). At 2 Hz field stimulation, DD was 28±4 mV/s (n=17/3) in optically paced ChR2-Ctrl-EHTs compared to 10±3 mV/s in unpaced ChR2-Ctrl-EHTs (n=15/3) (Figure 48B). This was not associated with increased gene expression of pacemaker channels as mRNA-levels of HCN4 after chronic tachypacing were only 57±15% of unpaced. mRNA-levels of SLC8A1 were slightly higher (110±2% of control) and CACNA1C mRNA levels did not differ between the groups (Figure

75

Results

48D). EHTs in which tachycardia could be induced showed higher DD than EHTs in which tachycardia was not inducible (31 ± 4 mV/s vs. 7 ± 3 mV/s, n=13-19/3, p<0.001, unpaired t-test). Of note, EHTs with chronic tachypacing showed 41% higher mRNA-levels of *CASQ2* in comparison to unpaced EHTs (n=6/3, p=0.04, unpaired t-test, Figure 48D), but 49% lower protein level of CASQ2 (n=6/3, p=0.008, unpaired t-test, Figure 49), respectively. This apparently contradictory finding was confirmed by immunofluorescence staining for CASQ2 (Figure 49).
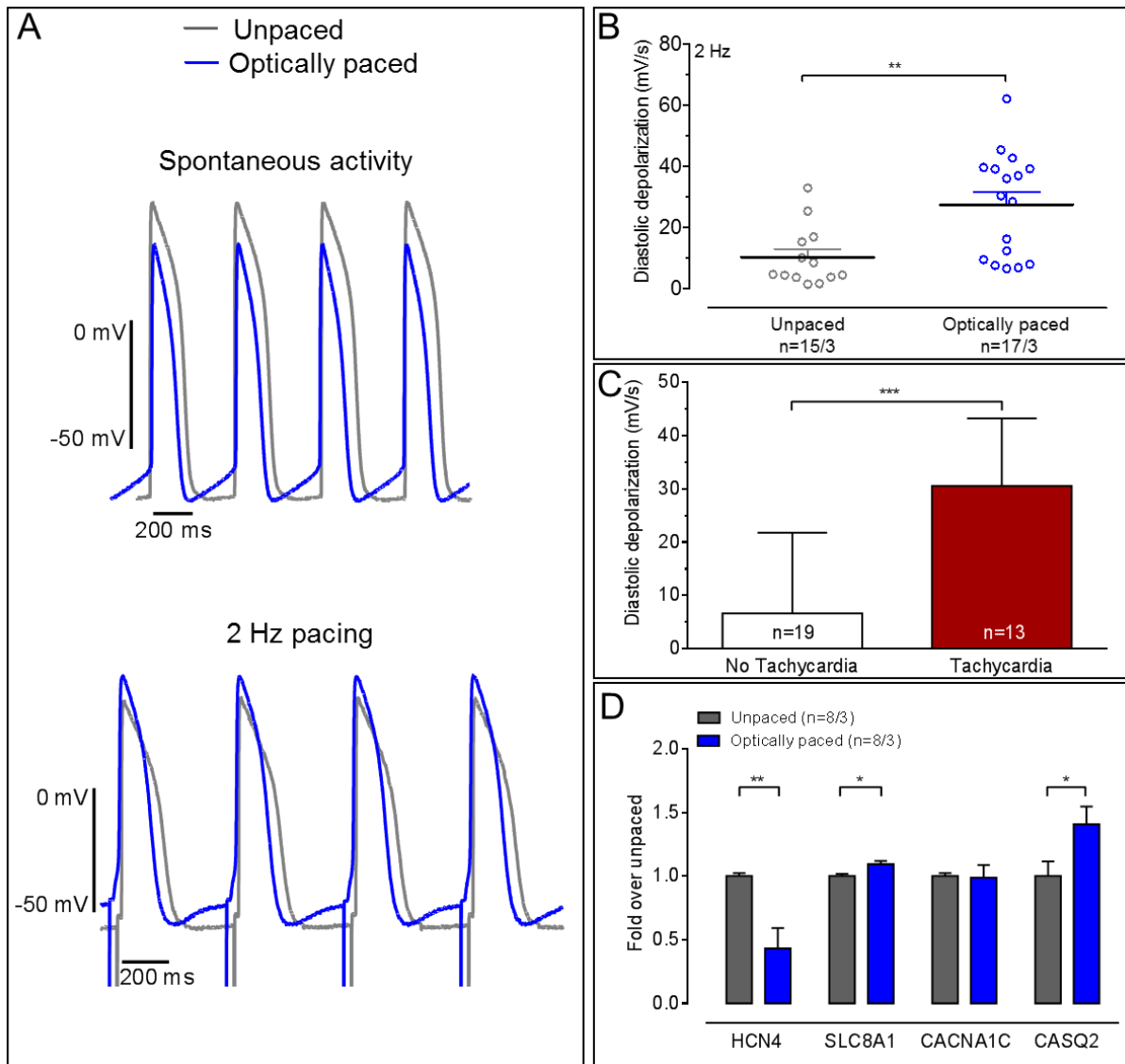
Figure 48: **Effect of chronic tachypacing on diastolic depolarization (DD) of ChR2-Ctrl-EHTs**. (A) Comparison of representative AP traces of optically paced vs. unpaced ChR2-Ctrl-EHTs during spontaneous activity and 2 Hz field stimulation. (B) Quantification of DD of optically paced vs. unpaced ChR2-Ctrl-EHTs at 2 Hz (p<0.05, unpaired t-test; n=15-17/3). (C) Quantification of DD in EHTs where tachycardia could or could not be induced. (p<0.05, unpaired t-test; n=19-13/3). (D) The mRNA levels of HCN4, SLC8A1, CACNA1C and CASQ2 of optically paced and unpaced ChR2-Ctrl-EHTs were determined with the nanoString nCounter Elements technology, normalized to housekeeping genes, and related to the unpaced group (p<0.05, unpaired t-test; n=8/3).
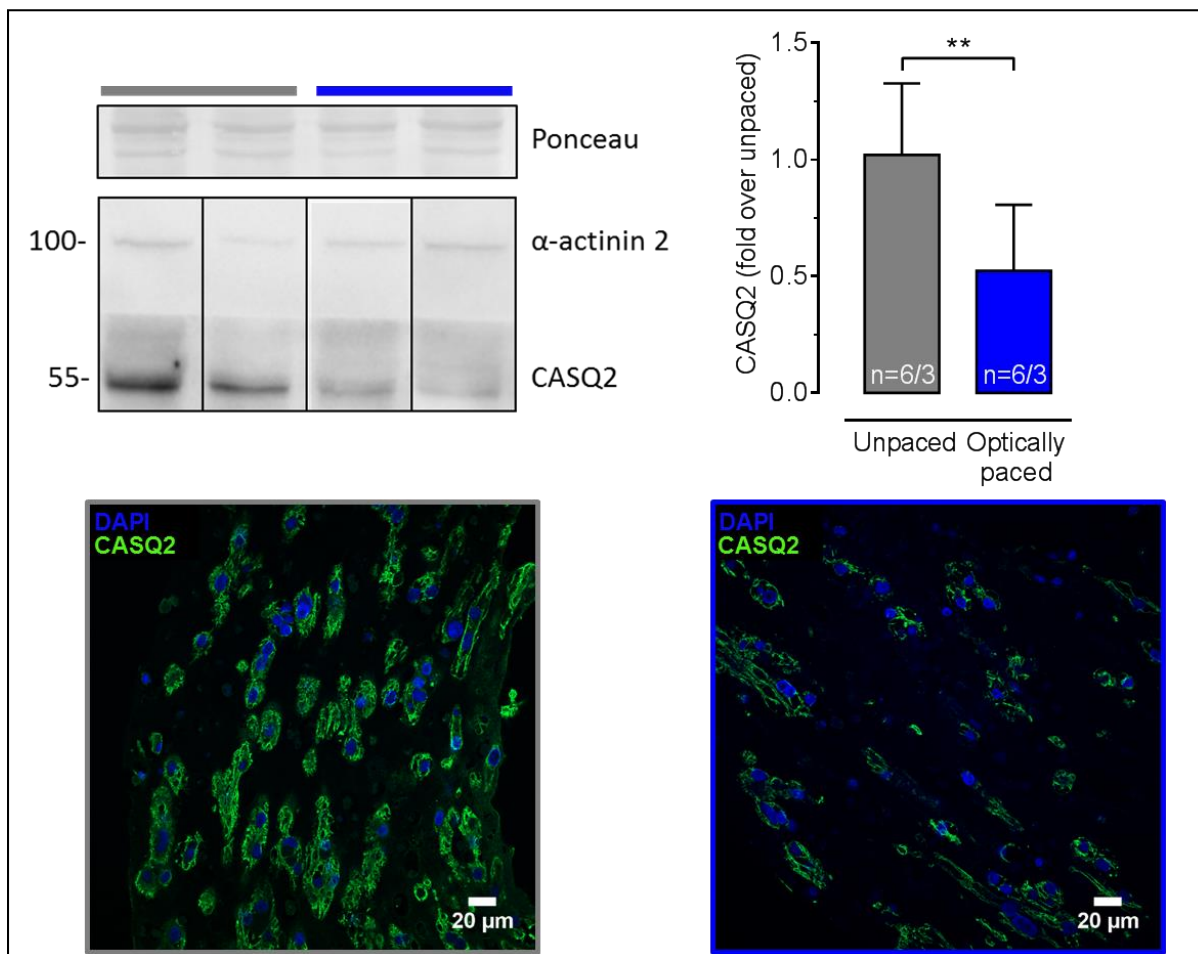
Figure 49: **Effect of chronic tachypacing on CASQ2 in ChR2-Ctrl-EHTs**. Protein level of CASQ2 was detected by western blot and normalized to α-actinin 2 level (p<0.05, unpaired t-test; n=6/3). Immunofluorescence of CASQ2 (green) and DAPI (blue) of optically paced vs. unpaced ChR2-Ctrl-EHTs. Data are expressed as mean±SEM with n=number of EHTs/number of batches.

3.2.8 Flecainide and JTV-519 terminated tachycardia

If tachycardia was inducible in ChR2-Ctrl-EHTs, it was sustained for a mean of 30 min (Figure 46B) and could be re-initiated by another burst pacing for several times. This allowed us to test different interventions to terminate these episodes. Tachycardia was terminated effectively and repeatedly by burst pacing applied by field electrodes (Fisher et al. 1978) or by continuous illumination with blue light (Figure 50). In contrast to the effect on spontaneous beating rate of EHTs (Lemoine et al. 2018), ivabradine exposure (1 µmol/L, 20 min of incubation) did not terminate tachycardias, neither in optically paced ChR2-Ctrl-EHTs, nor in the small number of unpaced ChR2-Ctrl-EHT where tachycardia could be induced. The class Ic antiarrhythmic flecainide (1 µmol/L) terminated tachycardia in 69% of the EHTs after 4.3±1.4 min, the ryanodine receptor-stabilizing drug JTV-519 (1 µmol/L) terminated tachycardia in 46% of the EHTs after 5.5±1.5 min (Figure 50).

Results
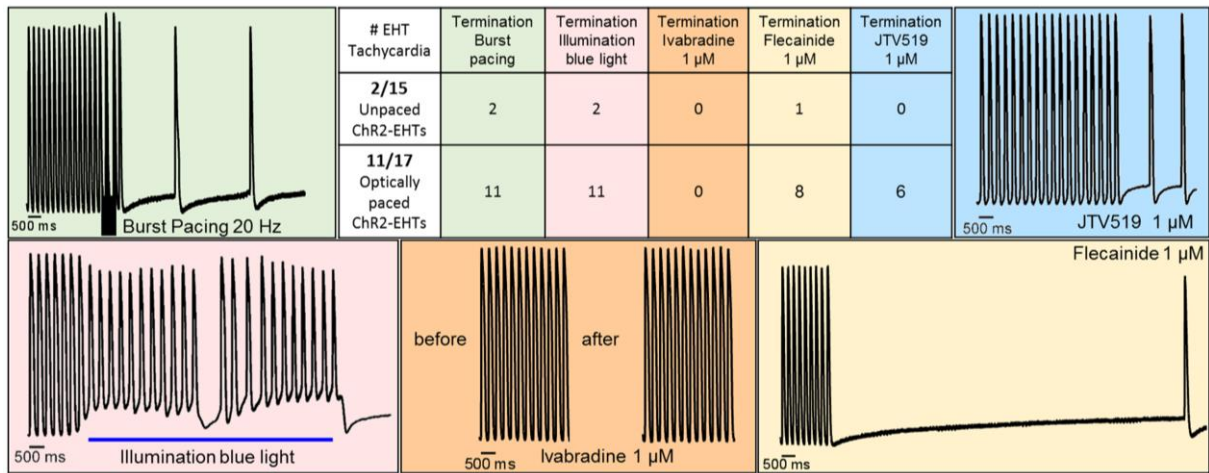
Figure 50: **Termination of tachycardia episodes**. Burst pacing (green box), blue light illumination (pink box) showed maximum tachycardia termination efficiency. Exposure to ivabradine (1 µmol/L) for 15 min could not terminate tachycardia (orange box). Flecainide (1 µmol/L, yellow box) and JTV-519 (1 µmol/L, blue box) showed 69% and 46% efficacy in termination of tachycardia after 15 min exposure, respectively.

3.2.9 Structural remodeling of EHT upon optical tachypacing

Chronic optical tachypacing decreased mRNA-levels of fibrosis markers *ACTA2*, *COL3A1*, *COL1A1* and *FN1* (Figure 51A). The lower mRNA expression of *ACTA2* in optically paced ChR2-Ctrl-EHTs compared to unpaced ChR2-Ctrl-EHTs (Figure 51A) was confirmed on protein level by western blot analysis (Figure 51B) and by immunohistochemistry of α-SMA and collagen type I (Figure 51C). Furthermore, mRNA expression of the pro- and anti-apoptotic markers *BAX* and *BLC2* increased after chronic optical tachypacing (Figure 52). Finally, mRNA expression of hypertrophy and fetal gene program markers did not show significant changes after chronic optical tachypacing (Figure 52).
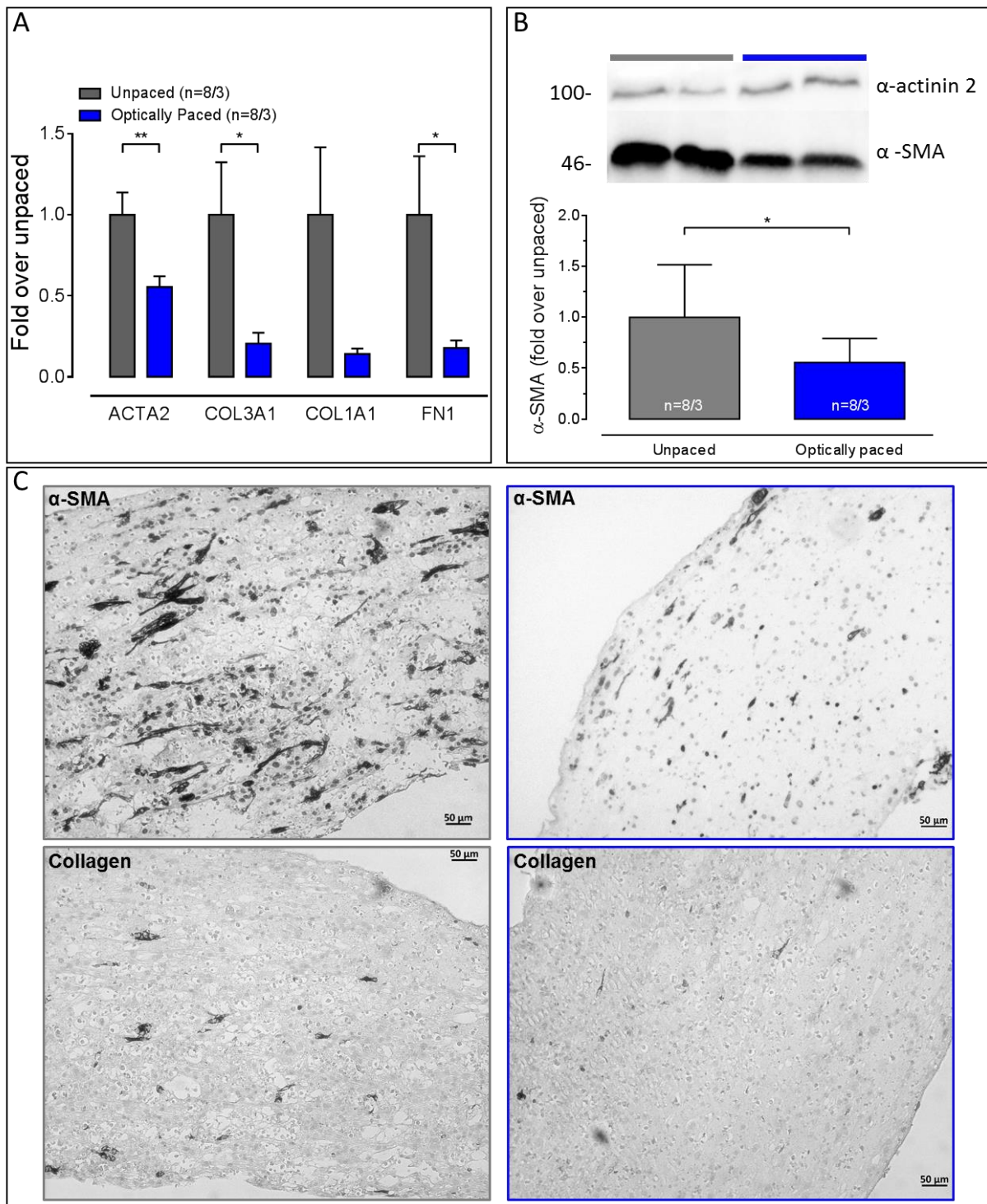
Figure 51: **Effect of chronic tachypacing on fibrosis markers in ChR2-Ctrl-EHTs**. (A) The mRNA levels of fibrosis markers (*ACTA2*, *COL3A1*, *COL1A1* and *FN1*) in optically paced and unpaced ChR2-Ctrl-EHTs were determined with the nanoString nCounter Elements technology, normalized to housekeeping genes, and related to unpaced ChR2-Ctrl-EHTs. (B) Protein levels of α-SMA in optically paced and unpaced ChR2-Ctrl-EHTs, normalized to α-actinin 2 and related to unpaced ChR2-Ctrl-EHT. (C) Immunohistochemistry of α-SMA and collagen type I expression in optically paced and unpaced ChR2-Ctrl-EHTs. Data are expressed as mean±SEM ($p<0.05$, unpaired t-test; n=8/3, with n=number of EHTs/number of batches).
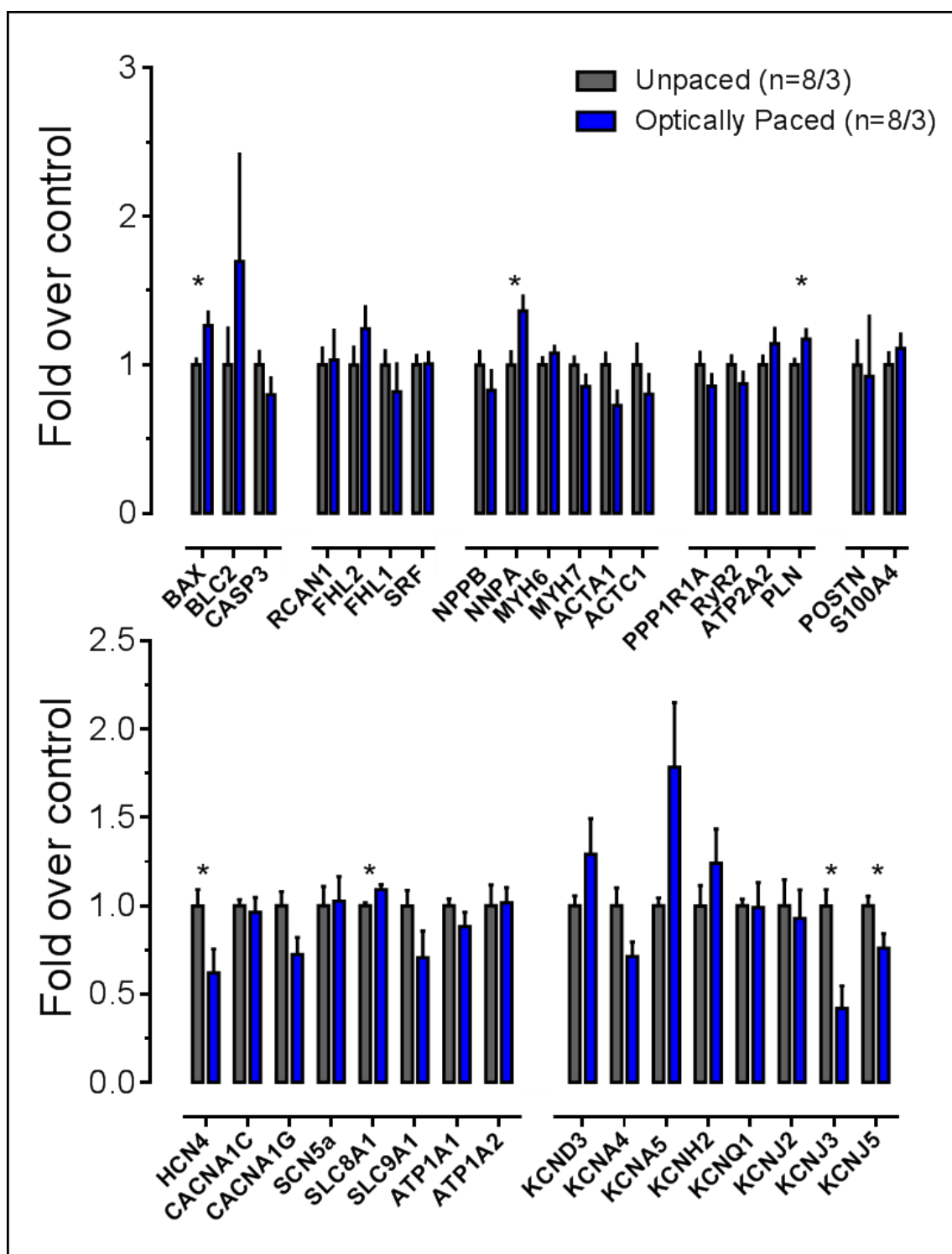
Figure 52: **The mRNA levels of optically paced and unpaced ChR2-Ctrl-EHTs**. Gene expression was determined with the nanoString nCounter Elements technology, normalized to housekeeping genes, and related to unpaced ChR2-Ctrl-EHTs. Data are expressed as mean±SEM (p < 0.05, unpaired t-test; n=8/3, with n=number of EHTs/number of batches).

Results

3.3   Effect of chronic optical tachypacing on RA-EHTs

The final step of the project combined the *in vitro* model of human atrium (RA-EHT described in the chapter 3.1) with chronic optical tachypacing (described in chapter 3.2). Analyses were performed to investigate whether the optical tachypacing could induce any electrical and structural remodeling in RA-EHTs and whether these changes resemble key findings in human AF. The results described in this chapter are preliminary data, which require further investigation.

3.3.1 Chronic optical tachypacing induces faster contraction and higher beating irregularities

ChR2 transduced RA-EHTs were casted using hiPSC-CMs with a percentage of cTnT positive cells equal to 92.3%±3.1% (n=3 batches). RA-EHTs were transduced during casting with ChR2-lentivirus (MOI=0.2). Their atrial-like phenotype was confirmed by a repolarization fraction $(APD_{90}\text{-}APD_{50})/APD_{90}$ equal to 0.38±0.02 (n=13 EHTs). ChR2-RA-EHTs showed a later onset of beating than ChR2-Ctrl-EHTs (10.5±0.3 days vs. 7.5±0.2 days), therefore the start of the optical tachypacing was postponed at day 14 in order to allow all the EHTs to develop a synchronous and coherent contraction (Figure 53). ChR2-RA-EHTs were optically stimulated with the same optogenetic platform and pacing protocol used for ChR2-Ctrl-EHTs described in section 3.2.3 and 3.2.4. The only difference was that ChR2-RA-EHTs could be paced faster than ChR2-Ctrl-EHTs and were therefore paced at 5 Hz instead of 3 Hz. At day 35 the contractions of ChR2-RA-EHTs were measured.
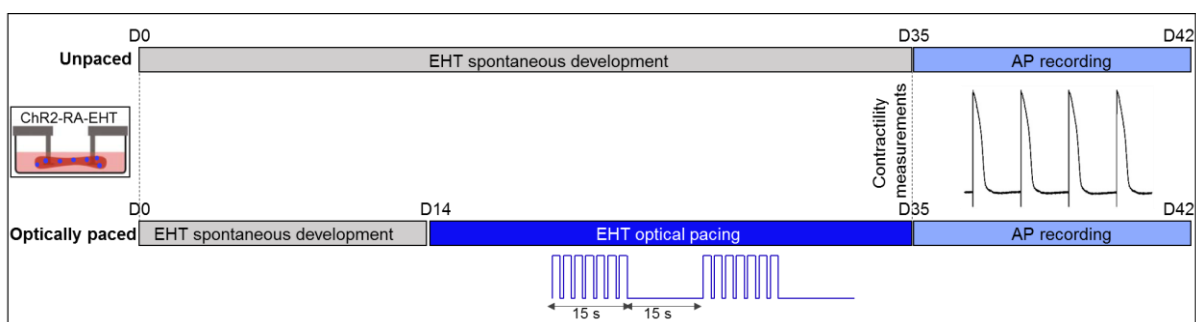
Figure 53: **Protocol to study the effect of chronic optical tachypacing on ChR2-RA-EHTs**. ChR2-RA-EHTs included in the optically paced group were paced with 15 sec burst at 5 Hz followed by 15 sec without pacing for three weeks. From day 35 functional analysis (contractility and action potential) of optically paced vs. unpaced ChR2-RA-EHTs were performed.

Force and contraction kinetic of ChR2-RA-EHTs were measured under 2.5 Hz field stimulation to override spontaneous beating. Chronic intermittent optical tachypacing did not affect force

81

Results

and relaxation time, but it accelerated time to peak compared to unpaced (94.5 ± 2.5 ms vs. 105 ± 4 ms, n=15-13/3; p=0.03, unpaired t-test, Figure 54). Time to peak force of RAA from patients with AF show a tendency to decrease compared to patients with sinus rhythm (Figure S11). Contraction recordings during spontaneous activity of ChR2-RA-ETHs showed that optical tachypacing did not affect the beating frequency (Figure 54D), but it increased the beating irregularity calculated with RR scatter (0.07 ± 0.01 s vs 0.03 ± 0.004 s, n=15-13/3; p=0.008, unpaired t-test, Figure 54E).
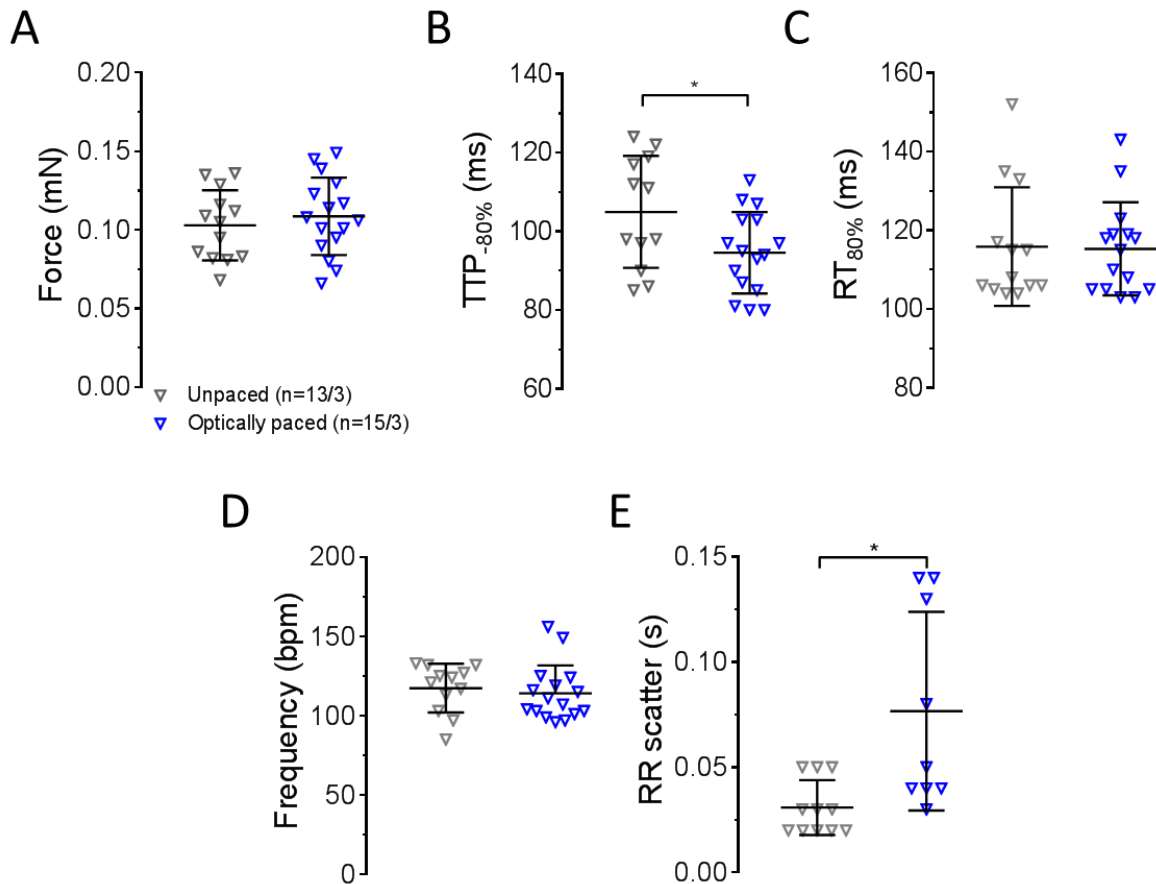
Figure 54: **Effect of chronic optical tachypacing on contractility of ChR2-RA-EHTs**. (A) Force and (B, C) contraction kinetics of unpaced and optically paced ChR2-RA-EHTs. These contraction parameters were calculated under 2.5 Hz field stimulation, while (D) beating frequency (E) and RR scatter during spontaneous activity. Measurements were performed at day 35. Data are expressed as mean±SEM (p<0.05, unpaired t-test; n=13-15/3, with n=number of EHTs/number of batches).

3.3.2 Chronic optical tachypacing induces faster upstroke and CV

After three weeks of optical interval pacing at 5 Hz, APs were measured under 3 Hz field stimulation to override spontaneous beating. Unpaced ChR2-RA-EHTs were used for comparison. Optical pacing did not affect TOP (Figure 55A), APA (Figure 55B), APD$_{90}$ (Figure 55D) and ERP (Figure 55E) of the APs. On the other hand, optically paced ChR2-RA-EHTs

Results

showed faster upstroke velocity than unpaced EHTs (138±15 V/s vs. 87±11 V/s, n=15-13/3; p=0.018, unpaired t-test, Figure 55C). In line with this finding, CV in optically paced EHTs was also faster compared to unpaced EHTs (94±16 cm/s vs. 49±8 cm/s, n=15-13/3; p=0.03, unpaired t-test, Figure 55F).
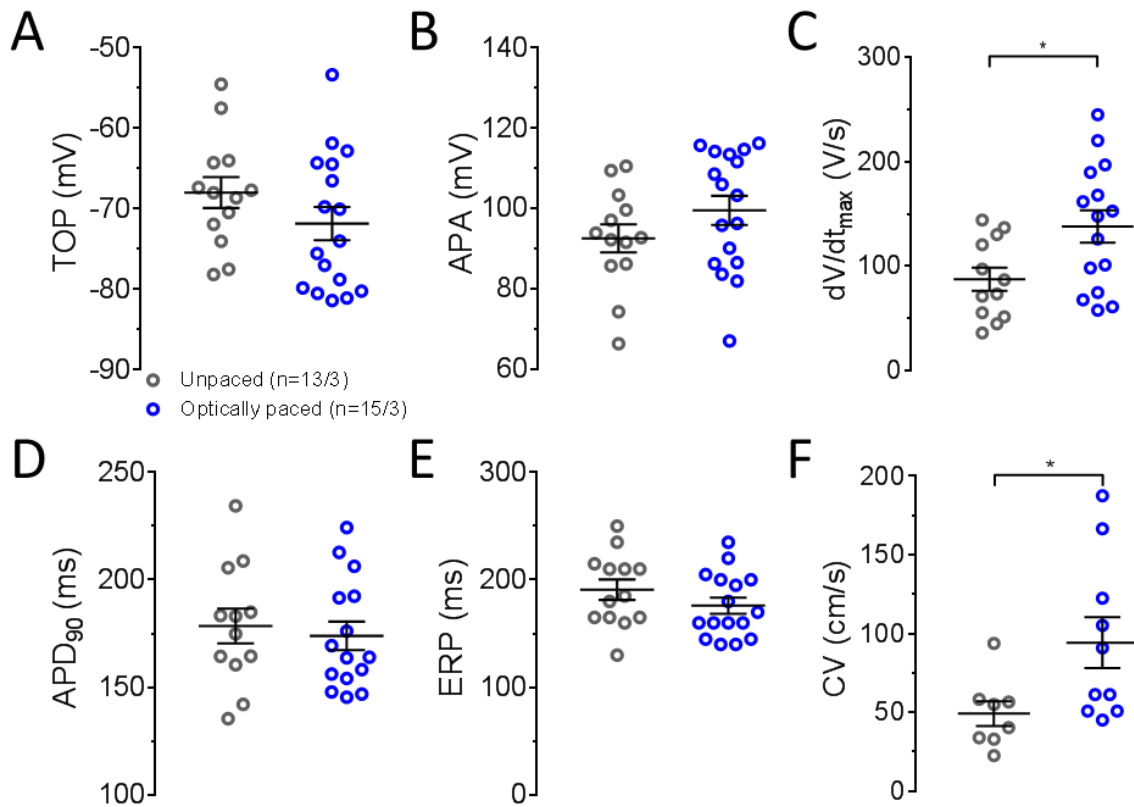
Figure 55: **Effect of chronic optical tachypacing on APs of ChR2-RA-EHT**. Mean values for (A) take-off potential (TOP), (B) action potential amplitude (APA), (C) upstroke velocity (dV/dt$_{max}$), (D) APD$_{90}$, (E) effective refractory period (ERP) and (F) conduction velocity (CV) of optically paced vs. unpaced ChR2-RA-EHTs were measured from day 35 to day 42. APs were recorded at 37 °C under electrical field stimulation at 3 Hz. Data are expressed as mean±SEM (p<0.05, unpaired t-test; n=13-15/3, with n=number of EHTs/number of batches).

3.3.3 Chronic optical tachypacing increases irregular beating rate of APs

Optically paced ChR2-RA-EHTs showed higher beating rate variability than unpaced EHTs (Figure 56). Rate variability was assessed with Poincaré plots of AP cycle length (see also Figure 18). Poincaré plots of optically paced ChR2-RA-EHTs showed higher dispersion than unpaced EHTs (Figure 57A). The higher dispersion was quantified by calculation of Poincaré plot indexes (SD1 and SD2, Figure 57B). SD1 and SD2 were higher in optically paced ChR2-RA-EHTs than in unpaced ChR2-RA-EHTs (0.11±0.013 s vs 0.06±0.006 s and 0.15±0.014 s vs 0.08±0.009 s, p<0.05, unpaired t-test; n=12-13/3).

Unpaced

0 mV

-50 mV

500 ms

Optically paced

0 mV

-50 mV

500 ms
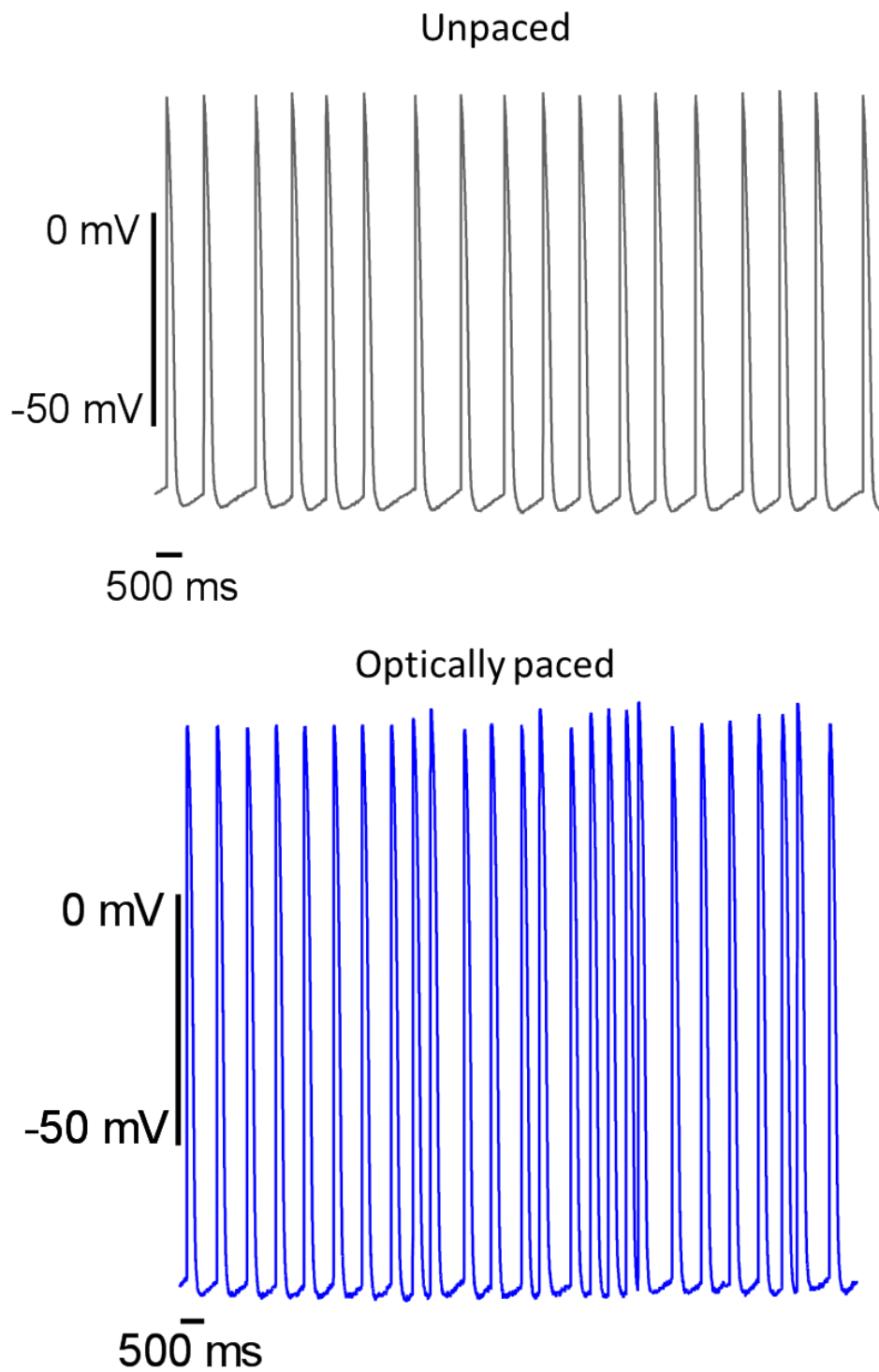
Figure 56: **Effect of chronic optical tachypacing on AP traces of ChR2-RA-EHTs**. Representative AP traces of optically paced and unpaced ChR2-RA-EHTs measured with sharp microelectrode during spontaneous beating.

Results
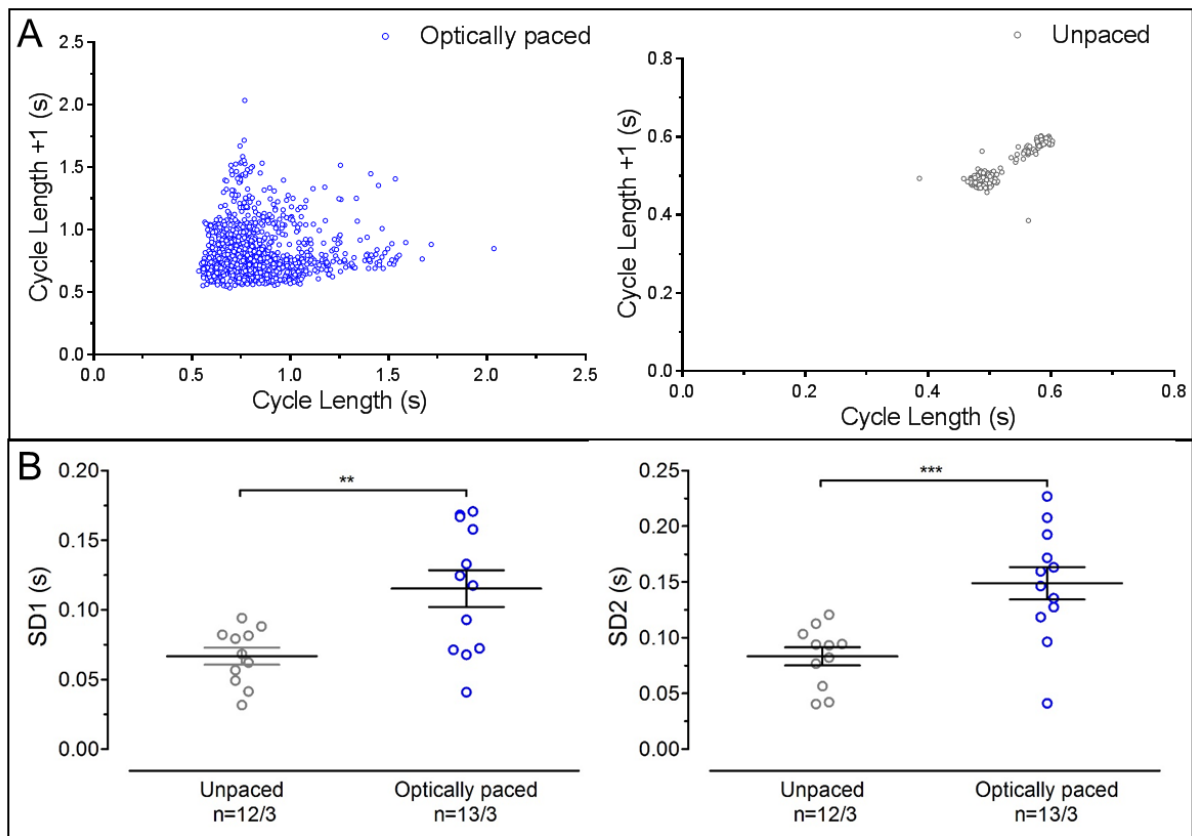
Figure 57: **Effect of chronic optical tachypacing on cycle length variability in ChR2-RA-EHTs**. (A) Representative Poincaré plots of cycle length of optically paced (blue) and unpaced (grey) ChR2-RA-EHTs. (B) Quantification of Poincaré plots: short term (SD1) and long term (SD2) standard deviation. Data are expressed as mean±SEM (p<0.05, unpaired t-test; n=12-13/3, with n=number of EHTs/number of batches).

During AP recordings, tachycardia induction through burst pacing was attempted in ChR2-RA-EHTs, but in contrast to ChR2-Ctrl-EHTs tachycardia was not stable and spontaneously reverted after few seconds.

3.3.4 Changes in mRNA expression and protein levels after chronic optical tachypacing in ChR2-RA-EHTs

Chronic optical tachypacing decreased significantly mRNA-levels of *POSTN* and *RyR2*, but upregulated *KCNJ12* and *NPPB* expression (Figure 58). Since chronic optical tachypacing of ChR2-Ctrl-EHTs primarily affected CASQ2, protein level of CASQ2 in optically paced ChR2-RA-EHTs was analyzed, but no change could be detected (Figure 59). Expression of fibrosis and apoptosis markers was not significantly altered after chronic optical tachypacing (Figure 58).
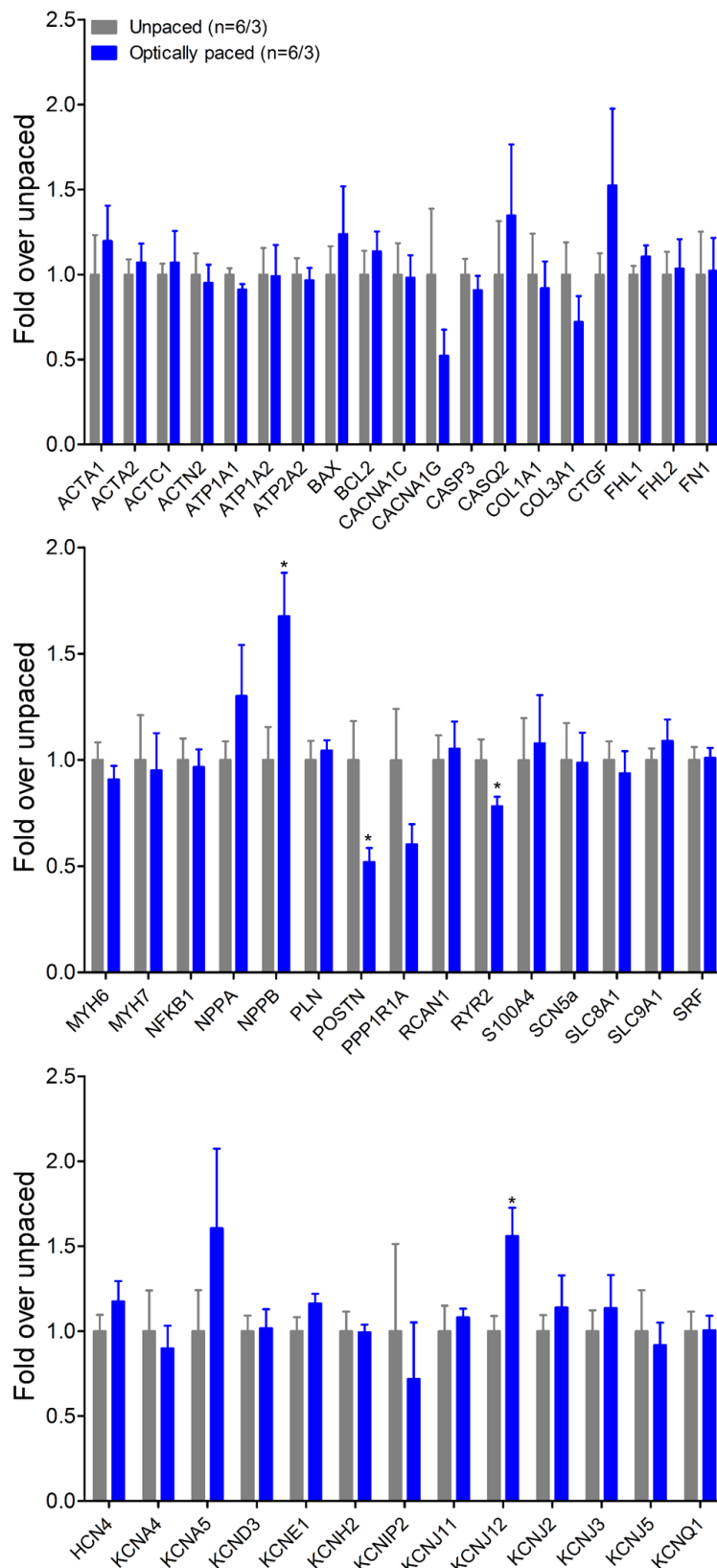
Figure 58: **Effect of chronic optical tachypacing on mRNA expression in ChR2-RA-EHTs**. Fold change of mRNA levels of optically paced and unpaced ChR2-RA-EHTs. All values were normalized to the housekeeping genes and expressed as fold change over unpaced ChR2-RA-EHTs. Data are expressed as mean±SEM ($p < 0.05$, unpaired t-test; n=6/3, with n=number of EHTs/number of batches).

Results
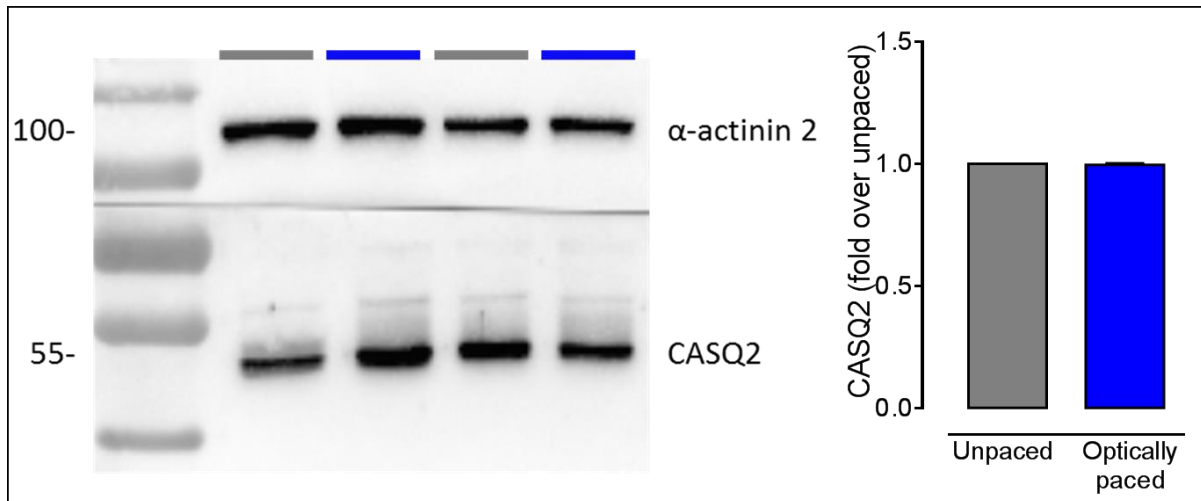
Figure 59: **Protein level of CASQ2 after chronic optical tachypacing in ChR2-RA-EHTs**. (Left) Western blot analysis of CASQ2 and α-actinin 2 total protein levels in unpaced and optically paced ChR2-RA-EHTs. (Right) CASQ2 protein level quantification normalized to the housekeeping gene α-actinin 2 and expressed as fold change over unpaced ChR2-RA-EHTs. Data are expressed as mean (n=2 EHTs).

3.3.5 Effect of chronic optical tachypacing on glycogen accumulation

To test whether the optical tachypacing increased glycogen content histological sections of ChR2-RA-EHTs were processed with PAS. Glycogen accumulation did not differ between optically paced and unpaced ChR2-RA-EHTs (Figure 60).
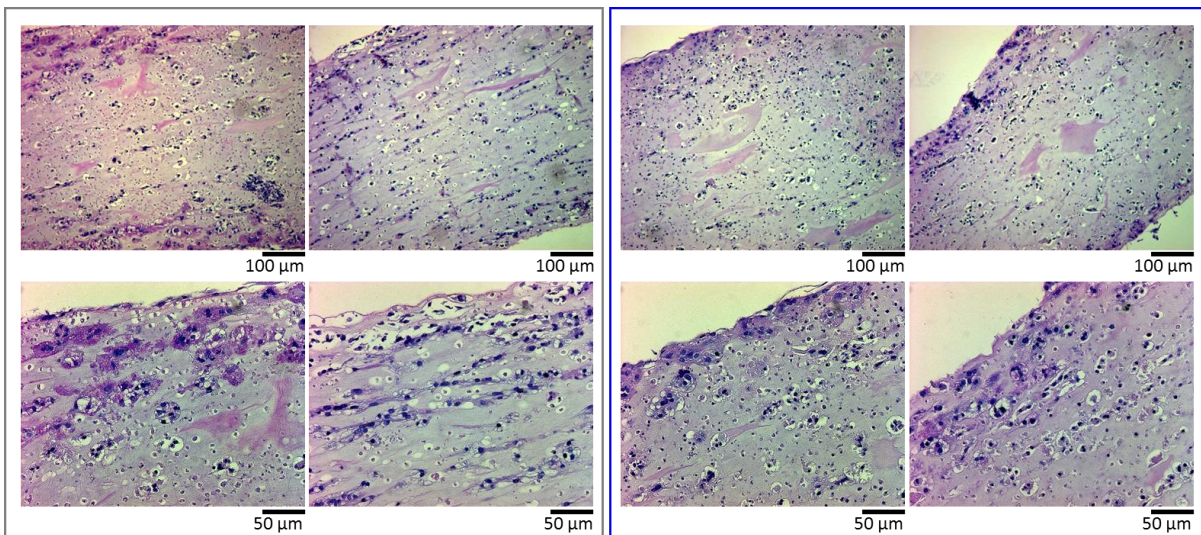
Figure 60: **Glycogen accumulation after chronic optical tachypacing in ChR2-RA-EHTs**. Glycogen storage of optically paced (right blue box) and unpaced (left grey box) histological sections of ChR2-RA-EHTs was processed with Periodic acid-Schiff (PAS) staining. Glycogen storage and nuclei are magenta and blue colored, respectively.

4. Discussion

The project aimed at generating an *in vitro* model of human atrium to test whether it is possible to induce classic signs of AF remodeling by chronic rapid pacing. To this end, atrial-like EHTs (RA-EHTs) were generated and compared to ventricular-like EHTs (Ctrl-EHTs). An optogenetic set-up was designed to perform chronic optical tachypacing of Ctrl- and RA-EHTs. Electrical remodeling induced by chronic optical tachypacing resulted in higher tachycardia inducibility in Ctrl-EHTs and greater beating irregularities in RA-EHTs.

4.1 Generation and characterization of atrial-like vs. ventricular-like EHTs (RA-EHTs vs. Ctrl-EHTs)

The aim of this part of the project was to generate a 3D model of human atrial heart muscle. RA-based protocol was used to differentiate atrial-like cells from hiPSC. Then 3D muscle strips were casted using the established fibrin-based EHT technique and directly compared to native human heart muscles.

RA-treated hiPSC-CMs could form contracting EHTs characterized by faster spontaneous beating rate compared to Ctrl-EHTs. Moreover, RA-EHTs exhibited lower force, faster contraction and relaxation kinetics, shorter APD_{90}, higher repolarization fraction and responsiveness to atrial-selective drugs compared to Ctrl-EHTs. These results suggest that RA-treatment during hiPSC-CM differentiation not only favor atrial specification on a molecular level, but also on a functional level.

4.1.1 Atrial gene expression induced by RA-treatment is higher in EHT than in ML

Expression analysis confirmed recent findings in hiPSC and hESC where RA-treatment induced upregulation and downregulation of atrial (*COUPTFI, COUPTFII, PITX2, ANP, MLC2A* and *SLN*) and ventricular specific genes (*IRX4* and *MLC2V*), respectively (Zhang et al. 2011; Wu et al. 2013; Josowitz et al. 2014; Devalla et al. 2015; Chen et al. 2017; Jee Hoon Lee et al. 2017; Cyganek et al. 2018). In this project, the EHT technology which promotes hESC- and hiPSC-CMs maturation (Besser et al., 2018; Fong et al., 2016; Mannhardt et al., 2016; Nunes et al., 2013; Ulmer et al., 2018; Uzun et al., 2016; Zhang et al., 2013) was used for 3D culture of Ctrl- and RA-treated hiPSC-CMs. Interestingly, expression of chamber specific genes was enhanced in EHT compared to ML. In fact, expression of more than 50% of the atrial specific genes measured was higher in 3D culture compared to 2D (Figure 23). In line with this finding, the

Discussion

enrichment of MLC2A^{+} CMs over MLC2V^{+} CMs upon RA-treatment was higher in EHT than in ML (Figure 27 and Figure 28). MLC2A and MLC2V distribution in RA- and Ctrl-EHTs reflects the difference observed in native human atrial and ventricular tissues (Figure 28). These data suggest that the combination of RA-treatment and 3D culture promotes atrial specification of hiPSC-CMs (Lemme et al. 2018).

4.1.2 Contractility of RA-EHTs resembles contractions of human atrial tissue

Previous studies have shown that contractile force per cross-sectional area in human EHTs ranges from 0.1 to 20 mN/mm^2 and absolute force ranges from 0.08 to 1.5 mN (Tulloch et al. 2011; Jackman et al. 2016) indicating the importance of 3D construct diameter for force development (Weinberger et al. 2017). In thin muscle strips of human heart, force values range from 40 to 80 mN/mm^2 (Van Der Velden et al. 1998). This discrepancy can be explained by the fact that the cross sectional area of most EHTs is not fully comprised of CMs, but it is also occupied by ECM and non-myocytes. Apart from the lower density of CMs, the lower force developed in EHTs may be also related to the lower sarcomere volume fraction and the general lower level of hiPSC-CM maturation (Zimmermann et al. 2006; Hirt et al. 2014a; Weinberger et al. 2017).

Atrial specific myosin is characterized by higher cross-bridge cycling rate than ventricular myosin. Developed force is inversely dependent on cross-bridge kinetics (Morano et al. 1991). Therefore, atrial myocardium shows lower Ca^{2+} sensitivity and lower tension generation compared to ventricular myocardium (Morano et al. 1991). In fact, human atrial skinned fibers exhibited two times lower Ca^{2+} sensitivity and force per cross-sectional area than ventricular skinned fibers (Ruf et al. 1998; Piroddi et al. 2007; Ng et al. 2010). In accordance with these data, RA-EHTs developed two times lower force than Ctrl-EHTs (Figure 30B). Differences in Ca^{2+} sensitivity due to different myosin expression in atrial and ventricular myocardium might influence the FFR. Both atrial and ventricular myocardium show a positive FFR, an increase in frequency translates into an increase in force of contraction (Schwinger et al. 1993). However, the degree of the increase in force upon increase in frequency was significantly lower in atrial than in ventricular myocardium (Schwinger et al. 1993). In contrast, Ctrl- and RA-EHTs both showed a similarly positive FFR until 1.8 Hz stimulation and a negative FFR at higher frequencies (Figure 29).

Contraction and relaxation kinetics are faster in human atrial myofibrils compared to ventricular myofibrils, probably due to the faster cross-bridge cycling rate (Piroddi et al. 2007; Ng et al.

Discussion

2010). This difference in contraction kinetics could be related to the fact that atrial light chain 1 has faster cross-bridge kinetics than ventricular light chain 1 (Lowey et al. 1993; Morano et al. 1996; Ng et al. 2010). In fact, isometric contractions of human atrial myocardium showed two time faster shortening velocity compared to ventricular myocardium (Ng et al. 2010; Molenaar et al. 2013; Berk et al. 2016). Therefore, shorter TTP and RT in human atrial myocardium compared to ventricular myocardium was in line with 47% shorter $TTP_{-50\%}$ and 35% shorter $RT_{50\%}$ in RA-EHTs compared to Ctrl-EHTs (Figure 30). Ctrl- and RA-MLs showed qualitatively similar differences in contraction kinetics, but these differences were smaller in ML than in EHTs (Figure 30). Faster contraction kinetics of RA-EHTs compared to Ctrl-EHTs might be due to different expression of myosin light chain isoforms (Figure 28) or different levels of sarcomere maturation (Figure 26).

It was reported that not only contraction and relaxation processes are faster in atrial than ventricular tissue, but also calcium transients are shorter in human atrial compared to ventricular trabeculae (Maier et al. 2000). Faster calcium transients in the atrial tissue might be associated with higher calcium uptake from the SR and faster calcium removal from the cytosol. These observations are consistent with faster calcium transients in RA-EHTs compared to Ctrl-EHTs (Figure 31). Moreover, a recent study demonstrated that RA-treatment of hiPSC-CMs increases the rate of Ca^{2+} uptake and release, thus generating atrial-like myocytes characterized by Ca^{2+} handling comparable to adult atrial myocardium (Argenziano et al. 2018). This finding is particularly relevant to model AF linked to calcium channel mutations.

4.1.3 RA-EHTs display atrial-like AP

RA-EHTs showed a faster spontaneous beating rate than Ctrl-EHTs (Figure 30). It is difficult to compare this finding with human adult cardiac muscle, because, in contrast to hiPSC-CMs, ventricular and atrial tissues do not show automaticity. The difference in basal rate might be explained with differential ion channel expression between Ctrl- and RA-EHTs. RA-treatment affected EHT electrophysiology. In fact, RA-EHTs showed a less negative TOP than Ctrl-EHTs (-70 ± 1.1 mV vs. -76 ± 1.5 mV, Figure S6), reflecting a similar difference in RMP between RAA and LV (-74.0 ± 0.5 mV vs. -78.5 ± 1.0 mV; Burashnikov et al. 2008). The less negative TOP in RA-EHTs translates into a lower upstroke velocity compared to Ctrl-EHTs (97.6 ± 2.4 V/s vs. 207.6 ± 10.6 V/s, Figure S6). TOP is in the steep phase of the steady-state inactivation curve of sodium channels, where small changes in TOP determine large difference of sodium channel availability, which in turn affects upstroke velocity (Skibsbye et al. 2016; Lemoine et al. 2017).

Discussion

As previously shown, EHTs casted from hiPSC-CMs showed shorter APD_{90} than human heart tissue (Horváth et al. 2018). RA-treatment induced an additional shortening of APD_{90} (Figure 32). The difference in APD was larger between RA- and Ctrl-EHTs than between RAA and LV. A shorter APD_{90} determines a shorter ERP, which in turn could facilitate induction of tachyarrhythmias. This result may represent an advantage to test new antiarrhythmic drugs.

As previously demonstrated (Du et al. 2015; Horváth et al. 2018), repolarization fraction could discriminate between atrial and ventricular APs. As observed in RAA and LV (Horváth et al. 2018), the repolarization fraction of Ctrl- and RA-EHTs did not overlap (Figure 32 and Figure S4), suggesting a marked effect of RA-treatment on the repolarization phase of APs. However, the AP shape of RA-EHTs did not fully resemble AP from atrial tissue, due to the lack of the steep initial repolarization phase resulting in the spike and dome phenomenon typical for human RAA. In fact, RA-EHTs displayed a triangular AP similar to patients in persistent AF. The different repolarization phase could underlie a low contribution of I_{to} and I_{Kur} in RA-EHTs.

4.1.4 RA-EHTs show responsiveness to atrial-selective drugs

KCNA5 and *KCNJ3* encode for the ion channels Kv1.5 and Kir3.1, respectively. These ion channels conduct the potassium currents I_{Kur} and $I_{K,ACh}$, which represent the major electrophysiological discriminators between atrial and ventricular CMs (Ravens et al. 2013). CCh was used to identify $I_{K,ACh}$ in EHTs. Activation of muscarinic receptors by CCh decreased spontaneous beating rate of both RA- and Ctrl-EHTs (Figure 35). This finding cannot be taken as proof of $I_{K,ACh}$ activation, because activation of muscarinic receptors also decreases I_f (Dario DiFrancesco, Pierre Ducouret 1989) and I_f plays an important role in spontaneous pacemaking in EHTs (Mannhardt et al. 2016; Lemoine et al. 2018). On the other hand, APD_{90} shortening upon CCh exposure in RA-EHT can be considered a proof of $I_{K,Ach}$ activation. CCh did not affect APD_{90} in Ctrl-EHTs, in accordance with the previously reported absence of $I_{K,ACh}$ in cells isolated from Ctrl-EHTs (Horváth et al. 2018). The CCh effect on APD_{90} is known to show a reverse rate-dependency, meaning that APD_{90} shortening decreases at higher frequency (Figure 33). According with this observation, APD_{90} shortening induced by CCh was smaller in C25 which beat at 3 Hz (7%) than in ERC18 which beat at 2 Hz (20%, Figure S5). Nevertheless, CCh induced APD_{90} shortening was smaller in RA-EHTs than in RAA where the effect reached 50% (Figure 34), probably due to the lower amplitude of $I_{K,Ach.}$ CCh has a transient negative inotropic effect on human atrial trabeculae (Figure 36), but it does not affect contraction force

Discussion

of ventricular heart muscle (Jakob et al. 1989). On the other hand, CCh (10 µmol/L) slightly decreased contraction force in both RA- and Ctrl-EHTs (Figure 35).

I_{kur} is another atrial-selective current involved in the repolarization phase of AP, which can be useful to discriminate between atrial and ventricular CMs. It was previously demonstrated that the I_{kur} blocker Xention D-0101 was effective in RA-treated, but not in control hESC-CMs (Ford et al. 2013; Devalla et al. 2015). Due to the unavailability of this compound, a low concentration of 4-AP (50 µmol/L) was tested to block I_{kur} in Ctrl-and RA-EHTs. A high concentration of 4-AP (1 mmol/L) did not have any effect on LV (Figure 38). This finding was unexpected because it is known that high concentrations of 4-AP block I_{to}. The absence of I_{to} blockade could be explained by the fact that these experiments were performed with subendocardial preparations from patients suffering from HF characterized by low I_{to} amplitudes (Wettwer et al. 1994). In contrast, a low concentration of 4-AP (50 µmol/L) had the same effect as D-0101 in RAA (Wettwer et al. 2004; Ford et al. 2013). Specifically, 4-AP (50 µmol/L) prolonged APD_{20} and shortened APD_{90} in RAA (Figure 38 and Figure 37). This apparently contradictory finding can be explained by the fact that APD_{20} prolongation leads to a more positive plateau voltage, which induces a stronger activation of I_{Kr} and thereby APD_{90} shortening (Wettwer et al. 2004). In RA-EHTs, 4-AP (50 µmol/L) prolonged APD_{20}, but it did not decrease APD_{90} (Figure 38 and Figure 37), probably due to the lack of a clear plateau phase (Lemme et al. 2018).

At the Institute of Experimental Pharmacology and Toxicology, UKE, Hamburg (UKE, Hamburg) RA-EHTs were established in parallel to rat atrial EHTs (Krause et al. 2018). As RA-EHTs, rat atrial EHTs exhibited faster spontaneous beating, smaller contraction force, faster contraction kinetics and shorter APD_{90} compared to rat ventricular EHTs (Krause et al. 2018). The decrease in force observed in the FFR from rat atrial EHTs started at higher frequency than in the FFR from rat ventricular EHTs, whereas FFR did not differ between Ctrl- and RA-EHTs (Figure 29). CCh showed a negative inotropic effect only in rat atrial EHTs, while CCh induced a force reduction, even though not significant, in both RA- and Ctrl-EHTs (Figure 35). Atrial myocyte purity is higher in rat atrial EHTs obtained from cells directly isolated from the rat atrium than in RA-EHTs generated from hiPSC differentiated into atrial-like myocytes without any purification step. On the other hand, the clinical relevance of RA-EHTs is greater than rat atrial EHTs, since rat physiology is different from human.

In conclusion, the results of the first part of the project overcome limitations related to cardiac chamber specification. In fact, RA-treatment could successfully direct cardiac differentiation

Discussion

of hiPSC towards an atrial phenotype. 3D culture further contributed to atrial specification of hiPSC-CMs. RA-EHTs exhibited distinctive features of human atrial tissue in terms of atrial-specific gene expression, protein levels, contraction force and kinetics, AP parameters and response to atrial-selective drugs. Although quantitative differences compared to RAA persist, RA-EHTs can be considered an experimental model of human atrium to be used in disease modeling and preclinical drug development (Lemme et al. 2018). Moreover, highly enriched populations of atrial or ventricular CMs are useful for cardiac repair, because they could reduce the risk of arrhythmias upon transplantation of mixed population of hPSC-CMs (Shiba et al. 2016).

4.2   Effect of chronic optical tachypacing on Ctrl-EHTs

In the second step of the project hiPSC technology, cardiac tissue engineering and optogenetics were combined to establish a novel model to study arrhythmia mechanisms *in vitro*. Three-weeks optical pacing (3 Hz) induced functional and molecular remodeling of ChR2 transduced Ctrl-EHTs associated with increased vulnerability to (electrically induced) burst pacing. The stable tachycardia induced by burst pacing in the 3D tissue could be terminated by classical and experimental antiarrhythmic drugs, but not by the I_f blocker ivabradine, indicating its usefulness to study underlying mechanisms and therapeutic interventions in the future.

4.2.1 EHT as a model for optical pacing

ChR2 has been successfully integrated into CMs in small animal models (Bruegmann et al. 2016; Crocini et al. 2016; Nyns et al. 2017) and in MLs of neonatal rat atrial myocytes (Majumder et al. 2018) and hiPSC-CMs (Lapp et al. 2017). Here the advantages of the optogenetic approach were combined with the advantage of the EHT system, which provides a 3D functional syncytium, promotes maturation of hiPSC-CMs and is stable over several weeks. Blue light illumination of ~50 myocytes was required to induce *in vivo* optical pacing of transgenic mice (Bruegmann et al. 2010). In line with this finding, lentivirus at an MOI of 0.2 that transduced ¼ of CMs in EHTs (Figure 40) produced light-sensitive, homogenously contracting tissues. Lentiviral ChR2 expression slowed down EHT development (start of spontaneous beating) and increased spontaneous beating rate. The initially unexpected finding is in accordance with a recent observation that lentiviral transduction and ChR2 expression in neonatal rat ventricular myocytes increased spontaneous beating rate, induced adverse morphological changes, and lowered cell viability (Li et al. 2017). However, in EHTs, it did

Discussion

not affect maximum force development or CM or tissue structure when compared to non-transduced controls, rather reflecting the results of transgenic ChR2 expression in mice that was devoid of changes in heart rate or cardiac structure (Bruegmann et al. 2010). It is notable, though, that maximum diastolic potential was less negative and AP upstroke velocity was lower than what was observed previously in control EHTs (Lemoine et al. 2018). These data indicate that expression of ChR2 in hiPSC-CMs has some background effects even if not illuminated that may be due to incomplete closure of the channel. Nevertheless, the effects appear small and did not interfere with stable tissue formation and force generation of EHTs.

Importantly, blue light illumination consistently paced ChR2 transduced Ctrl-EHTs but was without effect in non-transduced controls. Pacing followed the expected dependency on light intensity, light pulse duration and frequency up to 5 Hz. The lower limit of pacing frequency was around 1.8 Hz and attributed to the spontaneous beating rate. According to Figure 42B, pacing up to 2 Hz revealed a small positive FFR, higher rates were associated with progressively decreasing force. These data indicate normal behavior of the ChR2-transduced Ctrl-EHTs compared to non-transduced Ctrl-EHTs (Lemme et al. 2018). Chronic continuous tachypacing led to quick desensitization and lack of capture, a phenomenon observed previously (Lin 2012; Zamani et al. 2017). Therefore, it was necessary to establish an interval tachypacing protocol that allowed long-term pacing with complete capture over three weeks. The comparison between lentivirally transduced ChR2-EHTs with and without chronic tachypacing allowed to distinguish the effects on cardiac function caused by the chronic optical tachypacing from the effects caused by the transduction. Therefore, ChR2-EHTs can be considered a suitable model to investigate effects of chronic optical tachypacing.

4.2.2 Electrical remodeling of ChR2-Ctrl-EHT upon chronic optical tachypacing

ChR2-Ctrl-EHTs subjected to three weeks of optical tachypacing showed faster spontaneous contraction kinetics, indicating remodeling (Figure 44). Indeed, optical stimulation conditioned the contraction kinetics of CMs in a way that even after the removal of stimulation the spontaneous contraction kinetics remained adapted to the fast optical stimulus, similarly to previous reports (Eng et al. 2016). Faster contraction kinetics were accompanied by shorter APD_{90} (Figure 45D) upon chronic optical tachypacing, as it was previously reported for chronic electrical stimulation (Eng et al. 2016; Cui et al. 2017). Expression analysis did not reveal significant changes in the expression of depolarizing (*CACNA1C*) or repolarizing ion channels (*KCNH2* and *KCNQ1;* Figure 48D and Figure 52). While this does not exclude changes in

channel proteins or ion current density, the unchanged transcript levels did not guide us in determining a reason for the APD$_{90}$ shortening. Further work is necessary to determine the mechanism.

Similar to contraction kinetics and APD$_{90}$, TOP was consistently less negative after chronic optical tachypacing than in unpaced controls (Figure 45A) and remained so even if the stimulation was stopped, again indicating remodeling. On the mRNA level *KCNJ3* and *KCNJ5*, encoding for I$_{K,ACh}$ decreased (Figure 52) and *SLC8A1*, encoding for NCX, increased (Figure 48D). If translated in similar changes in ion channel abundance and currents, these changes could contribute to a more depolarized TOP. The difference in TOP could underlie the lower upstroke velocity in the optically paced group (38.9±4.2 V/s vs. 89.6±17.8 V/s in unpaced controls, Figure 45B), because TOP determines sodium channel availability and ultimately upstroke velocity (Skibsbye et al. 2016; Lemoine et al. 2017). In contrast to a previous publication, expression of *SCN5A* was not altered by chronic pacing (Eng et al. 2016; Figure 52). Taken together, chronic optical tachypacing of ChR2-Ctrl-EHTs induced shortening of contraction, shortening of APD and ERP and more depolarized TOP. Together, these factors favor arrhythmia induction (Tse 2016).

4.2.3 Chronic optical tachypacing decreases fibrosis markers in ChR2-Ctrl-EHTs

In former work, chronic electrical pacing showed inconsistent effect on fibrosis marker expression. Some reported an increase associated with higher cellular stress (Cui et al. 2017; Geng et al. 2018), others a decrease associated with reduced ECM production (Hirt et al. 2014a). Many other studies also showed that chronic pacing can improve indices of CM maturation, such as contraction force development (Hirt et al. 2014a; Richards et al. 2017; Ronaldson-Bouchard et al. 2018). In this part of the project, chronic optical tachypacing did not affect force and had no apparent effects on structural organization, but decreased mRNA-levels of fibrosis markers and led to lower number of SMA-positive cells (Figure 51). While the latter changes are compatible with beneficial remodeling due to pacing, the lack of higher force development argues against it. Furthermore, upregulation of ANP (Figure 52) after chronic optical tachypacing may suggest CM dysfunction. Previous studies have shown an increase of ANP secretion upon various stimuli, such as cardiac stress induced by cyclic stretch or rapid pacing (Peptides et al. 2007; Sun and Nunes 2017). Differences to the former studies include the form (optical vs. electrical), the duration and the pattern (interval vs. permanent) of

Discussion

pacing. It is not clear at present which of these differences account for the different phenotype.

4.2.4 Induction and stability of tachycardia episodes

One of the most interesting findings of this work was the higher arrhythmia vulnerability of ChR2-Ctrl-EHTs submitted to chronic optical interval pacing. It was previously demonstrated that burst pacing can successfully induce reentrant arrhythmias in circular cell sheet of hiPSC-CMs (Shaheen et al. 2018) and self-terminating nonsustained arrhythmias in cardiopatches (Shadrin et al. 2017). Here, burst pacing at 20 Hz can also initiate episodes of tachycardia in ChR2-Ctrl-EHTs and the susceptibility to these spontaneous events was higher after chronic optical tachypacing. This might be due to the shorter APD_{90} and ERP of the optically paced ChR2-Ctrl-EHTs. Surprisingly, the tachycardia episodes showed a long mean duration of 29.8 ± 3.4 min. As previously described (Brennan et al. 2001; Tertoolen et al. 2018), Poincaré plots were measured to assess potential beating irregularities during tachycardia episodes. The stability (Figure 47) and the possibility to induce tachycardia episodes several times in the same EHT represent a unique opportunity to test drug efficacy for tachycardia termination. In previous studies (Sasaki et al. 2016; Maizels et al. 2017), tachycardia was investigated by analyzing arrhythmogenesis and calcium abnormalities in hiPSC-CMs obtained from patients suffering from catecholaminergic polymorphic ventricular tachycardia (CPVT). This part of the project resulted in a 3D tissue composed of hiPSC-CMs in which sustained tachycardia episodes (~ 5 Hz) could be induced by burst pacing.

4.2.5 Mechanism and termination of tachycardia episodes

As described in other models, tachycardia was successfully terminated by overdrive suppression with 20 Hz burst pacing (Fisher et al. 1978) and by optogenetic defibrillation with continuous blue light illumination (Bruegmann et al. 2016). Acute pharmacological termination of tachycardia occurred with flecainide (1 µmol/L) in 69% of EHTs (Pölönen et al. 2018). The efficacy may be related to the effect of flecainide on sodium channels, but the ryanodine stabilizing effect of flecainide cannot be ruled out (Hilliard et al. 2010). In order to investigate the mechanism underlying these tachycardia episodes, DD of AP recordings at 2 Hz field stimulation was analyzed. Although, the spontaneous beating rate did not significantly change after chronic optical tachypacing, DD was faster in the optically paced compared to the unpaced ChR2-Ctrl-EHTs (Figure 48). A positive correlation between DD and tachycardia induction was observed (Figure 48). In a previous publication (Lemoine et al. 2018), almost complete

Discussion

elimination of DD and automaticity was achieved by the I_f blocker ivabradine (300 nmol/L) in EHTs beating spontaneously during culture. In contrast, ivabradine (1 µmol/L) was never successful to terminate tachycardia episodes, even at the high concentration of 1 µmol/L and with at least 15 min exposure time. In line with this finding, mRNA expression of *HCN4*, encoding for the I_f channel, was lower after chronic optical tachypacing (Figure 48). Similar data were previously reported in hiPSC-CMs upon chronic electrical pacing (Hirt et al. 2014a; Ronaldson-Bouchard et al. 2018). These data argue against the role of I_f and point to Ca^{2+}-clock pacemaking mechanisms (Lakatta et al. 2010) to underlie the tachycardia episodes. In this model, spontaneous release of Ca^{2+} from the SR causes an elevation of cytosolic Ca^{2+}, activation of the forward mode of NCX and an inward I_{NCX} depolarizing current that depolarizes the cell to a point where the threshold to activate Na channels is reached and an AP activated (Kane et al. 2015; Kim et al. 2015). If this was the mechanism, altered intracellular Ca^{2+} handling would be expected in the optically paced, remodeled ChR2-Ctrl-EHTs. Indeed CASQ2 protein level decreased after chronic optical tachypacing (Figure 49). CASQ2 plays a crucial role in calcium-induced calcium release, as it is a major calcium binding protein in the SR. A reduction of CASQ2 and a consequent reduction of Ca^{2+} binding capacity facilitates Ca^{2+}-release and increases the event frequency (Handhle et al. 2016). At lower level of CASQ2, the SR Ca^{2+} load threshold at which spontaneous Ca^{2+} release happens is lower, increasing the overall probability of arrhythmias (Faggioni and Knollmann 2012). Successful termination of the tachycardia by the ryanodine receptor stabilizing compound JTV-519 (46% of EHTs) provides support for this hypothesis. Moreover, increased expression of phospholamban (Figure 52; Periasamy et al. 2008; Kranias and Hajjar 2012) might cause more inhibition of sarco/endoplasmic reticulum Ca^{2+}-ATPase that could contribute to the higher cytoplasmic level of Ca^{2+}. Clearly more work is needed to substantiate these hypotheses.

In conclusion, an optogenetic 3D model composed of Ctrl hiPSC-CMs allows light pacing with simultaneous force measurements over several weeks. Chronic optical tachypacing induced functional and molecular remodeling associated with a high vulnerability to burst-induced tachycardia. The effectiveness of classical (flecainide) and experimental (JTV) compounds to terminate the tachycardia indicates that this model will be valuable in studying mechanisms of ventricular tachycardia in a human cardiac myocyte context.

Discussion

4.3   Effect of chronic optical tachypacing on RA-EHTs

In the final part of the project a limited number of RA-EHTs underwent three-week optical tachypacing (5 Hz). The aim was to investigate whether chronic optical tachypacing in RA-EHTs could induce an electrical remodeling similar to those observed in human AF. Interestingly, a different molecular and electrical remodeling upon optical tachypacing was observed in ChR2-RA-EHTs compared to ChR2-Ctrl-EHTs. Optical tachypacing induced greater beating irregularities resulting in higher short and long term variability of cycle length.

4.3.1 Electrical remodeling of ChR2-RA-EHT upon chronic optical tachypacing

Shortening of APD_{90} and the loss of physiologic rate adaptation of APD are key findings of AF electrical remodeling (Franz et al. 1997; Bosch et al. 1999). However, chronic optical tachypacing did not induce APD_{90} shortening in ChR2-RA-EHTs (Figure 55D). This could be due to the different rate dependency of APD_{90} in sinus rhythm and AF (Ford et al. 2016). Rate dependency curve is very flat in AF. As a result the difference in APD_{90} measured at 3 Hz between chronic AF and sinus rhythm is very small (Ford et al. 2016). Therefore, it cannot be excluded that APD_{90} of ChR2-RA-EHTs recorded at 3 Hz pacing was already shortened due to the rate-dependency of APD masking the effects of optical tachypacing.

In tachypaced ChR2-RA-EHTs TTP was decreased (Figure 54). This finding is in line with human atrial trabeculae where TTP tends to be faster (~ 5 ms) in AF than in sinus rhythm (unpublished observation, Figure S11).

TOP was not changed in optically tachypaced ChR2-RA-EHTs while in atrial trabeculae from patients in AF RMP is more negative (Sánchez et al. 2014). Hyperpolarization of RMP should result in higher sodium channel availability (Skibsbye et al. 2016). In AF the increase in upstroke velocity is rather small (Sánchez et al. 2014), less than 10%, most probably because sodium channel conductivity is 20% less in AF (Wettwer et al. 2013). In tachypaced ChR2-RA-EHTs upstroke velocity and CV were increased (Figure 55C and F). In contrast, CV is decreased in patients with AF (Zheng et al. 2017). It should be noted that structural remodeling may have a larger impact on CV in AF than changes in sodium channel conductivity and activation. In AF disruption of electrical connections between muscle bundles caused by fibrosis leads to impaired CV (Gharaviri et al. 2016). Therefore, increased CV in tachypaced ChR2-RA-EHTs indicate that structural remodeling contributes little in this model.

Discussion

Taken together, chronic optical tachypacing successfully induced electrical remodeling in ChR2-RA-EHTs, but classic signs of AF remodeling were missing. These findings could be related to some peculiarities of ChR2-RA-EHTs: already shortened APD_{90} because of high basal beating rate and triangulated AP even under control condition.

4.3.2 Chronic optical tachypacing induces irregular spontaneous beating

Optical tachypacing induced higher beating irregularity which was observed both when measuring contraction (Figure 54E) and recording AP (Figure 56). As previously reported (Sasaki et al. 2016; Bezzerides et al. 2017) in hiPSC-CMs obtained from CPVT patients, the strong propensity to arrhythmias was attributed to disturbed Ca^{2+} handling. In fact, in CPVT facilitated release of intracellular Ca^{2+} activates NCX during diastole, leading to DADs that trigger ventricular tachycardia. Higher irregular beating in optically paced ChR2-RA-EHTs could be interpreted as a sign for instability. In AF, increased spontaneous Ca^{2+} sparks and waves are capable of triggering DADs and focal atrial electrical activity (Faggioni et al. 2014). Therefore, the higher beating irregularity observed in ChR2-RA-EHTs upon chronic tachypacing might be related to altered Ca^{2+} handling. However, in ChR2-RA-EHTs burst pacing (20 Hz) induced only nonsustained arrhythmias that were self-terminating within less than one min. This finding is consistent with the vanishing of arrhythmic events in the myocardium of patients with chronic AF (Christ et al. 2014).

The higher CL variability in optically paced ChR2-RA-EHTs (Figure 57) mirrors the RR interval variability calculated with Poincaré plots of AF patients (Park et al. 2009). SD1 and SD2 indices, clinically used to distinguish between healthy and AF patients (Rezaei et al. 2017), increased after optical tachypacing.

The irregular beating pattern observed after chronic optical tachypacing in ChR2-RA-EHTs resembles the irregular activation of atria during AF. However, beating rate was not increased like in AF.

4.3.3 Molecular changes in ChR2-RA-EHTs after chronic optical tachypacing

Higher irregular beating following chronic optical tachypacing in ChR2-RA-EHTs could be related to instability in Ca^{2+} handling or repolarizing forces. A decrease in RyR2 expression (Figure 58) could be responsible for the observed arrhythmic beating. In patients with chronic AF expression levels of RyR2 were unaltered or reduced (Ohkusa et al. 1999; Voigt et al. 2012;

Discussion

Christ et al. 2014). Functional alterations in the RyR2 Ca^{2+} release channel complex can associate with highly irregular beating in an hiPSC model of CPVT (Knollmann 2013). In this model Ca^{2+} elevation during diastole activates NCX, which depolarizes the cell membrane, generates DADs and can trigger APs. Moreover, Shan et al. 2012 has demonstrated that in CPVT mice RyR2-mediated diastolic SR Ca^{2+} leak in atrial myocytes is associated with AF.

Chronic optical tachypacing did not increase fibrosis markers but it significantly decreased periostin (POSTN) expression (Figure 58). It was demonstrated that periostin, a secreted ECM protein associated with fibrosis development (Snider et al. 2009) is upregulated in atria of HF (Molina et al. 2018) and AF patients (Wu et al. 2015). Therefore, periostin may mediate process of atrial fibrosis and promote atrial structural remodeling in AF. Obviously, chronic optical tachypacing did not induce profibrotic remodeling in ChR2-RA-EHTs.

Chronic optical tachypacing resulted in the upregulation of brain natriuretic peptide (NPPB; Figure 58). High expression of NPPB is associated with immaturity of fetal CMs and with pathological hypertrophy of adult CMs. Downregulation of NPPB is associated with maturation of hPSC-CM and it was previously achieved by long-term electrical pacing (Nunes et al. 2013) and by extended time in culture with specific culture medium (Carlson et al. 2013). On the other hand, it was shown that rapid activation of atrial cells causes myocyte stress response, leading to transcriptional upregulation of NPPB (Mace et al. 2009; Sidorova et al. 2015). Moreover, AF recurrence is associated with higher baseline NPPB levels compared to sinus rhythm group (Zografos et al. 2014).

In conclusion, higher mRNA expression of NPPB and lower expression of RyR2 could be interpreted as signs of AF remodeling, but the lack of downregulation of CACNA1C (encoding for I_{CaL}) and upregulation of KCNJ12 and KCNJ3/5 (encoding for I_{k1} and I_{KACh}) argue against typical AF electrical remodeling.

4.3.4 Structural remodeling of ChR2-RA-EHTs after chronic optical tachypacing

To investigate potential AF structural remodeling, glycogen accumulation in ChR2-RA-EHTs was measured after chronic optical tachypacing (Figure 60). In human AF, glycogen accumulates against the intercalated discs providing an impediment to electrical conduction both longitudinally and laterally (Embi et al. 2014). These areas of slow conduction predispose the tissue for reentry circuit. In the goat model, pacing induced AF was associated with an increase of intracellular glycogen concentration, which was directly proportional to the duration

of pacing induced AF. These glycogen molecules replaced intracellular myofibrils (myolysis) and were associated with enlarged myocytes (Ausma et al. 1997; Zhang et al. 2015). PAS staining of ChR2-RA-EHTs did not show a clear increase of glycogen accumulation upon chronic optical tachypacing (Figure 60). Qualitative analysis showed that PAS stained glycogen molecules (magenta colored, Figure 60) at the outer layer of the EHTs, where the majority of the cells were located (Vollert et al. 2013; Hirt et al. 2014a; Lemme et al. 2018) and collagen fibers and/or endothelial cells (light magenta colored, Figure 60) in the middle of the EHTs.

It has to be stated, though, that the number of experiments with chronically paced RA-EHTs was limited and future work is necessary to substantiate the current conclusions.

5.   Conclusion and future perspective

There is a fundamental gap in understanding the pathophysiological processes that cause AF and the lack of *in vitro* models limits the testing of underlying cellular mechanisms of the arrhythmia and of drugs to treat them. This work aimed to evaluate whether hiPSC-CMs could contribute to filling this gap.

The first part of the project focused on the development of an atrial-like EHT constituted by atrial-like myocytes obtained from hiPSC treated with RA. RA-EHTs show remarkable similarities to the human atrium on molecular and functional level. However, APs of RA-EHTs miss the marked plateau phase typical of human atrial tissue and the APD_{90} shortening induced by CCh in RA-EHTs is small compared to the human atrium. Accordingly, no significant negative inotropic effect of CCh was observed. These dissimilarities underlie potential differences on an electrophysiological level. To further improve the RA-EHT, long-term electrical pacing or extended culture periods could be tested.

The second part of the work was dedicated to investigate the effect of chronic optical tachypacing on Ctrl-EHTs, showing ventricular-like characteristics. Chronic optical tachypacing induced APD_{90} and ERP shortening, classical mechanisms that favor arrhythmias. Accordingly, electrical remodeling resulted in higher tachycardia inducibility in Ctrl-EHTs. Induced tachycardia episodes were stable over ~ 30 min allowing drug testing.

Finally, the effect of chronic optical tachypacing was tested on a limited number of atrial-like EHTs to investigate whether typical signs of AF remodeling could be induced. Optically tachypaced RA-EHTs exhibited faster upstroke, CV and spontaneous beating irregularity.

Future work should test the effect of different tachypacing modalities on the electrical remodeling of EHTs: i) Frequency and duration of blue light pulses, ii) duration and rate of the train stimulation protocol. Further analyses, such as RNA sequencing or proteomics, could be performed to determine why chronic optical tachypacing induced different electrical remodeling in RA- and Ctrl-EHTs. Overall, optical tachypacing parameters should be optimized in order to observe typical signs of AF remodeling (reduction of APD and triangulation of AP) in RA-EHTs.

From a more general point of view, different experimental strategies could be implemented to improve this *in vitro* AF model. RA-EHTs could be generated from hiPSC of AF patients in order to include their genetic background. In fact, epidemiological studies provided evidence

that up to 30% of clinically diagnosed patients may have a family history of AF (Campuzano et al. 2016). Inclusion of the patient genetic background might help to observe a different phenotype between RA-EHTs casted from healthy and AF patients and to determine the cellular electrophysiological phenotype of genetic mutations associated with AF.

An additional approach could be to apply stimuli that should enhance structural remodeling in RA-EHTs to develop a more vulnerable AF substrate, which plays an important role in the induction and progression of this cardiac disease. Inflammation, apoptosis, fibrosis and oxidative stress represent the underlying atrial structural substrate for AF. *In vitro* inflammatory responses could be induced by exposure to lipopolysaccharides that increase the production of tumor necrosis factor-α (Comstock et al. 1998; Yücel et al. 2017). Inflammatory cytokines, in turn, can induce CM apoptosis, which is accompanied by fibroblast recruitment and ECM deposition, leading to fibrosis. Fibrosis could be induced by chronic aldosterone or TGFβ administration during culture of RA-EHTs (Lijnen and Petrov 2000). In AF interstitial fibrosis impairs O_2 diffusion, leading to upregulation of hypoxic marker, such as hypoxia-inducible factor (HIF)1-α (Gramley et al. 2010). Therefore, RA-EHTs could be exposed to hypoxia. In fact, it was demonstrated that intermittent hypoxia increase AF susceptibility in rats (Bober et al. 2018) and humans (Tobushi et al. 2016). Or angiotensin II could be employed to produce reactive oxygen species leading to cellular oxidative stress (Zablocki and Sadoshima 2013).

Finally, AF is a complex disease and probably EHTs cannot fully recapitulate the complexity of the human fibrillating atrium. However, matching the cellular composition of the heart by including fibroblasts and endothelial cells into RA-EHTs could improve this *in vitro* AF model.

6. Bibliography

Abilez OJ, Wong J, Prakash R, et al (2011) Multiscale Computational Models for Optogenetic Control of Cardiac Function. Biophysj 101:1326–1334. doi: 10.1016/j.bpj.2011.08.004

Andrikopoulos GK, Pastromas S, Tzeis S (2015) Flecainide: Current status and perspectives in arrhythmia management. World J Cardiol 7:76–85. doi: 10.4330/wjc.v7.i2.76

Anfinsen O, Berggren A, Frison L, et al (2015) Is the acetylcholine-regulated inwardly rectifying potassium current a viable antiarrhythmic target? Translational discrepancies of AZD2927 and A7071 in dogs and humans. 17:473–482. doi: 10.1093/europace/euu192

Argenziano M, Lambers E, Hong L, et al (2018) Electrophysiologic Characterization of Calcium Handling in Human Induced Pluripotent Stem Cell-Derived Atrial Cardiomyocytes. Stem Cell Reports 10:1867–1878. doi: 10.1016/j.stemcr.2018.04.005

Arrenberg AB, Stainier DYR, Herwig B, Huisken J (2010) Optogenetic Control of Cardiac Function. Science (80-) 330:971–975. doi: 10.1126/science.1195929.

Ausma J, Wijffels M, Thoné F, et al (1997) Structural changes of atrial myocardium due to sustained atrial fibrillation in the goat. Circulation 96:3157–63. doi: 10.1161/01.CIR.96.9.3157

Bauman LJ, Bauernfeind AR, Hoff VJ, et al (1984) Torsade de pointes due to quinidine : Observations in 31 patients. Am Heart J 107:425–430

Bazett HC (1997) an Analysis of the Time-Relations of Electrocardiograms. Ann Noninvasive Electrocardiol 2:177–194. doi: 10.1111/j.1542-474X.1997.tb00325.x

Behram PM, Anoshia R, Jason J, et al (2017) Ablation of longstanding persistent atrial fibrillation. Ann Transl Med 5:305. doi: 10.4022/jafib.v2i2.587

Bensley JG, De Matteo R, Harding R, Black MJ (2016) Three-dimensional direct measurement of cardiomyocyte volume, nuclearity, and ploidy in thick histological sections. Sci Rep 6:1–10. doi: 10.1038/srep23756

Berk E, Christ T, Schwarz S, et al (2016) In permanent atrial fibrillation, PDE3 reduces force responses to 5-HT, but PDE3 and PDE4 do not cause the blunting of atrial arrhythmias. Br J Pharmacol 173:2478–2489. doi: 10.1111/bph.13525

Bers DM (2002) Cardiac excitation–contraction coupling. Nature 415:198–205. doi: 10.1016/S0008-4182(06)80006-2

Besser RR, Ishahak M, Mayo V, et al (2018) Engineered microenvironments for maturation of stem cell derived cardiac myocytes. Theranostics 8:124–140. doi: 10.7150/thno.19441

Bezzerides VJ, Zhang D, Pu WT (2017) Modeling Inherited Arrhythmia Disorders Using Induced Pluripotent Stem Cell-Derived Cardiomyocytes. Circ J 81:12–21. doi: 10.1253/circj.CJ-16-1113

Bingen BO, Engels MC, Schalij MJ, et al (2014) Light-induced termination of spiral wave arrhythmias by optogenetic engineering of atrial cardiomyocytes. Cardiovasc Res 104:194–205. doi: 10.1093/cvr/cvu179

Blazeski A, Renjun Z, Hunter DW, et al (2012) Cardiomyocytes derived from human induced pluripotent stem cells as models for normal and diseased cardiac electrophysiology and contractility. Prog Biophys Mol Biol 110:166–77. doi: 10.1109/TMI.2012.2196707.Separate

Bober SL, Ciriello J, Jones DL (2018) Atrial arrhythmias and autonomic dysfunction in rats exposed to chronic intermittent hypoxia. Am J Physiol Circ Physiol 314:H1160–H1168. doi: 10.1152/ajpheart.00173.2017

Bosch RF, Zeng X, Grammer JB, et al (1999) Ionic mechanisms of electrical remodeling in human atrial fibrillation. Cardiovasc Res 44:121–31. doi: 10.1016/S0008-6363(99)00178-9

Bibliography

Boyle PM, Karathanos T V., Trayanova NA (2015) "Beauty is a light in the heart": The transformative potential of optogenetics for clinical applications in cardiovascular medicine. Trends Cardiovasc Med 25:73–81. doi: 10.1016/j.tcm.2014.10.004

Boyle PM, Karathanos T V., Trayanova NA (2018) Cardiac Optogenetics 2018. JACC Clin Electrophysiol 4:155–167. doi: 10.1016/j.jacep.2017.12.006

Breckwoldt K, Letuffe-Brenière D, Mannhardt I, et al (2017) Differentiation of cardiomyocytes and generation of human engineered heart tissue. Nat Protoc 12:1177–1197. doi: 10.1038/nprot.2017.033

Brennan M, Palaniswami M, Kamen P (2001) Do Existing Measures of Poincaré Plot Geometry Reflect Nonlinear Features of Heart Rate Variability? Communications 48:1342–1347. doi: 10.1109/10.959330

Bruegmann T, Boyle PM, Vogt CC, et al (2016) Optogenetic defibrillation terminates ventricular arrhythmia in mouse hearts and human simulations. J Clin Invest 126:3894–3904. doi: 10.1172/JCI88950

Bruegmann T, Malan D, Hesse M, et al (2010) Optogenetic control of heart muscle in vitro and in vivo. Nat Methods 7:897–900. doi: 10.1038/nmeth.1512

Burashnikov A, di Diego JM, Zygmunt AC, et al (2008) Atrial-Selective Sodium Channel Block as a Strategy for Suppression of Atrial Fibrillation. Ann N Y Acad Sci 1123:105–112. doi: 10.1111/j.1749-6632.2011.05958.

Burridge PW, Keller G, Gold JD, Wu JC (2012) Review Production of De Novo Cardiomyocytes : Human Pluripotent Stem Cell Differentiation and Direct Reprogramming. Cell stem celll 10:16–28. doi: 10.1016/j.stem.2011.12.013

Burton RAB, Klimas A, Ambrosi CM, et al (2016) Optical control of excitation waves in cardiac tissue. Nat Photonics 9:813–816. doi: 10.1038/nphoton.2015.196.

Campuzano O, Perez-Serra A, Iglesias A, Brugada R (2016) Genetic basis of atrial fibrillation. Genes Dis 3:257–262. doi: 10.1016/j.gendis.2016.09.003

Carlson C, Koonce C, Aoyama N, et al (2013) Phenotypic screening with human IPS cell-derived cardiomyocytes: HTS-compatible assays for interrogating cardiac hypertrophy. J Biomol Screen 18:1203–1211. doi: 10.1177/1087057113500812

Chelu MG, Sarma S, Sood S, et al (2009) Calmodulin kinase II-mediated sarcoplasmic reticulum Ca2+ leak promotes atrial fibrillation in mice. J Clin Invest 119:1940–1951. doi: 10.1172/JCI37059DS1

Chen Z, Xian W, Bellin M, et al (2017) Subtype-specific promoter-driven action potential imaging for precise disease modelling and drug testing in hiPSC-derived cardiomyocytes. Eur Heart J 38:292–301. doi: 10.1093/eurheartj/ehw189

Cheniti G, Vlachos K, Pambrun T, et al (2018) Atrial fibrillation mechanisms and implications for catheter ablation. Front Physiol 9:1–24. doi: 10.3389/fphys.2018.01458

Christ T, Pecha S, Jost N (2015) Treatment of atrial fibrillation and atrial flutter. In: Pathophysiology and Pharmacotherapy of Cardiovascular Disease. pp 1059–1079

Christ T, Rozmaristsa N, Engel A, et al (2014) Arrhythmias, elicited by catecholamines and serotonin, vanish in human chronic atrial fibrillation. PNAS 111:11193–11198. doi: 10.1073/pnas.1415306111

Clasen L, Eickholt C, Angendohr S, et al (2018) A modified approach for programmed electrical stimulation in mice: Inducibility of ventricular arrhythmias. PLoS One 13:e0201910. doi: 10.1371/journal.pone.0201910

Claycomb WC, Delcarpio JB, Guice SE, Moses RL (1989) Culture and characterization of fetal human atrial and ventricular cardiac muscle cells. Vitr Cell Dev Biol Tissue Cult Assoc 25:1114–1120

Bibliography

Comstock KL, Krown KA, Page MT, et al (1998) LPS-induced TNF-α release from and apoptosis in rat cardiomyocytes: Obligatory role for CD14 in mediating the LPS response. J Mol Cell Cardiol 30:2761–75. doi: 10.1006/jmcc.1998.0851

Crocini C, Ferrantini C, Coppini R, et al (2016) Optogenetics design of mechanistically-based stimulation patterns for cardiac defibrillation. Sci Rep 6:1–7. doi: 10.1038/srep35628

Cui C, Geng L, Shi J, et al (2017) Structural and electrophysiological dysfunctions due to increased endoplasmic reticulum stress in a long-term pacing model using human induced pluripotent stem cell-derived ventricular cardiomyocytes. Stem Cell Res Ther 8:1–13. doi: 10.1186/s13287-017-0566-6

Cyganek L, Tiburcy M, Sekeres K, et al (2018) Deep phenotyping of human induced pluripotent stem cell–derived atrial and ventricular cardiomyocytes. JCI Insight 3:e99941. doi: 10.1172/jci.insight.99941

Dario DiFrancesco, Pierre Ducouret RBR (1989) Muscarinic Modulation of Cardiac Rate at Low Acetylcholine Concentrations. Science (80-) 243:669–671. doi: 10.1126/science.2916119

Denayer T, Stöhr T, Van Roy M (2014) Animal models in translational medicine: Validation and prediction. New Horizons Transl Med 2:5–11. doi: 10.1016/j.nhtm.2014.08.001

Devalla HD, Schwach V, Ford JW, et al (2015) Atrial-like cardiomyocytes from human pluripotent stem cells are a robust preclinical model for assessing atrial-selective pharmacology. EMBO Mol Med 7:394–410. doi: 10.15252/emmm.201404757

Dobrev D, Graf E, Wettwer E, et al (2001) Molecular Basis of Downregulation of G-Protein – Coupled. Circulation 104:2551–2558. doi: 10.1161/hc4601.099466.

Dobrev D, Ravens U (2003) Remodeling of cardiomyocyte ion channels in human atrial fibrillation. Basic Res Cardiol 98:137–48. doi: 10.1007/s00395-003-0409-8

Dobrev D, Voigt N, Wehrens XHT (2011) The ryanodine receptor channel as a molecular motif in atrial fibrillation: Pathophysiological and therapeutic implications. Cardiovasc Res 89:734–743. doi: 10.1093/cvr/cvq324

Du DTM, Hellen N, Kane C, Terracciano CMN (2015) Action potential morphology of human induced pluripotent stem cell-derived cardiomyocytes does not predict cardiac chamber specificity and is dependent on cell density. Biophys J 108:1–4. doi: 10.1016/j.bpj.2014.11.008

Ebert AD, Liang P, Wu JC (2012) Induced Pluripotent Stem Cells as a Disease Modeling and Drug Screening Platform. J Cardiovasc Pharmacol 60:408–416. doi: 10.1097/FJC.0b013e318247f642

Echt DS, Liebson PR, Mitchell BL, et al (1991) Mortality and morbidity in patients receiving encainide, flecainide or placebo. N Engl J Med 324:781–788. doi: 10.1056/NEJM199103213241201

Ellinghaus P, Scheubel RJ, Dobrev D, et al (2005) Comparing the global mRNA expression profile of human atrial and ventricular myocardium with high-density oligonucleotide arrays. J Thorac Cardiovasc Surg 129:1383–90. doi: 10.1016/j.jtcvs.2004.08.031

Embi AA, Scherlag BJ, Ritchey JW (2014) Glycogen and the propensity for atrial fibrillation: Intrinsic anatomic differences in glycogen in the left and right atria in the goat heart. N Am J Med Sci 6:510–515. doi: 10.4103/1947-2714.143282

Eng G, Lee BW, Protas L, et al (2016) Autonomous beating rate adaptation in human stem cell-derived cardiomyocytes. Nat Commun 7:1–10. doi: 10.1038/ncomms10312

Faggioni M, Knollmann BC (2012) Calsequestrin 2 and arrhythmias. AJP Hear Circ Physiol 302:H1250–H1260. doi: 10.1152/ajpheart.00779.2011

Faggioni M, Savio-Galimberti E, Venkataraman R, et al (2014) Suppression of spontaneous ca elevations prevents atrial fibrillation in calsequestrin 2-null hearts. Circ Arrhythmia Electrophysiol 7:313–320. doi: 10.1161/CIRCEP.113.000994

Bibliography

Fareh S, Villemaire C, Nattel S (1998) Importance of Refractoriness Heterogeneity in the Enhanced Vulnerability to Atrial Fibrillation Induction Caused by Tachycardia-Induced Atrial Electrical Remodeling. Circulation 98:2202–2209. doi: 10.1161/01.CIR.98.20.2202

Feghaly J, Zakka P, London B, et al (2018) Genetics of Atrial Fibrillation. J Am Heart Assoc 7:e009884. doi: 10.1161/JAHA.118.009884

Fisher JD, Mehra R, Furman S (1978) Termination of ventricular tachycardia with bursts of rapid ventricular pacing. Am J Cardiol 41:94–102. doi: 10.1016/0002-9149(78)90138-8

Fong AH, Romero-López M, Heylman CM, et al (2016) Three-Dimensional Adult Cardiac Extracellular Matrix Promotes Maturation of Human Induced Pluripotent Stem Cell-Derived Cardiomyocytes. Tissue Eng Part A 22:1016–1025. doi: 10.1089/ten.tea.2016.0027

Ford J, Milnes J, El Haou S, et al (2016) The positive frequency-dependent electrophysiological effects of the IKurinhibitor XEN-D0103 are desirable for the treatment of atrial fibrillation. Hear Rhythm 13:555–564. doi: 10.1016/j.hrthm.2015.10.003

Ford J, Milnes J, Wettwer E, et al (2013) Human electrophysiological and pharmacological properties of XEN-D0101: A novel atrial-selective Kv1.5/IKur inhibitor. J Cardiovasc Pharmacol 61:408–415. doi: 10.1097/FJC.0b013e31828780eb

Franz MR, Karasik PL, Li C, et al (1997) Electrical remodeling of the human atrium: Similar effects in patients with chronic atrial fibrillation and atrial flutter. J Am Coll Cardiol 30:1785–1792. doi: 10.1016/S0735-1097(97)00385-9

Frayne SM, Phibbs CS, Yang F, et al (2014) Increased Mortality Associated With Digoxin in Contemporary Patients With Atrial Fibrillation. J Am Coll Cardiol 64:660–8. doi: 10.1016/j.jacc.2014.03.060

Gaborit N, Le Bouter S, Szuts V, et al (2007) Regional and tissue specific transcript signatures of ion channel genes in the non-diseased human heart. J Physiol 582.2:675–693. doi: 10.1113/jphysiol.2006.126714

Geng L, Wang Z, Cui C, et al (2018) Rapid electrical stimulation increased cardiac apoptosis through disturbance of calcium homeostasis and mitochondrial dysfunction in human induced pluripotent stem cell-derived cardiomyocytes. Cell Physiol Biochem 47:1167–1180. doi: 10.1159/000490213

Gharaviri A, Kuklik P, Kuijpers NHL, et al (2016) How disruption of endo-epicardial electrical connections enhances endo-epicardial conduction during atrial fibrillation. Europace euv445. doi: 10.1093/europace/euv445

Glitsch BYHG, Reuter H, Scholz H (1970) The effect of the internal sodium concentration on calcium fluxes in isolated guinea-pig auricles. 25–43. doi: 10.1113/jphysiol.1970.sp009153

Golińska AK (2013) Poincaré Plots in Analysis of Selected Biomedical Signals. Stud LOGIC, Gramm Rhetor 35:117–127. doi: 10.2478/slgr-2013-0031

Goodman IS, Gilman A (1966) The Pharmacological Basis of Therapeutics. J Med Chem. doi: 10.1021/jm00324a062

Gorski PA, Ceholski DK, Hajjar RJ (2015) Perspective Altered Myocardial Calcium Cycling and Energetics in Heart Failure — A Rational Approach for Disease Treatment. Cell Metab 21:183–194. doi: 10.1016/j.cmet.2015.01.005

Gramley F, Lorenzen J, Jedamzik B, et al (2010) Atrial fibrillation is associated with cardiac hypoxia. Cardiovasc Pathol 19:102–11. doi: 10.1016/j.carpath.2008.11.001

Grand B Le, Hatem S, Deroubaix E, et al (1994) Depressed transient outward and calcium currents in dilated human atria. Cardiovasc Res 28:548–556. doi: 10.1093/cvr/28.4.548

Greiser M, Dobrev D, Schotten U, et al (2014) Tachycardia-induced silencing of subcellular Ca^{2+} signaling in atrial myocytes Find the latest version : Tachycardia-induced silencing of subcellular

Bibliography

Ca 2 + signaling in atrial myocytes. 124:4759–4772. doi: 10.1172/JCI70102.

Hamazaki T, Iiboshi Y, Oka M, et al (2001) Hepatic maturation in differentiating embryonic stem cells in vitro. FEBS Lett 497:15–19. doi: 10.1016/S0014-5793(01)02423-1

Han W, Chartier D, Li D, Nattel S (2001) Ionic remodeling of cardiac purkinje cells by congestive heart failure. Circulation 104:2095–2100. doi: 10.1161/hc4201.097134

Handhle A, Ormonde CE, Thomas NL, et al (2016) Calsequestrin interacts directly with the cardiac ryanodine receptor luminal domain. J Cell Sci 2:3983–3988. doi: 10.1242/jcs.191643

Hansen A, Eder A, Bönstrup M, et al (2010) Development of a drug screening platform based on engineered heart tissue. Circ Res 107:35–44. doi: 10.1161/CIRCRESAHA.109.211458

Hasenfuss G, Mulieri LA, Blanchard EM, et al (1991) Energetics of Isometric Force Development in Control and Volume-Overload Human Myocardium Comparison With Animal Species. Myocyrdial Energ isomyosins 68:836–846

Hescheler J, Fleischmann BK, Lentini S, et al (1997) Embryonic stem cells: a model to study structural and functional properties in cardiomyogenesis. Cardiovasc Res 36:149–162. doi: S0008636397001934

Hilliard FA, Steele DS, Laver D, et al (2010) Flecainide inhibits arrhythmogenic Ca2+ waves by open state block of ryanodine receptor Ca2+ release channels and reduction of Ca2+ spark mass. J Mol Cell Cardiol 48:293–301. doi: 10.1016/j.yjmcc.2009.10.005

Hinson JT, Chopra A, Nafissi N, et al (2015) Titin Mutations in iPS cells Define Sarcomere Insufficiency as a Cause of Dilated Cardiomyopathy. Science (80-) 349:982–986. doi: 10.1126/science.aaa5458.Titin

Hirt MN, Boeddinghaus J, Mitchell A, et al (2014a) Functional improvement and maturation of rat and human engineered heart tissue by chronic electrical stimulation. J Mol Cell Cardiol 74:151–161. doi: 10.1016/j.yjmcc.2014.05.009

Hirt MN, Hansen A, Eschenhagen T (2014b) Cardiac tissue engineering: State of the art. Circ Res 114:354–367. doi: 10.1161/CIRCRESAHA.114.300522

Hortigon-Vinagre MP, Zamora V, Burton FL, et al (2016) The use of ratiometric fluorescence measurements of the voltage sensitive dye Di-4-ANEPPS to examine action potential characteristics and drug effects on human induced pluripotent stem cell-derived cardiomyocytes. Toxicol Sci 154:320–331. doi: 10.1093/toxsci/kfw171

Horváth A, Lemoine MD, Löser A, et al (2018) Low Resting Membrane Potential and Low Inward Rectifier Potassium Currents Are Not Inherent Features of hiPSC-Derived Cardiomyocytes. Stem Cell Reports 10:822–833. doi: 10.1016/j.stemcr.2018.01.012

Hove-Madsen L, Llach A, Bayes-Genís A, et al (2004) Atrial fibrillation is associated with increased spontaneous calcium release from the sarcoplasmic reticulum in human atrial myocytes. Circulation 110:1358–1363. doi: 10.1161/01.CIR.0000141296.59876.87

Humayun MS, Weiland JD, Chader G, Greenbaum E Artificial sight: basic research, biomedical engineering, and clinical advances

Hwang Seok H, Kryshtal DO, Feaster TK, et al (2015) Comparable calcium handling of human iPSC-derived cardiomyocytes generated by multiple laboratories. J Mol Cell Cardiol 85:79–88. doi: 10.1016/j.yjmcc.2015.05.003

Iwasaki YK, Nishida K, Kato T, Nattel S (2011) Atrial fibrillation pathophysiology: Implications for management. Circulation 124:2264–2274. doi: 10.1161/CIRCULATIONAHA.111.019893

Jackman CP, Carlson AL, Bursac N (2016) Dynamic culture yields engineered myocardium with near-adult functional output. Biomaterials 111:66–79. doi: 10.1016/j.biomaterials.2016.09.024

Jakob H, Oelert H, Rupp J, Nawrath H (1989) Functional role of cholinoceptors and purinoceptors in

Bibliography

human isolated atrial and ventricular heart muscle. Br J Pharmacol 97:1199–1208. doi: 10.1111/j.1476-5381.1989.tb12579.x

Jara-Avaca M, Kempf H, Rückert M, et al (2017) EBIO Does Not Induce Cardiomyogenesis in Human Pluripotent Stem Cells but Modulates Cardiac Subtype Enrichment by Lineage-Selective Survival. Stem Cell Reports 8:305–317. doi: 10.1016/j.stemcr.2016.12.012

Jayachandran JV, Sih HJ, Winkle W, et al (2000) Atrial fibrillation produced by prolonged rapid atrial pacing is associated with heterogeneous changes in atrial sympathetic innervation. Circulation 101:1185–1191. doi: 10.1161/01.CIR.101.10.1185

Jee Hoon Lee SIP, Zachary Laksman PHB, Keller GM (2017) Human Pluripotent Stem Cell-Derived Atrial and. Cell Stem Cell 21:179–194. doi: 10.1016/j.stem.2017.07.003

Josowitz R, Lu J, Falce C, et al (2014) Identification and purification of human induced pluripotent stem cell-derived atrial-like cardiomyocytes based on sarcolipin expression. PLoS One 9:e101316. doi: 10.1371/journal.pone.0101316

Kääb S, Nuss HB, Chiamvimonvat N, et al (1996) Ionic mechanism of action potential prolongation in ventricular myocytes from dogs with pacing-induced heart failure. Circ Res 78:262–73. doi: 10.1161/01.RES.78.2.262

Kane C, Couch L, Terracciano CMN (2015) Excitation–contraction coupling of human induced pluripotent stem cell-derived cardiomyocytes. Front Cell Dev Biol 3:1–8. doi: 10.3389/fcell.2015.00059

Karakikes I, Ameen M, Termglinchan V, Wu JC (2015) Human Induced Pluripotent Stem Cell-Derived Cardiomyocytes: Insights into Molecular, Cellular, and Functional Phenotypes. Circ Res 117:80–88. doi: 10.1161/CIRCRESAHA.117.305365

Karathanos T V., Boyle PM, Trayanova NA (2016) Light-based Approaches to Cardiac Arrhythmia Research: From Basic Science to Translational Applications. Clin Med Insights Cardiol 10s1:47–60. doi: 10.4137/CMC.S39711

Kaumann AJ, Olson CB (1999) Temporal Relation Between Long-Lasting Aftercontractions and Action Potentials in Cat Papillary Muscles. Science (80-) 161:293–295. doi: 10.1016/j.stemcr.2018.10.008

Kearney K, Stephenson R, Phan K, et al (2014) A systematic review of surgical ablation versus catheter ablation for atrial fibrillation. Ann Cardiothorac Surg 3:15–29. doi: 10.3978/j.issn.2225-319X.2014.01.03

Kim JJ, Yang L, Lin B, et al (2015) Mechanism of automaticity in cardiomyocytes derived from human induced pluripotent stem cells. J Mol Cell Cardiol 81:81–93. doi: 10.1016/j.yjmcc.2015.01.013

Knollmann BC (2013) Controversies in Cardiovascular Research: Induced pluripotent stem cell-derived cardiomyocytes – boutique science or valuable arrhythmia model? Circ Res 112:969–976. doi: doi:10.1161/CIRCRESAHA.112.300567

Kranias EG, Hajjar RJ (2012) Modulation of cardiac contractility by the phopholamban/SERCA2a regulatome. Circ Res 110:1646–1660. doi: 10.1161/CIRCRESAHA.111.259754

Krause J, Löser A, Lemoine MD, et al (2018) Rat atrial engineered heart tissue: a new in vitro model to study atrial biology. Basic Res Cardiol 113:41. doi: 10.1007/s00395-018-0701-2

Lakatta EG, Maltsev VA, Vinogradova TM (2010) A Coupled SYSTEM of Intracellular Ca2+ Clocks and Surface Membrane Voltage Clocks Controls the Timekeeping Mechanism of the Heart's Pacemaker. Circ Res 106:659–673. doi: 10.1161/CIRCRESAHA.109.206078.A

Lapp H, Bruegmann T, Malan D, et al (2017) Frequency-dependent drug screening using optogenetic stimulation of human iPSC-derived cardiomyocytes. Sci Rep 7:1–12. doi: 10.1038/s41598-017-09760-7

Bibliography

Lee JH, Protze SI, Laksman Z, et al (2017) Human Pluripotent Stem Cell-Derived Atrial and Ventricular Cardiomyocytes Develop from Distinct Mesoderm Populations. Cell Stem Cell 21:179–194.e4. doi: 10.1016/j.stem.2017.07.003

Lemme M, Ulmer BM, Lemoine MD, et al (2018) Atrial-like Engineered heart tissue: An In vitro Model of the Human Atrium, Stem Cell Reports. Stem Cell Reports 11:1–13

Lemoine MD, Krause T, Koivumäki JT, et al (2018) Human Induced Pluripotent Stem Cell–Derived Engineered Heart Tissue as a Sensitive Test System for QT Prolongation and Arrhythmic Triggers. Circ Arrhythmia Electrophysiol 11:e006035. doi: 10.1161/CIRCEP.117.006035

Lemoine MD, Mannhardt I, Breckwoldt K, et al (2017) Human iPSC-derived cardiomyocytes cultured in 3D engineered heart tissue show physiological upstroke velocity and sodium current density. Sci Rep 7:1–11. doi: 10.1038/s41598-017-05600-w

Li Q, Ni RR, Hong H, et al (2017) Electrophysiological Properties and Viability of Neonatal Rat Ventricular Myocyte Cultures with Inducible ChR2 Expression. Sci Rep 7:1–12. doi: 10.1038/s41598-017-01723-2

Liang X, Xie H, Zhu PH, et al (2008) Ryanodine receptor-mediated Ca2+ events in atrial myocytes of patients with atrial fibrillation. Cardiology 111:102–110. doi: 10.1159/000119697

Lijnen P, Petrov V (2000) Induction of cardiac fibrosis by aldosterone. J. Mol. Cell. Cardiol. 865–79

Lin JY (2012) A User's Guide to Channelrhodopsin Variants. Exp Physiol 96:19–25. doi: 10.1113/expphysiol.2009.051961.A

Lip GYH, Beevers DG (1995) ABC of atrial fibrillation. History, epidemiology, and importance of atrial fibrillation. BMJ 311:1361. doi: 10.1136/bmj.311.7016.1361

Lowey S, Waller SG, Trybus MK (1993) Skeletal muscle myosin light chains are essential for physiological speeds of shortening. Lett to Nat 366:461–464. doi: 10.1038/365454a0

Ma J, Guo L, Fiene SJ, et al (2011) High purity human-induced pluripotent stem cell-derived cardiomyocytes : electrophysiological properties of action potentials and ionic currents. Am J Physiol Hear Circ Physiol 301:2006–2017. doi: 10.1152/ajpheart.00694.2011.

Mace LC, Yermalitskaya L V., Yi Y, et al (2009) Transcriptional remodeling of rapidly stimulated HL-1 atrial myocytes exhibits concordance with human atrial fibrillation. J Mol Cell Cardiol 47:485–92. doi: 10.1016/j.yjmcc.2009.07.006

Mahida S (2014) Genetic Discoveries in Atrial Fibrillation and Implications for Clinical Practice. Arrhythmia Mech 3:69–75. doi: 10.15420/aer.2014.3.2.69

Maier LS, Barckhausen P, Weisser J, et al (2000) Ca2+ handling in isolated human atrial myocardium. Am J Physiol Circ Physiol 279:952–958. doi: 10.1152/ajpheart.2000.279.3.H952

Maizels L, Huber I, Arbel G, et al (2017) Patient-Specific Drug Screening Using a Human Induced Pluripotent Stem Cell Model of Catecholaminergic Polymorphic Ventricular Tachycardia Type 2. Circ Arrhythmia Electrophysiol 10:. doi: 10.1161/CIRCEP.116.004725

Majumder R, Feola I, Teplenin AS, et al (2018) Optogenetics enables real-time spatiotemporal control over spiral wave dynamics in an excitable cardiac system. Elife 1–17. doi: 10.7554/eLife.41076

Mannhardt I, Breckwoldt K, Letuffe-Brenière D, et al (2016) Human Engineered Heart Tissue: Analysis of Contractile Force. Stem Cell Reports 7:29–42. doi: 10.1016/j.stemcr.2016.04.011

Marczenke M, Piccini I, Mengarelli I, et al (2017) Cardiac subtype-specific modeling of Kv1.5 ion channel deficiency using human pluripotent stem cells. Front Physiol 8:1–11. doi: 10.3389/fphys.2017.00469

Marini C, De Santis F, Sacco S, et al (2005) Contribution of atrial fibrillation to incidence and outcome of ischemic stroke: Results from a population-based study. Stroke 36:1115–1119. doi: 10.1161/01.STR.0000166053.83476.4a

Bibliography

Merrill DR, Bikson M, Jefferys JGR (2005) Electrical stimulation of excitable tissue: Design of efficacious and safe protocols. J Neurosci Methods 141:171–198. doi: 10.1016/j.jneumeth.2004.10.020

Mirescu S, Harden S (2012) Nonlinear dynamics methods for assessing heart rate variability in patients with recent myocyrdial infarction. Rom J Biophys 22:117–124

Moe GW, Amstrong P (1999) Pacing-induced heart failure: a model to study the mechanism of disease progression and novel therapy in heart failure. Cardiovasc Res 42:591–599. doi: 10.1016/S0008-6363(99)00032-2

Molenaar P, Christ T, Hussain RI, et al (2013) PDE3, but not PDE4, reduces β1- and β2- adrenoceptor-mediated inotropic and lusitropic effects in failing ventricle from metoprolol-treated patients. Br J Pharmacol 169:528–538. doi: 10.1111/bph.12167

Molina CE, Abu-Taha IH, Wang Q, et al (2018) Profibrotic, electrical, and calcium-handling remodeling of the atria in heart failure patients with and without atrial fibrillation. Front Physiol 9:1–18. doi: 10.3389/fphys.2018.01383

Morano I, Bletz C, Wojciechowski R, Rüegg J. (1991) Brief Communication Modulation of Crossbridge Kinetics by Myosin Isoenzymes in Skinned Human Heart Fibers. Circ Res 68:614–619. doi: 10.1161/01.RES.68.2.614

Morano M, Zacharzowski U, Maier M, et al (1996) Regulation of human heart contractility by essential myosin light chain isoforms. J Clin Invest 98:467–473. doi: 10.1172/JCI118813

Morillo CA, Klein GJ, Jones DL, Guiraudon CM (1995) Chronic rapid atrial pacing: Structural, functional, and electrophysiological characteristics of a new model of sustained atrial fibrillation. Circulation 91:1588–1595. doi: 10.1161/01.CIR.91.5.1588

Mosqueira D, Mannhardt I, Bhagwan JR, et al (2018) CRISPR/Cas9 editing in human pluripotent stem cell-cardiomyocytes highlights arrhythmias, hypocontractility, and energy depletion as potential therapeutic targets for hypertrophic cardiomyopathy. Eur Heart J 0:1–16. doi: 10.1093/eurheartj/ehy249

Mummery CL, Zhang J, Ng ES, et al (2012) Differentiation of Human Embryonic Stem Cells and Induced Pluripotent Stem Cells to Cardiomyocytes A Methods Overview Differentiation of Human Embryonic Stem Cells and Induced Pluripotent Stem Cells to Cardiomyocytes : A Methods Overview The online versio. Circ Res 111:344–358. doi: 10.1161/CIRCRESAHA.110.227512

Nattel S, Dobrev D (2012) The multidimensional role of calcium in atrial fibrillation pathophysiology: Mechanistic insights and therapeutic opportunities. Eur Heart J 33:1870–1877. doi: 10.1093/eurheartj/ehs079

Ng SY, Wong CK, Tsang SY (2010) Differential gene expressions in atrial and ventricular myocytes: insights into the road of applying embryonic stem cell-derived cardiomyocytes for future therapies. Am J Physiol Physiol 299:C1234–C1249. doi: 10.1152/ajpcell.00402.2009.

Nielsen JB, Fritsche LG, Zhou W, et al (2018) Genome-wide Study of Atrial Fibrillation Identifies Seven Risk Loci and Highlights Biological Pathways and Regulatory Elements Involved in Cardiac Development. Am J Hum Genet 102:103–115. doi: 10.1016/j.ajhg.2017.12.003

Nunes SS, Miklas JW, Liu J, et al (2013) Biowire: a new platform for maturation of human pluripotent stem cell derived cardiomyocytes. Nat Methods 10:781–787. doi: 10.1038/nmeth.2524.

Nussinovitch U, Gepstein L (2015) Optogenetics for in vivo cardiac pacing and resynchronization therapies. Nat Biotechnol 33:750–754. doi: 10.1038/nbt.3268

Nyns ECA, Kip A, Bart CI, et al (2017) Optogenetic termination of ventricular arrhythmias in the whole heart: Towards biological cardiac rhythm management. Eur Heart J 38:2132–2136. doi: 10.1093/eurheartj/ehw574

Ohkusa T, Ueyama T, Yamada J, et al (1999) Alterations in cardiac sarcoplasmic reticulum Ca2+

Bibliography

regulatory proteins in the atrial tissue of patients with chronic atrial fibrillation. J Am Coll Cardiol 34:255–263. doi: 10.1016/S0735-1097(99)00169-2

Okabe S, Forsberg-Nilsson K, Spiro AC, et al (1996) Development of neuronal precursor cells and functional postmitotic neurons from embryonic stem cells in vitro. Mech Dev 59:89–102. doi: 10.1016/0925-4773(96)00572-2

Palpant NJ, Pabon L, Friedman CE, et al (2016) Generating high-purity cardiac and endothelial derivatives from patterned mesoderm using human pluripotent stem cells. Nat Protoc 12:15–31. doi: 10.1038/nprot.2016.153

Park J, Lee S, Jeon M (2009) Atrial fibrillation detection by heart rate variability in Poincare plot. Biomed Eng Online 8:1–12. doi: 10.1186/1475-925X-8-38

Patel C, Salahuddin M, Jones A, et al (2011) Atrial Fibrillation: Pharmacological Therapy. Curr Probl Cardiol 36:87–120. doi: 10.1016/j.cpcardiol.2011.01.001

Peptides BN, Ronkainen JJ, Vuolteenaho O, Tavi P (2007) Calcium-Calmodulin Kinase II Is the Common Factor in Calcium-Dependent Cardiac Expression and Secretion of. Endocrinology 148:2815–2820. doi: 10.1210/en.2006-1676

Periasamy M, Bhupathy P, Babu GJ (2008) Regulation of sarcoplasmic reticulum Ca2+ATPase pump expression and its relevance to cardiac muscle physiology and pathology. Cardiovasc Res 77:265–273. doi: 10.1093/cvr/cvm056

Piroddi N, Belus A, Scellini B, et al (2007) Tension generation and relaxation in single myofibrils from human atrial and ventricular myocardium. Pflugers Arch Eur J Physiol 454:63–73. doi: 10.1007/s00424-006-0181-3

Piskorski J, Guzik P (2007) Geometry of the Poincaré plot of RR intervals and its asymmetry in healthy adults. Physiol Meas 28:287–300. doi: 10.1088/0967-3334/28/3/005

Pölönen RP, Penttinen K, Swan H, Aalto-Setälä K (2018) Antiarrhythmic Effects of Carvedilol and Flecainide in Cardiomyocytes Derived from Catecholaminergic Polymorphic Ventricular Tachycardia Patients. Stem Cells Int 1–11. doi: 10.1155/2018/9109503

Prondzynski M, Krämer E, Laufer SD, et al (2017) Evaluation of MYBPC3 trans-Splicing and Gene Replacement as Therapeutic Options in Human iPSC-Derived Cardiomyocytes. Mol Ther - Nucleic Acids 7:475–486. doi: 10.1016/j.omtn.2017.05.008

Radisic M, Park H, Shing H, et al (2004) Functional assembly of engineered myocardium by electrical stimulation of cardiac myocytes cultured on scaffolds. Proc Natl Acad Sci 101:18129–18134. doi: 10.1073/pnas.0407817101

Ravens U, Poulet C, Wettwer E, Knaut M (2013) Atrial selectivity of antiarrhythmic drugs. J Physiol 591:4087–4097. doi: 10.1113/jphysiol.2013.256115

Rehnelt S, Malan D, Juhasz K, et al (2017) Frequency-Dependent Multi-Well Cardiotoxicity Screening Enabled by Optogenetic Stimulation. Int J Mol Sci 18:2634. doi: 10.3390/ijms18122634

Rezaei S, Moharreri S, Abdollahpur M, Parvaneh S (2017) Heart Arrhythmia Classification Using Extracted Features in Poincare Plot of RR Intervals? Comput Cardiol (2010) 44:1–4. doi: 10.22489/CinC.2017.115-399

Richards DJ, Tan Y, Coyle R, et al (2017) Nanowires and electrical stimulation synergistically improve functions of hiPSC cardiac spheroids. 16:1–8. doi: 10.1016/j.compmedimag.2015.12.001.

Ronaldson-Bouchard K, Ma SP, Yeager K, et al (2018) Advanced maturation of human cardiac tissue grown from pluripotent stem cells. Nature 556:239–243. doi: 10.1038/s41586-018-0016-3

Ruan JL, Tulloch NL, Razumova M V., et al (2016) Mechanical Stress Conditioning and Electrical Stimulation Promote Contractility and Force Maturation of Induced Pluripotent Stem Cell-Derived Human Cardiac Tissue. Circulation 134:1557–1567. doi:

Bibliography

10.1161/CIRCULATIONAHA.114.014998

Ruf T, Schulte-Baukloh H, Posival H, et al (1998) Alterations of cross-bridge kinetics in human atrial and ventricular myocardium. Cardiovasc Res 40:580–590. doi: 10.1016/S0008-6363(98)00164-3

Sala L, van Meer BJ, Tertoolen LT, et al (2018) MUSCLEMOTION: A Versatile Open Software Tool to Quantify Cardiomyocyte and Cardiac Muscle Contraction In Vitro and In Vivo. Circ Res 122:e5–e16. doi: 10.1161/CIRCRESAHA.117.312067

Sánchez C, Bueno-orovio A, Wettwer E, et al (2014) Inter-Subject Variability in Human Atrial Action Potential in Sinus Rhythm versus Chronic Atrial Fibrillation. PLoS One 9:e105897. doi: 10.1371/journal.pone.0105897

Sanders P, Elliott AD, Linz D (2017) Upstream Targets to Treat Atrial Fibrillation. J Am Coll Cardiol 70:2906–2908. doi: 10.1016/j.jacc.2017.10.043

Sasaki K, Makiyama T, Yoshida Y, et al (2016) Patient-specific human induced pluripotent stem cell model assessed with electrical pacing validates S107 as a potential therapeutic agent for catecholaminergic polymorphic ventricular tachycardia. PLoS One 11:. doi: 10.1371/journal.pone.0164795

Sasse P (2011) Optical pacing of the heart the long way to enlightenment. Circ Arrhythmia Electrophysiol 4:598–600. doi: 10.1161/CIRCEP.111.965400

Savelieva I, Kakouros N, Kourliouros A, Camm AJ (2011) Upstream therapies for management of atrial fibrillation: Review of clinical evidence and implications for European Society of Cardiology guidelines. Part I: Primary prevention. Europace 13:308–328. doi: 10.1093/europace/eur002

Schaaf S, Shibamiya A, Mewe M, et al (2011) Human engineered heart tissue as a versatile tool in basic research and preclinical toxicology. PLoS One 6:e26397. doi: 10.1371/journal.pone.0026397

Schlaeger TM, Daheron L, Brickler TR, et al (2015) A comparison of non-integrating reprogramming methods. Nat Biotechnol 33:58–63. doi: 10.1038/nbt.3070

Schotten U, Ausma J, Stellbrink C, et al (2001) Cellular Mechanisms of Depressed Atrial Contractility in Patients With Chronic Atrial Fibrillation. 103:691–698. doi: 10.1161/01.CIR.103.5.691

Schotten U, Verheule S, Kirchhof P, Goette A (2011) Pathophysiological Mechanisms of Atrial Fibrillation: A Translational Appraisal. Physiol Rev 91:265–325. doi: 10.1152/physrev.00031.2009

Schwinger RHG, Böhm M, Koch A, et al (1993) Force-frequency-relation in human atrial and ventricular myocardium. Mol Cell Biochem 119:73–78. doi: 10.1007/BF00926856

Shadrin IY, Allen BW, Qian Y, et al (2017) Cardiopatch platform enables maturation and scale-up of human pluripotent stem cell-derived engineered heart tissues. Nat Commun 8:. doi: 10.1038/s41467-017-01946-x

Shaheen N, Shiti A, Huber I, et al (2018) Human Induced Pluripotent Stem Cell-Derived Cardiac Cell Sheets Expressing Genetically Encoded Voltage Indicator for Pharmacological and Arrhythmia Studies. Stem Cell Reports 10:1879–1894. doi: 10.1016/j.stemcr.2018.04.006

Shan J, Xie W, Betzenhauser M, et al (2012) Calcium leak through ryanodine receptors leads to atrial fibrillation in 3 mouse models of catecholaminergic polymorphic ventricular tachycardia. Circ Res 111:708–717. doi: 10.1161/CIRCRESAHA.112.273342

Sharma PS, Dandamudi G, Naperkowski A, et al (2015) Permanent His-bundle pacing is feasible, safe, and superior to right ventricular pacing in routine clinical practice. Hear Rhythm 12:305–312. doi: 10.1016/j.hrthm.2014.10.021

Shiba Y, Gomibuchi T, Seto T, et al (2016) Allogeneic transplantation of iPS cell-derived cardiomyocytes regenerates primate hearts. Nature 1–16. doi: 10.1038/nature19815

Shunmugam SR, Sugihara C, Freemantle N, et al (2018) assessing the use of XEN-D0103 in patients

Bibliography

with paroxysmal atrial fibrillation and implanted pacemakers allowing continuous beat-to-beat monitoring of drug efficacy. J Interv Card Electrophysiol 51:191–197. doi: 10.1007/s10840-018-0318-2

Sidorova TN, Yermalitskaya L V., Mace LC, et al (2015) Reactive γ-ketoaldehydes promote protein misfolding and preamyloid oligomer formation in rapidly-activated atrial cells. J Mol Cell Cardiol. doi: 10.1016/j.yjmcc.2014.11.013

Sinner MF, Ellinor PT, Meitinger T, et al (2011) Genome-wide association studies of atrial fibrillation: Past, present, and future. Cardiovasc Res 89:701–709. doi: 10.1093/cvr/cvr001

Skibsbye L, Jespersen T, Christ T, et al (2016) Refractoriness in human atria: Time and voltage dependence of sodium channel availability. J Mol Cell Cardiol 101:26–34. doi: 10.1016/j.yjmcc.2016.10.009

Snider P, Standley KN, Wang J, et al (2009) Origin of cardiac fibroblasts and the role of periostin. Circ Res 105:934–947. doi: 10.1161/CIRCRESAHA.109.201400

Sun X, Nunes SS (2017) Bioengineering Approaches to Mature Human Pluripotent Stem. Front Cell Dev Biol 5:1–8. doi: 10.3389/fcell.2017.00019

Takahashi K, Tanabe K, Ohnuki M, et al (2007) Induction of Pluripotent Stem Cells from Adult Human Fibroblasts by Defined Factors. Cell 131:861–872. doi: 10.1016/j.cell.2007.11.019

Takahashi K, Yamanaka S (2006) Induction of Pluripotent Stem Cells from Mouse Embryonic and Adult Fibroblast Cultures by Defined Factors. Cell 126:663–676. doi: 10.1016/j.cell.2006.07.024

Tanaka A, Yuasa S, Node K, Fukuda K (2015) Cardiovascular disease modeling using patient-specific induced pluripotent stem cells. Int J Mol Sci 16:18894–18922. doi: 10.3390/ijms160818894

Tandon N, Cannizzaro C, Chao P-HG, et al (2009) Electrical stimulation systems for cardiac tissue engineering. Nat Protoc 4:155–173. doi: 10.1038/nprot.2008.183

Tertoolen LGJ, Braam SR, van Meer BJ, et al (2018) Interpretation of field potentials measured on a multi electrode array in pharmacological toxicity screening on primary and human pluripotent stem cell-derived cardiomyocytes. Biochem Biophys Res Commun 497:1135–1141. doi: 10.1016/j.bbrc.2017.01.151

Tobushi T, Ando S ichi, Kadokami T (2016) Recurrent paroxysmal atrial fibrillation induced by marked hypoxia during sleep-disordered breathing. J Cardiol Cases 14:87–89. doi: 10.1016/j.jccase.2016.04.007

Tse G (2016) Mechanisms of cardiac arrhythmias. J Arrhythmia 32:75–81. doi: 10.1016/j.joa.2015.11.003

Tu C, Chao BS, Wu JC (2018) Strategies for Improving the Maturity of Human Induced Pluripotent Stem Cell-Derived Cardiomyocytes. Circ Res 123:512–514. doi: 10.1161/CIRCRESAHA.118.313472

Tulloch NL, Muskheli V, Razumova M V., et al (2011) Growth of engineered human myocardium with mechanical loading and vascular coculture. Circ Res 109:47–59. doi: 10.1161/CIRCRESAHA.110.237206

Ulmer BM, Stoehr A, Schulze ML, et al (2018) Contractile Work Contributes to Maturation of Energy Metabolism in hiPSC-Derived Cardiomyocytes. Stem Cell Reports 10:834–847. doi: 10.1016/j.stemcr.2018.01.039

Uzun AU, Mannhardt I, Breckwoldt K, et al (2016) Ca2+-currents in human induced pluripotent stem cell-derived cardiomyocytes effects of two different culture conditions. Front Pharmacol 7:1–14. doi: 10.3389/fphar.2016.00300

Van den Berg CW, Elliott DA, Braam SR, et al (2016) Differentiation of Human Pluripotent Stem Cells to Cardiomyocytes Under Defined Conditions. Methods Mol Biol 1341:257–284. doi:

Bibliography

10.1007/7651

Van Der Velden J, Klein LJ, Van Der Bijl M, et al (1998) Force production in mechanically isolated cardiac myocytes from human ventricular muscle tissue. Cardiovasc Res 38:414–423. doi: 10.1016/S0008-6363(98)00019-4

Verheule S, Wilson E, Banthia S, et al (2004) Direction-dependent conduction abnormalities in a canine model of atrial fibrillation due to chronic atrial dilatation. Am J Physiol Circ Physiol 287:H634–H644. doi: 10.1152/ajpheart.00014.2004

Voigt N, Li N, Wang Q, et al (2012) Enhanced Sarcoplasmic Reticulum Ca2+ Leak and Increased Na+-Ca2+ Exchanger Function Underlie Delayed Afterdepolarizations in Patients With Chronic Atrial Fibrillation. Circulation 125:2059–2070. doi: 10.1161/CIRCULATIONAHA.111.067306

Vollert I, Seiffert M, Bachmair J, et al (2013) In-vitro perfusion of engineered heart tissue through endothelialized channels. Tissue Eng Part A 20:854–863. doi: 10.1089/ten.TEA.2013.0214

Volosin KJ, Beauregard LAM, Fabiszewski R, et al (1991) Spontaneous changes in ventricular tachycardia cycle length. J Am Coll Cardiol 17:409–414. doi: 10.1016/S0735-1097(10)80107-X

Waks JW, Josephson ME (2014) Mechanisms of Atrial Fibrillation – Reentry, Rotors and Reality. Arrhythmia Electrophysiol Rev 3:90. doi: 10.15420/aer.2014.3.2.90

Weinberger F, Mannhardt I, Eschenhagen T (2017) Engineering Cardiac Muscle Tissue: A Maturating Field of Research. Circ Res 120:1487–1500. doi: 10.1161/CIRCRESAHA.117.310738

Wettwer E, Amos GJ, Posival H, Ravens U (1994) Transient outward current in human ventricular myocytes of subepicardial and subendocardial origin. Circ Res 75:473–482. doi: 10.1161/01.RES.75.3.473

Wettwer E, Christ T, Endig S, et al (2013) The new antiarrhythmic drug vernakalant: Ex vivo study of human atrial tissue from sinus rhythm and chronic atrial fibrillation. Cardiovasc Res 98:145–154. doi: 10.1093/cvr/cvt006

Wettwer E, Hála O, Christ T, et al (2004) Role of IKur in controlling action potential shape and contractility in the human atrium: Influence of chronic atrial fibrillation. Circulation 110:2299–2306. doi: 10.1161/01.CIR.0000145155.60288.71

Wijffels MCEF, Kirchhof CJHJ, Dorland R, Allessie MA (1995) Atrial fibrillation begets atrial fibrillation: A study in awake chronically instrumented goats. Circulation 92:1954–1968. doi: 10.1161/01.CIR.92.7.1954

Wobus AM, Rohwedel J, Maltsev V, Hescheler J (1995) Development of Cardiomyocytes Expressing Cardiac-Specific Genes, Action Potentials, and Ionic Channels during Embryonic Stem Cell-Derived Cardiogenesis. Ann N Y Acad Sci 752:460–9. doi: 10.1111/j.1749-6632.1995.tb17456.

Wu H, Xie J, Li GN, et al (2015) Possible involvement of TGF-β/periostin in fibrosis of right atrial appendages in patients with atrial fibrillation. Int J Clin Exp Pathol 8:6859–6869

Wu S pin, Cheng CM, Lanz RB, et al (2013) Atrial Identity Is Determined by a COUP-TFII Regulatory Network. Dev Cell 25:417–426. doi: 10.1016/j.devcel.2013.04.017

Yang C, Al-Aama J, Stojkovic M, et al (2015) Concise Review: Cardiac Disease Modeling Using Induced Pluripotent Stem Cells. Stem Cells 33:2643–2651. doi: 10.1002/stem.2070

Ye L, Ni X, Zhao Z-A, et al (2018) The Application of Induced Pluripotent Stem Cells in Cardiac Disease Modeling and Drug Testing. J Cardiovasc Transl Res 11:366–374. doi: 10.1007/s12265-018-9811-3

Yücel G, Zhao Z, El-Battrawy I, et al (2017) Lipopolysaccharides induced inflammatory responses and electrophysiological dysfunctions in human-induced pluripotent stem cell derived cardiomyocytes. Sci Rep 7:1–13. doi: 10.1038/s41598-017-03147-4

Yue L, Melnyk P, Gaspo R, et al (1999) Molecular Mechanisms Underlying Ionic Remodeling in a Dog

Bibliography

Model of Atrial Fibrillation. Circ Res 84:776–784. doi: 10.1161/01.RES.84.7.776

Zablocki D, Sadoshima J (2013) Angiotensin II and Oxidative Stress in the Failing Heart. Antioxid Redox Signal 19:1095–1109. doi: 10.1089/ars.2012.4588

Zaffran S, Robrini N, Bertrand N (2014) Retinoids and Cardiac Development. J Dev Biol 2:50–71. doi: 10.3390/jdb2010050

Zaglia T, Pianca N, Borile G, et al (2015) Optogenetic determination of the myocardial requirements for extrasystoles by cell type-specific targeting of ChannelRhodopsin-2. Proc Natl Acad Sci 112:E4495–E4504. doi: 10.1073/pnas.1509380112

Zamani A, Sakuragi S, Ishizuka T, Yawo H (2017) Kinetic characteristics of chimeric channelrhodopsins implicate the molecular identity involved in desensitization. Biophys Physicobiology 14:13–22. doi: 10.2142/biophysico.14.0

Zhang C, He D, Ma J, et al (2018) Faradaic reactions in capacitive deionization (CDI) - problems and possibilities: A review. Water Res 128:314–330. doi: 10.1016/j.watres.2017.10.024

Zhang D, Shadrin I, Lam J, et al (2013) Tissue-engineered Cardiac Patch for Advanced Functional Maturation of Human ESC-derived Cardiomyocytes. Biomaterials 34:5813–5820. doi: 10.1002/ana.22528

Zhang L, Huang B, Scherlag BJ, et al (2015) Structural changes in the progression of atrial fibrillation: Potential role of glycogen and fibrosis as perpetuating factors. Int J Clin Exp Pathol 8:1712–1718

Zhang Q, Jiang J, Han P, et al (2011) Direct differentiation of atrial and ventricular myocytes from human embryonic stem cells by alternating retinoid signals. Cell Res 21:579–587. doi: 10.1038/cr.2010.163

Zhao Z, Lan H, El-battrawy I, et al (2018) Ion Channel Expression and Characterization in Human Induced Pluripotent Stem Cell-Derived Cardiomyocytes. Stem Cells Int 1–13. doi: 10.1155/2018/6067096

Zheng Y, Xia Y, Carlson J, et al (2017) Atrial average conduction velocity in patients with and without paroxysmal atrial fibrillation. Clin Physiol Funct Imaging 37:596–601. doi: 10.1111/cpf.12342

Zimmermann W, Didie M, Do S, et al (2006) Heart muscle engineering : An update on cardiac muscle replacement therapy. Cardiovasc Res 71:419–429. doi: 10.1016/j.cardiores.2006.03.023

Zografos T, Maniotis C, Katsivas A, Katritsis D (2014) Relationship between Brain Natriuretic Peptides and Recurrence of Atrial Fibrillation after Successful Direct Current Cardioversion: A Meta-Analysis. PACE - Pacing Clin Electrophysiol 37:1530–1537. doi: 10.1111/pace.12477

7. Supplements

7.1 Supplementary figures and tables
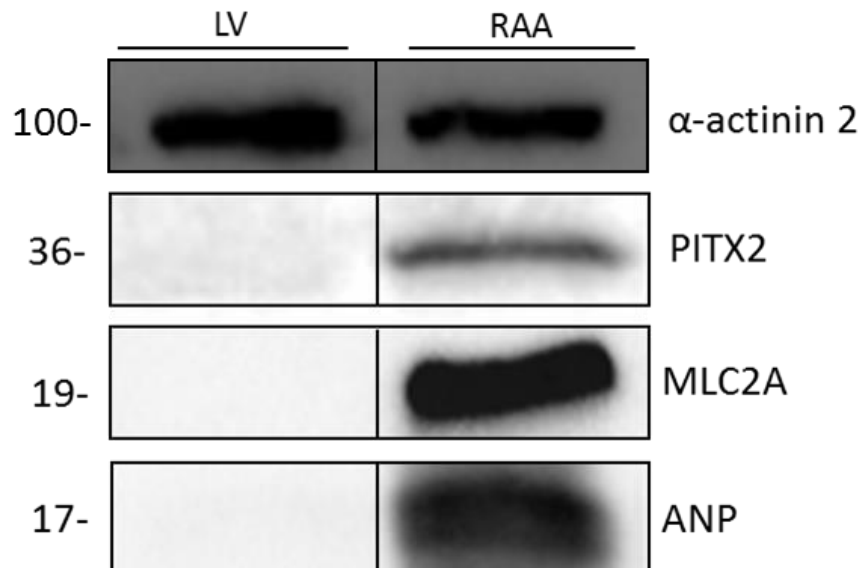
Figure S1: **Analysis of WB antibodies specificity**. Validation of WB antibodies to distinguish between ventricular and atrial phenotype. The antibodies were tested in left ventricular (LV) tissues and right atrial appendages (RAA; adapted from Lemme et al. 2018).
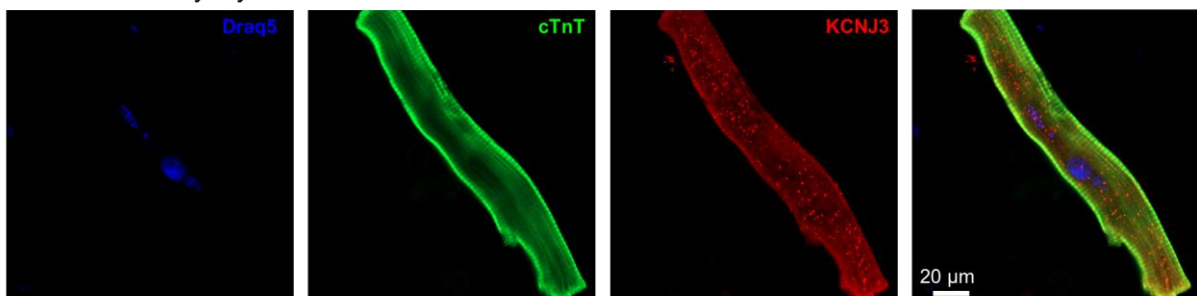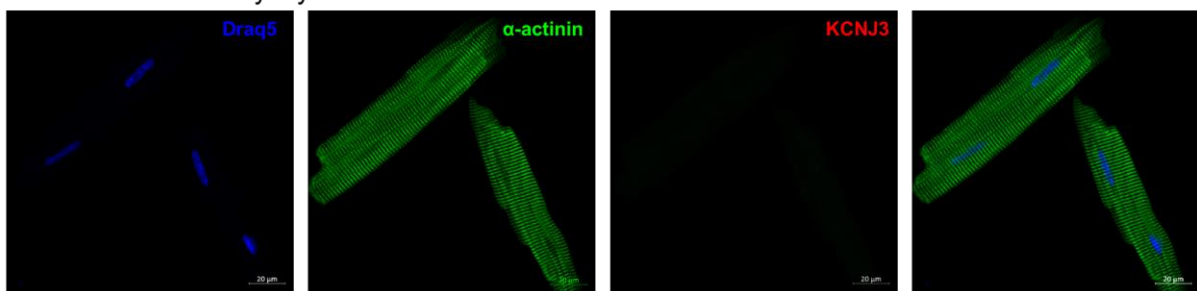
Figure S2: **Atrial specificity of KCNJ3 tested with immunofluorescence**. Immunofluorescence staining of KCNJ3 (red), cardiac protein (green) and nuclei (blue) in human atrial myocytes (top) and mouse ventricular myocytes (bottom).

Supplements
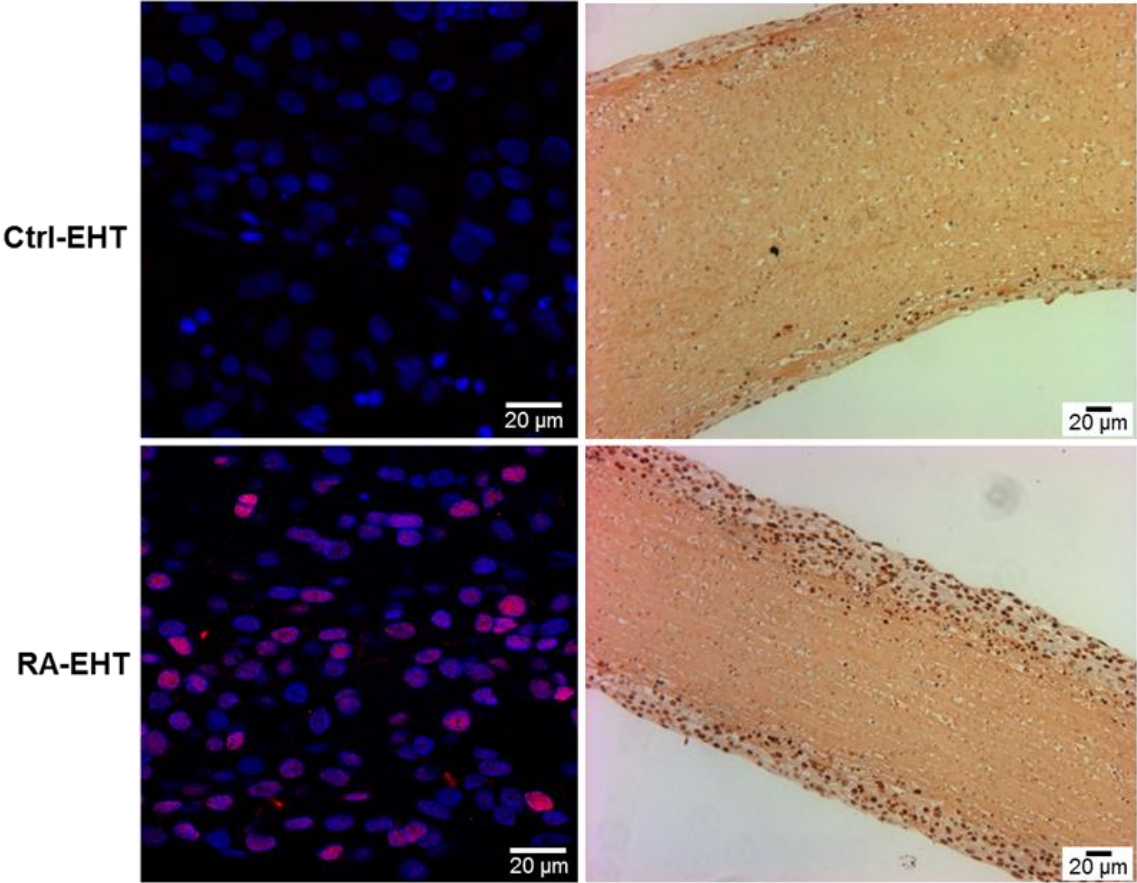
Figure S3: **Immunofluorescence and immunohistochemistry of COUPTFII**. Expression of COUPTFII in Ctrl- and RA-EHTs was investigated by immunofluorescence (left) and immunohistochemistry (right) analyses (adapted from Lemme et al. 2018).
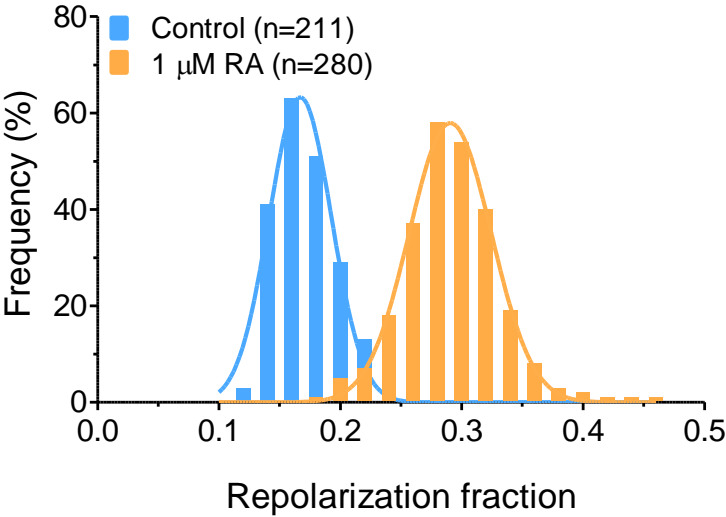
Figure S4: **Frequency distributions of repolarization fractions**. Repolarization fraction of Ctrl (n=211 wells, 2 batches) and RA-MLs (n=280 wells, 2 batches) calculated with CellOPTIQ.

118

Supplements
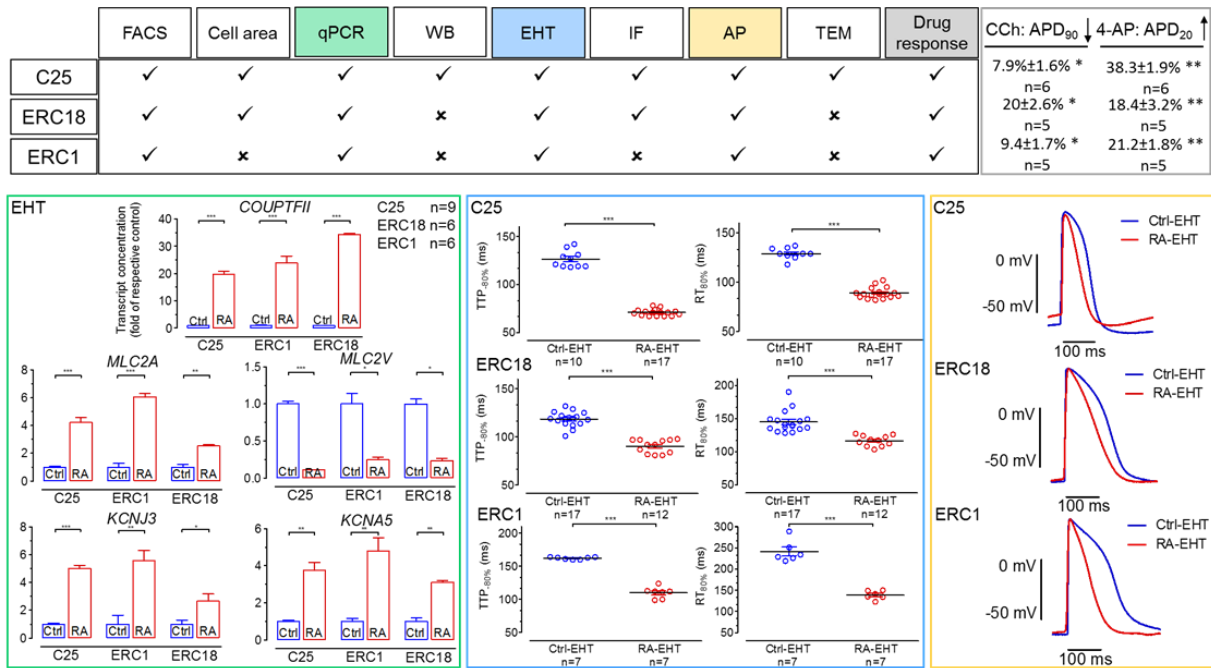
Figure S5: **Schematic overview of all the experiments performed on each control cell line (C25, ERC18 and ERC1)**. Expression of atrial-specific genes (green box), contraction analysis (blue box), AP recordings (yellow box) and response to atrial-selective drugs (grey box) were achieved in each cell line. n values represent EHT numbers obtained from 3 distinct batches of C25 and two batches of ERC18 and ERC1. Error bars show mean±SEM (adapted from Lemme et al. 2018).
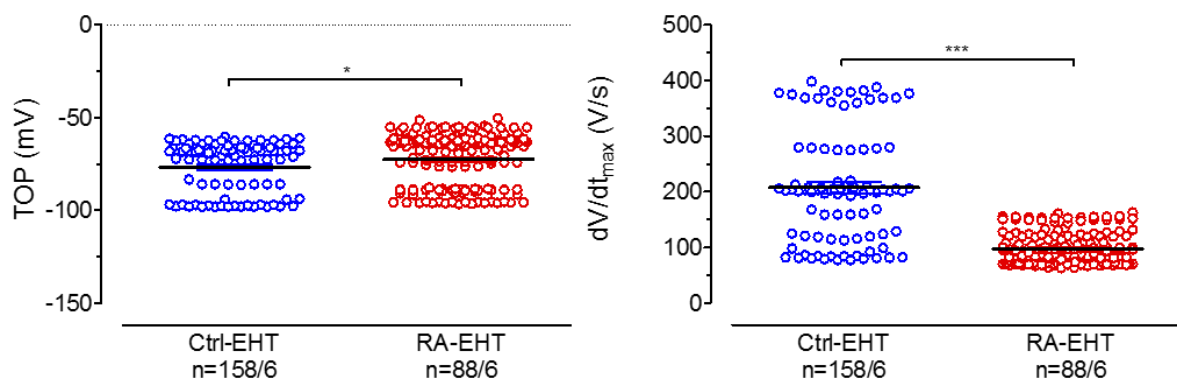
Figure S6: **Comparison of AP parameters between Ctrl- and RA-EHTs**. Take-off potential (TOP, left) and upstroke velocity (dV/dt$_{max}$, right) measured in Ctrl-EHTs (n=158/6, number of impalements/EHTs, 3 batches) and in RA-EHTs (n=88/6, number of impalements/EHTs, 3 batches). RA-EHTs showed a less negative TOP (-70±1.1 mV vs. -76±1.5 mV) with slower dV/dt$_{max}$ (97.6±2.4 V/s vs. 207.6±10.6 V/s, adapted from Lemme et al. 2018).

Supplements
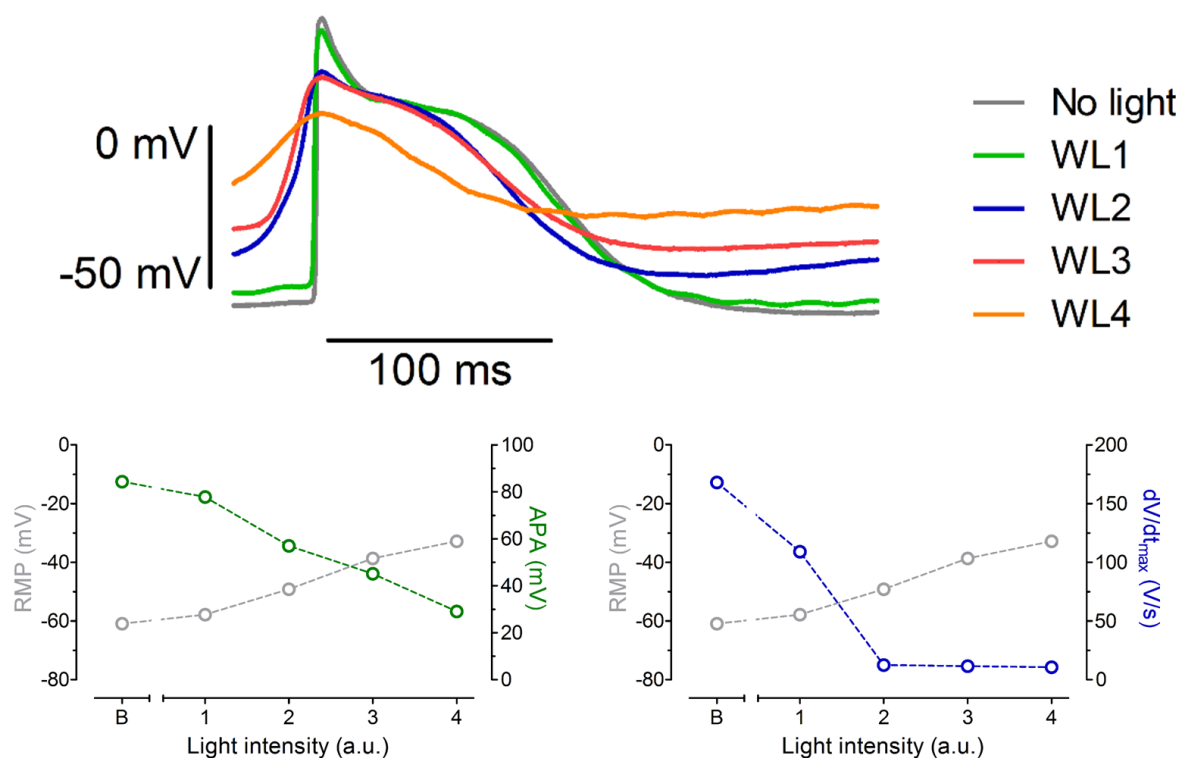
Figure S7: **Effect of white light illumination on action potential of ChR2-Ctrl-EHTs**. Action potentials (APs) of ChR2-Ctrl-EHTs recorded with sharp microelectrode. Original AP traces and AP parameters of ChR2-Ctrl-EHTs illuminated with 4 increasing levels of white light.
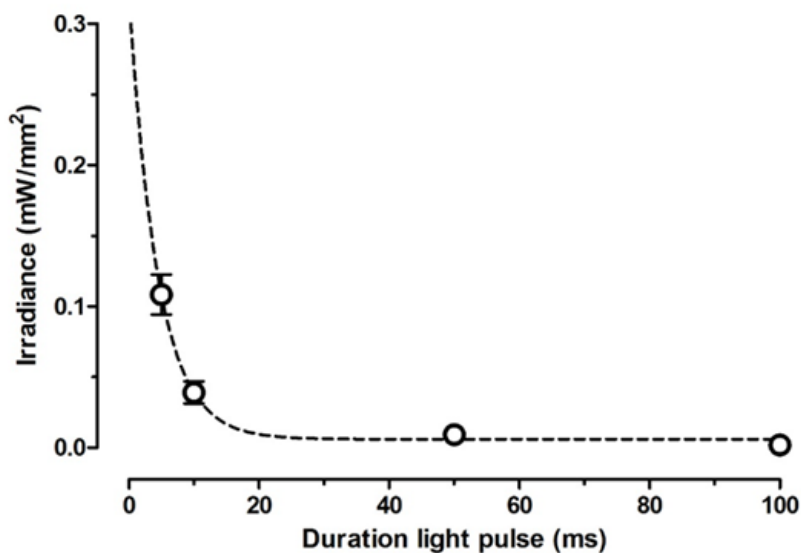
Figure S8: **Strength–duration curve of the custom-made optogenetic system**. The curve constructed by varying pulse duration and light intensity/irradiance (0.003–0.3 mW/mm^2). Duration of light pulse was fixed to 5, 10, 50 and 100 ms, whereas the lowest light intensity necessary to couple action potentials was evaluated by decreasing intensity until ChR2-Ctrl-EHTs could not follow the pacing rate. A nonlinear regression function was fitted to the data points.
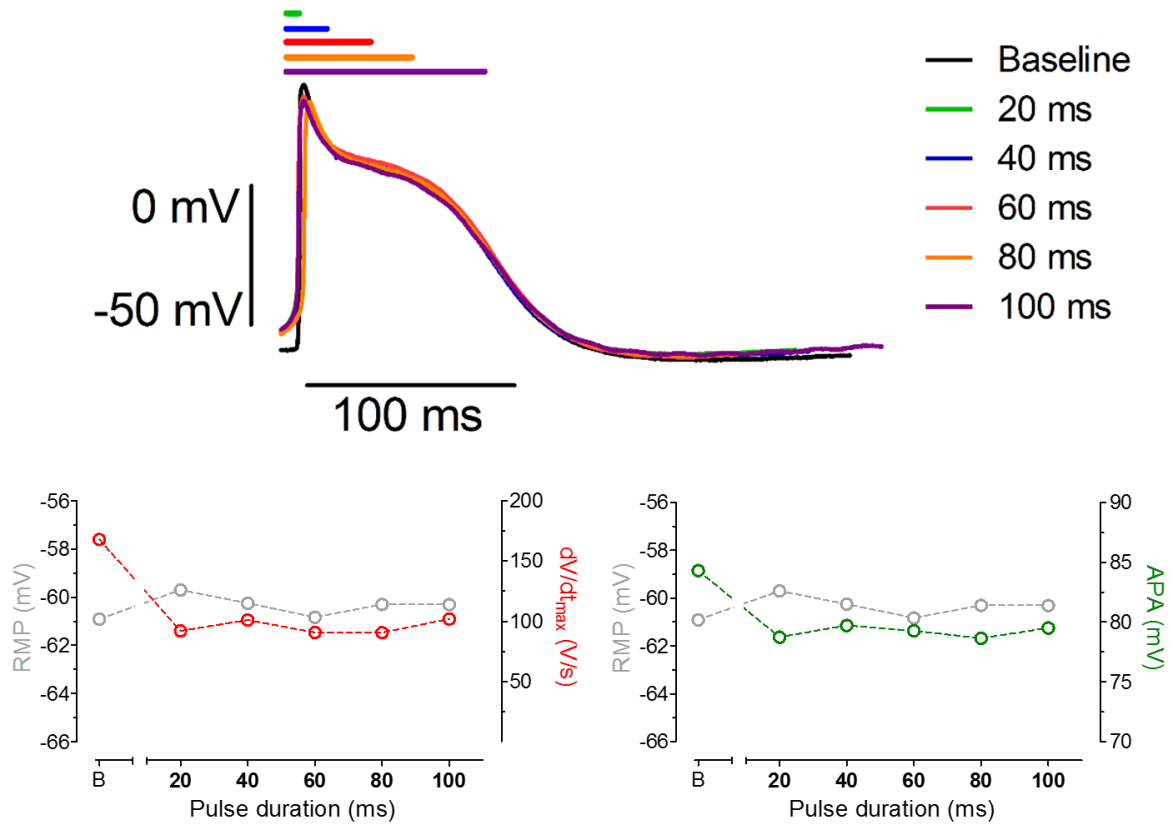
Figure S9: **Effect of different duration of blue light pulses**. Action potentials (APs) of ChR2-Ctrl-EHTs recorded with sharp microelectrode. Variation of blue light pulse duration (20, 40, 60, 80 and 100 ms) during optical pacing did not affect action potential.
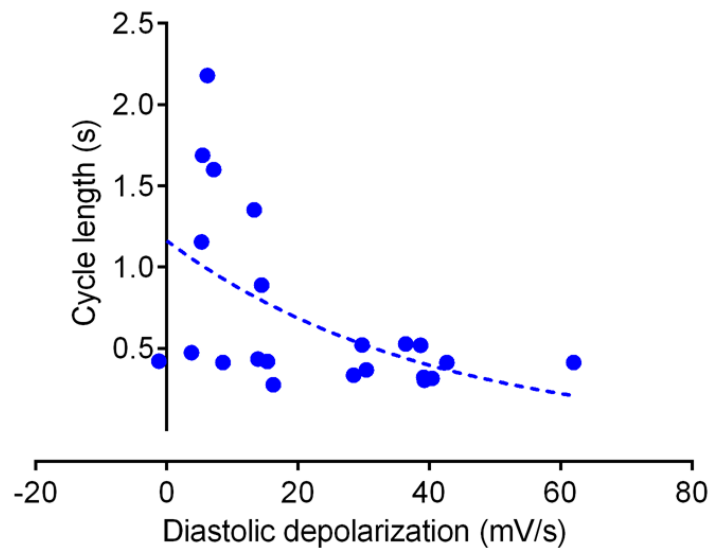
Figure S10: **Relation between diastolic depolarization (DD) and cycle length (CL) in ChR2-Ctrl-EHTs**. Action potentials of ChR2-Ctrl-EHTs measured with sharp microelectrode during spontaneous beating. One phase association demonstrated a weak correlation between DD and CL (R^2=0.27).

Supplements
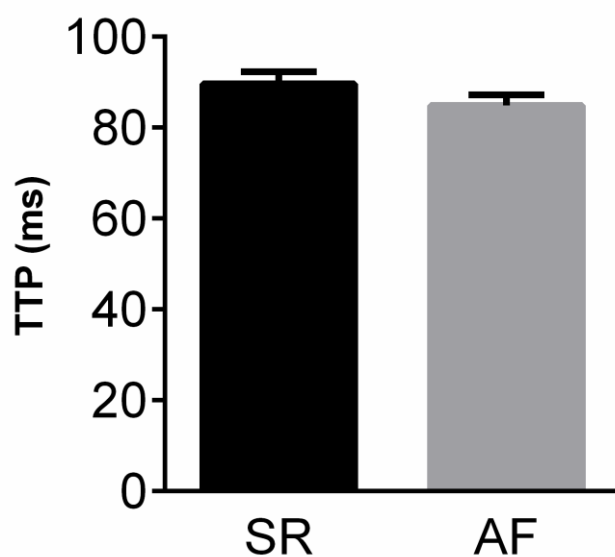
Figure S11: **Time to peak force (TTP) in atrial fibrillation (AF) vs. sinus rhythm (SR)**. Contractility of isolated trabeculae obtained from patients in SR and AF was measured with organ bath. TTP showed a tendency to decrease in AF (84.8±2.3 ms, n=42 trabeculae) compared to SR (89.6±2.6 ms, n=51 trabeculae).

7.2 Media, materials, reagents and devices

Table S1: Cell culture media.

Medium	Composition
FTDA	DMEM/F-12 without glutamine
	2 mmol/L L-glutamine
	1:1000 Lipid mix
	5 mg/L Transferrin
	5 μg/L Selenium
	0.1% (v/v) Human serum albumin
	5 μg/mL Human recombinant insulin
	2.5 ng/mL Activin-A
	30 ng/mL bFGF
	50 nmol/L Dorsomorphin
	0.5 ng/mL TGFß1
EB formation medium	FTDA
	4 mg/mL Polyvinyl alcohol
	10 μmol/L Y-27632
Basic cell culture medium	DMEM
	1% (v/v) Penicillin/streptomycin

Supplements

	10% (v/v) Heat inactivated fetal calf serum
Mesoderm induction medium	RPMI 1640 4 mg/mL Polyvinyl alcohol 10 mmol/L HEPES (pH 7.4) 0.05% (v/v) Human serum albumin 250 μmol/L Phosphoascorbate 5 mg/L Transferrin 5 μg/L Selenium 1:1000 Lipid mix 10 μmol/L Y-27632 3 ng/mL Activin-A 10 ng/mL BMP-4 5 ng/mL bFGF
Cardiac differentiation medium I	RPMI 1640 10 mmol/L HEPES (pH 7.4) 0.5% (v/v) Penicillin/streptomycin 0.05% (v/v) Human serum albumin 250 μmol/L Phosphoascorbate 1:1000 Lipid mix 1 μmol/L Y-27632 1 μmol/L XAV-939 5 mg/L Transferrin 5 μg/L Selenium 1 μmol/L Retinoic acid
Cardiac differentiation medium II	RPMI 1640 2% (v/v) B27 supplemented with insulin 10 mmol/L HEPES (pH 7.4) 0.5% (v/v) Penicillin/streptomycin 500 μmol/L 1-Thioglycerol 1 μmol/L Y-27632 1 μmol/L XAV-939
Cardiac differentiation medium III	RPMI 1640, 2% (v/v) B27 supplemented with insulin 10 mmol/L HEPES (pH 7.4) 0.5% (v/v) Penicillin/streptomycin 500 μmol/L 1-Thioglycerol 1 μmol/L Y-27632

Supplements

	DMEM
EHT casting medium	1% (v/v) Penicillin/streptomycin
	10% (v/v) Heat inactivated fetal calf serum
	2 mmol/L L-glutamine
	DMEM
	1% (v/v) Penicillin/streptomycin
EHT culture medium	10 µg/mL Human recombinant insulin
	10% (v/v) Horse serum
	33 µg/mL Aprotinin

Table S2: Primary antibodies.

Antibody	Details	Application and dilution	Company and order number
Anti-α actinin 2	Mouse monoclonal IgM, clone EA-53	WB (1:10000) IIHC/IF (1:800)	Sigma-Aldrich, A7811
Anti-cardiac troponin T-FITC	Recombinant human IgG1, clone REA400	FC (1:10)	Miltenyi Biotec, 130-106-687
REA Control (I)-FITC	Isotype control IgG1, clone REA400	FC (1:10)	Miltenyi Biotec 130-104-611
Anti-dystrophin	Purified mouse monoclonal IgG, clone 1808	IHC (1:200)	Merck, MAB1645
Anti-MLC2v	Mouse monoclonal purified IgG	IF (1:200)	Preteintech 10906-1-AP
Anti-ANP	Rabbit polyclonal IgG	WB (1:10000)	Abcam Ab91250
Anti-MLC2a	Mouse monoclonal purified IgG	WB (1:1000) IF (1:200)	Synaptic system 311011
Anti-PITX2	Rabbit polyclonal IgG	WB (1:250)	Invitrogen PA5-11479
Anti-COUPTFII	Mouse monoclonal purified IgG	WB (1:5000)	Perseus Proteomics H7147-00
Anti-CASQ2	Rabbit polyclonal IgG	WB (1:5000) IF (1:200)	Proteintech 18422-1-AP
Anti-α SMA	Mouse monoclonal purified IgG, clone 1A4	WB (1:1000) ICH (1:200)	RD system MAB1420

Supplements

Table S3: Secondary antibodies.

Antibody	Application and dilution	Company and order number
Alexa Fluor 488 goat anti-mouse IgG	IF (1:800)	Life technologies, A11029
Alexa Fluor 488 goat anti-rabbit IgG	IF (1:800)	Life technologies, A11034
Alexa Fluor 546 goat anti-rabbit IgG	IF (1:800)	Life technologies, A11010
Alexa Fluor 546 rabbit anti-mouse IgG	IF (1:800)	Life technologies, A11060
Anti-mouse IgG peroxidase-conjugated	WB (1:10000)	Sigma Aldrich, A3682
Anti-rabbit IgG peroxidase-conjugated	WB (1:10000)	Sigma Aldrich, A0545

Table S4: List of RT-qPCR primers.

Primer Name [HGNC gene name]		Primer Sequence [5'…3'] F: forward, R: reverse	Position CHR (GRCh37/ hg19)	Ampl. length [bp]	Primer T_m [°C]
COUPTFII	Chicken ovalbumin upstream promoter II	F: CCGAGTACAGCTGCCTCAA R: TTTTCCTGCAAGCTTTCCAC	Chr15: 96332648-96340955	91	59.41 57.11
COUPTFI	Chicken ovalbumin upstream promoter I	F: AAGCCATCGTGCTGTTCAC R: GCTCCTCAGGTACTCCTCCA	Chr5: 93586350-93595364	107	58.75 60.03
PITX2	Paired-like homeodomain transcription factor 2	F: AGCCATTCTTGCATAGCTCG R: GTGTGGACCAACCTTACGGA	Chr4: 110615342-110640316	109	58.41 59.61
IRX4	Iroquois Homeobox 4	F: TTGAGAGGTTAAGTTGGGGTTTG R: CCACCCAATTTCTAAAACTAATTACC	Chr5: 1878325-1878605	281	58.79 56.78
MLC2V	Myosin regulatory light chain 2, ventricular isoform	F: GATGTTCGCCGCCTTCCCCGC R: GCAGCGAGCCCCCTCCTAGT	Chr12: 110909841-110921578	106	68.75 66.01
MLC2A	Myosin regulatory light chain 2, atrial isoform	F: CACCGTCTTCCTCACACTCTT R: AGGCACTCAGGATGGCTTC	Chr7: 44138614-44141608	71	59.66 59.39
ANP	Atrial natriuretic peptide	F: ACAGGATTGGAGCCCAGAG R: GGAGCCTCTTGCAGTCTGTC	Chr1: 11845501-11847991	109	58.69 60.39
SLN	Sarcolipin	F: CTTGGTGTGCCCTCAGAAAT R: TCAGTCAATCCCAGGACCAT	Chr11: 107706906-107712530	179	58.08 58.03

KCNJ3	Potassium inwardly-rectifying channel, subfamily J, member 3	F: AAAAACGATGACCCCAAAGA R: TGTCGTCATCCTAGAAGGCA	Chr2: 154682604-154874329	98	55.46 58.15
KCNA5	Potassium voltage-gated channel subfamily A member 5	F: CGAGGATGAGGGCTTCATTA R: CTGAACTCAGGCAGGGTCTC	Chr12: 5043632-5047075	186	56.79 59.75
SK2	Small conductance calcium-activated potassium channel 2	F: ATGAGCAGCTGCAGGTACAA R: CTAGCTACTCTCTGATGAGG	Chr5: 114011956-114540550	1740	59.67 53.52
SK3	Small conductance calcium-activated potassium channel 3	F: GTTCTTTCACCCCCTCTTCTTTC R: TTGGCTTGCTTCGGTTCTCT	Chr1: 154680180-154887560	123	59.18 59.89
GUSB	β-Glucuronidase	F: AAACGATTGCAGGGTTTCAC R: CTCTCGTCGGTGACTGTTCA	Chr2: 140043116-142302796	171	57.21 59.41

Table S5: NanoString expression CodeSets.

HKG	Basic tag set		Arrhythmia extension tag set	
ABCF1	*ACTA1*	*FN1*	*ATP1A1*	*KCNJ11*
	ACTA2	*MEOX1*	*ATP1A2*	*KCNJ12*
ACTB	*ACTC1*	*MYH6*	*CACNA1C*	*KCNJ2*
	ACTN2	*MYH7*	*CACNA1G*	*KCNJ3*
CLTC	*ATP2A2*	*NFKB1*	*HCN4*	*KCNJ5*
	BAX	*NPPA*	*KCNA4*	*KCNMA1*
GAPDH	*BCL2*	*NPPB*	*KCNA5*	*KCNN3*
	CASP3	*PLN*	*KCND3*	*KCNQ1*
PGK1	*CASQ2*	*POSTN*	*KCNE1*	*SCN10A*
	CDH5	*PPP1R1A*	*KCNE2*	*SCN5a*
TUBB	*COL1A1*	*RCAN1*	*KCNH2*	*SLC8A1*
	COL3A1	*RYR2*	*KCNIP2*	*SLC9A1*
	CTGF	*S100A4*		
	FHL1	*SRF*		
	FHL2	*VWF*		

Supplements

Table S6: Composition of reagents, buffer and solutions.

Reagents, buffer and solutions	Composition
Agarose for EHT casting molds	2% (w/v) agarose dissolved in 300 mL 1xPBS Stored at 60 °C.
Antibody solution for immunofluorescence (EHT)	TBS 0.05 M (pH 7.4) 0.5% Triton X-100 1% BSA
Aprotinin	33 mg/mL Aprotinin dissolved in sterile water 250 µL aliquots stored at -20 °C up to one year
Blocking solution	TBS 0.05 mol/L (pH 7.4) 1% FCS 1% BSA 0.5% Triton X-100
Blotting buffer (5x)	125 mmol/L Trizma base 950 mmol/L Glycine Aqua dest
Blotting buffer (1x)	20% (v/v) 5x Blotting buffer 20% (v/v) Methanol 60% (v/v) Aqua dest
BTS solution	BTS dissolved in DMSO 250 µL aliquots stored at -20 °C up to one year
Dissociation buffer	HBSS without calcium/magnesium Collagenase II, 200 units/mL 1 mmol/L HEPES (pH 7.4) 30 µmol/L BTS 10 µmol/L Y-27632
DNase solution	100 mg DNase II dissolved in 50 mL 1xPBS 2 mL aliquots stored at -20 °C up to six months
EDTA	0.5 mmol/L EDTA in 1x PBS Stored at 4 °C
FACS buffer	PBS 5% (v/v) FCS 0,5% (w/v) Saponin 0,05% (v/v) Sodium azide
Fibrinogen	200 g/L fibrinogen dissolved in pre-warmed 0.9%-NaCl solution

Supplements

	33 g/L Aprotinin for a final concentration of 100 µg/mL
	Short term storage at -20 °C
	Long term storage at -80 °C
HEPES stock solution	1 mol/L HEPES in 1xPBS (pH 7.4)
	Stored at 4 °C for up to one year
Laemmli buffer (1x)	0.2 g SDS
	1 mg Bromphenol blue
	1 g Glycerol
	0.2 mL 0.5 M Tris (pH 6.8)
	0.155 g DTT
	Aqua dest
Permeabilization buffer for immunofluorescence (monolayers)	1x PBS
	3% (w/v) Milk powder
	0.1% (v/v) Triton X-100
Phosphoascorbate, 250 mM	1 g Phosphoascorbate
	12.4 mL PBS
Pluronic F-127 solution	1% (w/v) Pluronic F-127 dissolved in 1xPBS
	Stored at 4 °C up to one year.
Polyvinyl alcohol (50x)	20 g of polyvinyl alcohol dissolved in 100 mL of aqua dest
	Stored at 4 °C up to one year
SDS-PAGE electrophoresis buffer (10x)	250 mmol/L Trizma base
	1% or 50% (w/v) SDS
	1.92 mol/L Glycine
	Aqua dest
Separation gel SDS-Page	Acryl concentration (12%)
	Aqua dest (4.3 mL)
	40% Acrylamide (3.0 mL)
	1.5 mol/L Tris pH 8.8 (2.5 mL)
	10% SDS (0.1 mL)
	10% APS (0.1 mL)
	TEMED (4 µL)
Serum-free medium	DMEM
	1 mmol/L Sodium Pyruvate
	10 mmol/L Galactose

Supplements

Stacking gel SDS-Page	6.03 mL Aqua dest.
	1.28 mL 40% Acrylamide
	2.5 mL 0.5 M Tris (pH 6.8)
	0.1 mL 10% (w/v) SDS
	0.1 mL 10% (w/v) APS
	0.01 mL TEMED
TBS (10x)	1 mol/L Trizma base
	1.5 mol/L NaCl
	Aqua dest (pH 7.5)
Thrombin	100 U/mL Thrombin dissolved in 60% (v/v) 1xPBS and 40% (v/v) sterile water
	Stored at -20 °C for max. 1 year.
Transferrin–selenium	100 mg Transferrin dissolved in 2 mL sodium selenite (382 μmol/L)
	Stored at -80 °C up to six months
Transport solution	100 mmol/L NaCl
	10 mmol/L KCl
	1.2 mmol/L KH_2PO_4
	5 mmol/L $MgSO_4$
	50 mmol/L taurine
	5 mmol/L MOPS
	30 mmol/L BDM
Tris 0.5 M (pH 6.8)	60.6 g Trizma base
	1 L Aqua dest
Tris 1.5 M (pH 8.8)	181.7 g Trizma base
	1 L Aqua dest
Tyrode's solution	120 mmol/L NaCl
	5.4 mmol/L KCl
	1 mmol/L $MgCl_2$ x $6H_2O$
	22.6 mmol/L $NaHCO_3$
	5 mmol/L Glucose
	0.1-10 mmol/L $CaCl_2$
	0.4 mmol/L NaH_2PO_4
	0.05 mmol/L Na2EDTA
	25 mmol/L HEPES (pH 7.4)
	Aqua dest

Supplements

Table S7: Chemicals.

Product	Manufacturer, #
1,4-Dithiothreitol (DTT)	Roth, 6908.2
1-Thioglycerol	Sigma-Aldrich, M6145
2-Mercaptoethanol	Sigma-Aldrich, M6250
4-aminopyridine	Sigma-Aldrich, 275875
Accutase Cell Dissociation Reagent	Sigma-Aldrich, A6964
Acrylamide/Bis 40%	Bio-Rad Laboratories, 161-0146
Activin A	R&D Systems, 338-AC
Agarose	Invitrogen, 15510-027
Ammoniumpersulfate (APS)	Bio-Rad Laboratories, 161-0700
Aprotinin	Sigma-Aldrich, A1153
bFGF	PeproTech, 100-18B
B27 PLUS insulin	Gibco, 17504-044
BMP4	R&D Systems, 314-BP
BTS	TCI, B3082-25G
$CaCl_2$ x $2H_2O$	Merck, 2382
Carbachol	Sigma Aldrich, Y0000113
Collagenase II	Worthington, LS004176
cOmplete Mini, EDTA-free protease inhibitor cocktail	Roche, 11836153001
D(+)-Glucose anhydrous	Roth, X997.2
DAPI	Sigma Aldrich, D9564
Di-sodium hydrogen phosphate dihydrate (Na_2HPO_4-$2H_2O$)	Merck, 1065800
Di-4-ANEPPS	Thermo Fisher, D1199
DMEM	Biochrom, F0415
DMEM/F12	Gibco, 21331-046
DMEM High Glucose	Gibco, LS11965092
DMSO	Sigma-Aldrich, D4540
DNase	Sigma-Aldrich, D8764
Dorsomorphin	Tocris, 3093
DPBS	Gibco, 14040-133
EDTA	Roth, 8043.2
Ethanol, absolute	Chemsolute, 2246.1000
Ethidium bromide	Sigma-Aldrich, E1510
Fetal calf serum	Biochrom, S0615

Supplements

Fibrinogen	Sigma-Aldrich, F8630
Fibronectin	Sigma-Aldrich, F1141
Flecainide	Sigma-Aldrich, F6777
Fluo-4	Sigma-Aldrich F14201
Fluoromount-G	SouthernBiotech, 0100-01
Formaldehyde	Merck Millipore, 107022
Geltrex	Gibco, A1413302
GeneRuler 1 kb DNA Ladder	Thermo Fisher Scientific, SM0313
GeneRuler 100 bp DNA Ladder	Thermo Fisher Scientific, SM0243
HBSS minus Ca^{2+}/Mg^{2+}	Gibco, 14175-053
HEPES	Roth, 9105.4
Human serum albumin	Biological Industries, 05-720-1B
Human recombinant insulin	Sigma-Aldrich, I9278
Ivabradine	Sigma-Aldrich, SML0281
JTV-519	Sigma-Aldrich, SML0549
Knockout serum replacement	Gibco, 10828
L-Glutamine	Gibco, 25030-081
Lipidmix	Sigma-Aldrich, L5146
Matrigel Basement Membrane Matrix	Corning, 354234
Matrigel Growth Factor Reduced (GFR) Basement Membrane Matrix	Corning, 354230
Maxima SYBR Green/ROX	Thermo Scientific, K0243
Methanol	J. Baker, 8045
$MgCl_2$	Fuka, 63063
Milk powder	Roth, T145.2
M-PERTM Mammalian Protein Extraction Reagent	Thermo Fisher Scientific, 78501
N,N,N',N'-Tetramethyl ethylenediamine (TEMED)	Bio-Rad Laboratories, 161-0801
Osmium tetroxide solution	Science Services, 19110
Paraformaldehyde	Merck, 104005
Penicillin/streptomycin	Gibco, 15140
Periodic Acid	Carl Roth, 3257.1
Phosphoascorbate (2-Phospho-L-ascorbic acid trisodium salt)	Sigma-Aldrich, 49752
Pierce ECL Western Blotting Substrate	Thermo Fisher Scientific, 32106
Pluronic F-127	Sigma-Aldrich, P2443
Polyvinyl alcohol (PVA)	Sigma-Aldrich, P8136

Supplements

Potassium chloride (KCl)	Merck, 1.04936
Potassium di-hydrogen phosphate (KH_2PO_4)	Merck, 104873
Proteinase K	Thermo Scientific, 17916
Retinoic acid	Sigma-Aldrich, R2625
Roti-Histofix 4%	Roth, P087.3
RPMI 1640	Gibco, 21875
Saponin	Sigma-Aldrich, 47036 or Merck, 558255
Schiff's reagent	Carl Roth X900.2
Selenium	Sigma, S5261
Sodium azide	Sigma-Aldrich, 71290
Sodium chloride (NaCl)	JT Baker, 7647-14-5
Sodium di-hydrogen phosphate mono-hydrate (NaH_2PO_4 x H_2O)	Merck, 6346
Sodium hydrogen carbonate ($NaHCO_3$)	Merck, 106329
SuperSignal West Dura ECL	Thermo Fisher, 34075
TBS	Sigma-Aldrich, T6664
TGFß1	Peprotech, 100-21
Thrombin	Sigma-Aldrich, T7513; Biopur, BP11-10-1104
Transferrin	Sigma-Aldrich, T8158
Triton X-100	Roth, 3051.3
Trizma base	Sigma-Aldrich, T1503
Trypan blue	Biochrom, L 6323
Trypsin-EDTA (0.05%), phenol red	Thermo Fisher Scientific, 25300054
Tween 20	Sigma-Aldrich, P1379
XAV-939	Tocris, 3748
Y-27632	Biaffin, PKI-Y27632-010

Table S8: Consumable materials.

Product	Manufacturer, #
250 mL Vacuum Filtration "rapid"-Filtermax	TPP, 99500
500 mL Vacuum Filtration "rapid"-Filtermax	TPP, 99500
Aspiration pipette 2 mL	Sarstedt, 86.1252.011
Cell culture flask T175	Sarstedt, 83.3911.002
Cell culture flask T80	Nunc, 178905

Supplements

Cell culture flask T75/T175 for suspension culture	Sarstedt, 83.3911/2.502
Cell culture microplate 96 well µClear black CELLSTAR	Greiner Bio-One, 655090
Cell culture 96-well glass bottom plates	MatTek, p96G-1.5-5-F
Cell culture plate 6 / 12 / 24-well	Nunc
Cell scraper	Sarstedt, 83.1830
Cell strainer 30 µm	Sysmex, 04-004-2326
Cryovial CryoPure 1.6 mL	Sarstedt, 72.380
Flow cytometry tubes	Sarstedt, 55.1579
Light emitting diode (red)	NSPR510CS Nichia
Light emitting diode (blue)	NSPB510BS Nichia
Neubauer counting chamber	Karl-Hecht KG
Pacing adapter/cables	EHT Technologies, P0002
Pacing electrode carbon	EHT Technologies, P0001
Pipette tips	Sarstedt
Pipette tips with Biosphere filter	Sarstedt
Reaction tube graduated 15 mL	Sarstedt, 62.554.502
Reaction tubes conical 15 / 50 mL	Sarstedt
Reaction tubes Safe Lock 0.2 – 2 mL	Eppendorf
Round bottom tube 12 mL	Greiner Bio-One, 163160
Serological pipettes 1 / 2 / 5 / 10 / 25 / 50 mL	Sarstedt
Silicone rack	EHT Technologies, C0001
Slides with moulds	Carl Roth, H884.1
Polystyrene Particle Size	Spherotech, PPS-6K
Spinner flasks 500 / 1000 mL	Integra Biosciences, 182101 / 182051
Syringe filtration unit Filtropur S 0.2 µm	Sarstedt, 83.1826.001
Teflon Spacer	EHT Technologies, C0002
TissueLyser Steel Beads	QIAGEN, 69989

Table S9: Kits.

Kit	Manufacturer
Cyto tune kit	Life technologies
High-Capacity cDNA Reverse Transcription Kit	Applied Biosystems, 4368813
RNeasy Plus Mini Kit	QIAGEN, 74134
Ultra View Universal DAB Detection Kit	Ventana, 05269806001

Supplements

Table S10: Laboratory devices.

Product	Manufacturer
AbiPrism7900HT cycler	Applied Biosystems
Analytic Scale Genius	Sartorius AG
BD FACSCantoTM II	BD Biosciences
Benchmark XT	Ventana
Bioanalyzer 2100	Agilent
Cell culture incubator	Binder
Cell culture incubators S2020 1.8, HERAcell 240 & 150i	Thermo Fischer Scientific
Cell culture incubators MCO-19M & MCO-20AIC	Sanyo
CellOPTIQ	Clyde Bioscience
Centrifuges 5415 R & 5810 R	Eppendorf
Centrifuge J-6B	Beckmann
Centrifuges Rotanta/RP & Universal 30 RF	Hettich
ChemiDocTM Touch Imaging System	Bio-Rad Laboratories
Confocal microscope (LSM800, Airyscan)	Zeiss
Confocal microscope Nikon A1	Nikon
Cryopreservation system Asymptote EF600M	Grant Instruments
Electrophoretic Transfer Cell Mini Trans-Blot cell	Bio-Rad Laboratories
Gel electrophoresis cell Mini-PROTEAN 3 Cell	Bio-Rad Laboratories
Gel electrophoresis tank Sub-cell GT	Bio-Rad Laboratories
Inverted microscope IX73	Olympus
Magnetic stirring and heating plate IKA Combimag RET	Janke & Kunkel & Co KG
Magnetic stirring plate Variomag / Cimarec Biosystem Direct	Thermo Scientific
Magnetic stirring plate Variomag / Cimarec Biosystem 4 Direct	Thermo Scientific
Microscope Axioskop 2 with AxioCam Color	Zeiss
Microscope Axiovert 25 with ProgRes Speed XT core 5 camera	Jenoptik
Microscope EVOS FL Cell Imaging System	Thermo Fischer Scientific
NanoDrop ND-1000 Spectrophotometer	Thermo Fischer Scientific
nCounter SPRINT	NanoString
ORCA-flash4.0 V2 digital CMOS camera	Hamamatsu
Paraffin Dispenser EG 1120	Leica
Photomultiplier	Cairn Research
Pipettes 10 / 100 / 1000 μL	Eppendorf

Supplements

Pipette controller Accu-jet pro	Brand
Power supply PowerPac Bacic	Bio-Rad Laboratories
Precision Advanced Scale	Ohaus
Puller DMZ	Hilgenberg
S88X dual output square pulse stimulator	Grass
Safety workbench HeraSafe	Heraeus
Safety workbench Safe 2020	Thermo Fischer Scientific
Thermal cycler Hybaid PCR Sprint	Thermo Fischer Scientific
Thermal cycler vapo.protect	Eppendorf
Thermomixer comfort	Eppendorf
TissueLyser	QIAGEN
Transmission electron microscope LEO 912AB	Zeiss
UltraCut-E microtome	Leica Reichert Jung
Video-optical EHT analysis system	EHT Technologies GmbH

Table S11: Laboratory softwares.

Software name	Software owner
AxioVision Rel. 4.8.2	Zeiss
LabChart 5	ADInstruments
CytoVision image analysis system	Leica Biosystems
CTMV	Proprietary software
FACSDiva	BD Biosciences
GraphPad Prism 5.0	GraphPad Software
Image Lab Version 5.2.1	Bio-Rad Laboratories
ImageJ 1.47v	Wayne Rasband
LSM 800 Airyscan	Zeiss
Musclemotion	Proprietary software
NIS Elements Advanced Research software	Nikon
nSolver 4.0	Nanostring
ProgRes Capture Pro 2.8.8	Jenoptik
SDS 2.4.1	Applied Biosystem
SnapGene 3.3.4	SnapGene
Zen	Zeiss

Supplements

Table S12: List of GHS Hazard and Precautionary Statements (H-codes).

H statement	H phrases
H200	Unstable explosives.
H201	Explosive; mass explosion hazard.
H202	Explosive, severe projection hazard.
H203	Explosive; fire, blast or projection hazard.
H204	Fire or projection hazard.
H205	May mass explode in fire.
H220	Extremely flammable gas.
H221	Flammable gas.
H222	Extremely flammable aerosol.
H223	Flammable aerosol.
H224	Extremely flammable liquid and vapor.
H225	Highly flammable liquid and vapor.
H226	Flammable liquid and vapor.
H228	Flammable solid.
H229	Pressurized container: May burst if heated.
H230	May react explosively even in the absence of air.
H231	May react explosively even in the absence of air at elevated pressure and/or temperature
H240	Heating may cause an explosion.
H241	Heating may cause a fire or explosion.
H242	Heating may cause a fire.
H250	Catches fire spontaneously if exposed to air.
H251	Self-heating: may catch fire.
H252	Self-heating in large quantities; may catch fire.
H260	In contact with water releases flammable gases which may ignite spontaneously
H261	In contact with water releases flammable gases.
H270	May cause or intensify fire; oxidizer.
H271	May cause fire or explosion; strong oxidizer.
H272	May intensify fire; oxidizer.
H280	Contains gas under pressure; may explode if heated.
H281	Contains refrigerated gas; may cause cryogenic burns or injury.
H290	May be corrosive to metals.
H300	Fatal if swallowed.

Supplements

H300 + H310	Fatal if swallowed or in contact with skin.
H300 + H310 + H330	Fatal if swallowed, in contact with skin or if inhaled.
H300 + H330	Fatal if swallowed or if inhaled.
H301	Toxic if swallowed.
H301 + H311	Toxic if swallowed or in contact with skin.
H301 + H311 + H331	Toxic if swallowed, in contact with skin or if inhaled.
H301 + H331	Toxic if swallowed or if inhaled.
H302	Harmful if swallowed.
H302 + H312	Harmful if swallowed or in contact with skin.
H302 + H312 + H332	Harmful if swallowed, in contact with skin or if inhaled.
H302 + H332	Harmful if swallowed or if inhaled.
H304	May be fatal if swallowed and enters airways.
H310	Fatal in contact with skin.
H310 + H330	Fatal in contact with skin or if inhaled.
H311	Toxic in contact with skin.
H311 + H331	Toxic in contact with skin or if inhaled.
H312	Harmful in contact with skin.
H312 + H332	Harmful in contact with skin or if inhaled.
H314	Causes severe skin burns and eye damage.
H315	Causes skin irritation.
H317	May cause an allergic skin reaction.
H318	Causes serious eye damage.
H319	Causes serious eye irritation.
H330	Fatal if inhaled.
H331	Toxic if inhaled.
H332	Harmful if inhaled.
H334	May cause allergy or asthma symptoms or breathing difficulties if inhaled.
H335	May cause respiratory irritation.
H336	May cause drowsiness or dizziness.
H340	May cause genetic defects.
H341	Suspected of causing genetic defects.
H350	May cause cancer.
H351	Suspected of causing cancer.
H360	May damage fertility or the unborn child.
H361	Suspected of damaging fertility or the unborn child.

Supplements

H362	May cause harm to breast-fed children.
H370	Causes damage to organs.
H371	May cause damage to organs.
H372	Causes damage to organs through prolonged or repeated exposure.
H373	May cause damage to organs through prolonged or repeated exposure.
H400	Very toxic to aquatic life.
H410	Very toxic to aquatic life with long lasting effects.
H411	Toxic to aquatic life with long lasting effects.
H412	Harmful to aquatic life with long lasting effects.
H413	May cause long lasting harmful effects to aquatic life.
H420	Harms public health and the environment by destroying ozone in the upper atmosphere.

Table S13: List of GHS Hazard and Precautionary Statements (P-codes).

P statement	P phrase
P301+P310	IF SWALLOWED: Immediately call a POISON CENTRE/doctor/….
P301+P312	IF SWALLOWED: Call a POISON CENTRE/doctor/… if you feel unwell.
P301+P330+ P331	IF SWALLOWED: Rinse mouth. Do NOT induce vomiting.
P302+P334	IF ON SKIN: Immerse in cool water [or wrap in wet bandages].
P302+P335+ P334	IF ON SKIN: Brush off loose particles from skin. Immerse in cool water [or wrap in wet bandages].
P302+P352	IF ON SKIN: Wash with plenty of water/…
P303+P361+ P353	IF ON SKIN (or hair): Take off immediately all contaminated clothing. Rinse skin with water [or shower].
P304+P340	IF INHALED: Remove person to fresh air and keep comfortable for breathing.
P305+P351+ P338	IF IN EYES: Rinse cautiously with water for several minutes. Remove contact lenses, if present and easy to do. Continue rinsing.
P 306+P360	IF ON CLOTHING: rinse immediately contaminated clothing and skin with plenty of water before removing clothes.
P308+P311	IF exposed or concerned: Call a POISON CENTRE/doctor/…
P308+ P313	IF exposed or concerned: Get medical advice/attention.

Supplements

P101	If medical advice is needed, have product container or label at hand.
P102	Keep out of reach of children.
P103	Read label before use.
P201	Obtain special instructions before use.
P202	Do not handle until all safety precautions have been read and understood.
P210	Keep away from heat, hot surfaces, sparks, open flames and other ignition sources. No smoking.
P211	Do not spray on an open flame or other ignition source.
P220	Keep away from clothing and other combustible materials.
P222	Do not allow contact with air.
P223	Do not allow contact with water.
P230	Keep wetted with…
P231	Handle and store contents under inert gas/…
P231+P232	Handle and store contents under inert gas/… Protect from moisture.
P232	Protect from moisture.
P233	Keep container tightly closed.
P234	Keep only in original packaging.
P235	Keep cool.
P240	Ground and bond container and receiving equipment.
P241	Use explosion-proof [electrical/ventilating/lighting/…] equipment.
P242	Use non-sparking tools.
P243	Take action to prevent static discharges.
P244	Keep valves and fittings free from oil and grease.
P250	Do not subject to grinding/shock/friction/…
P251	Do not pierce or burn, aven after use.
P260	Do not breathe dust/fume/gas/mist/vapors/spray.
P261	Avoid breathing dust/fume/gas/mist/vapors/spray.
P262	Do not get in eyes, on skin, or on clothing.
P263	Avoid contact during pregnancy and while nursing.
P264	Wash … thoroughly after handling.
P270	Do not eat, drink or smoke when using this product.
P271	Use only outdoors or in a well-ventilated area.
P272	Contaminated work clothing should not be allowed out of the workplace.

Supplements

P273	Avoid release to the environment.
P280	Wear protective gloves/protective clothing/eye protection/face protection.
P282	Wear cold insulating gloves and either face shield or eye protection.
P283	Wear fire resistant or flame retardant clothing.
P284	[In case of inadequate ventilation] wear respiratory protection.
P301	IF SWALLOWED:
P302	IF ON SKIN:
P303	IF ON SKIN (or hair)
P304	IF INHALED:
P305	IF IN EYES:
P306	IF ON CLOTHING:
P308	IF exposed or concerned:
P310	Immediately call a POISON CENTRE/doctor/…
P311	Call a POISON CENTRE/doctor/….
P312	Call a POISON CENTRE/doctor/… if you feel unwell.
P313	Get medical advice/attention.
P314	Get medical advice/attention if you feel unwell.
P315	Get immediate medical advice/attention.
P320	Specific treatment is urgent (see … on this label).
P321	Specific treatment (see … on this label).
P330	Rinse mouth.
P331	Do NOT induce vomiting
P332	If skin irritation occurs:
P332+P313	If skin irritation occurs: Get medical advice/attention.
P333	If skin irritation or rash
P333+P313	If skin irritation or rash occurs: Get medical advice/attention.
P334	Immerse in cool water [or wrap in wet bandages].
P335	Brush off loose particles from skin.
P336	Thaw frosted parts with lukewarm water. Do no rub affected area.
P336+P315	Thaw frosted parts with lukewarm water. Do not rub affected area. Get immediate medical advice/attention.
P337	If eye irritation persists:
P337+P313	If eye irritation persists: Get medical advice/attention.
P338	Remove contact lenses, if present and easy to do. Continue rinsing.

Supplements

P340	Remove person to fresh air and keep comfortable for breathing.
P342	If experiencing respiratory symptoms:
P342+P311	If experiencing respiratory symptoms: Call a POISON CENTRE/doctor/…
P351	Rinse cautiously with water for several minutes.
P352	Wash with plenty of water/…
P353	Rinse skin with water [or shower].
P360	Rinse immediately contaminated clothing and skin with plenty of water before removing clothes.
P361	Take off immediately all contaminated clothing.
P361+P364	Take off immediately all contaminated clothing and wash it before reuse.
P362	Take off contaminated clothing.
P362+P364	Take off contaminated clothing and wash it before reuse.
P363	Wash contaminated clothing before reuse.
P364	And wash it before reuse.
P370+P372+ P380+ P373	In case of fire: Explosion risk. Evacuate area. DO NOT fight fire when fire reaches explosives.
P370+P376	In case of fire: Stop leak if safe to do so.
P370+P378	In case of fire: Use … to extinguish.
P370+P380+ P375	In case of fire: Evacuate area. Fight fire remotely due to the risk of explosion.
P370+P380+ P375 [+P378]	In case of fire: Evacuate area. Fight fire remotely due to the risk of explosion. [Use … to extinguish]. P371+P380+P375 In case of major fire and
P371	In case of major fire and large quantities:
P372	Explosion risk.
P373	DO NOT fight fire when fire reaches explosives.
P375	Fight fire remotely due to the risk of explosion.
P376	Stop leak if safe to do so.
P377	Leaking gas fire: Do not extinguish, unless leak can be stopped safely.
P378	Use … to extinguish.
P380	Evacuate area. P381 In case of leakage
P390	Absorb spillage to prevent material damage.
P391	Collect spillage.
P401	Store in accordance with…
P402	Store in a dry place.

Supplements

P402+P404	Store in a dry place. Store in a closed container.
P403	Store in a well-ventilated place.
P403+P233	Store in a well-ventilated place. Keep container tightly closed.
P403+P235	Store in a well-ventilated place. Keep cool.
P404	Store in a closed container.
P405	Store locked up.
P406	Store in a corrosion resistant/… container with a resistant inner liner.
P407	Maintain air gap between stacks or pallets.
P410	Protect from sunlight.
P410+P403	Protect from sunlight. Store in a well-ventilated place.
P410+P412	Protect from sunlight. Do not expose to temperatures exceeding 50°C/ 122°F.
P411	Store at temperatures not exceeding …°C/…°F.
P412	Do not expose to temperatures exceeding 50°C/ 122°F.
P413	Store bulk masses greater than … kg/… lbs at temperatures not exceeding …°C/…°F.
P420	Store separately.
P501	Dispose of contents/container to …
P502	Refer to manufacturer or supplier for information on recovery or recycling.

7.3   List of abbreviations

A	
α-MHC	α-Myosin heavy chain
ACTA2	Alpha smooth muscle actin
ACTB	Beta-actin
ACTC1	Cardiac muscle alpha actin
ACTN2	Alpha-actinin 2
AF	Atrial fibrillation
ANP	Atrial natriuretic peptide
AP	Action potential
APA	Action potential amplitude
APD	Action potential duration
APS	Ammonium persulfate
Aqua dest	Aqua destillata (distilled water)

Supplements

ATP	Adenosine triphosphate
ATP1A1	Sodium/potassium-transporting ATPase subunit alpha-1
ATP1A2	ATPase, Na+/K+ transporting, alpha 2 (+) polypeptide
ATP2A2	Sarco/endoplasmic reticulum Ca2+-ATPase
AV	Atrioventricular
B	
β-MHC	β-Myosin heavy chain
BAX	Bcl-2-associated X protein
BCL2	B-cell lymphoma 2
BDM	Butanedione monoxime
bFGF	Basic fibroblast growth factor
BMP-4	Bone-morphogenetic protein 4
BNP	Brain natriuretic peptide
bpm	Beats per minute
BSA	Bovine serum albumin
C	
CACNA1C	Calcium channel, voltage-dependent, L type, alpha 1C subunit
CACNA1G	Calcium channel, voltage-dependent, T type, alpha 1G subunit
CaMKII	Ca2+/calmodulin-dependent protein kinase II
CASP3	Caspase 3
CASQ2	Calsequestrin 2
CDH5	Cadherin 5
cDNA	Complementary DNA
ChR2	Channelrhodopsin 2
ChR2-Ctrl-EHT	Ventricular-like engineered heart tissue transduced with ChR2
ChR2-RA-EHT	Atrial-like engineered heart tissue transduced with ChR2
CLTC	Clathrin heavy chain 1
CM	Cardiomyocytes
COL1A1	Alpha-1 type I collagen
COL3A1	Collagen alpha-1(III) chain

COUPTFI	Chicken ovalbumin upstream promoter transcription factor I
COUPTFII	Chicken ovalbumin upstream promoter transcription factor II
CPVT	Catecholaminergic polymorphic ventricular tachycardia
CTGF	Connective tissue growth factor
c-Myc	Cellular myelocytomatosis
Ct	Cycle threshold
cTnI	Cardiac troponin I
cTnT	Cardiac troponin T
Ctrl	Control
Ctrl-EHT	Ventricular-like engineered heart tissue
CV	Conduction velocity
D	
DD	Diastolic depolarization
DAD	Delayed afterdepolarization
DMEM	Dulbecco's Modified Eagle Medium
DMSO	Dimethyl sulfoxide
DNA	Deoxyribonucleic acid
dNTP	Deoxy-nucleoside triphosphate
DTT	Dithiothreitol
dV/dtmax	Maximum upstroke velocity
E	
EAD	Early afterdepolarization
EB	Embryoid body
ECG	Electrocardiograph
ECM	Extracellular matrix
EDTA	Ethylenediaminetetraacetic acid
EHT	Engineered heart tissue
ERP	Effective refractory period
ESC	Embryonic stem cell
F	
FACS	Fluoresence-activated cell sorting
FCS	Fetal calf serum

Supplements

FFR	Force-frequency relationship
FHL1	Four and a half LIM domains protein 1
FHL2	Four and a half LIM domains protein 2
FITC	Fluorescein isothiocyanate
FN1	Fibronectin
FSC	Forward scatter
FTDA	bFGF, TGFβ1, dorsomorphin and activin A-based hiPSC culture medium
G	
GAPDH	Glyceraldehyde 3-phosphate dehydrogenase
GF	Growth factor
GFP	Green fluorescent protein
GUSB	Beta-glucuronidase
H	
h	Hour
HBSS	Hanks' Balanced Salt Solution
HCN4	Potassium/sodium hyperpolarization-activated cyclic nucleotide-gated channel 4
HEPES	4-(2-hydroxyethyl)-1-piperazineethanesulfonic acid
hERG	Human ether a-go-go-related gene
hESC	Human embryonic stem cell
HIF	hypoxia-inducible factor
hiPSC	Human induced pluripotent stem cell
hiPSC-CMs	Human induced pluripotent stem cell derived cardiomyocytes
hPSC	Human pluripotent stem cell
HRC	Histidine-rich calcium-binding protein
Hz	Hertz
I	
IEPT	Institute of Experimental Pharmacology and Toxicology
I_{CaL}	L-type Ca2+ current
I_f	Pacemaker current
IHC	Immunohistochemistry
I_{K1}	Inwardly rectifying potassium current

Supplements

I_{KACh}	Acetylcholine activated potassium current
I_{KAChC}	Constitutively active acetylcholine-dependent current
I_{KATP}	ATP-sensitive potassium current
I_{kr}	Rapid delayed rectifier potassium current
I_{ks}	Slow delayed rectifier potassium current
I_{Kur}	Ultra-rapidly activating delayed rectifier K+ current
I_{Na}	Sodium current
I_{NaL}	Late Na+ current
I_{NCX}	Sodium-calcium exchanger current
iPSC	Induced pluripotent stem cell
IRX4	Iroquois Homeobox 4
I_{to}	Transient outward potassium current
K	
KCl	Potassium chloride
KCNA4	Potassium voltage-gated channel subfamily A member 4
KCNA5	Potassium voltage-gated channel, shaker-related subfamily, member 5
KCND3	Potassium voltage-gated channel subfamily D member 3
KCNE1	Potassium voltage-gated channel subfamily E member 1
KCNE2	Potassium voltage-gated channel subfamily E member 2
KCNH2	human Ether-à-go-go-Related Gene (hERG)
KCNIP2	Kv channel-interacting protein 2
KCNJ11	Potassium voltage-gated channel subfamily J member 11
KCNJ12	ATP-sensitive inward rectifier potassium channel 12
KCNJ2	Potassium voltage-gated channel subfamily J member 2
KCNJ3	Potassium inwardly-rectifying channel, subfamily J, member 3
KCNJ5	G protein-activated inward rectifier potassium channel 4
KCNMA1	Calcium-activated potassium channel subunit alpha-1
KCNN3	Small conductance calcium-activated potassium channel 3

Supplements

KCNQ1	Potassium voltage-gated channel subfamily Q member 1
kDa	Kilodalton
Klf4	Kruppel-like factor 4
L	
LED	Light emitting diode
LV	Left ventricle
LTCC	Voltage-dependent L-type calcium channel
M	
MEOX1	Homeobox protein MOX-1
min	Minutes
ml	milliliters
ML	Monolayer
MLC2a	Myosin regulatory light chain 2, atrial isoform
MLC2v	Myosin regulatory light chain 2, ventricular isoform
mm	Millimiters
mN	Millinewton
MOI	Multiplicity Of Infection
mRNA	Messenger RNA
MYH6	Myosin heavy chain, α isoform
MYH7	Myosin heavy chain, β isoform
N	
NaOH	Sodium hydroxide
Na,K-ATPase	Sodium-potassium ATPase
NC	Nitrocellulose
NCX	Sodium-calcium exchanger
NFKB1	Nuclear factor NF-kappa-B
NPPA (or ANP)	Atrial natriuretic peptide
NPPB	Brain natriuretic peptide
O	
Oct4	Octamer-binding transcription factor 4
P	
PAS	Periodic Acid-Schiff
PBS	Phosphate-buffered saline

Supplements

PCR	Polymerase chain reaction
PGK1	Phosphoglycerate kinase 1
PKA	Protein kinase A
PLN	Phospholamban
PMCA	plasmamembrane calcium ATPase
POSTN	Periostin
PPAR	Peroxisome proliferator-activated receptor gamma
PPP1R1A	Protein phosphatase 1 regulatory subunit 1A
PS	Phase singularity
PS-iPSCs	Patient-specific iPSCs
PTFE	Polytetrafluoroethylene
PV	Pulmonary veins
PVDF	Polyvinylidene fluoride
Q	
qPCR	Quantitative real-time PCR
R	
RA	Retinoic acid
RA-EHT	Atrial-like engineered heart tissue
RAA	Right atrial appendage
RCAN1	Regulator of calcineurin 1
RMP	Resting membrane potential
RNA	Ribonucleic acid
RP	Refractory period
RPMI	Roswell Park Memorial Institute
RT	Room temperature
RyR2	Ryanodine receptor 2
S	
S100A4	S100 calcium-binding protein A4
SCN10A	Sodium voltage-gated channel alpha subunit 10
SCN5a	Sodium voltage-gated channel alpha subunit 5
SDS	Sodium dodecyl sulfate
SEM	Standard error of the mean
SERCA2a	Sarco/endoplasmic reticulum Ca^{2+}-ATPase
SK	Small conductance calcium-activated potassium

SLC8A1	Sodium-calcium exchanger
SLC9A1	Sodium-hydrogen antiporter 1
SLN	Sarcolipin
Sox2	Sex determining region Y-box 2
SR	Sarcoplasmic reticulum
SSC	Sideward scatter
T	
TBS	Tris-buffered saline
TEMED	Tetramethylethylenediamine
TGFβ	Transforming growth factor-β
Tm	Melting temperature
TN-C	Troponin-C
TOP	Take-off potential
TTP	Time to peak
TU	Transducing units
TUBB	Tubulin beta chain
U	
U	Unit
UKE	University Medical Center Hamburg Eppendorf
V	
V	Volt
VWF	Von Willebrand factor
W	
WB	Western Blot
WL	Wavelength
Others	
°C	Degree Celsius
µL	Microliter
2D	Two-dimensional
3D	Three-dimensional

8. Abstract

Atrial fibrillation (AF) is the most common cardiac arrhythmia occurring in about 2% of the general population. Current pharmacological therapies for AF are limited by low efficacy and disastrous side effects. Human atrial tissue is an invaluable model to develop new therapeutic options. However, access to human tissue is limited. Cardiomyocytes (CMs) generated from human induced pluripotent stem cells (hiPSCs) have repeatedly demonstrated their potential in disease modeling and preclinical drug development. However, they are predominantly ventricular-like myocytes. It was previously shown that all-trans retinoic acid (RA) favors atrial CMs differentiation from human pluripotent stem cells (hPSC). Here, hiPSC obtained from healthy donors were treated with RA (1 µmol/L) to differentiate them into atrial-like myocytes. RA-treated and Ctrl hiPSC-CMs resembling atrial and ventricular-like myocytes respectively were used to cast 3D engineered heart tissues (EHTs). Atrial-like EHTs exhibited important structural, molecular and functional characteristics of adult human atrium. Atrial and ventricular phenotype of EHTs was confirmed by direct comparison to left ventricular and right atrial tissues derived from patients undergoing open heart surgery.

Chronic tachypacing is commonly used in animals to induce cardiac dysfunction and to study mechanisms of heart failure and sustained arrhythmias (such as AF). Atrial-like EHTs were generated to investigate whether they can be used as a model for human AF. Optogenetic pacing was applied to avoid cell toxicity by long-term electrical pacing. Optogenetic is based on the use of channelrhodopsin 2 (ChR2), a light sensitive ion channel that once activated by blue light (470 nm), allows influx of cations, mainly Na^+ leading to depolarization and generation of action potentials (APs). Ventricular- and atrial-like EHTs, called Ctrl- and RA-EHTs respectively, were transduced with lentivirus expressing ChR2 (H134R) and were chronically optically paced at 3 Hz and 5 Hz, respectively. Optical tachypacing induced electrical remodeling in both Ctrl- and RA-EHTs. Specifically, in Ctrl-EHTs optical tachypacing shortened AP duration and effective refractory period leading to higher tachycardia inducibility. In RA-EHTs, upstroke and conduction velocity speeded up. Spontaneous beating became highly irregular. The tachypacing-induced propensity for arrhythmias of both ventricular- and atrial-like EHTs might be related to altered calcium handling.

In conclusion, this work combined the development of an *in vitro* model of human atrium and ventricle with a tachypacing protocol based on the recently developed optogenetic technique. Tachypacing induced different remodeling in ventricular- and atrial-like EHTs. These *in vitro*

Abstract

hiPSC-based models may be useful to improve insight in arrhythmia mechanism and to test new drug candidates.
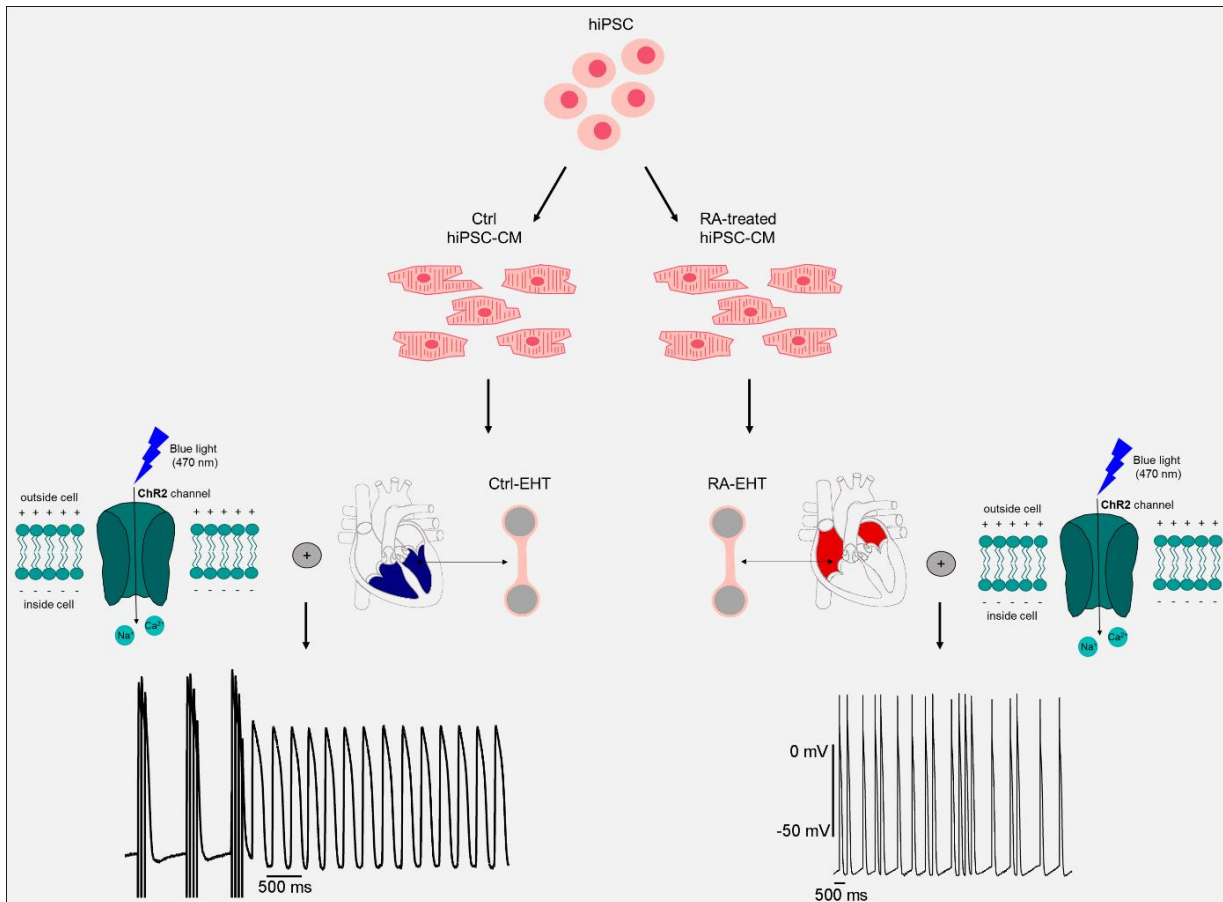
Graphical abstract. HiPSC obtained from healthy donors were differentiated with and without retinoic acid (RA) treatment. These cells were used to cast Ctrl- and RA-engineered heart tissues (EHTs). Ctrl- and RA-EHTs showed molecular and functional characteristics resembling human ventricular and atrial tissue, respectively. Both EHTs were transduced with channelrhodopsin 2 to perform optogenetic pacing. Ctrl- and RA-EHTs were optically paced for three weeks at 3 and 5 Hz, respectively. Chronic optical tachypacing induced higher vulnerability to tachycardia episodes in Ctrl-EHTs and higher beating irregularity in RA-EHTs.

9.   Zusammenfassung

Vorhofflimmern (VHF) tritt bei 2% der Gesamtbevölkerung auf und ist damit die häufigste Herzrhythmusstörung. Das Problem der derzeitigen pharmakologischen Therapien für VHF ist sowohl die geringe Wirksamkeit als auch schwerwiegende Nebenwirkungen. Für die Entwicklung von neuen pharmakotherapeutischen Ansätzen dient bislang menschliches Herzvorhofgewebe. Menschliches Gewebe ist jedoch nur begrenzt verfügbar. Kardiomyozyten (KM), die aus humanen induzierten pluripotenten Stammzellen (hiPSC) gewonnen werden, haben ihr Potenzial in der Entwicklung von Krankheitsmodellen und für die vorklinische Arzneimittelentwicklung wiederholt unter Beweis gestellt. Die bisher aus hiPSC differenzierten KM ähneln in ihrem Phänotyp allerdings überwiegend ventrikulären KM. Es ist bekannt, dass all-trans Retinsäure (RS) die Differenzierung von atrialen KM aus menschlichen pluripotenten Stammzellen begünstigt. Für die vorliegende Arbeit wurden hiPSC von gesunden Spendern mit RS (1 µmol/L) behandelt, um sie zu KM atrialen Phänotyps zu differenzieren. RS- und Kontroll-hiPSC-KM, die atrialen bzw. ventrikulären Myozyten ähneln, wurden verwendet, um künstliche Herzmuskelgewebe (EHTs) herzustellen. EHTs aus RS-hiPSC-KM zeigten wichtige strukturelle, molekulare und funktionelle Eigenschaften des menschlichen Atriums. Der atriale bzw. ventrikuläre Phänotyp der EHTs wurde im direkten Vergleich mit Gewebe aus dem linken oder rechten Ventrikel von Patienten bestätigt, die sich einer Operation am offenen Herzen unterzogen hatten.

Chronisches Tachypacing wird häufig bei Tieren eingesetzt, um Herzfunktionsstörungen zu induzieren und Mechanismen der Herzinsuffizienz und anhaltender Arrhythmien (wie VHF) zu untersuchen. EHTs aus phänotypisch atrialen KMs wurden generiert, um deren Nutzbarkeit für ein menschliches Vorhofflimmer-Modell zu untersuchen. Um Zelltoxizität durch langfristige elektrische Stimulation zu vermeiden, wurde ein optogenetisches Stimulationsverfahren angewendet. Dieses Verfahren basiert auf der Verwendung von Channelrhodopsin 2 (ChR2), einem lichtempfindlichen Ionenkanal, der, sobald er durch blaues Licht (470 nm) aktiviert wird, den Einstrom von Kationen (hauptsächlich Na^+) ermöglicht, was zur Depolarisation des Membranpotenzials und zur Entstehung von Aktionspotentialen (AP) führt. Ventrikuläre und atriale EHTs, die hier als Strg- und RA-EHTs bezeichnet werden sollen, wurden zunächst mit einem für ChR2 (H134R) codierenden Lentivirus transduziert und chronisch optisch mit einer Frequenz von 3 Hz bzw. 5 Hz stimuliert. Optogenetisches Tachypacing induzierte ein elektrisches Remodeling sowohl bei Strg- als auch bei RA-EHTs. Insbesondere in Strg-EHTs

verkürzte optisches Tachypacing die AP-Dauer und die effektive Refraktärzeit, was das Induzieren von Tachykardien vereinfachte. Bei RS-EHTs beschleunigten sich die Aufstrichgeschwindigkeit und Erregungsleitung. Die spontanen Kontraktionen wurden unregelmäßig. Die durch Tachypacing ausgelöste Neigung zu Arrhythmien sowohl ventrikulärer als auch atrialer EHTs könnte auf verändertes Calcium-Handling zurückzuführen sein.

Diese Arbeit kombiniert die Entwicklung eines in vitro-Modells für menschliches atriales und ventrikuläres Myokard mit einem Tachypacing-Modell, welches auf der erst kürzlich entwickelten optogenetischen Stimulationstechnik basiert. Tachypacing löste unterschiedliche elektrophysiologische Veränderungen in atrialen und ventrikulären EHTs aus. Diese hiPSC-KM basierten Modelle könnten neue Einblicke in die dem VHF zugrunde liegenden Mechanismen geben und außerdem die Testung neuer therapeutischer Substanzen in einem humanen Modell ermöglichen.

10. Acknowledgments

First of all I would like to thank my parents for supporting me throughout these three years of my PhD. I am very grateful to have two wonderful sisters, who share with me all the successful and difficult periods of my life. A special thanks goes to my boyfriend that encouraged me and took care of me every day during the last three years. I would like to thank also Andrea Arneri for being an amazing friend and always helping me whenever I need.

I would like to thank Bernardo Dolce who shared with me this experience since the first day and has been my italian family in Hamburg. I would like to thank also Antonia Zech and Miria Schulze because they have been perfect colleagues and more importantly great friends. I thank Zafar Iqbal and Pierre Bobin for their altruism. They always offered me their help with a big smile.

I want to thank Dr. Torsten Christ for supervising my work, helping me whenever I had a problem and especially for sharing with me his enthusiasm about cardiac electrophysiology.

I would like to thank Prof. Arne Hansen and Dr. Bärbel Ulmer for being always available and answering to all my questions. I want to highlight my thanks to Dr. Marc Lemoine for always giving me new ideas and challenging my scientific thinking. A very important thank you is dedicated to Anna Steenpass for her help, but most importantly for her smile and hugs.

I would like to thank all the people of Afib TrainNet for sharing this experience with me on a professional and personal level. Thanks to this network I had the opportunity to learn and get feedback from successful experienced researchers and young scientists. I will always have nice memories of our meetings around Europe.

Finally, the biggest thank is dedicated to Prof. Thomas Eschenhagen for giving me the opportunity to undertake this PhD program and for always supporting my ideas. He has been a great teacher and I will always have a profound admiration for his extraordinary knowledge.

I really appreciate the help from the members of the hiPSC-CM working group at the Department of Experimental Pharmacology and Toxicology with stem cell culture and CM differentiation. I would like to acknowledge the FACS Core unit and the Microscopy Imaging Facility (umif) of the UKE. I would also like to thank Susanne Krasemann and Kristin Hartmann (mouse pathology core facility of the UKE) for their assistance in

Acknowledgments

11. CV

Work experience

March 2016 – present *University Medical Center Hamburg-Eppendorf* **Hamburg, Germany**	**Marie Skłodowska-Curie ITN (AFib-TrainNet) PhD fellow** Optogenetics for modelling atrial fibrillation in 3D tissues composed of atrial-like hiPSC-CMs
March 2017 – May 2017 *Clyde Biosciences Ltd* **Glasgow, United Kingdom**	**Visiting PhD fellow** Voltage and contractility measurements in atrial and ventricular-like myocytes
Oct 2015 – March 2016 *Business Integration Partners* **Milan, Italy**	**Business Analyst** IT Consultancy for Energy Industries Analysis and Quality Assurance of IT platforms
Jul 2015 – Oct 2016 *Business Integration Partners* **Milan, Italy**	**Internship** IT Consultancy for Energy Industries Analysis and Quality Assurance of IT platforms
Oct 2014 – April 2015 *Laboratory of Cardiac Surgery Engineering of University hospital* **Basel, Switzerland**	**Research assistant** Responsible for Lab training for new Lab members

Education

Sep 2013 – April 2015 *Politecnico di Milano* **Milan, Italy**	**Master's Degree in Biomedical Engineering** with emphasis on Biomechanics and Biomaterials
Nov 2014 – April 2015 *Laboratory of Cardiac Surgery Engineering of University hospital* **Basel, Switzerland**	**Master Thesis** Generation of a microfluidic device to promote cardiac maturation Final score: 110/110
Feb 2013 – Jul 2013 *Eindhoven University of Technology* **Eindhoven, Netherlands**	**Master's Degree program Biomedical Engineering** Erasmus scolarship

Sep 2009 – Jul 2012	**Bachelor's Degree in Biomedical Engineering**
Politecnico di Milano	Final score: 107/110
Milan, Italy	

Jul – Aug 2010	**Business English course**
University of California at San Diego	
San Diego, USA	

Publication

Present	Submission of the scientific paper entitled:
	"Optogenetics for modelling tachycardia in engineered heart tissue"

Present	Submission of the scientific paper entitled:
	"DNA methylation profiling allows for rapid detection of atrial and ventricular cardiomyocyte lineage identity"

Present	Submission of the scientific paper entitled:
	"Generation of human engineered heart tissue patches for cardiac repair"

December 2018	Publication of the scientific paper entitled:
	"Atrial-like engineered heart tissue – a new in vitro model of the human atrium"

March 2018	Publication of the scientific paper entitled:
	"A three-dimensional in vitro dynamic micro-tissue model of cardiac scar formation"

February 2016	Publication of the scientific paper entitled:
	"Beating heart on a chip: a novel microfluidic platform to generate and assess functional 3D cardiac microtissues"

Congress participation

Poster	Establishment of an optogenetic human Engineered Heart Tissue platform
	ISHR, Hamburg, July 2017

Poster	Retinoic acid-treated HIPSC-CM: a suitable model for human atrium?
	EHRA, **Wien**, June 2017
Poster	Retinoic acid-treated HIPSC-CM: a suitable model for human atrium?
	Cardiac Arrhythmia Symposium, Copenhagen, June 2017
Presentation	Optogenetics for modelling tachycardia in engineered heart tissue
	NCCR Retreat, Tremsbütel, June 2018
Presentation	Establishment of an optogenetic human Engineered Heart Tissue platform
	ISHR, Hamburg, July 2017

Honors

21 December 2015	Award for the **Best Intern 2015 of Business Integration Partners**
24 September 2015	**Italian National Group of Bioengineering (GNB) award for the master thesis in Biomedical Engineering 2015**
	"Design of a microfluidic device for cyclic mechanical stimulation of three-dimensional cardiac cell constructs"

Additional information

Languages	**Italian:** native; **English:** fluent; **German:** basic; **Spanish**: basic;
Voluntary work	Volunteer at the Centro de Atenciòn y Educaciòn a la Familia (CAEF) in Trujillo (Peru), house for children without family that have been abused;
International Experience	Lived for six months in the Netherlands for Erasmus program and six months in Switzerland for the master thesis;
	Lived three years in Germany for PhD and 3 months in Scotland for PhD secondment;
Computer skills	

- MS Office Suite (Word, Excel, Power Point),
- Mac OS,
- European Computer Driving License (ECDL);
- Dev C ++ programming language,
- Matlab,
- Abaqus (finite elements analysis software),
- FreeFem, Comsol multiphysics ,
- Photoshop, Adobe Illustrator and ImageJ
- GraphPad Prism;

CV

Practical skills

- Biomechanical constructions,
- Biomaterials and instrumental analysis,
- Design and fabrication of PDMS based microfluidic devices,
- Nanoindentation,
- Atomic force microscopy,
- Cell culture, immunohistochemistry, immunofluorescence and confocal microscopy,
- Cardiac differentiation of hiPSC,
- Electrophysiology techniques: sharp microelectrodes, patch clamp,
- Molecular biology techniques: qPCR, WB, nanostring.

Driving license   European driving license type B

Other interests   **Ballet:** member of the ballet Academy in Milan (Italy) from 1995 to 2008

Attended international stage of ballet in 2006-2008

Synchronized swimming, traveling and photography.

12. Affidavit - Eidesstattliche Versicherung

I hereby expressly declare that I have written the work myself and without outside help, not used sources and tools other than those stated, and individually acknowledged the parts taken literally or in terms of content from the works used according to the edition (edition and year of publication), volume and page of the work used. Furthermore, I declare not to have submitted the dissertation to a subject representative at another university for review or otherwise applied for admission to a doctorate. I consent to my dissertation being examined by the Dean's Office of the Faculty of Medicine using a standard plagiarism detection software.

Signature: Marta Lemme

Ich versichere ausdrücklich, dass ich die Arbeit selbständig und ohne fremde Hilfe verfasst, andere als die von mir angegebenen Quellen und Hilfsmittel nicht benutzt und die aus den benutzten Werken wörtlich oder inhaltlich entnommenen Stellen einzeln nach Ausgabe (Auflage und Jahr des Erscheinens), Band und Seite des benutzten Werkes kenntlich gemacht habe.

Ferner versichere ich, dass ich die Dissertation bisher nicht einem Fachvertreter an einer anderen Hochschule zur Überprüfung vorgelegt oder mich anderweitig um Zulassung zur Promotion beworben habe.

Ich erkläre mich einverstanden, dass meine Dissertation vom Dekanat der Medizinischen Fakultät mit einer gängigen Software zur Erkennung von Plagiaten überprüft werden kann.

Unterschrift: Marta Lemme